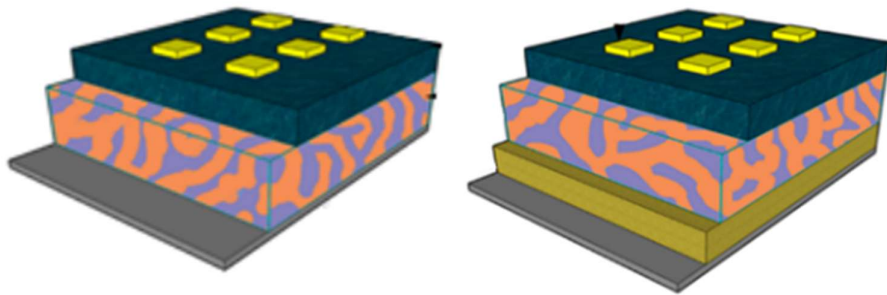


Journal of the National Science Foundation of Sri Lanka





JOURNAL OF THE NATIONAL SCIENCE FOUNDATION OF SRI LANKA

Editorial Board

Ajit Abeyssekera (Editor in Chief)
J.K.D.S. Jayanetti
L.P. Jayatissa
P. Prasad M. Jayaweera
Jagath Manatunge
S.S.N. Perera
Rohini de A. Seneviratne
Saman Seneweera
S.A.H.A. Suraweera
P. Wijekoon
M.J.S. Wijeyaratne

Language Editor

R.D. Guneratne
Sithy S. Iqbal

Editorial Office

Nadeeja Wickramarachchi (Principal Scientific Officer)
Uthpala T. Karunarathne (Senior Scientific Officer)
Upuli Ratnayake (Scientific Officer)

International Editorial Advisory Board

Chamil Abeykoon, UK
Dilanthi Amaratunga, UK
Dilantha Fernando, Canada
Leslie Gunatilaka, USA
Saman K. Halgamuge, Australia
Kithsiri W. Jayasena, Australia
Vassilios Kapaklis, Sweden
Wah Yun Low, Malaysia
Thomas Mathew, USA
Shanthi Mendis, Switzerland
Javier Francisco Ortega, USA
Malik Peiris, Hong Kong
Kamal Premaratne, USA
Nalin Samarasingha, USA
Ravi Silva, UK

Impact Factor: 0.682

Publication : Published quarterly (March, June, September and December) by the National Science Foundation of Sri Lanka.

Manuscripts: Research Articles, Research Communications, Reviews and Correspondences in all fields of Science and Technology may be submitted for consideration for publication. A guide to the preparation of manuscripts is provided in each issue. The guidelines may also be obtained by visiting the NSF website.

Disclaimer: No responsibility is assumed by the National Science Foundation of Sri Lanka for statement and opinions expressed by contributors to this Journal.

Manuscripts and all correspondence relating to them should be sent to the Editorial Office, National Science Foundation, 47/5, Maitland Place, Colombo 07, Sri Lanka.

Fax: 94-11- 2694754
E-mail: jnsf@nsf.gov.lk
JNSF home page: <http://www.nsf.gov.lk/index.php/nsfscience-magazine>

Publication : A publication fee of US\$ 250 will be levied for each manuscript except, when the corresponding author is affiliated to a Sri Lankan institution, in two stages.

- A processing fee of US\$ 20 will be levied for each manuscript at peer-review stage.
- Remaining US\$ 230 will be charged for accepted articles at the time of publication.

Copyright : © National Science Foundation of Sri Lanka

Articles in the Journal of the National Science Foundation of Sri Lanka are Open Access articles published under the Creative Commons CC-BY-ND License (<http://creativecommons.org/licenses/by/4.0/>). This license permits use, distribution and reproduction, commercial and non-commercial, provided that the original work is properly cited and is not changed anyway.

Indexing : The JNSF is indexed in Science Citation Index Expanded, Journal Citation Reports/Science Edition, BIOSIS Previews, Zoological Record, Biological Abstracts, Chemical Abstracts, Scopus, TEEAL, Ulrich's, AGRICOLA and EBSCOhost, CAB Abstracts

CONTENTS

EDITORIAL

- 183 Ethics of research**
Rohini de Alwis Seneviratne

REVIEW ARTICLE

- 185 Polycyclic aromatic hydrocarbons and food safety: A review**
U Samarajeewa

RESEARCH ARTICLES

- 205 Sea level variability at Colombo, Sri Lanka, inferred from the conflation of satellite altimetry and tide gauge measurements**
HMI Prasanna, MDEK Gunathilaka and HB Iz
- 215 Prevalence of histamine forming bacteria in selected nodes of the supply chain of Sri Lankan Yellowfin tuna**
PH Ginigaddarage, GJ Ganegama Arachchi, KWS Ariyawansa and CM Nanayakkara
- 225 Simulation and numerical analysis of SOA- based all optical NAND gate for high data rate communication**
V Anusooya, S Ponmalar, MSK Manikandan and S Gobalakrishnan
- 237 Effect of degree of saturation on pullout resistance of soil nailing in lateritic soil**
KASN Fernando and NH Priyankara
- 253 Efficiency boost of inverted polymer solar cells using electrodeposited n-type Cu₂O electrons selective transport layers (ESTLs)**
WTMAPK Wanninayake, DGKK Namawardana, RMG Wanigasekara, KMDC Jayathilaka, RP Wijesundera and W Siripala
- 263 Identification of depositional features in the Albian and Aptian sections over the hydrocarbon exploration block M2 on the Mannar Basin, Sri Lanka**
TM Munasinghe, U Premarathne and DA Weerasinghe
- 273 Study on compositional changes of king coconut (*Cocos nucifera* var. *aurantiaca*) water and kernel during maturation and evaluation of optimum quality characteristics targeting commercial applications**
MD Jayasinghe, MMNP Gunasekara, MGDS Perera, KDSM Karunaratna, GU Chandrasiri and IGN Hewajulige
- 287 Fluoride analysis in aqueous solutions - a comparison of two colorimetric methods**
A Fernando, S Liyanage and AT Cooray
- 299 Natural α -glucosidase inhibitors from selected medicinal plants in Malaysia**
SY Liew, Y Sivasothy, NN Shaikh, K Javaid, DM Isa, VS Lee, MI Choudhary and K Awang
- 311 Molecular and phenotypic characterization of *Colletotrichum plurivorum* and *Colletotrichum musae* causing banana anthracnose disease in the Central Province of Sri Lanka**
WMS Kurera, NKB Adikaram, DMD Yakandawala, SS Maharachchikumbura, L Jayasinghe and K Samarakoon
- 327 *In-vitro* wound healing potential of *Ziziphus oenoplia* (L.) Miller**
IACC Ilangakoon and AMRG Athapaththu

341 Spatial and temporal changes of land use land cover distribution in selected sites of the southern coastal zone of Sri Lanka

WMIC Wijesundara, DUV Gunathilaka, SK Madarasinghe, J Andrieu, G Muthusankar, NR Kankanamge and KAS Kodikara

359 Preliminary study on surface phytoplankton assemblages and physicochemical parameters, off the west and south-west coasts of Sri Lanka

HB Jayasiri

Guidelines for Contributors



Cover: Cross section of top illuminated inverted polymer solar cells on stainless steel substrates without (left) and with (right) n-Cu₂O electron selective transport layers
See *J.Natn.Sci.Foundation Sri Lanka* 2023 51 (2): 253 - 261

EDITORIAL

Ethics of research

Ethical conduct of research involving humans has gained relevance and importance over the years with the expansion of research beyond boundaries of traditional medical and clinical research into a multiplicity of disciplines with human participation. Human research is regarded as research conducted on or with or about people, or their tissues or cells or data obtained from them.

Historically, it is stated that the Greek Philosopher Aristotle (384-322 BCE) was probably the first to discuss principles of ethics 'by studying and offering criteria to assess human behaviour'. It is believed that he taught a course of ethics at the Lyceum during his mature years which was based on the many treatises he wrote on the subject. Increased attention to ethics in human research started after the Second World War following the judgment of the International Military Tribunal which also included 10 principles of permissible medical experiments which have since then been referred to as the Nuremberg Code (1949). Later discussions by the World Medical Assembly of the Code led to the adoption of the Helsinki Declaration (1964) which has been revised many times since then.

The Council for International Organizations of Medical Sciences (CIOMS) which in association with the World Health Organizations (WHO) undertook its work on ethics in biomedical research in late 1970s. It has published an updated version with a wider scope of coverage titled 'International Ethical Guidelines for Health-Related Research Involving Humans' (2016). Close cooperation with World Medical Assembly has ensured that the guidelines are closely aligned to the Helsinki Declaration.

Traditionally, ethics has received much attention both in clinical practice and in health research. Faculties of Medicine were the first to establish ethics review boards and ethics review committees in Sri Lanka to undertake review of research proposals with human participation for ethical aspects and issues and granting approval. The primary aim is to safeguard the interests and right of participants of research and prevent their exploitation. There is no doubt about the value of health research and the benefits it has brought and will continue to bring to ensure health, wellbeing, safety and quality of life of people. Most research on human participants is simple, observational, descriptive and non-invasive and the ethical issues though may be minimal, still needs explicit attention and review by an ethics review board before approval. The more complex research where human participants are subject to 'experimentation' or 'interventions' has many ethical issues that need to be assessed by recognized ethics review committees with experience and capability to do so. If a new drug, a new vaccine, medicinal product, device, or equipment not already in use by people is to be tested on humans before being granted approval for use in day-to-day life by the appropriate authority, the researcher should adopt recommended procedures, regulations and registration mechanism prescribed. In Sri Lanka any interventional research requires applying and obtaining approval of ethics review committees that have been gazetted under the National Medicines Regulatory Authority (NMRA) as being approved by name to undertake ethics review. The interventional research should also be registered with the Sri Lanka Clinical Trials Registry. Both these need to be submitted to the Clinical Trials Evaluation Committee of the NMRA in order to be evaluated prior to being granted approval and registration. These approvals and registrations are also requested by peer reviewed high impact journals to consider such research manuscripts for publication.

There are certain values which provides the framework for principles guiding formulation of research proposals and ethics of research. These include and are not limited to respect, integrity, justice, beneficence and research merit. It is implicit in research that badly designed, conducted, analysed and reported research is unethical. Clinical Centre researchers at National Institute of Health of USA have enunciated seven principles to guide the conduct of ethical research. These are social and clinical value, scientific validity, fair subject selection, favourable risk benefit ratio, independent review, informed consent, respect for potential and enrolled subjects.

Given the importance of scientific merit and integrity of research, good research practice needs much attention both by researchers and research institutions. In order to meet these needs the National Health Research Council and the Education, Training and Research Unit of the Ministry of Health have taken steps to publish, 'The Code of Conduct on Health Research in Sri Lanka' (2018) (available at http://www.health.gov.lk/moh_final/english/public/elfinder/files/publications/2018/TheCodeofConduct.pdf)

The Code covers aspects of: formulation of research proposals; management of research data and primary materials; collaborative research; conflict of interest; supervision of research; peer review, and dissemination of research findings, publication and responsible authorship.

With the expansion of research on human participation into many other sciences such as branches of engineering, computing, bio technology, genetics, artificial intelligence, machine learning, nano technology and others, the ethical issues of human research have reached a new dimension. It has to be emphasized that whatever the branch of science or discipline, if the research requires human participants, then approval of an ethics review committee is a must. Thus, it behoves on research institutes, universities, and faculties to establish ethics review committees beyond the traditional practice of having ethics review committees in medical faculties. It is necessary that members of such a committee, function within the set terms of references, standard operating procedures, ensure confidentiality and also have appropriate training in ethics of research, approval processes and documentation. In Sri Lanka too universities have gone one step ahead to establish ethics review committees at university level to facilitate research on humans in disciplines other than health and medical practice.

Time has come when universities and research institutions take steps to develop codes of conduct on research, conduct courses on such practices and ethics of research for all researchers in order to safeguard the interests and safety of both researchers and participants of research.

Rohini de Alwis Seneviratne

REVIEW ARTICLE

Food Safety

Polycyclic aromatic hydrocarbons and food safety: A review

U Samarajeewa*

Department of Food Science and Technology, Faculty of Agriculture, University of Peradeniya, Peradeniya, Sri Lanka.

Submitted: 26 September 2022; Revised: 05 January 2023; Accepted: 27 January 2023


Summary: Polycyclic aromatic hydrocarbons (PAHs) are of petrogenic or pyrogenic origin. Of the known few hundred PAHs, 16 are identified to be toxic, of which 8 are teratogenic. Of the 8, 4 are carcinogens. Among them, Benzo[*a*]pyrene (BaP) possesses the highest carcinogenicity and is used as a marker in toxicity studies. PAHs of petrogenic origin contaminate soil, water and air. They may occur in air associated with dust particles. PAHs of pyrogenic origin are generated during burning of wood and other organic matter. They are also produced from lipids and carbohydrates during heating of foods. PAHs are mostly identified with grilling, smoking, frying, roasting and toasting of foods. Among the foods, formation of PAHs is studied mostly in association with grilling of fish and meat, where contacts occur between the dripping lipids and naked flames. The generated PAHs get deposited back on fish and meat muscles. PAHs in smoke are deposited on food surfaces on exposure to contaminated air from the vehicle fumes and smoke curing of foods. PAHs are formed during mechanical expulsion of edible oils. Presence of markers, carcinogenic PAHs and total PAHs in different foods and their extent of formation and deposition is discussed in relation to food safety hazards and health implications. Among the local foods and food preparation habits, the role of coconut oil, smoke curing of foods and formation of PAHs even under mild conditions of heat such as manufacture of black tea are reviewed. Recommendations for future actions, research and implementing food regulations to minimize PAHs in foods are presented.

Keywords: Carcinogens, deep frying, PAHs, smoke curing.

INTRODUCTION

Polycyclic aromatic hydrocarbons (PAHs) are a group of organic compounds containing two or more aromatic rings linked in linear, angular or clustered forms. Mainly they contain carbon and hydrogen in their structures. A few PAHs containing nitrogen, oxygen and sulphur are derived from coal tar and petroleum products. Distillation and fractionation of coal tar and petroleum products, and operation of engines release PAHs to the atmosphere (Dabestani & Ivanov, 1999). Airborne PAHs tend to cause lung cancer. Among several hundreds of the PAHs, 16 implicated with toxic properties to humans are identified by International Agency for Research on Cancer (WHO, 2010). The PAHs are formed during incomplete combustion of organic matter including foods. They may be formed directly in foods during processing or cooking or may contaminate foods from the environment along the food chain (Figure 1).

The PAHs are produced as mixtures of compounds in all situations. Their presence in uncooked or unprocessed foods indicates environmental contamination of unprotected foods (Phillips, 1999). Food processing generates more PAHs than what is deposited from the environment. PAHs are lipid soluble, making them easily available for absorption through gastrointestinal tract when ingested with foods. WHO (2010) indicates that there is notable exposure to Benzo[*a*]pyrene (BaP) and other PAHs among the populations consuming toasted bread and grilled meats frequently. In Europe, high concern on PAHs associated with olive oil and smoked meats is evident in 1110 research publications during 1997 to 2010 (Sun *et al.*, 2019). The publications recognized formation of PAHs during food processing, presence of high concentrations in edible oils, and in smoked foods.

* smrjee@gmail.com;  <https://orcid.org/0000-0003-4481-5204>



This article is published under the Creative Commons CC-BY-ND License (<http://creativecommons.org/licenses/by-nd/4.0/>). This license permits use, distribution and reproduction, commercial and non-commercial, provided that the original work is properly cited and is not changed in anyway.

In Sri Lanka, the exposure of humans to PAHs would be predominantly through food, and to a lesser extent through the smoke in firewood kitchens, food processing kilns and vehicle emissions. The exposure through marine or inland fish is non-existent as the country is not engaged in coal or petroleum industries or major chemical extraction processes. Probable relationship between the high incidence of lung cancer in Sri Lanka (National Cancer Control Programme, 2021) and the exposure to PAHs through air is yet to be investigated.

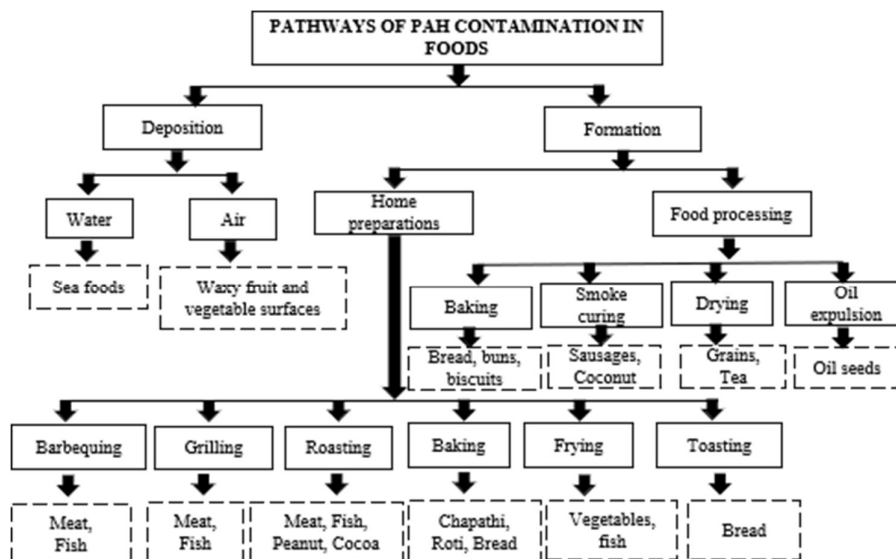


Figure 1: Pathways of entry of polycyclic aromatic hydrocarbons into human food chain

Chemistry and toxicity

There are a few hundred PAH compounds and their derivatives. They are pyrolytic products of organic matter such as wood and petroleum derivatives exposed to temperatures in the range 350–1500 °C under limited access to oxygen (Abdel-Shafy & Mansour, 2016). The chemical pathways generating PAHs and soot from simple molecules during combustion are well understood (Richter & Howard, 2000). Petrogenic PAHs may form at low temperatures but under high pressure in the earth crust. The PAHs exhibit low solubility in water and high solubility in the lipids. Their lipophilic nature leads to easy association with foods and interactions with cellular systems in the human body. In general, up to 16 PAHs have been identified by different authorities as hazardous to humans (Table 1). Zelinkova and Wenzl (2015) reviewed the hazardous PAHs identified by the United States Environmental Protection Agency, the International Agency for Research on Cancer, the Scientific Committee on Food, the Joint FAO/WHO Expert Committee on Food Additives, the International Programme on Chemical Safety, and the European Food Safety Authority (EFSA, 2008).

The research on hazards associated with PAHs in foods initially focused on the total PAHs and the BaP. Of the PAHs in Table 1, BaP is the most carcinogenic and is used as a marker to assess the carcinogenicity of foods. Due to variations in the carcinogenic activity among PAHs, it is difficult to quantify the collective hazardous nature of them in foods. With time, more hazardous clusters of 2 (BaP & Chr) as carcinogenic, 4 (BaA, BaP, BbFA & Chr) as mutagenic, and 8 (BaA, BaP, Chr, BkFA, BbFA, IP, DBahA & BghiP) as toxic were recognized. They are expressed as sum of 2 (Σ_2), sum of 4 (Σ_4) and sum of 8 (Σ_8) in discussing the food safety hazards (Table 1).

Generally, the PAHs by themselves are non-reactive towards biological molecules in living systems. The metabolic activation of PAHs leads to notable toxic reactions (Hongtao, 2002). The PAHs may also react with sulphur and nitrogen oxides in the environment mediated by solar energy, increasing their toxicity (Naccari *et al.*, 2011). Increased hazards due to synergistic effects among the PAHs and their derivatives may occur. The diols and epoxides of PAHs are powerful oxidizing agents capable of inducing biological damage to cells.

Wilkinson *et al.* (1993) reported activation of anthracenes by active oxygen. BaP diols and epoxides undergo bio-transformations to bind covalently to DNA, initiating mutations and tumor formation in the animal and human cells (Dabestani & Ivanov, 1999).

Table 1: PAH compounds identified to be associated with food safety hazards

Name (Abbreviation)	Hazard*	IARC carcinogenicity	(Rings) mol wt.	Sum ^Δ
Benzo[<i>a</i>]anthracene [†] (BaA)	m/g/c	2B	(4) 228	8, 4
Benzo[<i>b</i>]fluoranthene [†] (BbFA)	m/g/c	2B	(5) 252	8, 4
Benzo[<i>j</i>]fluoranthene (BjFA)	m/g/c	2B	(5) 252	
Benzo[<i>k</i>]fluoranthene [†] (BkFA)	m/g/c	2B	(5) 252	8
Benzo[<i>g,h,i</i>]perylene [†] (BghiP)	m/g	3	(6) 276	8
Benzo[<i>a</i>]pyrene [†] [BaP]	m/g/c	1	(5) 252	8, 4
Chrysene [†] [Chr]	m/g/c	2B	(4) 228	8, 4
Cyclopenta[<i>c,d</i>]pyrene (CPP)	m/g/	3	(5) 226	
Dibenzo[<i>a,h</i>]anthracene [†] (DBahA)	m/g/c	2A	(5) 278	8
Dibenzo[<i>a,e</i>]pyrene (DBaeP)	m/g	3	(6) 302	
Dibenzo[<i>a,h</i>]pyrene (DBahP)	m/g/c	2B	(6) 302	
Dibenzo[<i>a,i</i>]pyrene (DBaiP)	m/g/c	2B	(6) 302	
Dibenzo[<i>a,l</i>]pyrene (DBalP)	m/g/c	2A	(6) 302	
Indeno[1,2,3- <i>cd</i>] pyrene [†] (IP)	m/g/c	2B	(6) 276	8
5 methyl chrysene (MCH)	m/g/c	2B	(4) 242	
Benzo[<i>c</i>]fluorene (BcFL)	m/g	3	(4) 216	

[†]Identified by US EPA as priority 16 PAHs causing human health risks including Acenaphthene, Acenaphthylene, Anthracene, Naphthalene, Fluorene, Phenanthrene, Fluoranthene and Pyrene (Hussar *et al.*, 2012). * m = mutagenic; g = genotoxic; c = carcinogenic.

Sum^Δ Indicate the group of 8 or 4 identified to use in expressing combined carcinogenic effect in interpreting test reports. It appears that sum of 8 does not give additional advantage over sum of 4 and there are situations where BaP is absent, but Chrysene present in foods.

IARC classified carcinogenicity as 1 = highly carcinogenic, 2A = probably carcinogenic, 2B = possibly carcinogenic and 3 = not classifiable as carcinogenic to humans, 4 = probably not carcinogenic to humans

Kazerouni *et al.* in 2001 have established correlation coefficient of 0.87 between BaP and total PAHs, and 0.98 between Σ_8 PAHs and BaP after testing many foods, justifying the use of BaP as a marker. However, Kelly *et al.* (2021) examining the atmospheric exposure of humans to PAHs and the cancer risk indicated that only 11% of cancer is associated with BaP and the rest is with the other PAHs. They do not justify the use of BaP as a marker. The PAHs reach the organs of the human body through inhalation, skin absorption and ingestion of food, taking different routes and undergoing different interactions making it difficult to apply information from inhalation to that of dietary exposure.

Some PAHs may be present as vapour in the air or absorbed into dust and other particles forming solid particulates. PAHs with 2-3 rings tends to be present predominantly in the vapour phase and those with 5 or more rings in particulate phase. Their molecular nature governs absorption or deposition in foods. The PAHs with 2-3 rings tend to get adsorbed by waxy surfaces in plants. The PAHs originating from petroleum sources could also enter the food chain through the water and fishes that consume them, or the plants that may adsorb

them, or absorb from soil. Filter feeding mollusks tend to accumulate more PAHs (Afolabi *et al.*, 1983). Moriji *et al.* (2019) identified bioaccumulation of 16 PAHs in fish at concentrations in the region of 11 - 4208 ng/L in water. However, PAHs in fish muscles is reported to get metabolized leaving no toxic residues to enter the human food chain. Tolerance limits are therefore not established in food regulatory systems for PAHs in fresh fish (Zelinkova & Wenzl, 2015). Stringent tolerance limits are set for foods containing lipids or fried in lipids, which may generate PAHs on exposure to high temperatures.

The regulatory limit for PAHs varies in different countries. The Regulations of the European Commission (EC) stipulates maximum limits for BaP and Σ_4 consisting of benzo[*a*]pyrene, benzo[*a*]anthracene, benzo[*b*]fluoranthene and chrysene (European Commission, 1998). The EC regulations are revised regularly based on new evidence from EU countries. Current regulations are summarized in Table 2.

Table 2: Regulatory limits of European Commission

Food group	Regulatory limits in $\mu\text{g}/\text{kg}$ BaP & Σ_4 (products)	EC regulations
Cereals	1 & 1 (Processed cereal foods)	835/2011 (BaP & Σ_4)
Fats & oils	2 & 10 (Except cocoa butter and coconut oil) 2 & 20 (Coconut oil)	
Cocoa	5 & 30 (Fats from cocoa beans and derived products with certain exceptions) 5 & 15 (Fibre and fibre products as food ingredients)	1933/2015 (BaP & Σ_4)
Smoked/barbequed	5 & 30 (Smoked meat and products, smoked fish and products) 5 & 30 (Smoked sprats, mollusks, heat treated meat products) 6 & 35 (Smoked bivalve mollusks)	1327/2014 (BaP & Σ_4) 835/2011 (BaP & Σ_4)
Special foods	1 & 1 (Infant formulae, processed cereal based foods for infants)	
Banana	2 & 20 (Banana chips)	1933/2015 (BaP & Σ_4)
Supplements	10 & 50 (Containing botanicals, royal jelly, spirulina)	
Herbs	10 & 50 (Dried herbs)	
Spices	10 & 50 (Dried spices except cardamum and smoked capsicum species)	1255/2020 (BaP & Σ_4)
Drinking water	0.010 & 0.10 $\mu\text{g}/\text{L}$	835/2011 (BaP & Σ_4)

Table 3: Regulatory approach and limits in other systems and countries

System/ country	Regulatory approach / limits	Reference
Australia	Drinking water – BaP 0.01 ng/L	NHMRC, 2011
Brazil	Smoke flavourings – 30 $\mu\text{g}/\text{kg}$, Olive oil – 2.0 $\mu\text{g}/\text{kg}$, Drinking water – BaP 0.70 $\mu\text{g}/\text{L}$	Sampaio <i>et al.</i> , 2021
Canada	Olive pomace oils – BaP 3.0 $\mu\text{g}/\text{kg}$, Drinking water – BaP 0.04 $\mu\text{g}/\text{L}$	Health Canada (cited 2022)
China	Paddy rice, wheat, smoked or baked meat and aquatic products – BaP 5 $\mu\text{g}/\text{kg}$, Fats oils and oil emulsions – BaP 10 $\mu\text{g}/\text{kg}$	CFDA, 2017
Codex	No regulatory limits. Recommend code of good practices	CAC/RCP 68, 2009
India	Smoked fish – BaP 5 $\mu\text{g}/\text{kg}$	Indian Standard, 2016
USA	Drinking water – BaP 2.0 ng/L	US EPA (cited 2022)

EC also has regulations on the use of smoke liquids as flavouring agents in foods. The producers of smoke liquid are required to provide analytical information on 15 PAHs recognized by EC and the presence of BaP and BaA at concentrations below 10 and 20 $\mu\text{g}/\text{kg}$ respectively (European Commission, 2003). The regulatory approach and the limits in other countries are summarized in Table 3.

Quantification of PAHs require well designed sampling techniques as they are not distributed homogeneously in the foods. The glassware needs to be cleaned with special techniques to prevent cross contaminations.

The test samples need purifications using solid phase cartridges (SPE) prior to quantitation. Among the several SPE cartridges, the QuEChERS procedure has gained recognition (Gratz *et al.*, 2011). The quantitation of PAH uses GC-MS or LC-UVA or fluorescence detector techniques more commonly, with application of validated test methods practiced with strict laboratory quality control.

Biological effects

The biological effects are caused by the interference of PAHs with the cellular membranes and their enzymes. The PAHs can cause carcinogenic, mutagenic and immunosuppressive actions. Acute toxicity due to ingestion

of the PAHs is almost non-existent. There is much evidence on the chronic effects from dietary PAHs. The PAHs being lipophilic are absorbed by the cells. BaP with the highest lipophilic character could possibly enter chylomicrons and reach many body tissues. The PAHs undergo different biochemical reactions depending on the number of rings in the molecule and the conformational features. PAHs get modified into more active metabolites including epoxides, dihydrodiols and phenols. The metabolites may interact with Glutathione (GSH) or glucuronic acid in cells. The epoxides and dihydrodiols of the PAHs produced during cellular metabolism carry higher capacity to bind with DNA and cellular proteins leading to cell damage, mutations and cancer (Armstrong *et al.*, 2004). The genotoxic and carcinogenic effects through the epoxide and -diol derivatives of PAHs are well documented (Tarantini *et al.*, 2011). Interaction of the PAHs appears to cleave DNA molecules affecting cellular biochemical activities. The mechanisms used by each of the PAHs in cleaving DNA is shown to vary depending on the presence or absence of light (Hongtao, 2002).

The PAHs may follow mechanisms similar to tumor promoter 12-O-tetradecanoylphorbol-13-acetate in addition to serving as tumor initiators (Baird *et al.*, 2005). Shen *et al.* (2022) followed metabolomics with a focus on proteomics to explore BaP related intracellular responses through the viability and migration of KYSE-150 human oesophageal cells. They showed that BaP impedes the migration of oesophageal cells causing serious cellular damage even at short term exposure. The study suggests initiation of cancer risk at the cellular entry point of BaP to the human body through oral route. In contrast, Li *et al.* (2011) reported detoxification of PAHs through o-methylation of PAHs catechols in humans. Both biochemical activities may be happening in the body depending on the dosages of exposure and other factors specific to target organs and cells of the human body.

Van Grevenynghe *et al.* (2003) reported that several PAHs with known toxicological trends possess the capacity to impair differentiation of blood monocytes into functional macrophages *in vitro*. The same effect was not observed with the non-toxic Benzo[e]pyrene which is structurally close to BaP. The authors suggest that impairing of functional macrophages formation by PAHs may cause immunotoxicity leading to weakening of the human immune defense system. The concentrations of PAHs used in this study were of the same order as that reported in charcoal-broiled foods. Controlling the entry of PAHs to human body through foods appears to be an important step in protecting the immune systems.

The first step in carrying out risk assessments due to PAHs is through the exposure studies. Phillips (1999) reported that 96.2 % PAHs enter the human body through the diets of non-smoking persons of the age group 19–50 years. Representative mean dietary BaP intakes of 4 ng/kg bw/d with a high level of 10 ng/kg bw/d were established by WHO/FAO Joint Expert committee on Food Additives and Contaminants (JEFCA, 2005). Chronic effects such as reduced immune functions, cataracts, kidney and liver damages, breathing problems and asthma like symptoms are reported with the exposure to PAHs (Abdel-Shafy & Mansour, 2016).

There is much research on exposure of humans to PAHs from the air, especially through coal, coke, other industries and directly to soot and shale. After examining research data for 40 years, Mastrangelo *et al.* (1996) suggests that the safety levels established for air pollution does not seem to reflect real risk. Exposure to smoke containing PAHs associated with food preparations, mainly cooking, appears to be far below that of the industrial exposure situations in triggering hazards. Exposures to PAHs through use of firewood appears insignificant in the light of above information. Unfortunately, while the smoke gets detected sensorily by humans easily, the high amounts of the PAHs produced within foods is not. It is known that the amounts of PAHs deposited by smoke and visible on copra is 6–7 times less than PAHs generated during expulsion of coconut oil, which is not visible.

Contamination of PAHs in foods

The PAHs may be deposited in foods from the air and smoke or generated during heat processing or cooking. Ingestion of BaP by humans is reported to be in the range of 2-500 ng/d against inhalation of 10-50 ng/d (Singh *et al.*, 2016). The foods form a main pathway of exposure of humans to the PAHs, other than the workers engaged in industries emanating PAHs. The grilled foods and edible oils constitute major sources of PAHs in human diet. There is much research on PAHs in grilled fish and meat. Edible oils acquire PAHs pyrolytically during mechanical expulsion or frying of the foods.

Table 4: PAHs reported in foods ($\mu\text{g}/\text{kg}$)

Food	BaP	Σ_4 PAH	Σ_8 PAH	Total PAH	Reference
Olive oil from canned tuna	1.9			11.3	Moret <i>et al.</i> , 2005
Oil from grilled mushroom cans	11.3			47.1	
Charcoal grilled pork	2.9			Σ_{15} 144.7	Food and Environmental Hygiene Department, 2004
Charcoal barbequed beef	12 (median)			Σ_{15+1} 221 (median)	Rose <i>et al.</i> , 2015
Donor (kebab) meat	nd	2.21	3.17	Σ_{16} 6.08	Sahin <i>et al.</i> , 2020
Donor chicken	nd	2.45	3.15	Σ_{16} 4.42	
Meat balls	0.70	1.95	2.74	Σ_{16} 4.45	
Grilled chicken	nd	2.13	3.68	Σ_{16} 4.91	
Grilled fish	0.73	3.30	5.13	Σ_{16} 7.26	
Gas grilled pork	< 0.1			Σ_{15} 5.7	Food and Environmental Hygiene Department, 2004
Electric oven roasted pork	< 0.1			Σ_{15} 7.2	Olatunji <i>et al.</i> , 2014
Blended oil	2.04	Σ_3 5.34			
Sunflower seed oil	1.71	Σ_3 5.90			
Vegetable oil	0.5				Siddique <i>et al.</i> , 2021b
Sunflower oil	0.4				
Sesame oil	0.2				
Market edible oils Iran	0.90–11.33	3.51–84.03	7.41–117.12	129.28–195.4	Yousefi <i>et al.</i> , 2018
Chocolate	0.22	1.75		Σ_{15} 2.58	Ziegenhals <i>et al.</i> , 2009
Fresh grated coconut	nd		1		Wijeratne <i>et al.</i> , 1996a
Desiccated coconut	nd		11		
Copra (smoke dried)	3		102		
Parings (smoked)	5		109		
Copra meal	1		68		
Crude coconut oil	12		359		
Amaranth oil	1.32	10.5		Σ_{19} 101.6	Ciecierska & Obiedzinski, 2013b
Linseed oil	nd	0		Σ_{19} 115.0	
Common flax oil	nd	1.21		Σ_{19} 170.9	
Camelina oil	nd	2.47		Σ_{19} 41.3	
Pumpkin oil	15.7	35.0		Σ_{19} 234.3	
Sesame oil	1.23	4.25		Σ_{19} 30.1	
Poppy oil	nd	1.71		Σ_{19} 23.4	
Mustard oil	nd	2.73		Σ_{19} 35.0	
Safflower oil	nd	2.93		Σ_{19} 53.7	
Blackseed oil	1.98	15.84		Σ_{19} 221.2	
Walnut oil	nd	3.15		Σ_{19} 46.0	
Borage oil	1.0	4.12		Σ_{19} 66.2	
Evening primrose	nd	4.04		Σ_{19} 68.9	
Breast milk				Σ_{13} 0.84–696	Ssepuya <i>et al.</i> , 2022
Milk raw	0.27		5.4		Naccari <i>et al.</i> , 2011
Pasteurized milk	0.27		6.5		
Skimmed milk UHT	0.35		5.9		
Whole milk UHT	0.25		7.8		
Mullet fish (fresh)	4			Σ_{16} 65	Tongo <i>et al.</i> , 2018
Prawn (fresh)	2			Σ_{16} 106	
Crabs (fresh)	4			Σ_{16} 57	
Fish (unprocessed)			Σ_6 9.5–31.2	Σ_{15} 17–70	Dhananjayan & Muralidharan, 2012
Cocoa butter				Σ_{19} 16–74	Ciecierska, 2020
Chocolate candy	1.62	8.16		Σ_{14} 67.62	Kumari <i>et al.</i> , 2012
Chocolate	0.22	1.75		Σ_{15} 2.85	Ziegenhals <i>et al.</i> , 2009
Tea leaves		25–115			Duedhal-Olesen <i>et al.</i> , 2015a
Black tea	51	218			Zachara <i>et al.</i> , 2018
Green tea	13	76			
Red tea	13	90			
White tea	12	57			
Black dry tea		54.3			Phan <i>et al.</i> , 2020
Herbal dry tea		16.4			
Oolong dry tea		14.2			
Green dry tea		6.6			

Continued on page 191 –

- continued from page 190

Food	BaP	Σ_4 PAH	Σ_8 PAH	Total PAH	Reference
Black tea	9.42			Σ_{18} 23.32	Tran-Lam <i>et al.</i> , 2018
Fried noodles	3.6			Σ_{18} 9.6	
Fried snacks	0.93			Σ_{18} 1.74	
Dried vegetables	1.2			Σ_{18} 1.93	
Cherry coffee	4.52			Σ_{18} 15.0	
Stove grilled meat	1.08			Σ_{18} 1.43	
Coffee		2.2–5.1			Duedhal-Olesen <i>et al.</i> , 2015a
Bread				Σ_{19} 1.59–13.6	Ciecierska & Obiedziński, 2013a
Bread		0.19–0.46			Kacmaz, 2016
Breakfast cereals		0.10–0.87			
Jujube dried			2.32		Kim <i>et al.</i> , 2020
Milk bread			1.25		
Black sesame			1.17		
Barbequed pork		195			Duedahl-Olesen <i>et al.</i> , 2015b
Barbequed chicken		0.1			
Controlled barbeque		< 0.1			

nd – Not detected

The PAHs entering foods are grouped as ‘light’ and ‘heavy’ PAHs. Light PAHs (Naphthalene, Acenaphthene, Anthracene, Fluorene, Phenanthrene, and Pyrene) consists of 2-4 member rings and heavy PAHs (BaA, BaP, BbFA, BkFA, Chr, DBahA, BghiP, and IP) consists of 5 or more rings. The groups may best be described as low molecular weight and high molecular weight PAHs following information on Table 1. The hazardous PAHs in foods belongs to the heavy group.

The exposure of food lipids to high temperatures generates PAHs. In grilling, the melting lipids from meat and fish muscles drips direct on to flames producing PAHs. The PAHs get deposited back on the muscles. The formation of PAHs depends on the temperature, the distance of the foods from the flame and other factors. Comparing fuel sources in grilling fish and meat, BaP concentrations of 2.4–31.2 $\mu\text{g}/\text{kg}$ were reported with woodfire, against laboratory grilling with charcoal producing 0.7–2.8 $\mu\text{g}/\text{kg}$ (Akpambang *et al.*, 2009). Adeyeye and Ashaolu (2020) reported high concentrations of PAHs in commercially smoked catfish and grilled meat in Nigeria. They observed BaP and Σ_4 PAHs concentrations above the EU tolerance limits of 2 and 12 $\mu\text{g}/\text{kg}$ respectively.

Fish consume microplastics and nano-plastics in the seabed. Petrogenic BaP in the sea bottoms get absorbed into microplastics readily. While the nano-plastics by themselves have been shown non-toxic to brine shrimps and zebrafish, they were shown to serve as vectors to spread BaP in brine shrimps and zebrafish embryos causing toxicity (Martínez-Álvarez *et al.*, 2022). Entry of PAHs to the marine fish chain through microplastics may provide a pathway for exposure of humans to BaP. Increasing pollution of rivers and oceans with the microplastics pose an increasing challenge through PAHs in the aquatic food chain.

In a study on 15 PAHs in five fish types from Mumbai harbour in India, total PAHs of 17–70 $\mu\text{g}/\text{kg}$ and carcinogenic PAHs (Σ BaA, BbFA, BkFA, BaP, IP, and DBahA) 9.5–31.2 $\mu\text{g}/\text{kg}$ were reported (Dhanajayan & Muralidharan, 2012). The authors postulated exposure of the general population to 1.77–10.70 ng/kg bw /d. Of the 15 PAHs examined in this study, only 6–10 PAHs were observed in any of the 5 types of fish examined, suggesting variations in PAH accumulation among different fish types from the same contaminated water. The harbours tend to be polluted with petrogenic PAHs due to movement of ships and being physically protected regions of water. Dhanajayan and Muralidharan (2012) indicated that the exposure of persons to PAHs in fish from Mumbai is less than the values reported in Spain (626–712 ng/d), Kuwait (231 ng/d), and Korea (13.8–16.7 ng/kg bw/d). These variations are probably associated with both accumulation rates of PAHs and consumption rates of fish by the respective human populations. In the sea water of Cimandari river estuary in Indonesia, the PAHs concentrations were reported to be low. Of the 15 PAHs examined, the highest value reported for low molecular weight PAHs was 0.0096 $\mu\text{g}/\text{kg}$ and for high molecular weights was 0.0021 $\mu\text{g}/\text{kg}$ (Helfinalis *et al.*, 2021). Estuary is not polluted by discharge of fuel waste from ships.

A study examined 16 PAHs in 30 samples of fish of 3 species from the Niger Delta. The Niger Delta has 360 and 246 oil wells onshore and offshore respectively, allowing petrogenic contamination of waters. The concentrations of PAHs were reported to vary from nondetectable to 171 $\mu\text{g}/\text{kg}$ within Niger Delta (Nwaichi & Ntorgbo, 2016). The study recognized areas having PAHs of pyrogenic and petrogenic sources separately, based on the ratios of different PAHs in fish samples. Similar results for fresh mullet fish, prawns and crabs from Bonny River in Niger Delta are given in Table 4 (Tongo *et al.*, 2018). The presence of PAHs in bile of fish from Atlantic coastal waters near Columbia and in contaminated zones suggest it as a pathway for entry of petrogenic PAHs to the human food chain (Johnson-Restrepo *et al.*, 2008). The Indian, Nigerian, Columbian and Indonesian situations indicate that the major contaminations by PAHs in waters and the fish, are of petrogenic origin.

The contamination of Maldive-fish (cured tuna, traditionally produced in Maldives; local name: *Umbalakada*) and fried cutlets by PAHs have been reported in Sri Lanka (Wijeratne *et al.*, 1995). Jinadasa *et al.*, (2020) have observed unsafe concentrations of PAHs in fish and fishery products. They suggest the need to establish good manufacturing guidelines for fish products in Sri Lanka. The contaminations in both situations arise from deposition of smoke during fish preparations.

The PAHs get dissolved in lipids of the milk readily. Milk may generate PAHs on exposure to heat during processing. Ssepuya *et al.*, (2022) reported $\Sigma_{13}\text{PAHs}$ in concentrations of 3–696 $\mu\text{g}/\text{kg}$ from Kampala and 0.84–88 $\mu\text{g}/\text{kg}$ from Nakaseke in Uganda in breast milk. They attributed at least 33% of variation of $\Sigma_{13}\text{PAHs}$ in breast milk to the types of fuels used in the kitchen. Exposures are suggested to be linked to the extent of PAHs in home prepared foods, as high concentrations of PAHs were observed in households consuming charcoal grilled and fried foods in Uganda. Though increasing $\Sigma_8\text{PAHs}$ were reported with higher lipid content and higher temperatures of treatment of milk in Table 4, the BaP concentrations reported did not show notable differences related to heat treatments (Naccari *et al.*, 2011). The presence of the PAHs shown in the breast milk in this study also suggests possible pathways beginning with animal feed materials.

Junmin *et al.*, (2021) examining 86 market vegetable oils for 16 PAHs, reported that 37 and 34 oil samples contained BaP and $\Sigma_4\text{PAHs}$ respectively at concentrations above the EC tolerance limits. They postulated that the high contaminations of PAHs observed in peanut oil and sesame oil are due to heat processing of the raw materials prior to oil expulsion. In a study of 40 samples of olive oils in Brazil, up to 164 $\mu\text{g}/\text{kg}$ of BaP is reported with almost all tested samples giving positive results (Marcos *et al.*, 1996). The reported concentrations probably indicate pyrolytic PAHs formed during the expulsion of oils.

Of the 43 samples of market edible oils identified as frying, sunflower, corn and canola in Iran, 12 samples contained BaP above the EC tolerance limit of 2 $\mu\text{g}/\text{kg}$. Of the PAHs observed in all oils, 65% were light PAHs. The results are summarized in Table 4 (Yousefi *et al.*, 2018). The authors did not recognize a serious food safety hazard through the market oils. Fromberg *et al.* (2007) reports that PAHs in the sunflower oil is 50% light PAH and in the rapeseed oil it is 70%. The coconut oil produced from smoke cured copra contained 47–81% light PAHs (Wijeratne *et al.*, 1996a). The light PAHs are not implicated in food safety hazards. A higher tolerance limit is established by EC for total PAHs in coconut oil, to accommodate high BaA and Chr is notable.

On the analysis of 296 samples of edible oils in India including coconut, groundnut, hydrogenated vegetable, linseed, mustard, olive, palm, refined vegetable, rice bran, safflower, sesame, soybean, and sunflower oils, Pandey *et al.* (2004) reported that 262 (88.5%) were contaminated with PAHs. Of the contaminated oils 66.4% had total PAHs above the tolerance limit of 25 $\mu\text{g}/\text{kg}$. Among them, olive oil showed the highest contamination of 624 $\mu\text{g}/\text{kg}$ and the lowest of 40.2 $\mu\text{g}/\text{kg}$ was refined vegetable oils. It is not clear whether the refining is chemical or physical. Physical refining adsorbs only a part of the PAHs in edible oils in the bleaching step, whereas chemical refining destroys the PAHs totally. In a similar study examining 28 oil samples, notably high contamination of olive oils with light PAHs (53.0–105.6) $\mu\text{g}/\text{kg}$ is reported (Speer *et al.*, 1990). In a study on coconut, safflower, evening primrose and linseed oils, 96% samples contained more than 15 $\mu\text{g}/\text{kg}$ of $\Sigma_4\text{PAHs}$. Of them, the BaP concentrations exceeded tolerance limit in 12% samples and $\Sigma_4\text{PAHs}$ in 28% samples (Silva *et al.*, 2018). In contrast to the observations in USA, where bread is considered a major source of BaP (Kazerouni *et al.*, 2001), vegetable oils appear to be the major contributor of PAHs in most Asian and African diets.

Roasting of cocoa beans at 160 °C was reported to produce predominantly non-carcinogenic light PAHs. Reduction of the roasting temperature to 140 °C with extended exposure time has not reduced the concentrations of PAHs notably (Ciecierska, 2020).

In the rice plants, high concentrations of PAHs have been observed in roots with low concentrations in the grains and leaves, suggesting low translocation of PAHs from soil to grains (Tao *et al.*, 2006). It is not known whether the low molecular PAHs are metabolized in shoots of rice. Metabolism of phenanthrene by millets have been observed in pot experiments (Tarigholizadh *et al.*, 2022). Based on the trends in PAHs contaminations associated with boiling of other foods, cooked rice consumed globally may not be an alarming contributor of PAHs to human diet. BaP concentrations of up to 11.9 µg/kg with mean of 3.6 µg/kg have been detected in fried noodles in Hanoi (Tran-Lam *et al.*, 2018).

Martena *et al.* (2011) examined botanicals supplementing foods for BaP and Σ_4 PAHs. Recognizing high variations of the PAHs in different botanicals, they summarized an overall lower mean of 3.37 µg/kg during 2003–2009 for Σ_4 PAHs. They also reported high concentrations of BaP in dong quai, green tea and valerian. The black tea is kiln dried during manufacture against green tea, which is steam treated. In a study on market teas in USA, Adisa *et al.* (2015) reported PAHs in all the tea samples, except one green tea sample. They reported the presence of 5–12 PAHs out of 18 PAHs tested in the teas. The concentrations of BaP reported in black tea was four-fold higher than that of the green, red and white teas (Table 4) from Polish market (Zachara *et al.*, 2018). Studies in several countries on BaP and Σ_4 PAHs concentrations in different types of teas showed high concentration of PAHs in the black tea suggesting process induced contamination (Zachara *et al.*, 2018). They reported that the transfer of PAHs from the black tea to the tea infusions is of the order of 0.5%, whereas the comparable results by other authors were around 1.5%. Lin *et al.* (2006) observed 51.6% of the PAHs transfer to infusions during brewing. They also report 30.4% reduction of the transfer of PAHs, on washing the black tea before brewing. Phan *et al.*, (2020) observed 1.9%, 15.4% and 40.7 % transfer of Σ_4 PAHs in black, herbal and green teas respectively from the processed leaves to the infusions. Girelli *et al.* (2017) observed lower transfer of PAHs to tea infusion from market tea in Italy compared to Chinese and Indian observations. Transfer of PAHs from black tea to the infusion appears to be less with lower contact time between tea leaves and infusion (El-Aty *et al.*, 2014). The tea oils facilitate transfer of PAHs by solubilizing them.

Plant materials may get contaminated with PAHs from the air, or in contact with the soils carrying PAHs of petrogenic and pyrolytic origins. A summary of BaP in fruits and vegetables from USA and Italy is reported in Table 1.15 of the IARC monograph 92 (WHO, 2010). The reported values of BaP vary from 0.003–0.52 µg/kg. They probably represent PAHs adsorbed on to surfaces from the environment.

The concentrations of PAHs summarized in Table 4 from different sources indicate the difficulty in recognizing trends or taking a statistical approach in predicting the contamination patterns. Though the test methods for PAHs have been well defined and practiced with high degree of quality control, the conditions leading to formation of the PAHs during food processing vary widely. In test reports there is less uniformity in the examination of PAHs as a group, because authors use different criteria such as Σ_4 , Σ_8 and total PAHs. The definitions of total PAHs tend to vary. A review by Singh *et al.* (2016) on PAHs in processed foods has tabulated information up to 2015. His work also shows the difficulty of recognizing food associated or process linked trends of contaminations.

Foods carrying unacceptable concentrations of PAHs are rejected or notified by the EU countries. The notifications over a two-year period ending on 18 September 2022 is given in the Table 5 (RASFF, 2022).

Table 5 indicates that a variety of foods in international trade continue to be hazardous due to PAHs.

Table 5: Notifications and rejections of foods at EU country borders due to presence of PAHs.

Code	Notification/rejection	Origin
2021.519	PAHs in reduced fat cocoa powder	Slovakia
2021.563	BaP & Σ_4 PAHs in smoked sardinella	Senegal
2021.662	BaP and PAHs in sausages	Slovakia
2021.687	BaP & PAHs in sausages	Slovakia
2021.716	PAHs in Green wheat, roasted	Turkey
2021.563	BaP & Σ_4 PAHs in smoked sardinella	Senegal
2022.043	PAHs in sausages	Portugal
2022.140	BaP & PAHs in cabamos sausages	Poland
2022.221	PAHs in lutein powder	Netherlands
2022.260	BaP & PAHs in paprika powder	Spain
2022.260	BaP & PAHs in refined sunflower oil	Ukraine
2022.307	PAHs in turmeric	India
2022.458	BaP & PAHs tea powder	China
2022.477	PAHs in sliced garlic	Germany
2022.541	PAHs coconut oil	Philippines

Formation of PAHs in foods

Formation of the PAHs during food processing and home food preparations leads to food safety hazards. The home food preparations do not come under food regulatory controls. It leaves room for hazards. The lipid concentrations in foods, exposure to heat, the methods of heating, the proximity of heat source to the food, and the contaminated frying oils contribute to PAHs in the foods.

Singh *et al.* (2016) reviewing PAHs in processed foods observed higher concentrations of PAHs in deep fried and grilled foods. The deep fried and grilled foods form excellent delivery systems of PAHs to the human body tissues. Chen & Chen (2001) observed decreasing order of the PAHs formed from methyl esters of linolenate, linoleate, oleate to stearate in model systems. They reported higher concentrations of PAHs in the soyabean oils than canola and sunflower oils. The fatty acid composition of edible oils appears to influence the formation of PAHs.

Purcaro *et al.* (2006) reported no notable increase of BaP when olive oils and peanut oils containing 8.1 and 0.1 $\mu\text{g}/\text{kg}$ BAP were heated at 180 °C up to 25 h. Barranco *et al.* (2004) had similar observations on heating of Spanish fatty foods. Kim *et al.* (1993) reported increase of BaP in the soybean oil on heating up to 200 °C for 10–20 h. Dost and Ideli (2012) reported 2 to 8-fold increase of the PAHs during barbequing of meat and fish using corn, sunflower and olive oils containing 0.44–99 $\mu\text{g}/\text{kg}$ of BaP. In several less commonly used edible oils, formation of light Σ_4 PAHs (Phenanthrene, Anthracene, Fluorene, and Pyrene) appears to be predominant (>70%) compared with the carcinogenic Σ_4 PAHs (Ciecierska & Obiedzinski, 2013b).

Smoke curing of coconut kernels to produce copra and mechanical expulsion of oil from the copra is a major industry in coconut producing countries. The concentrations of PAHs in coconut products (Table 4) reflect the individual effects of copra curing, expulsion and chemical refining of coconut oil (Wijeratne *et al.*, 1996a). Wijeratne *et al.* (1998) observed more than 10-fold increase of Σ_8 PAHs (367 $\mu\text{g}/\text{kg}$) than predicted (24 $\mu\text{g}/\text{kg}$) in oils mechanically expelled from copra. The increase is shown to be due to pyrolysis during expelling the oil in screw press at 140–160 °C, by experimentally expelling oil from desiccated coconuts free of the PAHs. This may be happening during the mechanical expulsion of other edible oils, too. Water jacketed expellers maintained at 50 °C are used in extracting the virgin coconut oil to prevent pyrolysis leading to formation of PAHs. Figure 2 indicates the gradual increase in formation of the PAHs starting around 55 °C on exposure of coconut oil in laboratory ovens at temperatures from 40–250 °C (Wijeratne *et al.*, 1998). The exact cut off temperature cannot be established as convection currents in oil and other compositional conditions, too contribute to the reactions. Manually extracted coconut milk is boiled to break the emulsion in home preparation of coconut oil. During boiling, the liquid near the bottom of the pot reaches temperatures around 170 °C. The sediment gets charred and is high in PAHs. It is consumed as a delicacy (*Theilka*) mostly by children (Wijeratne *et al.*, 1996b).

Copra is smoke cured, anticipating reduced fungal spoilage and aflatoxin production on storage. This assumption needs validation as both aflatoxins and BaP are class 1 carcinogens that require equal concern (Samarajeewa, 2003). Laboratory experiments comparing liquid smoke produced by burning coconut shells (containing PAHs) and Zesti™ liquid smoke (free of PAHs) showed that suppression of fungal growth in grated coconuts was not due to the PAHs in smoke, but other chemicals (Rodrigo *et al.*, 1995).

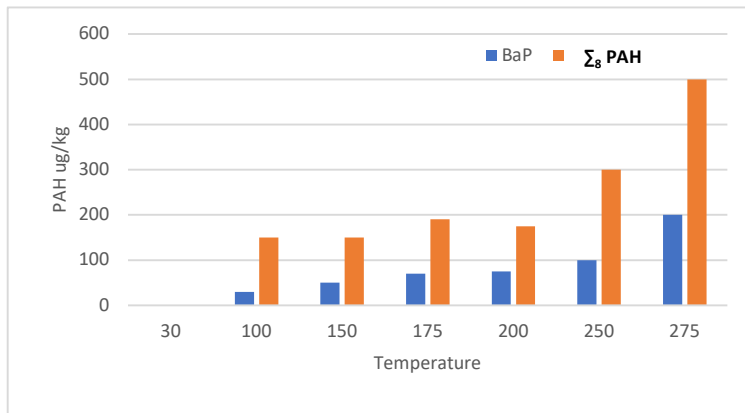


Figure 2: Formation of PAHs in coconut oil on exposure to different temperatures

A study describes increased formation of PAHs on three successive frying of fish with the same oil (Chukwujindu *et al.*, 2020). The concentrations of Σ_{22} PAHs in the unused oils were in the range of 43.3–2107 $\mu\text{g}/\text{kg}$, whereas those in the used oil ranged from 40.8–4090 $\mu\text{g}/\text{kg}$. The increase of PAHs appears to depend on the type of oil and also the type of fish.

In comparing the PAHs in 60 samples of BBQ pork, roasted pork and roasted duck collected from sales points, grilled pork showed highest concentrations with lower concentrations in the gas grilled or electric oven roasted meats (Table 4). Incomplete combustion during grilling may be contributing more to the formation of PAHs (Food and Environmental Hygiene Department, 2004). In controlled experiments with steam heated meat, carcinogenic Σ_3 PAHs were not detected and the concentrations of total PAHs [Σ_{15}] observed were below the tolerance limit. It is known that the lipids in meats tend to drip on to fire undergoing pyrolysis to produce PAHs, which gets deposited on the meat. The lipids reaching the flame tend to reach temperatures of 500 °C or above instantly producing PAHs. A study comparing in-house preparations (shallow frying on electric hot plate, grilling in electric oven, barbecuing in charcoal & wood chips, roasting in electric oven and toasting) showed no recognizable increase of PAHs [Σ_{27+1}] compared with the raw materials (Rose *et al.*, 2015). Experiments in this study were conducted under well-defined conditions. However, BaP was produced in most foods when barbecued using charcoal and wood chips together. Rose *et al.* (2015) have observed highest concentrations of Σ_8 PAHs in the barbecues using charcoal as fuel. The values PAHs were higher when the distance between charcoal and food was 4 cm against 7 cm. Halagarda and Wojciak (2022) reviewing the health and safety aspects of European meat products showed that the use of uncontrolled smoking in traditional /conventional products tend to cause heavier contamination with the PAHs. The overall observations suggest that the concentrations of PAHs in home prepared foods, where conditions are not well controlled, could be above the tolerance limits.

Siddique *et al.*, (2021a) reported no further increase of the BaP after poaching, boiling, frying, grilling, microwaving and oven roasting using 4 types of oils containing BaP concentrations within the tolerance limits (Table 4). They detected fluorene (non-toxic) as the main PAH formed during frying. Their experiments were conducted under defined conditions, not allowing over exposure of the rabbit muscles to heat with the edible oils maintained below 140 °C in deep frying. Another study by Siddique *et al.* (2021b) examining the impact of conventional oil on frying of rabbit meat reported that PAHs are outside the toxic Σ_8 . The PAHs outside toxic Σ_8 are of low carcinogenic relevance.

Baking exposes products to high temperatures. Most bakery products are rich in carbohydrates and low in lipids. Bread dough may get contaminated with PAHs from the environment or due to pyrolysis during baking. Bread was found to contain Σ_{19} PAHs at concentration range of 1.59 to 13.6 $\mu\text{g}/\text{kg}$ in different locations of the bread and in relation to the baking temperatures (Ciecierska & Obiedziński, 2013a). In this study from 1.07 to 3.65 $\mu\text{g}/\text{kg}$ Σ_{19} PAHs have been found in the dough even before baking. Authors suggest the concentrations of PAHs detected in baked products are of low health significance, considering probable dietary exposure. Comparable PAHs concentrations were observed in bread and breakfast cereals in bakery and cereal products in Turkish markets (Kacmaz, 2016). Research is needed on formation of PAHs in some of the flour-based sweets and foods prepared by frying in oils, or direct heating on pans respectively in the South Asian countries.

Roasting of coffee results in formation of PAHs due to heat while developing the aroma of consumer preference. Compared with hot air roasting, the superheated steam roasting of arabica coffee at 250 °C has shown to contain less light PAHs. Superheat treatment by steam was done in a fluidized bed drier (Rattanarat *et al.*, 2021). Kinetic models were developed to predict formation of PAHs, namely Py, BaA, Chr and Anthracene, where good correlations between predictions and formation of PAHs on roasting at 180–260 °C for 5–10 min. were observed (Houessou, 2008).

Kim *et al.* (2020) reported Σ_8 PAHs from several agricultural commodities in South Korea. Martorell *et al.* (2010) reported PAHs in randomly collected food groups in Spain. High levels of total PAHs were detected in the meat and meat products (38.99 $\mu\text{g}/\text{kg}$), followed by oils and fats (18.75 $\mu\text{g}/\text{kg}$), and dairy products (7.57 $\mu\text{g}/\text{kg}$). These concentrations were less than the values reported previously.

Prevention and removal

Preventing formation or deposition of the PAHs is the most rational approach to ensure food safety. The traditional smoking techniques are currently replaced by spraying of smoke flavours on foods to ensure consumer satisfaction avoiding hazards from PAHs. It is practical to monitor PAHs in smoke liquids prior to their application on foods.

Essumang *et al.*, (2014) described modification of traditional smoke kilns using a filter system for PAHs. The filter was able to reduce the total PAHs by 21–69%. They reported mean BaP concentrations below the tolerance limit of 2 $\mu\text{g}/\text{kg}$ in fish smoked by the modified kiln. Mechanisms to minimize PAHs during smoke curing by marinades, fuel-wood types, low fat raw materials, and the use of smoke filters are developed now to reduce food safety hazards (Dutta *et al.*, 2022). While preventing contact of the meat with the flames during barbequing, the removal of drippings and smoke was reported to reduce Σ_4 PAHs by 48–89% and 41–74% respectively in ready to consume meats (Lee *et al.*, 2016). Controlled barbequing could notably reduce the PAHs in meats (Duedahl-Olesen *et al.*, 2015b). This aspect is reviewed by Afe *et al.* (2020) projecting possible re-engineering approaches in food preparations for the future.

Edible oils are refined by deodorizing and bleaching to remove pigments and other constituents originating from the raw materials. Physical refining removes the PAHs in edible oils only partially. Olatunji *et al.* (2014) reported presence of three PAHs BaP, BkF and Phe (Phenanthrene) in sunflower oils and mixtures of sunflower and soya oils at concentration ranges of 5.3–7.7 $\mu\text{g}/\text{kg}$. They report reduction of Σ_{13} PAHs from the range 10–316 to 3–69 $\mu\text{g}/\text{kg}$ in the soybean oil on refining (neutralization and deodorization). Rojo Carmago *et al.*, (2012) described the possibility of reducing PAHs up to 88% by physical refining. The percent reduction seems to depend on the initial concentrations of PAHs in the foods. Chemical refining is far more effective in reducing the PAHs in edible oils as the alkali interacts with PAHs chemically, making them hydrophilic to be removed in the aqueous fraction.

The PAHs possess the capacity to absorb energy in the ultraviolet (wave length: 320 - 400 nm) and visible (400 nm) regions generating reactive species. This effect may be enhanced using catalysts and oxygen to degrade the PAHs. There is much interest currently to carry out catalysed photodegradation of soil PAHs in solid phase. Wang *et al.*, (2009) describe application of iron oxide to photodegrade pyrene. They describe a photo-fenton-like system operating with added hydrogen peroxide effectively to degrade PAHs in soil. An effort to degrade PAHs in coconut oil was made using moving layers of oil in a cascade set up used previously for solar

degradation of aflatoxins in coconut oil (Samarajeewa *et al.*, 1985). The pilot experiments worked effectively (Wijeratne *et al.*, 1997). It is also noted that the molecules of PAHs activated by light have their toxicity increased 100-fold than in the dark (Hongtao, 2002) forming active toxic derivatives. The energized molecules tend to breakdown readily in their active phase. The principle may be applied with sunlight and catalysts to remove PAHs in the edible oils.

In smoke drying of coconut kernels, a variety of plant-based fuels are used in the industrial kilns. A comparison of smoke produced from different parts of coconut palm, burned under the same conditions and absorbed into grated coconut (free of PAH) showed high variations in content and concentrations (Figure 3). It is interesting to note that Sri Lanka uses only coconut shells as fuel for copra curing, whereas the fuels differ in other countries.

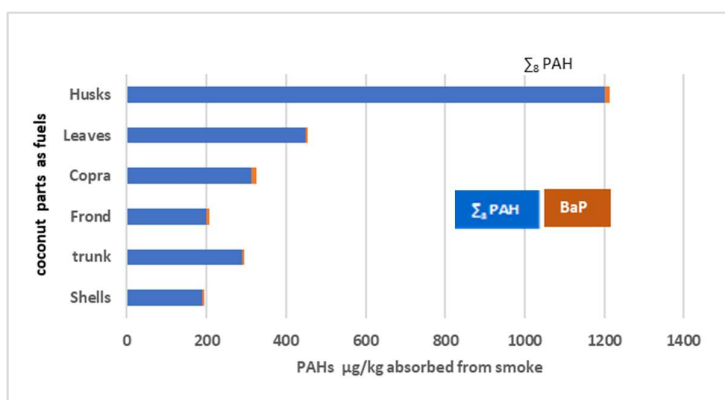


Figure 3: PAHs absorbed into grated coconut when exposed to smoke generated by different parts of the coconut palm used commonly as fuels (Rodrigo *et al.*, 1999)

Smoke flavourings are sprayed on meat products to provide consumer satisfaction preventing contaminations by the PAHs. Analysis of 18 commercial liquid smoke flavourings have shown total PAHs concentrations in the range of 6.3–43.7 µg/kg and carcinogenic PAHs concentrations of 0.3–10.2 µg/kg. Since the amounts of liquid smoke sprayed on to foods are of the order of few millilitres, food safety hazards cannot be expected (Gomma *et al.*, 1993). Smoke flavourings appear to be a better option as the most lipophilic PAHs do not appear in the condensates of watery smoke liquids (McDonald, 2015).

There are new approaches to use microorganisms to remediate PAHs and their toxicity from soil and other sources including food. This is an emerging area to minimize hazards (Kanaly & Haryama, 2000; Patel *et al.*, 2020; Premnath *et al.*, 2021).

Preventing food contaminations with the PAHs by environmental and industrial controls appears to be a need to address food safety hazards. Shift from smoke drying of copra using coconut shell to more mild drying using charcoal that was established in Sri Lanka is one such approach. Some of the photochemical methods could also possess prospects to eliminate PAHs in the foods.

Recommendations

1. The Environmental and Occupational Health Division of the Ministry of Health and Environment Authority in Sri Lanka need to establish limits for PAHs in air quality in smoke houses and major cities as the PAHs are proven to cause lung cancer. Incidence of lung cancer is the highest among cancers in Sri Lanka.
2. Research to recognize occupational exposure levels of persons to smoke as a probable cause of lung cancer needs to be initiated.
3. Research to assess formation of the PAHs during frying of foods is needed.

4. There should be strict regulatory measures introduced to test the edible oil imports for PAHs or get accredited certification from exporting countries on the PAHs.
5. Restaurants need to shift barbequing of fish and meat from direct flame fires to gas or electric heating combined with spray of liquid smokes free of PAHs.
6. The coconut administration needs to assist the industry to move away from smoke copra kilns to indirect heating methods.
7. Considering the research evidence and methods of food manufacture, preparation and consumption patterns in Sri Lanka, regulatory limits given in Table 6 to ensure the safety of market foods from PAHs is suggested.

Table 6: Suggested regulatory guidelines for PAHs in foods in Sri Lanka

Foods	BaP µg/kg	Σ ₄ PAHs µg/kg	Notes
Chemically refined coconut oil	2	10	Chemical refining removes all PAHs in the oil totally
Virgin coconut oil	2	10	Extraction is carried out below 55 °C to prevent formation of PAHs
Crude coconut oil and Coconut parings	10	50	Expulsion leads to formation of PAH at the screw press operating around 140 °C
Oil fried foods	5	10	Fraction of PAHs would be absorbed into foods during frying
Vegetable oils	2	10	Imported oils are expected to be chemically refined
Palm oil	2	10	
Desiccated coconut	2	10	There is no deposition or production of PAHs in the process
Food for children and sick using roasted rice	2	10	Minimize over-roasting of rice.
Spices (whole or powdered)	10	50	They are not smoke dried and used in small quantities in foods
Tea (Black)	10	50	PAHs are formed during kilning of black tea
Smoke cured fish, meat and sausages	5	12	Smoke deposition itself and action of heat on lipids in fish or meat produce PAHs

CONCLUSION

Of the PAHs, 16 compounds have been recognized scientifically to bring in food safety hazards in humans. They may be of petrogenic origin entering the food chain through fish. PAHs also may be airborne as a part of vehicle fumes, distillation of petroleum products and burning of wood and similar organic matter. PAHs are generated during contact between edible lipids and hot surfaces during roasting and frying or contacts between naked flames and fatty tissues of meat during grilling. BaP and some of the PAHs interfere with cellular metabolism in the body leading to interactions with DNA leading to mutagenicity. Controlled exposure of foods to heat during manufacture and cooking could reduce the PAHs to acceptable levels.

REFERENCES

- Abdel-Shafy H.I. & Mansour M.S.M. (2016). Source, environmental impact, effect on human health and remediation. *Egyptian Journal of Petroleum* **25**: 107–123.
DOI: <https://doi.org/10.1016/j.ejpe.2015.03.011>
- Adeyeye S.A.O. & Ashaolu T.J. (2020). A study on polycyclic aromatic hydrocarbon and heavy metal concentrations of commercial grilled meat (suya) and smoked catfish (*Clarias gariepinus* Burchell, 1822) fish from South-West, Nigeria. *Polycyclic Aromatic Compounds* **42**(6): 3281–3290.
DOI: <https://doi.org/10.1080/10406638.2020.1858883>
- Adisa A., Jimenez A., Woodham C., Anthony K., Nguyen T. & Saleh M.M. (2015). Determination of polycyclic aromatic hydrocarbons in dry tea. *Journal of Environmental Science and Health* **50**: 552–559.
DOI: <https://doi.org/10.1080/03601234.2015.1028832>
- Afé O.H., Douny C., Kpoclou Y.E., Igout A., Mahillon J., Anihouvi V., Hounhouigan D.J. & Scippo M-L. (2020). Insight about methods used for polycyclic aromatic hydrocarbons reduction in smoked or grilled fishery and meat products for future re-engineering: A systematic review. *Food and Chemical Toxicology* **141**: 111372.
DOI: <https://doi.org/10.1016/j.fct.2020.111372>
- Afolabi A.O., Adesulu E.A. & Oke O.L. (1983). Polynuclear aromatic hydrocarbons in some Nigerian preserved freshwater fish species. Comparative ratio of Benzo(a)pyrene (%) in fish and oil fractions. *Journal of Agricultural and Food Chemistry* **31**: 1083–1090.
DOI: <https://doi.org/10.1021/JF00119A040>

- Akpambang V.O.E., Purcaro G., Lajide L., Amoo I.A., Conte L.S. & Moret S. (2009). Determination of polycyclic aromatic hydrocarbons (PAHs) in commonly consumed Nigerian smoked/grilled fish and meat. *Food Additives and Contaminants* **26**(7): 1096–1103.
DOI: <https://doi.org/10.1080/02652030902855406>
- Armstrong B., Hutchinson E., Unwin J. & Fletcher T. (2004). Lung cancer risk after exposure to polycyclic aromatic hydrocarbons: A review and meta-analysis. *Environmental Health Perspectives* **112**(9): 970–978.
- Baird W.M., Hooven L.A. & Mahadevan B. (2005). Carcinogenic polycyclic aromatic hydrocarbon-DNA adducts and mechanism of action. *Environmental and Molecular Mutagenesis* **45**(2–3): 106–114.
DOI: <https://doi.org/https://doi.org/10.1002/em.20095>
- Barranco A., Alonso-Salces R.M., Crespo I.L.A., Berrueta L.A., Gallo B., Vicente F. & Sarobe M. (2004). Polycyclic aromatic hydrocarbon content in commercial Spanish fatty foods. *Journal of Food Protection* **67**: 2786–2791.
- CAC/RCP 68–2009 (2009). Code of practice for the reduction of contamination of food with polycyclic aromatic hydrocarbons (PAH) from smoking and direct drying processes, pp. 16.
- National Cancer Control Programme (2021). *Cancer Incidence and Mortality Data, Sri Lanka*. National Cancer Control Programme, Ministry of Health, Colombo.
- CFDA (2017). *National Food Safety Standards for Maximum Levels of Contaminants of Foods (GB 2762–2017)*, p. 10. China Foods and Drugs Authority, China.
- Chen B.H. & Chen Y.C. (2001). Formation of polycyclic hydrocarbons in the smoke from heated model lipids and food lipids. *Journal of Agriculture and Food Chemistry* **49**(11): 5238–5243.
DOI: <https://doi.org/10.1021/jf0106906>
- Chukwujindu M., Iwegbue A., Osijaye K.O., Igbuku A.U., Egobueze F.E., Tesi G.O., Bassey F.I. & Martincigh B.S. (2020). Effect of the number of frying cycles on the composition, concentrations and risk of polycyclic aromatic hydrocarbons (PAHs) in vegetable oils and fried fish. *Journal of Food Composition and Analysis* **94**: 103633.
DOI: <https://doi.org/10.1016/j.jfca.2020.103633>
- Ciecierska M. (2020). Cocoa beans of different origins and varieties and their derived products contamination with polycyclic aromatic hydrocarbons. *Food Chemistry* **317**: 10–15.
DOI: <https://doi.org/10.1016/j.foodchem.2020.126408>
- Ciecierska M. & Obiedzinski M.W. (2013a). Polycyclic aromatic hydrocarbons in the bakery chain. *Food Chemistry* **141**: 1–9.
DOI: <https://doi.org/10.1016/j.foodchem.2013.03.006>
- Ciecierska M. & Obiedzinski M.W. (2013b). Polycyclic aromatic hydrocarbons in vegetable oils from unconventional sources. *Food Control* **30**: 556–562.
DOI: <http://dx.doi.org/10.1016/j.foodcont.2012.07.046>
- CODEX STAN 311–2013. *Standard for Smoked Fish, Smoke Flavoured Fish and Smoke-dried fish*. p. 9.
- Dabestani R. & Ivanov I.L. (1999). A compilation of physical, spectroscopic and photophysical properties of polycyclic aromatic hydrocarbons. *Photochemistry and Photobiology* **170**(1): 10–34.
- Dhananjayan V. & Muralidharan S. (2012). Polycyclic aromatic hydrocarbons in various species of fishes from Mumbai harbour, India, and their dietary intake concentration to human. *International Journal of Oceanography*: Article ID 645178.
DOI: <https://doi.10.1155/2012/645178>
- Dost K. & İdeli C. (2012). Determination of polycyclic aromatic hydrocarbons in edible oils and barbecued food by HPLC/UV-Vis detection. *Food Chemistry* **133**(1): 193–199.
DOI: <https://doi.org/10.1016/j.foodchem.2012.01.001>
- Duedahl-Olesen L., Navaratnam M.A., Jewula J. & Jensen A. (2015a). PAH in some brands of tea and coffee. *Polycyclic Aromatic Compounds*. **35**: 74–90.
DOI: <https://doi.org/10.1080/10406638.2014.918554>
- Duedahl-Olesen L., Aaslyng M., Meinert L., Christensen T., Jensen A.H. & Binderup M.L. (2015b). Polycyclic aromatic hydrocarbons (PAH) in Danish barbecued meat. *Food Control* **57**: 169–176.
DOI: <https://doi.org/10.1016/j.foodcont.2015.04.012>
- Dutta K., Shityakov S., Zhu W. & Khalifa I. (2022). High-risk meat and fish cooking methods of polycyclic aromatic hydrocarbons formation and its avoidance strategies. *Food Control* **142**: 10925.
DOI: <https://doi.org/10.1016/j.foodcont.2022.109253>
- EFSA (2008). Polycyclic aromatic hydrocarbons in foods. Scientific opinion of the panel on contaminants in the food chain. *EFSA Journal* **724**: 1–114.
- El-Aty A.M.A., Choi J-H., Rahman M.M., Kim S-W., Tosun A. & Shim J-H. (2014). Residues and contaminants in tea and tea infusions: a review. *Food Additives & Contaminants: Part A* **31**(11): 1794–1804.
DOI: <https://doi.org/10.1080/19440049.2014.958575>
- Essumang D.K., Dodoo D.K. & Adjei J.K. (2014). Effective reduction of PAH contamination in smoke cured fish products using charcoal filters in a modified traditional kiln. *Food Control* **35**: 85–93.
- European Commission (1998). Council Directive 98/83/EC. *Official Journal of European Union* L330/32 98/83/EC. Publications Office of the European Union, Luxembourg.

- European Commission (2003). Regulation No. EC 2065/2003 of the European Parliament and of the Council. *Official Journal of European Union* L309/1 2065/2003. Publications Office of the European Union, Luxembourg.
- European Commission (2011). Regulation No. EC 835/2011 of 19 August 2011 amending Regulation (EC) No 1881/2006 as regards maximum levels for polycyclic aromatic hydrocarbons in foodstuffs. *Official Journal of the European Union* L 215: 4–7.
- European Commission (2014). Regulation No EC 1327/2014 amending Regulation (EC) No 1881/2006 as regards maximum levels of polycyclic aromatic hydrocarbons (PAHs) in traditionally smoked meat and meat products and traditionally smoked fish and fishery products. Publications Office of the European Union, Luxembourg.
- European Commission (2015). Regulation 1933/2015 amending Regulation (EC) No. 1881/2006 as regards maximum levels for polycyclic aromatic hydrocarbons in cocoa fibre, banana chips, food supplements, dried herbs and dried spices. Publications Office of the European Union, Luxembourg.
- European Commission (2020). Regulation 1255/2020 amending Regulation (EC) No. 1881/2006 as regards maximum levels of polycyclic aromatic hydrocarbons (PAHs) in traditionally smoked meat and meat products and traditionally smoked fish and fishery products. Publications Office of the European Union, Luxembourg.
- Food and Environmental Hygiene Department (2004). *Polycyclic Aromatic Hydrocarbons (PAHs) in Barbecued Meat*. Risk assessment studies. Report No. 14. Risk Assessment Section, Food and Environmental Hygiene Department 43/F, Queensway Government Offices, 66 Queensway, Hong Kong.
- Fromberg A., Hojgard A. & Duedahl-Olesen L. (2007). Analysis of polycyclic aromatic hydrocarbons in vegetable oils combining gel permeation chromatography with solid-phase extraction clean-up. *Food Additives & Contaminants* 24: 758–767.
- Girelli A.M., Apriceno A., Tarola A.M. & Tortora F. (2017). Determination of polycyclic aromatic hydrocarbons in tea infusions samples by high performance liquid chromatography with fluorometric detection. *Journal of Food Quality* 2017: Article ID 1076876s.
DOI: <https://doi.org/10.1155/2017/1076876>
- Gomaa E.A., Ian Gray J.I., Rabie S., Lopez-Bote C. & Booren A.M. (1993). Polycyclic aromatic hydrocarbons in smoked food products and commercial liquid smoke flavourings. *Food Additives & Contaminants* 10(5): 503– 521.
DOI: <https://doi.org/10.1080/02652039309374174>
- Gratz S.R. et al. (15 authors) (2011). Screening and determination of polycyclic aromatic hydrocarbons in seafoods using QuEChERS-based extraction and high-performance liquid chromatography with fluorescence detection. *Journal of Association of Official Analytical Chemists International* 94(5): 1601–1616.
- Halagarda M. & Wojciak K.M. (2022). Health and safety aspects of traditional European meat products. A review. *Meat Science* 184: 108623.
DOI: <https://doi.org/10.1016/j.meatsci.2021.108623>
- Health Canada (2022). *Maximum Levels of Contaminants in Foods*. Available at <http://www.hc-sc.gc.ca/fn-an/securit/chem-chim/contaminants-guidelines-directives-eng.php>. Accessed 18 Sept 2022.
- Helfinalis E., Rugebregt M.J. & Opier R.D.A. (2021). Polycyclic aromatic hydrocarbon (PAHs) compound in sea-water of Cimandiri river estuary, Pelabuhan Ratu. *Earth Environmental Science* 925: 012046.
DOI: <https://doi.org/10.1088/1755-1315/925/1/012046>
- Hongtao Y. (2002). Environmental carcinogenic polycyclic aromatic hydrocarbons; photochemistry and phototoxicity. *Journal of Environmental Science and Health C: Environmental Carcinogenic Ecotoxicology Reviews* 20(2): 149–183.
DOI: <https://doi.org/10.1081/GNC-120016203>
- Houessou J.K., Goujot D.B., Heyd B. & Camel V. (2008). Modeling the formation of some polycyclic aromatic hydrocarbons during the roasting of arabica coffee samples. *Journal of Agricultural and Food Chemistry* 56: 3648–3656.
DOI: <https://doi.org/10.1016/j.fct.2020.111372>
- Hussar E., Richards S., Lin Z-Q., Dixon R.P. & Johnson K.A. (2012). Human health risk assessment of 16 priority polycyclic aromatic hydrocarbons in soils of Chattanooga. *Water Air Soil Pollution* 223(9): 5535–5548.
DOI: <https://doi.org/10.1007/s11270-012-1265-7>
- Indian Standards (2016). Food safety and standards (contaminations, toxins and residues). Amended regulations. Gazetted 6th January 2016.
- Johnson-Restrepo B., Olivero-Verbel J., Lu S., Guette-Fernandez J., Baldiris-Avila R., O’Byrne-Hoyos I., Aldous K.M., Addin R. & Kannan K. (2008). Polycyclic aromatic hydrocarbons and their hydroxylated metabolites in fish bile and sediments from coastal waters of Colombia. *Environmental Pollution* 151: 452– 459.
DOI: <https://doi.org/10.1016/j.envpol.2007.04.011>
- Jinadasa B.K.K.K., Monteau F. & Fowler S.W. (2020). Review of polycyclic aromatic hydrocarbons (PAHs) in fish and fisheries products; a Sri Lankan perspective. *Environmental Science Pollution Research Institute* 27(17): 20663–20674.
DOI: <https://doi.org/10.1007/s11356-020-08305-2>
- Junmin J., Zhang Y., Sun S. & Liu X. (2021). Concentrations of the 16 US EPA PAHs in 86 vegetable oil samples. *Polycyclic Aromatic Compounds* 12: 1–18.
DOI: <https://doi.org/10.1080/10406638.2021.1998154>
- Kacmaz S. (2016). Polycyclic aromatic hydrocarbons in cereal products on the Turkish market. *Food Additives and Contaminants* 9(3): 191–197.

- DOI: <https://doi.org/0.1080/19393210.2016.1164761>
- Kanaly R. & Harayama S. (2000). Biodegradation of high-molecular-weight polycyclic aromatic hydrocarbons by bacteria. *Journal of Bacteriology* **182**(8): 2059–2067.
- Kazerouni N., Sinha R., Hsu C.H., Greenberg A. & Rothman N. (2001). Analysis of 200 food items for benzo[a]pyrene and estimation of its intake in an epidemiologic study. *Food Chemical Toxicology* **39**: 423–436.
- Kelly J.M., Ivatt P.D., Evans M.J., Kroll J.H., Amy I.H., Shwar H.I., Kohale N., White F.M. Engelward B.P. & Selin N.E. (2021). Global cancer risk from unregulated polycyclic aromatic hydrocarbons. *GeoHealth* **6**(9): GH000401.
DOI: <https://doi.org/10.1029/2021GH000401>
- Kim I.S., Ahn M.S. & Jang D.K. (1993). A study on the occurrence of benzo(a)pyrene in fats and oils by heat treatment. *Journal of Korean Society for Food Science and Nutrition* **9**: 323–328.
- Kim W., Choi J., Kang J.H., Lee J-W., Moon B., Joo Y-S. & Lee K-W. (2020). Monitoring and risk assessment of eight polycyclic aromatic hydrocarbons (PAH8) in daily consumed agricultural products in South Korea. *Polycyclic Aromatic Compounds* **42**(4): 1141–1156.
DOI: <https://doi.org/10.1080/10406638.2020.1768564>
- Kumari R., Chaturvedi P., Ansari N.G., Murthy R.C. & Patel D.K. (2012). Optimization and validation of an extraction method for the analysis of polycyclic aromatic hydrocarbons in chocolate candies. *Journal of Food Science* **71**(1): 34–40.
DOI: <https://doi.org/10.1111/j.1750-3841.2011.02488.x>
- Lee J.G., Kim S-Y., Moon J-S., Kim S-H., Kang D-H. & Yoon H-J. (2016). Effects of grilling procedures on levels of polycyclic aromatic hydrocarbons in grilled meats. *Food Chemistry* **199**: 632–638.
DOI: <https://doi.org/10.1016/j.foodchem.2015.12.017>
- Li Z., Jin Y., Chen M., Huang M., Harvey R.G., Blair I.A. & Penning T.M. (2011). Detoxication of structurally diverse polycyclic aromatic hydrocarbon (PAH) o-quinones by human recombinant catechol-O-methyltransferase (COMT) via O-methylation of PAH catechols. *Journal of Biological Chemistry* **286**(29): 25644–25654.
DOI: <https://doi.org/10.1074/jbc.M111.240739>
- Lin D., Zhu L. & Luo L. (2006). Factors affecting transfer of polycyclic aromatic hydrocarbons from made tea to tea infusion. *Journal of Agricultural and Food Chemistry* **54**: 4350–4354.
- Marcos A., Maria P. & Toledo C.F. (1996). Benzo(a)pyrene in olive oils on the Brazilian market. *Food Chemistry* **55**(2):185–188.
DOI: [https://doi.org/10.1016/0308-8146\(95\)00075-5](https://doi.org/10.1016/0308-8146(95)00075-5)
- Martena M.J., Grutters M.M.P., De Groot H.N., Konings E.J.M. & Rietjens I.M.C.M. (2011). Monitoring of polycyclic aromatic hydrocarbons (PAH) in food supplements containing botanicals and other ingredients on the Dutch market. *Food Additives and Contaminants* **28**(7): 925–942.
DOI: <https://doi.org/10.1080/19440049.2011.569573>
- Martínez-Álvarez I., Le Menach K., Devier M.H., Cajaraville M.P., Budzinski H. & Orbea A. (2022). Screening of the toxicity of polystyrene nano- and microplastics alone and in combination with benzo(a)pyrene in brine shrimp larvae and zebrafish embryos. *Nanomaterials (Basel)* **12**(6): 941.
DOI: <https://doi.org/10.3390/nano12060941>
- Martorell I., Perelló G., Martí-Cid R., Castell V., Llobet J.M. & Domingo J.L. (2010). Polycyclic aromatic hydrocarbons (PAH) in foods and estimated PAH intake by the population of Catalonia, Spain: Temporal trend. *Environment International* **36**(5): 424–432.
DOI: <https://doi.org/10.1016/j.envint.2010.03.003>
- Mastrangelo G., Fadda E. & Marzia V. (1996). Polycyclic aromatic hydrocarbons and cancer in man. *Environmental Health Perspectives* **104**(11): 1166–1170.
- McDonald S.T. (2015). Comparison of health risks of smoked foods as compared to smoke flavorings: are smoke flavors ‘healthier’? *Advances in Food Technology and Nutrition Science* **1**(6): 130–134.
DOI: <http://dx.doi.org/10.17140/AFTNSOJ-1-122>
- Mojiri A., Zhou, J.L., Ohashi A., Ozaki N. & Kindaichi T. (2019). Comprehensive review of polycyclic aromatic hydrocarbons in water sources, their effects and treatments. *Science of Total Environment* **696**: 133971.
DOI: <https://doi.org/10.1016/j.scitotenv.2019.133971>
- Moret S., Purcaro G. & Conte L. (2005). Polycyclic aromatic hydrocarbons in vegetable oils from canned foods. *European Journal of Lipid Science and Technology* **107**(7–8): 488–496.
DOI: <https://doi.org/10.1002/ejlt.200501060>
- Naccari C.M., Cristani M., Giofre F., Ferrante M., Siracusa L. & Trombetta D. (2011). PAHs concentration in heat-treated milk samples. *Food Research International* **44**: 716–724.
- NHMRC, NRMCC (2011). *Australian Drinking Water Guidelines Paper 6. National Water Quality Management Strategy*, pp. 1223. National health and medical research council, National resource management ministerial council, Commonwealth of Australia, Canberra, Australia.
- Nwaichi E.O. & Ntorgbo S.A. (2016). Assessment of PAHs levels in some fish and seafood from different coastal waters in the Niger Delta. *Toxicology Reports* **3**: 167–172.

- Olatunji S.O., Fatoki O.S., Bhekumusa J. & Opeolu B.O. (2014). Polycyclic aromatic hydrocarbons (PAHs) in edible oil: Temperature effect on recovery from base hydrolysis product and health risk factor. *Food and Public Health* **4**(2): 23–30.
DOI: <https://doi.org/10.5923/j.fph.20140402.02>
- Scientific Committee on Foods (2002). Opinion of the Scientific Committee on Food on the risks to human health of polycyclic aromatic hydrocarbons in food. Available at https://food.ec.europa.eu/system/files/2020-12/sci-com_scf_out153_en.pdf
- Pandey M., Mishra K.K., Subhash K., Khanna S.K. & Das M. (2004). Detection of polycyclic aromatic hydrocarbons in commonly consumed edible oils and their likely intake in Indian population. *Journal of the American Oil Chemists' Society* **81**(12): 1131–1136.
DOI: <https://doi.org/10.1007/s11746-004-1030-4>
- Patel A.B., Shaikh S., Kunal R., Jain K.R., Desai C. & Madamwar D. (2020). Polycyclic aromatic hydrocarbons: Sources, toxicity, and remediation approaches. *Frontiers in Microbiology* **11**: 1–23.
DOI: <https://doi.org/10.3389/fmicb.2020.562813>
- Phan Thi L-A., Ngoc N.T., Thi Quynh N., Nguyen T.V., Kim T.T., Anh D.H. & Viet P.H. (2020). Polycyclic aromatic hydrocarbons (PAHs) in dry tea leaves and tea infusions in Vietnam: Contamination levels and dietary risk assessment. *Environmental Geochemistry and Health* **42**: 2853–2863.
DOI: <https://doi.org/10.1007/s10653-020-00524-3>
- Phillips D.H. (1999). Polycyclic aromatic hydrocarbons in the diet. *Mutation Research/Genetic Toxicology and Environmental Mutagenesis* **443**(1–2): 139–147.
DOI: [https://doi.org/10.1016/S1383-5742\(99\)00016-2](https://doi.org/10.1016/S1383-5742(99)00016-2)
- Premnath N., Mohanrasu K., Raj Rao R.G., Dinesh G.H., Prakash G.S., Ananthi V., Ponnuchamy K., Muthusamy G. & Arun A. (2021). A crucial review on polycyclic aromatic hydrocarbons - environmental occurrence and strategies for microbial degradation. *Chemosphere* **280**: 130608.
DOI: <https://doi.org/10.1016/j.chemosphere.2021.130608>
- Purcaro G., Navas J.A., Guardiola F., Conte L.S. & Moreti S. (2006). Polycyclic aromatic hydrocarbons in frying oils and snacks. *Journal of Food Protection* **69**(1): 199–204.
- RASFF (2022). Notifications on PAHs and BaP for one year ending on 18 September 2022. Available at https://food.ec.europa.eu/safety/rasff-food-and-feed-safety-alerts_en. Accessed 18 September 2022.
- Rattanarat P., Chindapan N. & Devahastin S. (2021). Comparative evaluation of acrylamide and polycyclic aromatic hydrocarbons contents in Robusta coffee beans roasted by hot air and superheated steam. *Food Chemistry* **341**(Pt 1): 128266.
DOI: <https://doi.org/10.1016/j.foodchem.2020.128266>
- Richter H. & Howard J.B. (2000). Formation of polycyclic aromatic hydrocarbons and their growth to soot—a review of chemical reaction pathways. *Progress in Energy and Combustion Science* **26**: 565–608.
- Rodrigo M.C.P., Samarajeewa U. & Wijeratne M.C.P. (1995). Use of liquid smoke to prevent aflatoxin contamination of coconut. *Tropical Agricultural Research* **7**: 31–38.
- Rodrigo M.C.P., Samarajeewa U. & Wijeratne M.C.P. (1999). Deposition of polycyclic aromatic hydrocarbons from different coconut-based fuels in smoke curing of copra. *Tropical Agricultural Research* **11**: 103–109.
- Rojo Camargo M.C., Antonioli P.R. & Vicente E. (2012). Evaluation of polycyclic aromatic hydrocarbons content in different stages of soybean oils processing. *Food Chemistry* **135**(3): 937–942.
DOI: <https://doi.org/10.1016/j.foodchem.2012.06.031>
- Rose M., Holland J., Dowding A., Petch S., White S., Fernandes A. & Mortimer D. (2015). Investigation into the formation of PAHs in foods prepared in the home to determine the effects of frying, grilling, barbecuing, toasting and roasting. *Food and Chemical Toxicology* **78**: 1–9.
- Sahin S., Ulusoy H.I., Alemdar S., Erdogan S. & Agaoglu S. (2020). The presence of polycyclic aromatic hydrocarbons (PAHs) in grilled beef, chicken and fish by considering dietary exposure and risk assessment. *Food Science Animal Resources* **40**(5): 675–688.
DOI: <https://doi.org/10.5851/kosfa.2020.e43>
- Samarajeewa U. (2003). Aflatoxin and polycyclic aromatic hydrocarbon contamination in foods and its implications in human health in *Fungi in Human and Animal Health* (ed. R.K.S. Kushwaha), pp. 403–422. Science Publishers, Jodhpur, India.
- Samarajeewa U., Jayatilake C.L.V., Ranjithan A., Gamage T.V. & Arseculeratne S.N. (1985). A pilot plant for detoxification of aflatoxin B1 contaminated coconut oil by solar irradiation. *Mircen Journal of Applied Microbiology and Biotechnology* **1**: 333–343.
DOI: <https://doi.org/10.1007/BF01553418>
- Sampaio G.R., Guizzellini G.M., da Silva S.A., de Almeida A.P., Pinaffi-Langley A.C.C., Rogero M.M., de Camargo, A.C. & Torres & E.A.F.S. (2021). Polycyclic aromatic hydrocarbons in foods: Biological effects, legislation, occurrence, analytical methods, and strategies to reduce their formation. *International Journal of Molecular Science* **22**: 6010.
DOI: <https://doi.org/10.3390/ijms22116010>

- Shen Y., Xie G., Lin S., Zhu L., Zhang H., Yang Z. & Cai Z. (2022). Metabolomics and proteomics study reveals the effects of benzo[a]pyrene on the viability and migration of KYSE-150 esophageal cells. *Science of the Total Environment* **10**: 824.
DOI: <https://doi.org/10.1016/j.scitotenv.2022.153761>
- Siddique R., Zahoor A.F., Ahmad H., Zahid F.M. & Karrar E. (2021a). Impact of different cooking methods on polycyclic aromatic hydrocarbons in rabbit meat. *Food Science and Nutrition* **9**: 3219–3227.
DOI: <https://doi.org/10.1002/fsn3.2284>
- Siddique R., Zahoor A.F., Ahmad H., Zahid F.M., Abid M. & Siddeeq A. (2021b). Probing the impact of conventional oil frying on the formation of polycyclic aromatic hydrocarbons in rabbit meat. *Food Science and Nutrition* **9**(3): 1698–1703.
DOI: <https://doi.org/10.1002/fsn3.2144>
- Silva S.A.D., Torres E.A.F.D.S., Almeida A.P. & Sampaio G.R. (2018). Polycyclic aromatic hydrocarbons content and fatty acids profile in coconut, safflower, evening primrose and linseed oils. *Food Chemistry* **245**: 798–805.
DOI: <https://doi.org/10.1016/j.foodchem.2017.11.109>
- Singh L., Varshney J.G. & Agarwal T. (2016). Polycyclic aromatic hydrocarbons' formation and occurrence in processed food. *Food Chemistry* **199**: 768–781.
- Speer K., Steeg E., Horstmann P., Kühn Th. & Montag A. (1990). Determination and distribution of polycyclic aromatic hydrocarbons in native vegetable oils, smoked fish products, mussels and oysters, and bream from the river Elbe. *Journal of High-Resolution Chromatography* **13**(2): 104–111.
DOI: <https://doi.org/10.1002/jhrc.1240130206>
- Ssepuya F. *et al.*, (12 authors) (2022). Polycyclic aromatic hydrocarbons in breast milk of nursing mothers: Correlates with household fuel and cooking methods used in Uganda, East Africa. *Science of the Total Environment* **842**: 156892.
DOI: <https://doi.org/10.1016/j.scitotenv.2022.156892>
- Sun Y., Wu S. & Gong G. (2019). Trends of research on polycyclic aromatic hydrocarbons in food: A 20-year perspective from 1997 to 2017. *Trends in Food Science & Technology* **83**: 86–98.
DOI: <https://doi.org/10.1016/j.tifs.2018.11.015>
- Tao S., Jiao X.C., Chen S.H., Liu W.X., Coveney R.M. (Jr), Zhu L.Z. & Luo Y.M. (2006). Accumulation and distribution of polycyclic aromatic hydrocarbons in rice (*Oryza sativa*). *Environmental Pollution* **140**(3): 406–415.
DOI: <https://doi.org/10.1016/j.envpol.2005.08.004>
- Tarantini A., Douki T., Personnaz M-B., Besombes J-L., Jafrezo J-L. & Maître A. (2011). Effect of the chemical composition of organic extracts from environmental and industrial atmospheric samples on the genotoxicity of polycyclic aromatic hydrocarbons mixtures. *Toxicological and Environmental Chemistry* **93**(5): 941–954.
DOI: <https://doi.org/10.1080/02772248.2011.573621>
- Tarigholizadeh S., Motafakkerzad R., Salehi-Lisar S.Y., Kazemi E.M., Svetlana Sushkova S. & Minkina T. (2022). Phenanthrene uptake and translocation by *Panicum miliaceum* L. tissues: an experimental study in an artificial environment. *Environmental Geochemistry and Health* **2022**: 01294.
DOI: <https://doi.org/10.1007/s10653-022-01294-w>
- Tongo I., Etor E.E. & Ezemonye L. (2018). Human health risk assessment of PAHs in fish and shellfish from Amariaria community, Bonny River. *Nigeria Journal of Applied Science and Environment Management* **22**(5): 731–736.
DOI: <https://dx.doi.org/10.4314/jasem.v22i5.19>
- Tran-Lam T-T., Dao Y.H., Nguyen L.K.T., Ma H.K., Tran H.N. & Le G.T. (2018). Simultaneous determination of 18 polycyclic aromatic hydrocarbons in daily foods (Hanoi metropolitan area) by gas chromatography–tandem mass spectrometry. *Foods* **8**(7): 201.
DOI: <https://doi.org/10.3390/foods7120201>
- Tuvikene A. (1995). Responses of fish to polycyclic aromatic hydrocarbons (PAHs). *Annales Zoologici Fennici* **32**: 295–309.
- US Environmental Protection Agency (US EPA). Environmental Protection Agency Consumer Factsheet on: BENZO(A)PYRENE. Available at <https://archive.epa.gov/water/archive/web/pdf/archived-consumer-factsheet-on-benzo.pdf>, accessed 23 September 2022.
- van Grevenynghe J., Rion S., Ferrec E.L., Vee M.L., Amiot L., Fauchet R. & Fardel O. (2003) Polycyclic aromatic hydrocarbons inhibit differentiation of human monocytes into macrophages. *Journal of Immunology* **170**: 2374–2381.
DOI: <https://doi.org/10.4049/jimmunol.170.5.2374>
- Wang Y., Liu C.S., Li F.B., Liu C.P. & Liang J.B. (2009). Photodegradation of polycyclic aromatic hydrocarbon pyrene by iron oxide in solid phase. *Journal of Hazardous Materials* **162**(2–3): 716–723.
DOI: <https://doi.org/10.1016/j.jhazmat.2008.05.086>
- WHO (2010). *IARC Monographs on Evaluation of Carcinogenic Risks to Humans*, volume 92. Some non-heterocyclic polycyclic aromatic hydrocarbons and related exposures. Lyon, France.
- WHO/FAO Joint Expert committee on Food Additives and Contaminants (JEFCA) (2005). Sixty-fourth Meeting (JECFA/64/SC), 8–17 February, Rome, Italy.
- Wijeratne M.C.P., Samarajeewa U. & Rodrigo M.C.P. (1996a). Polycyclic aromatic hydrocarbons in coconut products. *Journal of the National Science Council of Sri Lanka* **24**(4): 285–297.

- Wijeratne M.C.P., Samarajeewa U. & Chandralekha A.P.L. (1995). Polycyclic aromatic hydrocarbons in some fried and smoked foods in Sri Lanka. *Proceedings of the Third Asia Pacific Food Analysis Conference, Manila, Philippines*. 22–25 May. Food and Nutrition Research Institute, Philippines, pp. 133.
- Wijeratne M.C.P., Samarajeewa U., Rodrigo M.C.P. & Werapitiya I. (1996b). Production of polycyclic aromatic hydrocarbons during home preparation of coconut oil. *Chemistry in Sri Lanka*. Proceedings of the 25th Annual session of the Institute of Chemistry, Ceylon **13**(1): 6.
- Wijeratne M.C.P., Samarajeewa U. & Karunaratne G.D.D.P. (1997). Irradiation of polycyclic aromatic hydrocarbons in coconut oil. *Chemistry in Sri Lanka*. Proceedings of the 26th Annual Session of the Institute of Chemistry, Ceylon **14**(1): 8.
- Wijeratne M. C. P., Samarajeewa U., Rodrigo M. C. P. Werapitiya I. & Metcalfe E. (1998). Generation of polycyclic aromatic hydrocarbons during expulsion and thermal processing of coconut oil. *Proceedings of the EC Project Seminar on Polycyclic Aromatic Hydrocarbons in Copra and Derived Products*. Taj Samudra Hotel, Colombo. 12–16th January.
- Wilkinson F., McGarvey D.J. & Olea A.F. (1993). Factors governing the efficiency of singlet oxygen production during oxygen quenching of singlet and triplet states of anthracene derivatives in cyclohexane solution. *Journal of the American Chemical Society* **115**: 12144–121518.
- Yousefi M., Shemshadi G., Khorshidian N., Ghasemzadeh-Mohammadi V., Fakhri Y., Hosseini H. & Khaneghah A.M. (2018). Polycyclic aromatic hydrocarbons (PAHs) content of edible vegetable oils in Iran: A risk assessment study. *Food and Chemical Toxicology* **118**: 480–489.
DOI: <https://doi.org/10.1016/j.fct.2018.05.063>
- Zachara A., Gałkowska D. & Juszczak L. (2018). Contamination of tea and tea infusion with polycyclic aromatic hydrocarbons. *International Journal of Environmental Research and Public Health* **15**: 45.
DOI: <https://doi.org/10.3390/ijerph15010045>
- Zelinkova Z. & Wenzl T. (2015). The occurrence of 16 EPA PAHs in food - A review. *Polycyclic Aromatic Compounds* **35**: 248–284.
DOI: <https://doi.org/10.1080/10406638.2014.918550>
- Ziegenhals K., Speer K. & Jira W. (2009). Polycyclic aromatic hydrocarbons (PAH) in chocolate on the German market. *Journal für Verbraucherschutz und Lebensmittel Sicherheit* **4**: 128–135.
DOI: <https://doi.org/10.1007/s00003-009-0478-1>

RESEARCH ARTICLE

Geodetic Science

Sea level variability at Colombo, Sri Lanka, inferred from the conflation of satellite altimetry and tide gauge measurements

HMI Prasanna^{1*}, MDEK Gunathilaka¹ and HB Iz²

¹ Department of Surveying and Geodesy, Faculty of Geomatics, Sabaragamuwa University of Sri Lanka, P.O. Box 02, Belihuloya, Sri Lanka.

² Division of Geodetic Science, School of Earth Sciences, The Ohio State University Columbus, Ohio, USA.

Submitted: 29 September 2021; Revised: 02 June 2022; Accepted: 26 August 2022

Abstract: Accurate long-term measurements of sea level are fundamental to evaluating coastal risks, such as the impact of sea-level rise on near-shore ecosystems, groundwater dynamics, and coastal flooding. This study examines sea-level variability at Colombo, Sri Lanka using satellite altimetry, tide gauge measurements separately and their conflated solution under a single model. Modelling of conflated satellite altimetry and tide gauge measurements shows a geocentric (absolute) local sea-level rise of 3.56 ± 0.32 mm/y without any signature of a uniform acceleration since 1981 at this locality. The measurements disclosed statistically significant periodic changes in sea level of luni-solar origin. The conflated model solution enabled the estimation of a statistically significant in-situ vertical land motion (0.58 ± 0.19 mm/yr) without the aid of global positioning measurements. The conflation model explains 98% of the sea-level variability, which makes it suitable for accurate sea level predictions for coastal risk assessments in Colombo, Sri Lanka.


Keywords: Colombo Sri Lanka tide gauge, satellite altimetry, sea-level rise, sea-level trend and acceleration, vertical land motion.

INTRODUCTION

Located in the Indian Ocean, off the Southeast Coast of India, Sri Lanka is a small island with diverse geography and a tropical climate. Its 1,700 km of coastline sounds highly vulnerable to the impact of climate change. This sounds alarming when considering the fact that roughly 50% of its inhabitants live in coastal areas on the West. Therefore, evaluating past and current sea-level changes is essential in this region for coastal risk assessment.

There have not been many studies that rigorously assess the sea-level variability in Sri Lanka. Wijeratne *et al.* (2008) analysed seasonal sea-level variability in this region using altimetric, meteorological and hydrographic information, including results from numerical modelling, to understand the main factors which contribute to the observed Mean Sea Level (MSL) changes. Gunathilaka *et al.* (2017) has estimated the sea-level trend at Colombo Port using 20 years of satellite altimetry (SA) data and tide gauge (TG) data from 1993 to 2012. Their estimated absolute sea-level trend in Colombo was around 2.50 ± 0.53 mm/y. Previous studies of sea-level fluctuations in different regions have confirmed that the sea level has increased during the 20th century and still escalating at a global scale of the absolute sea-level trend of about 3.2 ± 0.4 mm/y (Unnikrishnan *et al.*, 2015). A recent study by Palamakumbure *et al.* (2020) investigated risk assessment of sea-level inundation along the south and southwest coasts of Sri Lanka using two tide gauges, together with Digital Elevation Models (DEMs). The time span of their local data was markedly short (2006–2017) to capture sea-level variability in this locality to be useful for reliable predictions. Their study was extensive, but the effect of the vertical land motion (VLM) in this region was not taken into account as a correction. Therefore, the results refer to relative sea-level changes, which are of limited use for coastal risk assessments. More importantly, their investigation was based on tide gauge (TG) data that were not corrected for the effect of the atmospheric pressure (Inverted Barometer, IB) effect, which is markedly noisy at this station.

In this study, we address all these issues which were not considered in the previous studies and deploy not only longer TG data (1981–2018) corrected for the IB, but also incorporate SA data (1992–2018) and take into

* Corresponding author (indika@geo.sab.ac.lk;  <https://orcid.org/0000-0001-8689-4647>)



This article is published under the Creative Commons CC-BY-ND License (<http://creativecommons.org/licenses/by-nd/4.0/>). This license permits use, distribution and reproduction, commercial and non-commercial, provided that the original work is properly cited and is not changed in anyway.

consideration the effect of the VLM at the Colombo TG station. We rigorously evaluate sea-level variability at the Colombo TG station records and estimate sea-level rise using TG data and the SA in combination under a single model for optimal assessment of the results. The mathematical and statistical models used in this study permit concurrent estimation of absolute and relative sea-level trend and acceleration, low-frequency sea-level variations, including periodic annual and semi-annual sea-level changes together with VLM without Global navigation satellite system (GNSS) measurements.

In the following sections, we provide information on monthly SA, TG and GNSS data nearby Colombo, Sri Lanka TG station. Then we calculate separately the relative and absolute sea-level trend and acceleration using monthly TG and SA data, respectively. The discrepancy between the calculated relative and absolute sea-level trends provides an estimate of the linear rate of VLM experienced at the TG station. These findings will serve as a benchmark for evaluating the conflated model solution estimations. The model parameters mentioned above estimated simultaneously using restricted (constrained) least squares (Iz *et al.*, 2020). Finally, the concurrently estimated VLM rate of the conflation model is compared with the VLM rate estimated from the GNSS data observed in the vicinity of the tide gauge station. The latter data is from the GNSS solution ‘NGL14’ produced by the Nevada Geodetic Laboratory (NGL) using a precise point positioning daily position time series for over 17,000 globally distributed stations.

MATERIALS AND METHODS

Tide gauge and satellite altimetry records at Colombo, Sri Lanka

The Colombo Port floating-type TG records span from 1981 to 2018 (Figure 1). Originally, this was an hourly data set and converted to the daily mean and then into monthly mean values to comply with the SA data. This TG time series are referenced to the Low Water Ordinary Spring Tide (LWOST) datum, which is close to the Lowest Astronomical Tide (LAT), and the difference between the observed MSL and the LWOST datum at the TG station is around 0.4 m (Prasanna *et al.*, 2021). These TG time series records refer to relative sea-level changes since the corrections for the VLM have not been applied. The TG time series were corrected for the IB effect (Figure 2) using a near-real-time update of the Mean Sea-level Pressure (MSLP) data set, HadSLP2r, of the Met Office Hadley Centre. This data set is a unique combination of monthly globally complete fields of land and marine pressure observations on a 5-degree geographic grid from 1850 to 2019 (Allan & Ansell, 2006).

Among the various SA products that are available at this location, for our study region, we used SA sea-level anomaly data produced by NASA in its MEaSUR (Making Earth Science Data Records for Use in Research Environments) program, downloaded in July 2021 for the period from October 1992 to June 2019 (Figure 3). These are fully corrected gridded Sea Surface Height Anomalies (SSHA) above a mean sea surface on a 1/6th degree grid every 5 days. The gridded data are derived from the SSHA data of TOPEX/Poseidon, Jason-1, Jason-2 and Jason-3 as reference data from the level 2 swath data found (Zlotnicki *et al.*, 2019).

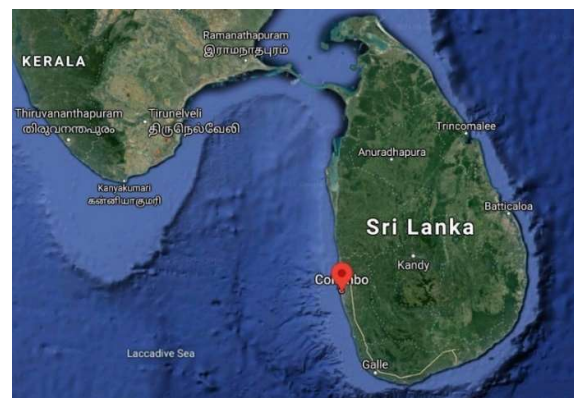


Figure 1: Tide gauge location at Colombo in Sri Lanka (Google Maps, 2021).

RESULTS AND DISCUSSION

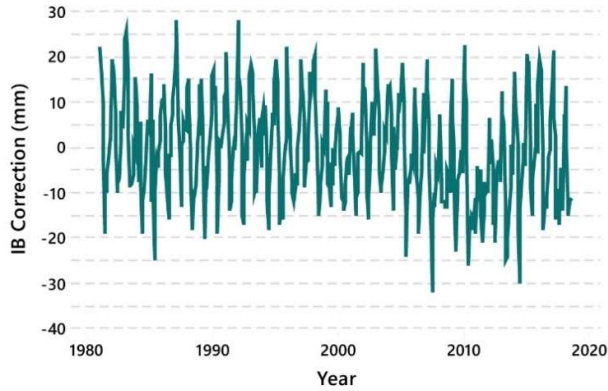


Figure 2: Inverted barometer correction (IB) for the TG records.

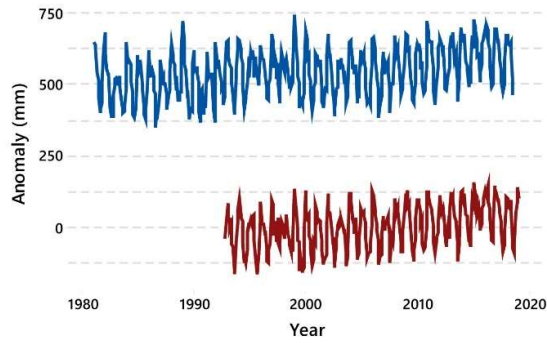


Figure 3: Monthly SA (red) and TG (blue) sea-level measurements at Colombo, Sri Lanka. The time series of the data refer to their own datum. TG time series are corrected for the IB effect.

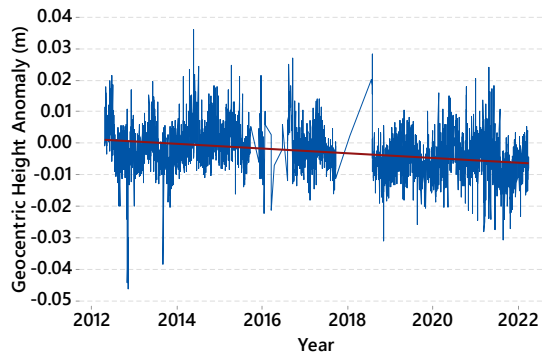


Figure 4: Daily averaged GPS measurements during 2012–2022 at the station SGOC, Narahenpita, Sri Lanka. The estimated linear trend (red line), the rate of VLM, is -0.82 ± 0.08 mm/y. Note that downloaded NSL records reported a trend of -0.19 ± 0.89 mm/y.

There is no co-located GNSS station to monitor VLM at this TG station. The nearest site is 5 km away, located at Surveyor General's Office Colombo (SGOC), Narahenpita, Sri Lanka. GNSS measurements are maintained by German Research Centre for Geosciences (GFZ), and processed time series are available from the University of Nevada at Reno (NGL), which are shown in Figure 4. The station is identified as Site ID: SGOC # DOMES: 23501M003, and the VLM data shown were downloaded from NGL in May 2022. The sporadic measurement span was carried out during 2012–2022 with an approximately two-year gap. The reported VLM -0.19 ± 0.89 mm/y recorded in the download GNSS NGL differed significantly from the estimated trend -0.82 ± 0.08 mm/y using weighted least squares (WLS); here weights are assigned to be the inverse of the squared standard deviations of the daily measurements in this study. The standard error of the estimated linear rate was also corrected for the AR(1) effect in this analysis.

In the following section, sea-level anomalies monitored by these two diverse technologies (TG and SA) are modelled and analysed separately.

Individual kinematic model solutions for satellite altimetry and tide gauge records

Sea-level variations were customarily modelled using quadratics, and this research goes back over three decades (Douglas, 1992). However, it must be noted that the quadratic model is ambiguous. The underlying physics of a quadratic model is kinematics, which describes the motion of objects without reference to the forces which cause the motion. The quadratic model is also misleading. It hides important issues for its implication of the uniformity of the acceleration and dependency of the trend estimate on the initial epoch when there is a uniform acceleration and unified datum definition. The quadratic representation of the sea-level variations is equivalent to the following basic kinematic model,

$$h_t = h_{t_0} + v_{t_0}(t - t_0) + \frac{a}{2}(t - t_0)^2 + u_t, \quad \dots(01)$$

and

$$v_t = v_{t_0} + a(t - t_0), \text{ if } a \neq 0 \quad \dots(02)$$

where, h_t refers to the monthly averaged tide gauge data observed and v_t is the velocity at an epoch t . To improve the numerical stability of the solution, the epochs of the measurements are moved to the middle of the series t_0 . The unknown sea-level reference height is defined at t_0 and denoted by h_{t_0} . The uniform acceleration/deceleration in sea level and the initial velocity are denoted as a and v_{t_0} respectively. When there is no acceleration $v_t = v = \text{constant}$. If the observations are referenced to the TG records, the initial velocity would be a relative trend. If the observations are from the nearby SA, they are inherently geocentric. The assumed statistical properties of the random variable are assumed to be $u_t \sim iid(0, \sigma_u^2)$, where σ_u^2 is the variance of the random variable.

We used this model, given by equations (1) and (2), to represent and estimate the trends and uniform accelerations for SA and TG time series using Ordinary Least Squares (OLS) procedure. The solutions serve as baselines to compare the conflation model presented in the following sections conjured to be an improvement over the individual models.

Table 1 shows the estimated relative and absolute sea-level trends, their standard errors, SE, and adjusted R^2 values. Sea-level trends are statistically significant at a 95% confidence level (CL) for solutions of both TG and SA models, but the estimated acceleration parameters are both rejected at 95% CL for the TG and SA measurements. Therefore, the estimated trends/velocities are constant.

The difference between the relative TG and absolute SA trends is an estimate of the VLM experienced at this station. The magnitude of this estimated VLM rate is large, but it is not statistically significant (-0.68 ± 0.63), i.e., the null hypothesis $H_0: v_{VLM} = v_{SA} - v_{TG} = 0$ cannot be rejected (Table 1). Nonetheless, the GNSS measurements carried out at 5 km away from the TG station indicate a statistically significant VLM (-0.82 ± 0.08 mm/y). Although the magnitudes of the VLM from two different sources agree, it is not conclusive because v_{VLM} estimate is noisy.

The solution statistics and the display of the residuals show that this model is inappropriate for representing the sea-level variations at this locality. The residuals exhibit unmodeled systematic variations, and their non-random behaviour is supported by their histograms (Figure 5a and Figure 5b). The adjusted R^2 values explain only 13% and 11% of the anomalies in TG and SA measurements, respectively. Some of the reasons for the poor performance of these basic kinematic models are the topics of the following sections.

A confluence model for the SA and TG measurements and its solution

One of the reasons for the failure of the above basic kinematic model is the unmodelled effect of low-frequency sea-level variations, as evidenced in the residuals (Figure 5a, Figure 5b). Iz (2014; 2015) identified and developed an improved kinematic model consisting of a linear velocity, uniform acceleration, and statistically significant and globally prevalent specific low frequency sea-level variations. Their origins are luni-solar forcings impacting sea-level variations with periods of 18.6 years for the lunar node changes and 11.1 years for solar variation (ibid.). Inspired by the findings of the study of Wijeratne *et al.* (2008), representations for annual and semi-annual periodic sea-level variations are also incorporated into the model.

The following model accounts for the effects of low-frequency changes in the extended kinematic model and can be used in the analyses of both SA and TG records,

$$h_t = h_{t_0} + v_{t_0}(t - t_0) + \frac{a}{2}(t - t_0)^2 + \sum_{k=1}^4 \left\{ \alpha_k \sin \left[\left(\frac{2\pi}{P_k} \right) (t - t_0) \right] + \gamma_k \cos \left[\left(\frac{2\pi}{P_k} \right) (t - t_0) \right] \right\} + \varepsilon_t \quad \dots(03)$$

$$v_t = v_{t_0} + a(t - t_0)t, \text{ if } a \neq 0 \quad \dots(04)$$

The unknown parameters α_k “and” γ_k in the above model are the components of the periods P_k to be estimated and used in computing the amplitudes and the phase angles of the luni-solar periodicities and the annual and semi-annual variations for eight additional parameters.

Note that the variable ε_t that represents the disturbance is different from u_t of the basic kinematic model. It refers to a first order autoregressive process, AR(1), and other random effects, including instrument errors in sea-level changes. This property of the disturbances is not recognized by the basic kinematic model given by equation (1), which is another source of inaccuracy in the separate model solutions. The AR(1) error ε_t is represented as,

$$\varepsilon_t = \rho\varepsilon_{t-1} + u_t \quad t = \dots, -2, -1, 0, 1, 2, \dots \quad \dots(05)$$

where, $-1 \leq \rho \leq 1$ is the unknown autocorrelation coefficient of AR(1) process. Like before, the properties of the random noise u_t , is $u_t \sim iid(0, \sigma_u^2)$.

The estimated AR(1) correlation coefficients for the SA and TG records are $\hat{\rho}_{SA} = 0.15$ and $\hat{\rho}_{TG} = 0.20$. They reduce the effective time span of the SA records from 27 to 20 years and TG records from 37 to 25 years, resulting in an artificial overestimation of the SE of the parameters.

This model can now be used to *conflate* records of SA and TG measurements under a single model, namely, the confluence model, which was introduced by Iz *et al.* (2020). The following confluence model represents absolute and relative linear sea-level trends in SA, TG and VLM together with the periodic sea level changes. The model is expressed as,

$$h_t^{TG} = h_{t_0}^{TG} \pm v^{VLM}(t^{TG} - t_0^{TG}) + v^{SA}(t^{TG} - t_0^{TG}) + \sum_{k=1}^m \left\{ \alpha_k \sin \left[\left(\frac{2\pi}{P_k} \right) (t^{TG} - t_0^{TG}) \right] + \gamma_k \cos \left[\left(\frac{2\pi}{P_k} \right) (t^{TG} - t_0^{TG}) \right] \right\} + \varepsilon_t^{TG} \quad \dots(06)$$

$$h_t^{SA} = h_{t_0}^{SA} \pm v^{VLM} (t^{SA} - t_0^{TG}) + v^{TG} (t^{SA} - t_0^{TG}) + \sum_{k=0}^m \left\{ \alpha_k \sin \left[\left(\frac{2\pi}{P_k} \right) (t^{SA} - t_0^{TG}) \right] + \gamma_k \cos \left[\left(\frac{2\pi}{P_k} \right) (t^{SA} - t_0^{TG}) \right] \right\} + \varepsilon_t^{SA} \quad \dots(07)$$

$$\varepsilon_t^{TG} = \rho_{TG} \varepsilon_{t-1}^{TG} + u_t^{TG} \quad 0 \leq |\rho_{TG}| < 1, \quad u_t^{TG} \sim iid(0, \sigma_{u^{TG}}^2) \quad \dots(08)$$

$$\varepsilon_t^{SA} = \rho_{SA} \varepsilon_{t-1}^{SA} + u_t^{SA} \quad 0 \leq |\rho_{SA}| < 1, \quad u_t^{SA} \sim iid(0, \sigma_{u^{SA}}^2) \quad \dots(09)$$

The superscripts SA and TG identify the origin of the measurements in the observation equations. The sign of the v^{VLM} is decided depending on the nature of the VLM being a subsidence or an uplift. Because the estimated uniform accelerations were not statistically significant in SA and TG records, the trends or velocities are constant; hence they are no longer part of the confluence model.

The corresponding variance (V) or covariance (C) matrix of the autocorrelated disturbances for any one of the time series can be written as (Kendall, 1968; İz & Chen, 1999),

$$\Sigma = \sigma^2 \cdot \begin{bmatrix} 1 & \rho & \rho^2 & \dots & \rho^{n-1} \\ \rho & 1 & \dots & \dots & \rho^{n-2} \\ \vdots & \vdots & \vdots & \ddots & \vdots \\ \rho^{n-1} & \rho^{n-2} & \rho^{n-3} & \dots & 1 \end{bmatrix} = \sigma^2 \cdot P^{-1} \quad \dots(10)$$

where P is the corresponding $n_{TG} \times n_{TG}$ or $n_{SA} \times n_{SA}$ weight matrix depending upon which records are in consideration and σ^2 is the variance of the disturbances, ε . Implicit in this expression is the assumption that measurements are equally spaced in time. The correlation decreases with increasing time lag because $|\rho| < 1$. The above patterned V/C matrix has an analytical inverse and is given by (ibid.),

$$\Sigma^{-1} = \frac{\sigma^{-2}}{1-\rho^2} P = \begin{bmatrix} 1 & -\rho & 0 & \dots & 0 & 0 \\ -\rho & 1+\rho^2 & -\rho & \dots & 0 & 0 \\ 0 & -\rho & 1+\rho^2 & \dots & 0 & 0 \\ \vdots & \vdots & \vdots & \ddots & \vdots & \vdots \\ 0 & 0 & 0 & \dots & 1+\rho^2 & -\rho \\ 0 & 0 & 0 & \dots & -\rho & 1 \end{bmatrix} \quad \dots(11)$$

Assuming SA and TG measurements are uncorrelated, we construct the following V/C matrix for the confluence model,

$$\Sigma^{-1} = \begin{bmatrix} \frac{\sigma_{TG}^{-2}}{1-\rho_{TG}^2} P_{TG} & 0 \\ 0 & \frac{\sigma_{SA}^{-2}}{1-\rho_{SA}^2} P_{SA} \end{bmatrix} \quad \dots(12)$$

At this point, another difficulty arises because, in the above observation, equations of the coefficients of v^{VLM} and v^{SA} for SA and v^{VLM} and v^{TG} for TG are co-linear. Nonetheless, the following constraint between the relative and absolute velocities, v^{TG} and v^{SA} , and v^{VLM} , enables a unique solution for estimating the confluence model parameters.

$$\pm v^{VLM} + v^{TG} - v^{SA} = 0 \quad \dots(13)$$

The confluence model was evaluated using the Restricted (constrained) Least Squares Solution (RLSS) method (Iz et al., 2020). The residuals of the solution of the confluence model for the SA and TG records are shown in Figure 5c and Figure 5d. The unknown first-order autoregressive correlation coefficients, AR(1), for the TG and SA, denoted by $\hat{\rho}_{TG} = 0.2$ and $\hat{\rho}_{SA} = 0.15$, respectively, were calculated from the residuals iteratively by evaluating their autocorrelation functions. According to the Durbin-Watson (DW) statistics, the expected value for random distributions is 2. In this solution, the calculated DW for the TG residuals and the SA

residuals are 2.1 and 1.85, respectively, which shows that the confluence model removes systematic sea-level variations at this station effectively.

The amplitudes of luni-solar forcing and annual and semi-annual sea-level variations are also statistically significant, as tabulated in Table 2.

VLM estimate using the confluence model is consistent with the one obtained by differencing absolute and relative velocities, namely, -0.58 ± 0.19 mm/y vs -0.68 ± 0.63 mm/y, respectively. Moreover, the null hypothesis for the estimated VLM rate using the confluence model $H_0: VLM_{SA} - VLM_{TG} = 0$ is rejected, i.e., the linear rate of VLM is statistically significant. The VLM trend estimated from the conflation model is also compared to the one obtained from daily GNSS measurements. They agree in magnitude, -0.58 ± 0.19 mm/y vs -0.82 ± 0.08 mm/y, and both estimates are statistically significant ($\alpha = 0.05\%$). Their difference, $H_0: VLM_{SA} - VLM_{TG} = 0$, can no longer be rejected.

Table 1: Comparison of individual solution statistics using TG and SA records to those using the conflated model. The SE of the estimates are 1σ . Note that the subsidence rate estimated in this study is significantly different from the reported rate, -0.19 ± 0.89 mm/y in the downloaded file. N/A Not Applicable.

Solution	SA records	TG records	Conflated SA & TG records		GNSS
v (mm/yr.)	3.50 ± 0.53	2.82 ± 0.34	3.56 ± 0.32	2.98 ± 0.19	N/A
SE (mm)	71.6	77.6	37.2		1.5
Adj. R ² %	11	13	98		12
VLM (mm/yr.)	-0.68 ± 0.63		-0.58 ± 0.19		-0.82 ± 0.08

Table 2: Estimated components of the periodic sea-level variations

Period (y)	Sine (mm)	Cosine (mm)
18.6	-16.48 ± 2.85	N/S
11.1	NS	6.17 ± 2.70
Annual	84.73 ± 2.50	-19.77 ± 2.50
Semi-annual	20.91 ± 2.08	4.70 ± 2.10

N/S: Not Significant

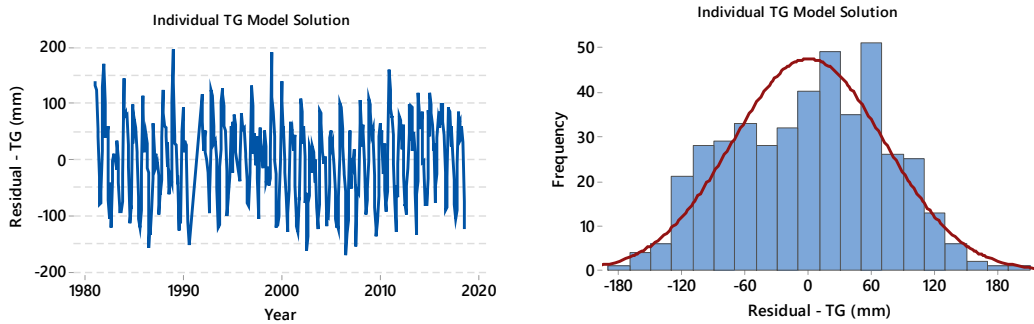


Figure 5a: Residuals and their histograms for the TG-only model solution

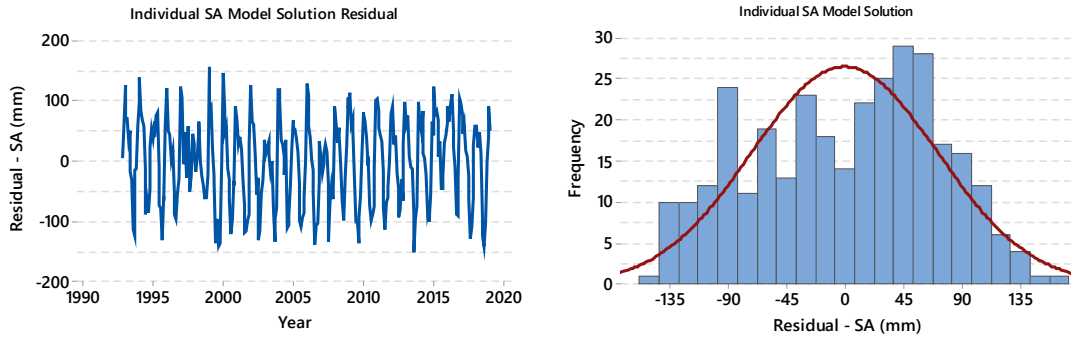


Figure 5b: Residuals and their histograms for the SA-only model solution

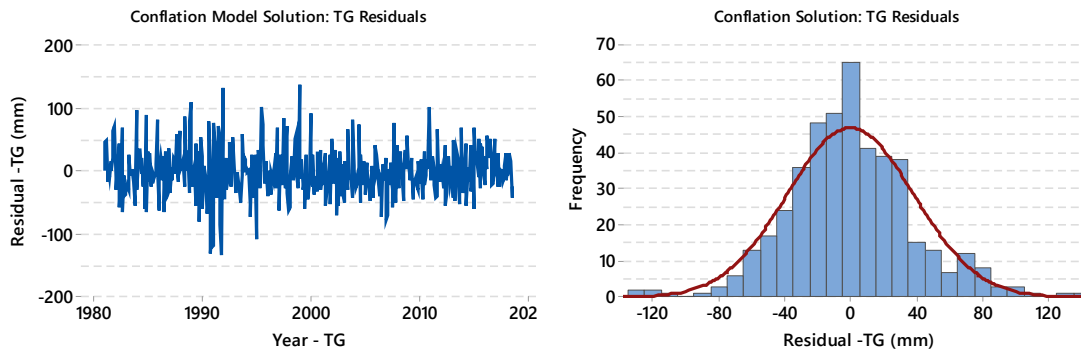


Figure 5c: Residuals and their histograms for SA from the conflation model solution

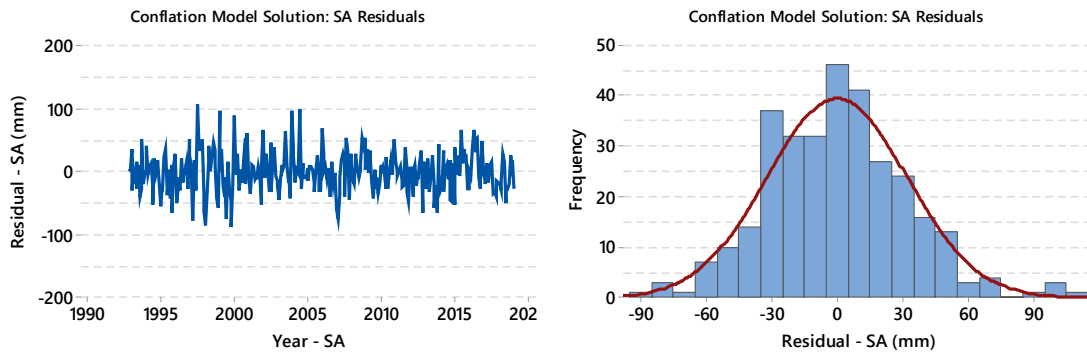


Figure 5d: Residuals and their histograms for TG from the conflation model solution

CONCLUSION

This study analysed the sea-level variability at Colombo, Sri Lanka using tide gauge and satellite altimetry measurements combined under a single model. This is the first-ever study of sea level in this locality. Relative and absolute sea-level trends and acceleration with a linear rate of change in VLM at this locality were estimated simultaneously using SA and TG records. Modelling conflated satellite altimetry and tide gauge measurements revealed that since 1981 the tide gauge station experienced a geocentric local sea-level rise of 3.56 ± 0.32 mm/y, with no evidence of uniform acceleration. The measurements also disclosed statistically significant periodic changes in sea level of luni-solar origin

and strong contributions by the annual and semi-annual variations. This investigation also quantified the statistically significant VLM at the TG station 0.58 ± 0.19 mm/y, which is verified using the GNSS measurements carried out independently at a nearby monitoring station. The conflation model explains 98% of the sea-level variability at the station in Colombo, Sri Lanka, and it is suitable for accurate sea level predictions at this locality.

Conflicts of interest

The authors declare that they have no conflict of interest.

Availability of data and material

Four types of datasets were used for this study:

Tide Gauge data (TG): A floating-type TG data was obtained from the Colombo Port Authority of Sri Lanka. The data set in different time periods is available at Permanent Service for Mean Sea Level (PSMSL) website: <http://www.ioc-sealevelmonitoring.org/station.php?code=colo>
<http://www.psmsl.org/data/obtaining/>

Satellite Altimetry data (SA): SA data obtained from the data set produced by the NASA's MEASURE's program, which were downloaded in July 2021 for the region 6°N , 79°E – 7°N , 80°E for the period October 1992 to June 2019. The data available at: https://podaac.jpl.nasa.gov/dataset/SEA_SURFACE_HEIGHT_ALT_GRIDS_L4_2SATS_5DAY_6THDEG_V_JPL1812

GNSS data: VLM data were downloaded from the continuous GNSS station, SGOC, from SONEL. Data is available at: <https://www.sonel.org/?page=gps&idStation=3582>

Mean Sea Level Pressure (MSLP) data: MSLP data from 1981 to 2019 were used for IB computation. The data set was extracted from the Mean Sea-level Pressure (MSLP) data set of the Met Office Hadley Centre at: <https://www.metoffice.gov.uk/hadobs/hadslp2/>

REFERENCES

- Allan R. & Ansell T. (2006). A new globally complete monthly historical gridded mean sea-level pressure dataset (HadSLP2): 1850–2004. *Journal of Climate* **19**(22): 5816–5842.
DOI: <https://doi.org/10.1175/JCLI3937.1>
- Douglas B.C. (1992). Global sea-level acceleration. *Journal of Geophysical Research* **97**: 12699–12706.
DOI: <https://doi.org/10.1029/92JC01133>
- Gunathilaka M.D.E.K., Kannangara K.K.D.W.S. & Samarapperuma S.A.H.M. (2017). Estimation of sea-level rise in Colombo with satellite altimetry data. *Conference Proceedings*, General Sir John Kotelawala Defence University International Research Conference, Ratmalana, Sri Lanka, 3–4 August.
- İz H.B., Shum C.K. & Yang T.Y. (2020). Conflation of satellite altimetry and tide gauge records at coast. *Journal of Geodetic Science* **10**: 62–68.
DOI: <https://doi.org/10.1515/jogs-2020-0113>
- İz H.B. (2015). More confounders at global and decadal scales in detecting recent sea-level accelerations. *Journal of Geodetic Science* **5**: 192–198.
DOI: <https://doi.org/10.1515/jogs-2015-0020>
- İz H.B. (2014). Sub and super harmonics of the lunar nodal tides and the solar radiative forcing in global sea-level changes. *Journal of Geodetic Science* **4**: 150–165.
- İz H.B. & Chen Y. (1999). VLBI rates with first order autoregressive disturbances. *Journal of Geodynamics* **28**(2–3): 131–145.
DOI: [https://doi.org/10.1016/S0264-3707\(98\)00033-7](https://doi.org/10.1016/S0264-3707(98)00033-7)
- Nevada Geodetic Laboratory (NGL) (2021). http://geodesy.unr.edu/MIDAS_release.tar
- Palamakumbure L., Ratnayake A.S., Premasiri H.R., Ratnayake N.P., Katupotha J., Dushyantha N., Weththasinghe S. & Weerakoon W.P. (2020). Sea-level inundation and risk assessment along the south and southwest coasts of Sri Lanka. *Geo environmental Disasters* **7**(1): 1–9.

- DOI: <https://doi.org/10.1186/s40677-020-00154-y>
- Prasanna H.M.I., Gunathilaka M.D.E.K. & Welikanna D.R. (2021). Development of a unified vertical reference framework for Land and Hydrographic surveying in Sri Lanka. *Marine Geodesy* **44**(3): 1–13.
DOI: <https://doi.org/10.1080/01490419.2021.1902889>
- Unnikrishnan A.S., Nidheesh A.G. & Lengaigine M. (2015). Sea-level-rise trends off the Indian coasts during the last two decades. *Journal of Current Science* **108**(5): 966–971.
- Wijeratne E.M.S., Woodworth P.L. & Stepanov, V.N. (2008). The seasonal cycle of sea level in Sri Lanka and Southern India Western Indian Ocean. *Western Indian Ocean Journal of Marine Science* **7**(1): 29–43.
DOI: <https://doi.org/10.4314/wiojms.v7i1.48252>
- Zlotnicki V., Qu Zheng & Willis J. (2019). Sea Surface Height ALT GRIDS L4 2SATS 5DAY 6THDEG V JPL1609. Ver. 1812. PO.DAAC, CA, USA. Accessed 12 July 2021.
DOI: <https://doi.org/10.5067/SLREF-CDRV2>

RESEARCH ARTICLE

Food Microbiology

Prevalence of histamine forming bacteria in selected nodes of the supply chain of Sri Lankan Yellowfin tuna

PH Ginigaddarage^{1*}, GJ Ganegama Arachchi¹, KWS Ariyawansa¹ and CM Nanayakkara^{2,3}

¹ Institute of Post Harvest Technology, National Aquatic Resources Research and Development Agency, Nara Road, Colombo 15, Sri Lanka.

² Department of Plant Sciences, Faculty of Science, University of Colombo, Colombo 03, Sri Lanka.

³ Sri Lanka Institute of Biotechnology, Pitipana, Homagama, Sri Lanka.

Submitted: 02 December 2021; Revised: 21 June 2022; Accepted: 23 September 2022


Abstract: This study aimed to identify histamine-forming bacteria (HFB) and the sources of introduction of such bacteria to recommend control measures to mitigate histamine formation in yellowfin tuna (YFT). Field samples were collected from multi-day boats that landed at Dikkowita, Negombo, Trincomalee and Dondra fishery harbours. Ice from the fish holds (n=63) and chill transport vehicles (n=63), and swabs from the fish holds (n=63), the boat decks (n=63) and the skin of YFT (n=63) were collected. Fish loin samples (n=15), ice samples (n=36) and swabs from the skin of YFT (n=18), floor (n=18) and chill transport vehicles (n=18) were collected from fish processing plants. Presumptive HFB isolated from Nivens medium and Violet Red Bile Glucose (VRBG) agar were screened for histamine forming ability in Trypticase soy broth (TSB) supplemented with 1.0% L-histidine. HFB isolates were characterized by sequencing approximately 1400 bp of the 16S rDNA. Seven isolates that produced histamine in the range of 3000–4000 ppm in TSB isolated from ice samples, and a swab sample collected from the boat deck, were confirmed as *Klebsiella aerogens* (n=6) and *Morganella morganii* (n=1) respectively. *Hafnia alvei* (n=1), *Serratia* sp. (n=2), *Citrobacter freundii* (n=1), *Rahnella* sp. (n=1) and *Aeromonas salmonicida* (n=8) were also among the isolated histamine forming bacteria. *Pseudomonas* sp. (n=24) and *Shewanella baltica* (n=7), which are known as spoilage bacteria were also isolated and showed weak histamine formation. Hence, it is evident that histamine-forming bacteria could be introduced into the fish from ice and contacting surfaces. This necessitates the practice of rigorous cleaning procedures and adaptation of proper postharvest handling procedures to minimize contamination of the fish.

Keywords: Fish processing factories, histamine forming bacteria, multiday boats, yellowfin tuna.

INTRODUCTION

Histamine is formed by the bacterial decarboxylation of free histidine in fish muscle when the fish are subjected to temperature abuse during or after harvest. Histamine toxicity or scombroid poisoning is generally a mild illness with a range of symptoms, including rash, nausea, vomiting, diarrhea, flushing and tingling, and itching of the skin (Taylor & Sumner, 1987). Scombroid fish (e.g. tuna, mackerel, bonito) contain high levels of free histidine in their muscles and are related to scombroid poisoning (Taylor *et al.*, 1989). Several fish species, which are not categorized as scombroid fish, such as mahi-mahi, bluefish, herring, and sardine are also found to be associated with incidents of scombroid poisoning (Price & Melvin, 1994). In most cases, the histamine levels in illness-causing fish have been above 200 ppm, often above 500 ppm (USFDA, 2021). Scombrototoxin food poisoning will only occur in healthy individuals when a dose of at least 50 mg histamine is consumed, and this generally implies that the fish would have histamine levels exceeding 200 mg/kg (FAO, 2013).

Once the fish is killed, its immune system is inactivated enabling the gill and gut colonizing bacteria to invade the internal tissues. The growth of histamine forming bacteria is more rapid at high-abuse temperatures (e.g. 21.1 °C or higher) than at moderate-abuse temperatures (e.g. 7.2 °C). Most of the histamine forming bacterial growth is particularly rapid at temperatures near 32.2 °C (USFDA, 2021). Despite maintaining the

* Corresponding author (hasangi_g@yahoo.com;  <https://orcid.org/0000-0003-4815-719X>)



This article is published under the Creative Commons CC-BY-ND License (<http://creativecommons.org/licenses/by-nd/4.0/>). This license permits use, distribution and reproduction, commercial and non-commercial, provided that the original work is properly cited and is not changed in anyway.

recommended chilling conditions, the production of toxic concentrations of histamine by psychrotolerant bacteria is the main reason for fish spoilage and poisoning at 0–5 °C (Dalgaard & Emborg, 2008). The enzyme histidine decarboxylase can remain stable in frozen fish and can be reactivated after thawing. Once it is formed, the production of histamine can continue at or near refrigeration temperatures (Visciano *et al.*, 2014).

A variety of histamine forming bacteria have been isolated and identified in different studies carried out around the world. Gram-negative enteric and marine bacteria are mainly associated with histamine formation in fish (Kim *et al.*, 2003). Taylor and Speckard (1983) have reported that *Morganella morganii*, *Klebsiella pneumonia* and *Hafnia alvei* were isolated from fish, which caused scombroid poisoning. Several studies have reported that some enteric bacteria, including *Proteus vulgaris*, *Proteus mirabilis*, *Enterobacter aerogenes*, *Enterobacter cloacae*, *Serratia fonticola*, *Serratia liquefaciens* and *Citrobacter freundii* were able to produce histamine (Yoshinaga & Frank 1982; Taylor & Speckard 1983; Middlebrooks *et al.*, 1988; Kim *et al.*, 2003; Tsai *et al.*, 2004). *Clostridium* sp., *Vibrio alginolyticus*, *Acinetobacter lowffi*, *Plesiomonas*, *shigelloides*, *Pseudomonas putida*, *Pseudomonas fluorescens*, *Aeromonas* sp. and *Photobacterium* sp. have also been reported as histamine producers (Middlebrooks *et al.*, 1988; Yatsunami & Echigo 1991; Okuzumi *et al.*, 1994). Tsai *et al.*, in 2004 reported that *Proteus*, *Enterobacter*, *Klebsiella*, *Rahnella* and *Acinetobacter* isolated from sailfish fillets are histamine producers.

Sri Lanka is a small tropical island in the Indian Ocean claiming an Exclusive Economic Zone (EEZ) area of 517,000 km². According to the Ministry of Fisheries and Aquatic Resources of Sri Lanka (MFAR, 2021), the total fisheries production of the marine sector in 2019 was 415,490 Mt. with tuna exports amounting to 14,252 Mt. Approximately 40% of the Yellowfin tuna (YFT) has been rejected when selecting for exports because of their poor quality (NARA, 2017, *Unpublished data*). Elevated histamine content and improper handling practices are some of the reasons for tuna fish rejections. Since histamine is formed due to the presence of contaminant bacteria, identification of histamine producers and investigation of their sources would help to control histamine formation in fish to a certain extent. Large size YFT (>30 kg) have a high demand in export markets including the European countries, USA, and Japan. Hence controlling the growth of histamine forming bacteria in fish can increase the fish quality resulting in an expansion of the export market for fish. However, detailed information is scarce on large size YFT (>30 kg) contamination by histamine forming bacteria in the supply chain. Thus, the aim of this study was to investigate histamine forming bacteria in export size YFT in selected nodes of the supply chain to isolate, characterize, and identify the sources of contamination.

MATERIALS AND METHODS

Field sampling

Fish, ice and swab samples were collected from multi-day boats and chill transport vehicles during unloading of fish at Dikkowita (DK) (7.0049°N, 79.8664°E), Negombo (NE) (7.2040°N, 79.8277°E), Trincomalee (TM) (8.5693°N, 81.1958°E), and Dondra (DO) (5.921°N, 80.5837°E) fishery harbours, and from selected fish processing plants located in the Western Province of Sri Lanka. The number of samples and sampling locations are given in Table 1.

Table 1: Sampling points and number of samples collected from different locations

Sample description	Number of samples						
	Fishery harbours				Processing plants		
	Dikkowita	Negombo	Trincomalee	Dondra	P1	P2	P3
Ice from fish holds of multiday boats	24	15	15	09	-	-	-
Swabs from fish holds	24	15	15	09	-	-	-
Swabs from boat decks	24	15	15	09	-	-	-
Swabs from skin of YFT	24	15	15	09	06	06	06
Ice from chill transport vehicles	24	15	15	09	06	06	06
Fish loin samples	-	-	-	-	06	03	06
Swabs of floor of processing plant	-	-	-	-	06	06	06
Ice from processing plant	-	-	-	-	06	06	06
Swabs from chill trucks	-	-	-	-	06	06	6

Surface sampling using swabs

Surface sampling was done as per ISO 18593 (2018). A stick swab was removed from its sterile wrapping and dipped in a tube containing the neutralizer (Dey-Engley neutralizing broth, Himedia M1062) to moisten the tip of the swab. The tip of the swab was pressed against the wall of the tube to remove any excess neutralizer. The moistened tip of the swab was placed on the sampling surface to be examined and an area of 100 cm² was streaked using a sterile template. The stick swab was returned to the tube containing sterile phosphate buffer as the diluent and the tube was closed properly to ensure that the swab was moist until analysis. Samples were brought to the Quality Control Laboratory (Microbiology Unit) of the National Aquatic Resources Research and Development Agency (NARA) under chilled conditions for analysis.

Collection of ice and fish samples

About 500 g of ice samples and 500 g of fish loin samples of YFT with a weight in the range of 30–64 kg were collected aseptically in sterile polythene bags and brought to the laboratory under chilled conditions for analysis.

Isolation and identification of histamine forming bacteria

Isolation of histamine-forming bacteria was done using two selective media: Nivens medium fortified with L-histidine (Niven *et al.*, 1981) and Violet Red Bile Glucose (VRBG) agar (OXOID CM0485). Sample dilutions (10⁻¹, 10⁻² and 10⁻³) were carried out, and 1 mL of the diluted solution was spread on the respective medium. The Nivens medium plates were incubated at 35 °C and 25 °C for 4 days, and the VRBG agar plates were incubated at 25 °C for 48 h. Colonies that were blue or purple color on the Niven's plates and purple/pink on the VRBG agar plates were picked and streaked on Trypticase Soy Agar (TSA). Purple/pink colonies on the VRBG agar plates at 25 °C were considered as Enterobacteriaceae and counted using a colony counter. Repeated streaking was performed to isolate bacteria into pure cultures for further analysis.

Histamine content in fish samples

The histamine content of the fish samples was analysed according to the AOAC 977.13 method (AOAC, 2012).

Histamine formation by bacterial isolates

Histamine production by the bacterial isolates was determined in duplicate by the modified AOAC 977.13 method (Kim *et al.*, 2004). One loopful of bacterial culture from a TSA slant was inoculated into 10 mL of Tryptone Soy Broth (TSB), supplemented with 1% L-histidine and 3% NaCl, and incubated at 35 °C for 24 h. After incubation, 1 mL of the bacterial culture broth was added to 9 mL of 75% methanol and heated at 60 °C for 15 minutes in a water bath to extract histamine. The concentration of histamine in the extract was determined by column elution, and o-phthalaldehyde (OPT) derivatization followed by measuring the fluorescence intensity using a spectrofluorometer (RF 1501 - Shimadzu).

Characterization of histamine forming bacterial isolates

Cultures that were positive for histamine formation were biochemically tested using API 20E. These cultures were further confirmed by amplifying and sequencing approximately 1400 bp of the 16S ribosomal DNA (rDNA) for bacteria. Primers used for the amplification were UNI-L-5'-AGAGTTTGATCATGGCTCAG-3' and UNI-R-5'-GTGTGACGGGCGGTGTGTAC-3' (Huang *et al.*, 2010). PCR amplification was performed in a 50 µL reaction mixture containing IX buffer, 1.5 mM MgCl₂, 0.3 µM of each primer, 200 µM deoxynucleotide triphosphates, 1.25 U of Taq DNA polymerase (Promega), and template DNA (10 ng). Amplifications were conducted for 35 cycles at 94 °C for 30 s, 55 °C for 30 s, and 72 °C for 60 s with an initial denaturation at 94 °C for 4 min and a final extension at 72 °C for 7 min (Huang *et al.*, 2010). Amplicons were detected by electrophoresis on a 2.0% agarose gel using Diamond Nucleic acid dye (Promega). PCR products were sent to Macrogen Inc., South Korea for purification and sequencing. Extraction of bacterial DNA was done by using HiPurA bacterial genomic DNA extraction and purification kit (Himedia MB505) according to their instructions. *M. morgani* (ATCC25830) and *Klebsiella aerogens* (ATCC13048) were used as positive controls.

Sequences obtained for each isolate were compared with sequences of other reference strains from the US National Center for Biotechnology Information (NCBI) data base using the BLAST tool. MEGA X software with the maximum likelihood method taking *Acidicapsa borealis* as the out group and bootstrap value of 1000 replicates was used to construct the phylogenetic tree of 16S rDNA sequences of major histamine producing bacterial species.

RESULTS AND DISCUSSION

Detection of HFB in fish processing plants

Samples collected from fish processing plants contained *Aeromonas salmonicida*, *Aeromonas* sp., *Pseudomonas* sp., *C. freundii*, *Shwenella baltica* and *Rahnella* sp. (Table 2). These bacteria were isolated from swabs taken from the surface of fish skin and chill trucks, ice samples, and fish loin samples. The isolated bacteria formed histamine in 1% histidine broth in the range of 4–200 ppm. The weight of fish from which loin samples were obtained was in the range of 30–64 kg and histamine content ranged from 4–49 ppm. Ice samples produced by the fish processing factories and the swabs collected from the floor of the fish processing plants did not give histamine positive isolates.

Table 2: Isolated bacterial species from the fish processing plants and the number of isolates, the place from which the samples were obtained and the amount of histamine formed by each species

No.	Isolated bacterial species	No of isolates	Places from which the samples were obtained	Amount of histamine formed (ppm)
1	<i>C. freundii</i>	01	Fish loin	180
2	<i>A. salmonicida</i>	07	Surface of fish skin, Ice from chill truck, truck inner surface	04–50
3	<i>S. baltica</i>	02	Truck inner surface	08–15
4	<i>Rahnella</i> sp.	01	Surface of fish skin	08
5	<i>Pseudomonas</i> sp.	01	Surface of fish skin	07
6	<i>Aeromonas</i> sp.	01	Surface of fish skin	05

Ice samples collected from the fish processing plants contained <1 CFU/mL of Enterobacteriaceae indicating that the ice produced by the factories was of good quality. Enterobacteriaceae counts of fish loin samples were less than 1.0×10^2 CFU/g.

Table 3: Average Enterobacteriaceae counts in the samples obtained from fish processing plants

Sample location/type	Average Enterobacteriaceae count
Swabs from fish skin	2.0×10^5 CFU/cm ²
Swabs from inner surface of chill transport vehicles	6.8×10^3 CFU/cm ²
Swabs from the floor of processing plant	7.0×10^3 CFU/cm ²
Ice samples from chill transport vehicles	1.8×10^4 CFU/mL
Ice from processing plant	< 1 CFU/mL
Fish loin samples	< 1.0×10^2 CFU/g

Klebsiella ozaenae, *Vibrio alginolyticus* and *Aeromonas* sp. have been reported as contaminants in fish processing facilities (Gingerich et al., 2001). Hu et al., (2015) have reported *C. freundii* as a histamine forming species in Blue Scad (*Decapterus maruadsi*) and Chub Mackerel (*Scomber japonicas*), which corroborates the findings of the present study.

Detection of HFB in fishery harbours

Histamine forming bacteria isolated from samples collected from multiday boats (MDB) landed at the fishery harbours are given in Table 4. Histamine forming *K. aerogenes*, *Pseudomonas* sp., and *Serratia* sp. were detected from the ice samples collected from chill transport vehicles at the Dikkowita fishery harbour. Swab samples collected from boat decks contained *Pseudomonas* sp. and *M. morgani*. Two swab samples taken from fish surface were positive for *Pseudomonas* sp. and *A. salmonicida*. Samples collected from the Negombo fishery harbour contained mostly *Pseudomonas* sp. and formed less than 30 ppm of histamine in the trypticase soy broth supplemented with 1% L-histidine.

H. alvei and *Pseudomonas* sp. were isolated from ice samples collected from the chilled transport vehicles at the Trincomalee fishery harbour. In addition, *Pseudomonas* sp. were also isolated from swab samples collected from fish holds, fish skin and boat decks.

A *Serratia* sp. isolated from an ice sample, was capable of producing histamine at a concentration above 1000 ppm under laboratory conditions; this sample was collected from a multiday boat landed at the Dondra fishery harbour. Further, from the same location, isolates of *S. baltica* were identified in a swab sample collected from the fish hold of a multiday boat, ice samples collected from fish holds, and swab sample collected from fish skin. Pure cultures of *K. aerogenes* (ATCC 13048) and *M. morgani* (ATCC 25830) produced 3300 ppm and 3400 ppm of histamine, respectively, in tryptic soy broth supplemented with 1% L-histidine.

Table 4: Isolated bacterial species from the fishery harbours and the number of isolates, the place from which the samples were obtained and the amount of histamine formed by each species

Isolated bacterial species	No. of isolates	Places from which the samples were obtained	Amount of histamine formed (ppm)
<i>K. aerogenes</i>	06	Ice collected from chill transport vehicles	3000–4000
<i>Pseudomonas</i> sp.	23	Ice collected from chill transport vehicles, swabs from boat decks, swabs from fish skin, ice collected from fish holds, swabs from fish holds	05–35
<i>Serratia</i> sp.	02	Ice collected from chill transport vehicles; ice collected from fish holds	100–1600
<i>M. morgani</i>	01	Swab from boat deck	3500
<i>A. salmonicida</i>	01	Swabs from fish skin	30
<i>H. alvei</i>	01	Ice collected from chill transport vehicles	75
<i>Shewanella</i> sp.	01	Swabs from fish skin	26
<i>S. baltica</i>	05	Swabs from fish holds, ice collected from fish holds, Ice collected from chill transport vehicles	05–17

Hu *et al.*, (2014) reported several histamine forming bacterial species such as *Arthrobacter bergeri*, *Pseudomonas* sp., *Psychrobacter*, *S. baltica* and *A. salmonicida* in Blue scad where *A. salmonicida* produced the highest amount, i.e., 115 ppm. In the present study, eight isolates of *A. salmonicida* produced histamine at <50 ppm and *S. baltica* (07 isolates) and *Pseudomonas* sp. (24 isolates) showed weak histamine formation under laboratory conditions. Lou *et al.* (2021) have reported that *S. baltica* has a high potential to decompose nutrients in fish. Even though *S. baltica* does not produce high amounts of histamine, because of its spoilage capacity, these bacteria should be controlled to prevent contamination of fish to reduce spoilage potential. *Pseudomonas* sp. isolated in the present study indicated weak ability to form histamine as the amount of histamine formed was in the range of 5–35 ppm. This is in agreement with the studies of Nor-khaizura *et al.* (2009), Koohdar *et al.* (2011), Soliman *et al.* (2017), and Simora and Peralta (2018). However, Fernandez-No *et al.*, (2011) reported that a *Pseudomonas fragi* strain isolated from turbot was a stronger histamine producer than the known histamine producing strain *Enterobacter aerogenes* ATCC 13048. In addition, *Pseudomonas* sp. is also known as an indicator of food quality as it is a spoilage organism (Koutsoumanis & Nychas, 2000; Jeyasekaran *et al.*, 2006; Yagoub, 2009). Therefore, growth of such spoilage bacteria on direct fish contacting surfaces should be controlled to minimize contamination. *M. morgani* isolated from a swab collected from a boat deck formed 3500 ppm of histamine under laboratory conditions. Six isolates of *K. aerogenes* found in ice samples collected from chill transport vehicles produced histamine in the range of 3000–4000 ppm. These findings on *M. morgani* and *K. aerogenes* are supported by the studies of Kim *et al.* (2001), Koohdar *et al.* (2011) and Butler *et al.* (2015).

Kim *et al.*, (2001) and Tsai *et al.*, (2004) also reported *Serratia* sp., *Rahnella* sp., and *H. alvei* as histamine forming bacteria.

It was noted that the swab samples drawn from the skin of fish had an Enterobacteriaceae count ranging from 2.0×10^5 to 8.0×10^5 CFU/cm² (Table 5). Swabs from boat decks and fish holds varied from 1.8×10^5 to 9.6×10^5 and 1.8×10^5 to 7.6×10^5 CFU/cm², respectively. Ice samples collected from chill transport vehicles contained an Enterobacteriaceae count ranging from 6.6×10^2 to 1.2×10^5 CFU/mL while ice samples collected from fish holds of multiday boats had counts in the range of 3.0×10^6 to 8.6×10^7 CFU/mL. These results indicate that there is a considerable amount of Enterobacteriaceae present in all the samples analysed.

Table 5: Average Enterobacteriaceae counts (at 25 °C) of samples collected from the fishery harbours

Sampling location/type	Fishery harbour			
	Dikkowita	Negombo	Trincomalee	Dondra
Swabs from fish skin (CFU/cm ²)	5.3×10^5	2.6×10^5	8.0×10^5	2.0×10^5
Swabs from boat decks (CFU/cm ²)	2.1×10^5	9.6×10^5	1.8×10^5	4.7×10^5
Swabs from fish holds (CFU/cm ²)	1.9×10^5	7.6×10^5	4.7×10^5	1.8×10^5
Ice samples from chill transport vehicles (CFU/mL)	3.0×10^4	6.6×10^2	4.8×10^3	1.2×10^5
Ice from fish holds (CFU/mL)	3.0×10^6	8.6×10^7	4.6×10^7	4.2×10^6

Normally, the total number of microorganisms on the skin surface of fish varies in the range of 10^2 – 10^7 CFU/cm², while both the gills and the intestines contain 10^3 – 10^7 CFU/g (Huss, 1995). The Enterobacteriaceae count is considered as an index of fish quality and can be used for routine monitoring. The presence of Enterobacteriaceae warrants further testing for specific pathogens. The main sources of contaminants are apparently the fish contact surfaces, which suggests the necessity of a good cleaning procedure for the contact surfaces.

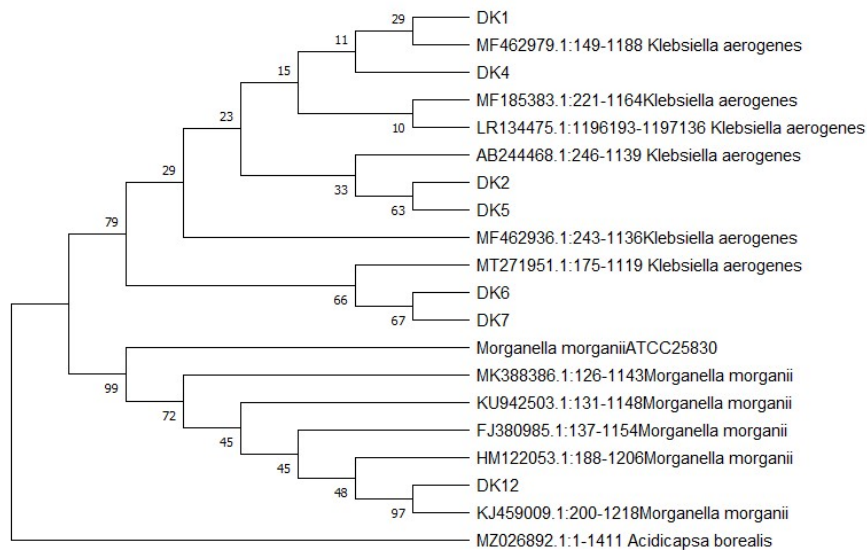


Figure 1: Phylogenetic analysis of the 16S rDNA sequences of major histamine-forming bacteria. Numbers above and below branches indicate bootstrap values from the maximum likelihood method.

In the present study, *K. aerogenes*, known as a prolific histamine producer, was isolated on several occasions from ice samples collected from chill transport vehicles. Besides *K. aerogenes*, other strong and weak histamine producers were also isolated from ice samples collected from chill transport vehicles and ice from fish holds of

multiday boats. Boat decks and the surface of fish holds were also found to contain histamine forming bacteria. *Pseudomonas* sp. and *S. baltica*, which are weak histamine producers and known to be spoilage bacteria, were also isolated from fish contact surfaces and ice samples. Subburaj *et al.*, (1984) have isolated histamine forming bacteria in fish market environments and from ice, water, and baskets used when handling fish in India. In a study conducted in Greece, Economou *et al.*, (2016) have also reported that considerable amounts of histamine producing bacteria were present in ice used to preserve fish.

Identification of isolated bacteria by sequencing of 16S rDNA

The phylogenetic tree constructed using the 16S rDNA sequences of isolated major histamine forming bacterial species is given in Figure 1. The six isolates, DK1, DK2, DK4, DK5, DK6 and DK7, were clustered together with *K. aerogens* MF185383.1:221-1164, LR134475.1:1196193-1197136, MF462936.1:243-1136, AB244468.1:246-1139, MF462979.1:149-1188 and MT271951.1:175-1119 strains.

Sequences of the isolated organisms had more than 99% similarity values when compared with the NCBI database (Table 6). The isolate DK12 clustered with KJ459009.1:200-1218 *M. morgani* strain and had more than 98% similarity with the NCBI database.

Table 6: Identification of isolated major histamine producers by using 16s rDNA based on the NCBI database with the % similarity and E value

Isolate	Organism	% Similarity	E value	Accession number
DK1	<i>K. aerogens</i>	99.33	0.0	OL468744
DK2	<i>K. aerogens</i>	99.79	0.0	OL468745
DK4	<i>K. aerogens</i>	99.57	0.0	OL468746
DK5	<i>K. aerogens</i>	100.00	0.0	OL468747
DK6	<i>K. aerogens</i>	99.59	0.0	OL468748
DK7	<i>K. aerogens</i>	99.89	0.0	OL468749
DK12	<i>M. morgani</i>	98.92	0.0	OL468707

Out of the six *K. aerogenes* isolates, DK1, DK4 clustered closely with MF462979, while DK 2 and DK 5 clustered separately showing some clear genetic differences. In addition, DK 6 and DK 7 formed a distinctly separate cluster indicating further drifting from the earlier four isolates. The bootstrap percentages for the clustering of DK1 was 29% and DK4 was 11% while for DK6 and DK7 it was 67%. Divergence of DK 6 and 7 from the main cluster has a bootstrap percentage of 66. Hence, although different clustering patterns were observed, it can be concluded that all the isolates are *K. aerogenes*. Interestingly, although clustering with *M. morgani*, the current isolate of DK 12 showed a distinct genetic diversity from the recorded isolates as evident by a bootstrap percentage of 97.

CONCLUSION

It can be concluded that histamine forming bacteria were present on direct fish contacting surfaces such as ice, boat deck, etc. Similarly, the direct fish contacting surfaces were the sources of *Pseudomonas* sp. and *S. baltica*, which are known as weak histamine producers (<35 ppm of histamine was produced in this study) and spoilage bacteria. Hence a risk of cross-contamination of fish is evident. It is necessary to control the occurrence and growth of these bacteria by adopting proper handling and cleaning practices. The quality of ice used in the fishery industry should be improved using good quality water for manufacturing ice and providing clean and hygienic storage facilities. Crushing and transportation of ice should also be done in a hygienic manner to reduce bacterial contaminations.

Acknowledgement

The authors gratefully acknowledge the staff of Institute of Post-Harvest Technology of the National Aquatic Resources Research and Development Agency (NARA), Sri Lanka and staff of fishery harbours and fish processing plants for the support given during this study.

REFERENCES

- AOAC (2012). *Histamine in Sea food, AOAC Official Method 977.13*. AOAC International, Gaithersburg, MD, USA.
- Butler K.B., Bowers J.C. & Benner Jr R.A. (2015). Prevalence and characterization of high histamine-producing bacteria in Gulf of Mexico fish species. *Journal of Food Protection* **78**(7): 1335–1342.
DOI: <https://doi.org/10.4315/0362-028X.JFP-15-012>
- Dalgaard P. & Emborg J. (2008). Histamine and biogenic amines: formation and importance in seafood. In: *Improving Seafood Products for the Consumer* (ed. Torger BØrresen), pp. 292–324. Woodhead publishing Limited, Cambridge, England.
- Economou V., Gousia P., Kemenetzi D., Sakkas H. & Papadopoulou C. (2016). Microbial quality and histamine producing Microflora analysis of the ice used for fish preservation. *Journal of Food Safety* **37**: 1–8.
DOI: <https://doi.org/10.1111/jfs.12285>.
- Fernández-No I.C., Böhme K., Calo-Mata P. & Barros-Velázquez J. (2011). Characterisation of histamine-producing bacteria from farmed blackspot seabream (*Pagellus bogaraveo*) and turbot (*Psetta maxima*). *International Journal of Food Microbiology* **151**(2011): 182–189.
DOI: <https://doi.org/10.1016/j.ijfoodmicro.2011.08.024>.
- FAO (2013). *Public Health Risks of Histamine and other Biogenic Amines from Fish and Fishery Products*. Meeting report. FAO Headquarters, Rome, Italy. Available at <https://www.fao.org/3/i3390e/i3390e.pdf>. Accessed 16 June 2021.
- Gingerich T.M., Lorca T., Flick Jr G.J., Mc Nairand H.M. & Pierson M.D. (2001). Isolation of histamine-producing bacteria from fish-processing facilities and fishing vessels. *Journal of Aquatic Food Product Technology* **10**(3): 61–66.
DOI: https://doi.org/DOI:10.1300/J030v10n03_06.
- Hu J.W., Cao M.J., Guo S.C., Zhang L.J., Su W.J. & Liu G.M. (2015). Identification and inhibition of histamine-forming bacteria in Blue Scad (*Decapterus maruadsi*) and Chub Mackerel (*Scomber japonicus*). *Journal of Food Protection* **78**(2): 383–389.
DOI: <https://doi.org/10.4315/0362-028X.JFP-14-296>
- Hu Y., Huang Z. & Chen X. (2014). Histamine producing bacteria in Blue Scad (*Decapterus maruadsi*) and their abilities to produce histamine and other biogenic amines. *World Journal of Microbiology and Biotechnology* **30**(8): 2213–2221.
DOI: <https://doi.org/10.1007/s11274-014-1642-z>.
- Huang Y.R., Liu K.J., Hsieh H.S., Hsieh C.H., Hwang D.F. & Tsai Y.H. (2010). Histamine level and histamine-forming bacteria in dried fish products sold in Penghu Island of Taiwan. *Food Control* **21**: 1234–1239.
DOI: <https://doi.org/10.1016/j.foodcont.2010.02.008>.
- Huss H.H. (1995). *Quality And Quality Changes in Fresh Fish*, FAO Fisheries Technical Paper (FAO), p. 348. FAO Headquarters, Rome, Italy.
- International Organization for Standardization (ISO) (2018). Microbiology of the food chain — Horizontal methods for surface sampling ISO Standard No.18593:2018
- Jeyasekaran G., Ganesan P., Anandaraj R., Shakila R.J. & Sukumar D. (2006). Quantitative and qualitative studies on the bacteriological quality of Indian white shrimp (*Penaeus indicus*) stored in dry ice. *Food Microbiology* **23**(6): 526–533.
DOI: <https://doi.org/10.1016/j.fm.2005.09.009>
- Kim S.H., Barros-Velazquez J., Ben-Gigrey B., Eun J.B., Jun S., Wei C.I. & An H. (2003). Identification of the main bacteria contributing to histamine formation in seafood to ensure product safety. *Food Science and Biotechnology* **12**: 451–460.
- Kim S.H., Eun J.B., Chen T.Y., Wei C.I., Clemens R.A. & An H. (2004). Evaluation of histamine and other biogenic amines and bacterial isolation in canned anchovies recalled by the USFDA. *Journal of Food Science* **69**: 157–162.
- Kim S.H., Field K.G., Morrissey M.T., Price R.J., Wei C.I. & An H. (2001). Source and identification of histamine-producing bacteria from fresh and temperature-abused Albacore. *Journal of Food Protection* **64**(7): 1035–1044.
DOI: <https://doi.org/10.4315/0362-028x-64.7.1035>.
- Koohdar V.A., Razavilar V., Motalebi A.A., Mosakhani F. & Valinassab T. (2011). Isolation and identification of histamine-forming bacteria in frozen Skipjack tuna (*Katsuwonus pelamis*). *Iranian Journal of Fisheries Sciences* **10**(4): 678–688.
- Koutsoumanis K. & Nychas G.J. (2000). Application of systemic experimental procedure to develop a microbial model for rapid fish shelf-life predictions. *International Journal of Food Microbiology* **60**(2–3): 171–184.
DOI: [https://doi.org/10.1016/s0168-1605\(00\)00309-3](https://doi.org/10.1016/s0168-1605(00)00309-3).
- Lou X., Zhaia D. & Yanga H. (2021). Changes of metabolite profiles of fish models inoculated with *Shewanella baltica* during spoilage. *Food Control* **123**(2021)107697: 1–12.
DOI: <https://doi.org/10.1016/j.foodcont.2020.107697>

- Middlebrooks B.L., Toom P.M., Douglas W.L., Harrison R.F. & MCDowell S. (1988). Effects of storage time and temperature on the microflora and amine development in Spanish mackerel (*Scomberomorus maculatus*). *Journal of Food Science* **53**(4): 1024–1029.
DOI: <https://doi.org/10.1111/j.1365-2621.1988.tb13522.x>
- MFAR (2021). Fisheries Statistics 2020. Available at: https://www.fisheries.gov.lk/web/images/statistics/annual_report/FISHERIES_STATISTICS_2020-min.pdf. Accessed on 16 June 2021.
- Niven C.F., Jeffreg M.B. & Corlett D.A. (1981). Differential plating medium for quantitative detection of histamine-producing bacteria. *Applied Environment and Microbiology* **41**(1): 321–322.
- Nor-khaizura M.A.R., Zaiton H., Jamilah B., Rusul R.A.G. & Smail-Fitry M.R. (2009). Histamine and histamine-forming bacteria in *Keropoklekor* (Malaysian Fish Sausage) during processing. *Food Science and Technology Research* **15**(4): 395–402.
- Okuzumi M., Hiraishi A., Kobayashi T. & Fujii T. (1994). *Photobacterium histaminum* sp. nov., a histamine-producing marine bacterium. *International Journal of Systematic Bacteriology* **44**(4): 631–636.
DOI: <https://doi.org/10.1099/00207713-44-4-631>.
- Price R.J. & Melvin E.F. (1994). *Recommendations for on Board Handling of Albacore Tuna*. Sea Grant Extension Program, Food Science and Technology Extension, University of California, USA.
- Simora R.M.C & Peralta E.M. (2018). Occurrence of Histamine and Histamine-forming bacteria in Philippine traditional dried-salted fish products. *Asian Fisheries Science* **31**(2018): 73–88.
DOI: <https://doi.org/10.33997/j.afs.2018.31.2.001>
- Soliman W.S., Shaapan R.F., Mohamed L.A., Younes A.M., Elgendy M.Y. & El din D.A.S. (2017). Laboratory screening of biogenic amines producing bacteria potentially threatens human health in some Egyptian fish and fish products. *Journal of Fisheries and Aquatic Science* **12**(3): 134–140.
DOI: <https://doi.org/10.3923/jfas.2017.134.140>
- Subburaj M., Karunasagar I. & Karunasagar I. (1984) Incidence of histidine decarboxylating bacteria in fish and market environs. *Food Microbiology* **1**: 263–267.
DOI: [https://doi.org/10.1016/0740-0020\(84\)90060-1](https://doi.org/10.1016/0740-0020(84)90060-1)
- Taylor S.L. & Speckard M. (1983). Isolation of histamine-producing bacteria from frozen tuna. *Marine Fisheries Review* **45**: 35–39.
- Taylor S.L., Stratton J.E. & Nordlee J.A. (1989). Histamine poisoning (scombroid fish poisoning): An allergy-like intoxication. *Clinical Toxicology* **27**(4&5): 225–240.
DOI: <https://doi.org/10.3109/15563658908994420>
- Taylor S.L. & Sumner S.S. (1987). Determination of histamine, putrescine and cadaverine. In: *Seafood Quality Determination* (eds. D.E. Kramer & J. Liston), pp. 235–245. Elsevier Science, New York, USA.
- Tsai Y.H., Kung H.F., Lee T. M., Lin G.T. & Hwang D.F. (2004). Histamine-related hygienic qualities and bacteria found in popular commercial scombroid fish fillets in Taiwan. *Journal of Food Protection* **67**(2): 407–412.
DOI: <https://doi.org/10.4315/0362-028x-67.2.407>
- USFDA (2021). *Fish and Fishery Products Hazards and Controls Guidance*, chapter 7, fourth edition. Department of Health and Human Services, Public Health Service, Food and Drug Administration, Center for Food Safety and Applied Nutrition, Office of Food Safety, USA. Available at <https://www.fda.gov/media/80637/download>. Accessed 16 June 2021.
- Visciano P., Schirone M., Tofalo R. & Suzzi G. (2014). Histamine poisoning and control measures in fish and fishery products. *Frontiers in Microbiology* **5**: 1–3.
DOI: <https://doi.org/10.3389/fmicb.2014.00500>
- Yagoub S.O. (2009). Isolation of *Enterobacteriaceae* and *Pseudomonas spp.* from raw fish sold in fish market in Khartoum state. *Journal of Bacteriology Research* **1**(7): 85–88.
- Yatsunami K. & Echigo T. (1991). Isolation of salt tolerant histamine forming bacteria from commercial rice-bran pickle sardine. *Nippon Suisan Gakkaishi* **57**(9): 1723–1728.
DOI: <https://doi.org/10.2331/SUISAN.57.1723>
- Yoshinaga D.H. & Frank H.A. (1982). Histamine-producing bacteria in decomposing skipjack tuna (*Katsuwonus pelamis*). *Applied and Environmental Microbiology* **44**(2): 447–452.
DOI: <https://doi.org/10.1128/aem.44.2.447-452.1982>

RESEARCH ARTICLE

Photonics Technology

Simulation and numerical analysis of SOA- based all optical NAND gate for high data rate communication

V Anusooya¹, S Ponmalar², MSK Manikandan³ and S Gopalakrishnan⁴

¹ Department of Electronics and Communication Engineering, Amrita College of Engineering and Technology, Tamil Nadu 629901, India.

² Department of Computer Science and Engineering, Velammal College of Engineering and Technology, Tamil Nadu 625009, India.

³ Department of Electronics and Communication Engineering, Thiagarajar College of Engineering, Tamil Nadu 625015, India.

⁴ Department of Nanotechnology, Noorul Islam Centre for Higher Education, Tamil Nadu 629180, India.

Submitted: 18 February 2022; Revised: 15 August 2022; Accepted: 28 October 2022

Abstract: As a result of the development of advanced semiconductor-based optical switching devices and their commercialization, concepts and technologies in all-optical signal processing have evolved significantly in the past few years. Universal gates are required for the realization of logical processes in photonic computing. In this study, a straightforward and small-footprint all-optical NAND gate was created utilizing semiconductor optical amplifier and simulated at high data rates between 10 to 40 Gbps. Numerical analysis of the performance of the suggested NAND gate for various input combinations and semiconductor optical amplifier (SOA) is shown. A numerical study is carried out by varying the wavelength, injection current, confinement factor, and optical elements such as sources, amplifiers, and filters. Unique results were obtained at a 10 Gbps to 40 Gbps data rate for NRZ-L user-defined bit sequences. This type of all-optical NAND gate will be the perfect alternative in the field of all-optical computing to realize a high-speed optical communication network. An extinction ratio of 15.323 dB is achieved at a high data rate of 40 Gbps. The output spectrum of the designed NAND logic is also obtained for a wide input spectrum and the system responds selectively to the input wavelength at 1548.3 nm, which is the probe signal wavelength.

Keywords: Cross-gain modulation, erbium doped fibre amplifier, extinction ratio, gain saturation, optical logic gate, semiconductor optical amplifier.

INTRODUCTION

Considerable research has gone into making all-optical integrated circuits, which are widely useful for doing ultrafast computing to handle ultrahigh bandwidth in the field of communication engineering technology. This technology is very helpful in developing miniaturized and noise-free integrated circuits, which are very difficult to realize using conventional electronic components. Among all the digital logic gates, these are the primary elements for performing any kind of function in electronic circuits. Therefore, similar kinds of gates will be replaced by optical logic gates so that all functions can be done with light.

All-optical logic gates are unique due to their small physical size, negligible electronic interference, excellent immunity against short circuits, and high bandwidth transmission with negligible loss. Implementing a nonlinear medium is essential to complete the design of an all-optical system which plays a major role in modulating the input light signals into the desired output. At a data rate of 80 Gbps, the configuration of the NAND logic gates employing a semiconductor optical amplifier (SOA) and PC-SOA with Mach-Zehnder interferometer (MZI) structure has been designed to achieve an extinction ratio of 7.1 dB and 16.2 dB, respectively (Heydarian *et al.*, 2022). In addition, a three-input all-optical NAND gate that makes use of polarisation rotation in an SOA was demonstrated. The goal of this demonstration was to achieve a high extinction ratio with an unsaturated gain of 30 dB, despite the fact that the output signals had non-uniform amplitudes (Mukherjee & Raja, 2020).

* Corresponding author (v.anusooya@gmail.com;  <https://orcid.org/0000-0003-2608-5738>)



This article is published under the Creative Commons CC-BY-ND License (<http://creativecommons.org/licenses/by-nd/4.0/>). This license permits use, distribution and reproduction, commercial and non-commercial, provided that the original work is properly cited and is not changed in anyway.

The design of all-optical logic gates comprises an encoding system, a frequency generator, and a frequency converter. For the representation of binary states, hybrid encoding techniques are preferred. A four-wave mixing semiconductor amplifier was adopted to develop a frequency generator, and a cross-polarization rotation effect was adopted to develop a frequency converter. With these designed components, a universal all-optical NAND logic system has been studied (Mukherjee *et al.*, 2019). The use of filters along with SOA can help improve the efficiency of the NAND gate.

Continuous improvement is made by the research community from the existing SOA-based NAND gate designs into the SOA-MZI configuration, which enables high switching efficiency, ER ratio, and high bit rate operation (Mehra *et al.*, 2012). To achieve miniaturization, an integrated SOA-based MZI was used at a data rate of 10 Gbps, which opens a new horizon to realize all-optical routing (Ye *et al.*, 2006). The enhancement of the existing design has been attained by introducing a distributed Bragg reflector laser integrated SOA. By increasing the signal rate between 1.25 Gbps and 10 Gbps, the extinction ratio was reduced from 28 dB to 6 dB (Yu *et al.*, 2014).

Kim *et al.* (2006a) found that the NAND, NOR, and their combinations have the best chance of being able to do all kinds of logical operations in the future high-capacity optical communication networks. Excellent recovery time and high-speed operations have been achieved at 5 ps and 10 Gb/s, respectively, using nonlinear vertical-cavity semiconductor gates (Porzi *et al.*, 2008). All-optical AND and NAND gates were designed using silicon-based micro ring resonators, which showed the free carrier dispersion effect (Ibrahim *et al.*, 2003). To achieve 15 dB at 10 Gbps, one research team developed a structure with parallel SOA and MZI logic gates. These gates include XOR, OR, NOR, and NAND (Kim *et al.*, 2006b).

To obtain an ER of 11 dB and a low penalty of 2.3 dB with a gate operating data rate of 42.6 Gbps, differently switched SOAs are used in a MZI configuration (Dailey *et al.*, 2009). The design and modelling of an all-optical NAND gate employing an SOA with a high ER of 15.323 and a data rate of 40 Gbps are reported in this research. The necessary mathematical support from the current literature is used to effectively address the theoretical background of the EDFA and SOA. User defined random input sequences were used in the NAND gate simulations, and the accompanying numerical analyses are documented. The performance of the designed NAND operation was compared with those reported previously.

MATERIALS AND METHODS

Design arrangement

Figure 1 shows the block diagram of the proposed SOA-based all-optical NAND gate. It consists of an EDFA along with a TWSOA, which is the important optical component for the design of the NAND gate. As input sequences, A and B are combined by the optical multiplier and amplified by the EDFA, whereas the reference or probe signal from a continuous wave laser is combined with the amplified input data by an X-coupler. Continuous laser light from port 3 can be used as a reference signal to achieve an all-optical NAND gate function.

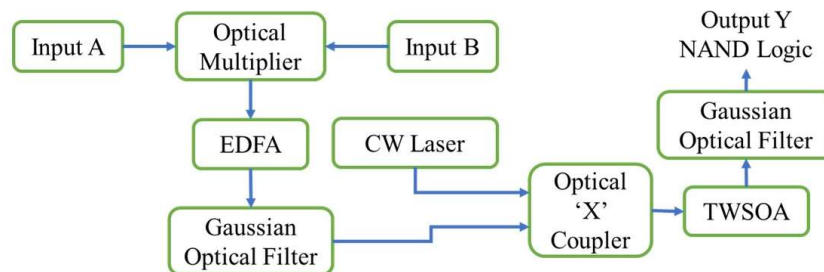


Figure 1: Block diagram representation of proposed NAND gate

Working principles of NAND logic

In the principles of operation, the two binary inputs A and B are converted into an analog waveform using an optical pulse generator, and will be given to the multiplier, which generates the multiplication of binary data. It looks like an AND logic operation. The Erbium-Doped Fibre Amplifier is used to boost the output of the multiplier. It has the lowest loss in all of the optical fibre telecommunication wavelength bands, so it can also be used to make up for signal loss as it travels.

The amplified data is further processed through a tuned Gaussian optical filter to get a specific centre wavelength. A continuous wave laser is employed to generate a probe or reference signal. An optical X coupler receives a combined input and probe signal simultaneously and its outputs are fed to a TWSOA where cross gain modulation (XGM) of carrier induced changes takes place in accordance with the changes in the input A and B (intensity modulation). During cross gain modulation, the gain is changed in SOA by the effect of gain saturation.

The modulated output wavelength of continuous wave (CW) laser is caused by gain variations of the intensity modulated input signals. The output of SOA module carries data that precisely matches the intensity-modulated input signals. The output signal is influenced by the directional characteristics of two signals, such as the reference signal and combined input signals, which can both enter the SOA in a co-directional or counter-directional manner. The optical bandpass filter receives the output of the amplifier.

The Gaussian optical filter centred at wavelength 1548.3 nm and bandwidth 40 GHz selects the desired NAND operation. To get the optimum performance, the SOA parameters were adjusted. When inputs A and B are high, XGM can be generated at SOA, producing a low output (logic 0). If any one of the inputs is low, then the multiplier output is also low and then the output of SOA corresponds to CW laser only, which is the logic high output (logic 1). By filtering and amplifying the power of the CW laser, the NAND output can be seen.

The 'X' coupler is used to couple the output of the multiplier and the output of the CW laser; the coupling coefficient selected was 0.5 dB. The semiconductor optical amplifier receives the coupler output as its input. When either input A or B, or both, is low, a high-power output is produced. Because the multiplier output is low, cross gain modulation cannot take place. On the other hand, the CW laser reference signal makes the logic output high.

The XGM modulated signal can be generated with the combined use of the multiplier output and the signal from the continuous wave laser, whereas the output of the multiplier is high when all the two inputs are logic high. The Gaussian optical filter is used to select a preferred centre frequency from the SOA output and to remove unwanted noise. Then the output will be considered as logic "0". At least one of the inputs goes to zero (low), the output logic becomes logic "1", which indicates that the constructed logic gate reflects the NAND operations.

Theoretical background of EDFA and SOA

Erbium-doped fibre amplifiers (EDFA) are used to boost signals with a loss of less than 0.2 dB/km in the 1550 nm wavelength range. The amplification is purely optical and independent of the data rate (Durhuus *et al.*, 1996). The proposed NAND gate has EDFA parameters of 2.2 μm for the core radius and doping radius. The EDFA's numerical aperture is 0.24, and the losses at 1500 nm are 0.1 dB/m. The wavelength and power for forward transmission are 1553 nm and 100 mW, respectively. Similar to this, the EDFA's backward pump wavelength and power are 980 nm and 0 mW, respectively. This demonstrates that there will be no back reflection while the gate is operating.

Simulated emission is the guiding principle behind the operation of the amplifier in erbium-doped fibre (Nakazawa *et al.*, 1989). When the data is introduced into the fibre at a wavelength ranging from 1520 nm to 1560 nm, the desired result of stimulated emission can be attained. During the stimulated emission process, the signal is amplified by the photon that is just made (Agrawal, 1997).

The rate equation stated the working principles of EDFA. The population of the upper, middle, and ground state is represented by P_u , P_m and P_g , respectively. When T_p is the pumping rate, T_{ab} is the absorption of photons from the signal and τ_{12} is the lifetime of spontaneous emission, the following equations can be written as

$$\frac{dP_g}{dt} = \frac{P_m}{\tau_{mg}} + T_{ab}(P_m - P_g) - T_p(P_g - P_u), \quad \dots(1)$$

$$\frac{dP_m}{dt} = \frac{P_u}{\tau_{um}} - T_{ab}(P_m - P_g), \quad \dots(2)$$

$$\frac{dP_u}{dt} = -\frac{P_u}{\tau_{um}} + T_p(P_g - P_u). \quad \dots(3)$$

In a SOA, population inversion refers to the condition, in which the population of electrons in the conduction band exceeds the population of holes in the valence band, $P_m > P_g$. Under steady state conditions, the time derivatives are not present. Since the photon lifetime at state u is much smaller than the lifetime of a photon at state m , the population of the excited state is defined by the Boltzmann distribution, β .

$$\text{The population of upper level is } P_u = P_m e^{-\frac{E_u - E_m}{kT}} = \beta P_m, \quad \dots(4)$$

$$\text{where } \beta = e^{-\frac{E_u - E_m}{kT}},$$

$$\text{From (1), } \frac{P_m}{\tau_{mg}} + T_{ab}(P_m - P_g) - T_p(P_g - P_u) = 0.$$

This gives the inversion level as

$$n = \frac{P_m}{P_m - P_g} = \frac{(T_p + T_{ab})\tau}{T_p\tau(1 - \beta) - 1}. \quad \dots(5)$$

Equations (1) to (4) related with population inversion, while (5) shows the degree of inversion needed for a signal to successfully flow through the EDFA (Desurvire, 1994). The inversion level n is thus related to both the probe and input signal powers, probe signal wavelength through β (Sabella & Lugli, 1999).

The nonlinear optical effect and the carrier density of SOA can be theoretically analysed by rate equations (Ishikawa, 2008). The device considered for this work is the Travelling Wave Semiconductor Optical Amplifier (TWSOA), which is used to amplify modulated light signals in which the input signal power and the internal noise have an impact on the gain of SOA. Gain saturation will occur if the input power is high, which will decrease the lasing operation in SOA (Liou *et al.*, 1997), which will result in low output.

The carrier recombination lifetime decides the gain dynamics of the SOA and the condition underneath specified appears the carrier density which is created spatially along the whole length of the active region of the device. The carrier recombination lifetime decides the gain dynamics of the SOA and the condition underneath specifies the carrier density, which is created spatially along the whole length of the active region of the device. It combines the forward and turn-around traveling signal as well as the ASE mentioned in (6) (Manimaran & Madhan, 2020). The dynamic equation for the change in carrier density inside the device's active zone is provided by

$$\frac{dn(z)}{dt} = \frac{1}{edLW} - R(n(z)) - \frac{\Gamma}{aw} \left\{ \sum_{k=1}^{N_s} [g_m(v_k, n(z))(N_{sk}^+(z) + N_{sk}^-(z))] \right\} - \frac{2\Gamma}{aw} \left\{ \sum_{k=1}^{N_m-1} [g_m(v_k, n(z))K_j(N_j^+(z) + N_j^-(z))] \right\}, \quad \dots(6)$$

where Γ is the confinement factor, g_m is the material gain, while L , W are the length and the width of the active region of the SOA, respectively. The recombination rate is $R(n(z))$, an emitted photon in the positive and negative Z-direction are $N_{sk}^+(z)$ and $N_{sk}^-(z)$. For the transverse electric (TE) mode, the spontaneous emission

photon rate is $N_j^+(z)$, and for the transverse magnetic (TM) mode, it will be $N_j^-(z)$. The carrier density can be altered within the active region by varying a few parameters or processes which are shown in (6). The infused current, unconstrained radiative and nonradiative recombination, forecast recombination process of carriers, invigorated recombination by the signal, and ASE photons. In the case of a traveling wave amplifier, the mirror losses will not affect the photon lifetime (Eisenstein, 1989; Obermann *et al.*, 1997). In the proposed system, the parameters chosen for the SOA are confinement factor $\Gamma = 0.35$, length $L = 0.5$ mm, width $W = 3$ μm , height $H = 80$ nm, Line width enhancement factor = 5, differential gain $A_d = 27.8 \times 10^{-021}\text{m}^2$.

RESULTS AND DISCUSSION

The study of this numerical simulation explored the dynamics transfer characteristics of the NAND gate for user-defined or random sequence input of A and input B with a data rate of 40 Gbps. The wavelength of 1553.05 nm and 1557.75 nm was selected for A and B with a power of -1.21 dBm and -0.223 dBm, respectively. The centre wavelength of the Gaussian optical filter is 1555.40 nm, which is the average wavelength of both inputs A and B, whereas the wavelength, injection current, and power of the probe or reference signal are 1548.3 nm, 0.95A, and -2.6 dBm, respectively.

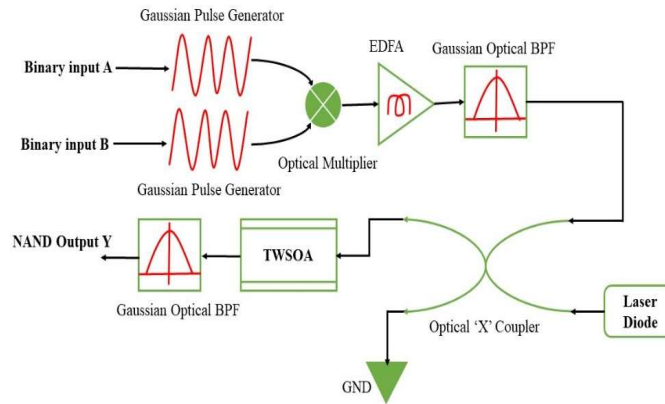


Figure 2: The schematic diagram of the proposed NAND gate design

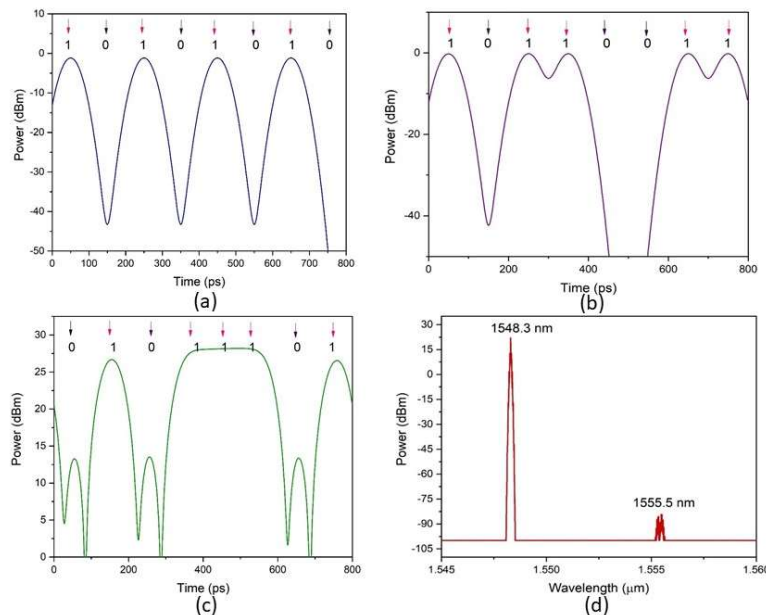


Figure 3: (a). Input sequence A; (b) Input sequence B; (c) Output of NAND logic; (d) Output Power spectrum of designed NAND logic.

The SOA parameters are set as 0.5 mm length, 3 μm width, 80 nm height, and the optical confinement factor is 0.35. The centre wavelength of the Gaussian optical filter placed before SOA is 1555.4 nm and after SOA is 1548.3 nm. Figure 2 shows the schematic of the proposed NAND gate. Figures (3a) and (3b) represent the user-defined input sequence of A: 10101010 and B: 10110011, and Figure (3c) shows the output of NAND logic Y: 01011101. From the NAND gate logic output, we observe that, the output power for logic 1 is 28.575 dBm and the output power for logic 0 is 13.252 dBm. The figure (3d) shows the output spectrum of the NAND logic and it was measured for different wavelengths ranging from 1545 to 1560 nm. The system gives a highly selective response at a 1548.3 nm input wavelength with about 28.5 dBm of output power. All other wavelengths are forbidden from transmission. Around 1555.5 nm, a small output signal (-82 dBm) arises, but it is negligible when compared to 28.5 dBm. Table 1 shows the proposed NAND gate logic output for user-defined input sequences with corresponding logical outputs with power in dBm.

Table 1: Truth table for NAND gate logic (user defined input)

User defined sequence		NAND gate logic	Output power
Input 1 logic	Input 2 logic	$y = \overline{A * B}$	(dBm)
1	1	0	13.252
0	0	1	28.575
1	1	0	13.252
0	1	1	28.575
1	0	1	28.575
0	0	1	28.575
1	1	0	13.252
0	1	1	28.575

Numerical analysis

The analysis of the proposed design can be performed by varying the parameters as well as the optical components. Different wavelengths of output for NAND logic can be observed. At a wavelength of 1548.3 nm, the performance of the pump laser is compared with the CW laser output shown in Figure 4. Even though the optical output power of the pump laser is more stable than the CW laser output, we have chosen a continuous wave laser, which is mainly used in optical low-loss applications.

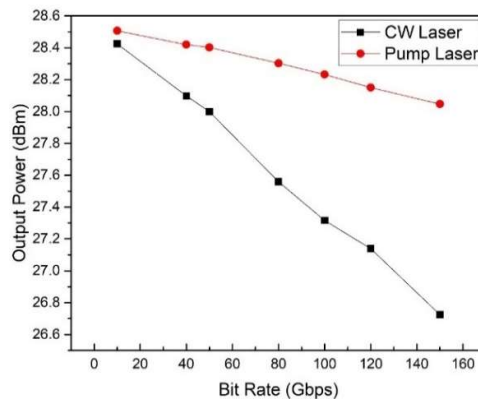


Figure 4: Output optical power at various data rates for CW and pump lasers

The impact of various types of amplifiers on the output power of NAND logic can be seen in Figure 5, in which we observe that the output is greater in optical fibre amplifiers and TWSOA. Likewise, filters were also tested to identify the better performance of the proposed logic gate. In the input stage of the proposed system, the impact of filters is high, but in the case of filters at the output stage, no impact is there, as mentioned in Table 2.

Table 2: Types of filters (vs) output power at $\lambda = 1548.3$ nm and bandwidth= 10 GHz

Sl. no	Types of filters	Output power (dBm)
1	Trapezoidal optical filter	27.416
2	Gaussian optical filter	28.575
3	Butterworth optical filter	28.202
4	Bessel optical filter	28.202
5	Fabry Perot optical filter	24.217
6	Optical digital filter	26.622
7	Periodic optical filter	28.231

The selected components from the analysis can be used for the design of a universal optical NAND gate. Figure 4 shows the relationship between the optical laser source and the operating data rate. Here the same structure can be further tested for various data rates of 10 Gbps to 200 Gbps.

Finally, the required performance can be attained at a bit rate from 10 Gbps to 40 Gbps. Afterward, its output power value can be reduced considerably, and finally, no proper transmission has occurred at a speed of 180 Gbps to 200 Gbps. The rate of change of output power for pump laser and CW laser was calculated from the plot based on the simulated output values of 0.00382 dBm/Gbps and 0.0126 dBm/Gbps, respectively. In order to improve the quality of the output signal, it is recommended to use the appropriate filter in front of the SOA.

In this study, various filters have been analysed and their outputs are observed and listed in Table 2. From the tabulated values, it is obvious that the Gaussian filter and Periodic Optical filter showed better output power compared to other filters, and their output power values are 28.575 dBm and 28.231 dBm, respectively. Since the Gaussian optical filter shows the best output power and also has an optimum shape to get high resolution in the output, it has been selected for the development of the NAND gate logic system.

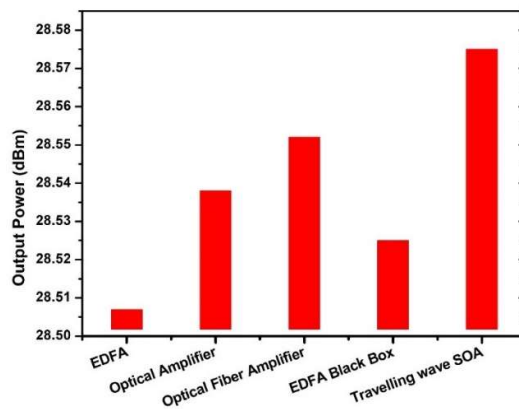
**Figure 5:** Output optical power for different amplifiers

Figure 6, shows the tuning of the wavelength of the carrier signal in order to get the maximum output power, which will favour efficient information transmission. After doing a large-scale variation from 1400 nm to 1600 nm, it has been identified that the system responds better around 1548 nm. Then, the signal wavelength varied from 1548.0 to 1548.9 nm with an increment of 0.1 nm. The output power is maximal when the wavelength is set as 1548.3 nm. The output power drastically decreases on the higher and lower side of the spot of 1548.3 nm, which can be interpreted as the window being optimum for the proposed system. The third optical window, which has a wavelength between 1400 and 1600 nm, was identified in the literature as an appropriate one for achieving low-loss transmission.

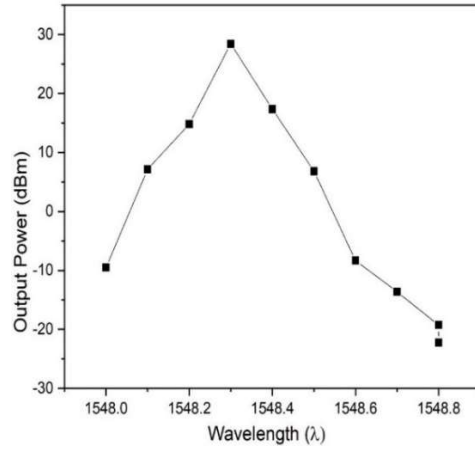


Figure 6: Wavelength (vs) output optical power using CW laser.

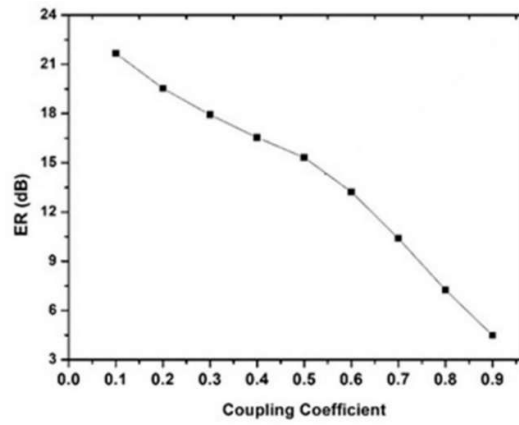


Figure 7: The response of ER to variation in coupling coefficient.

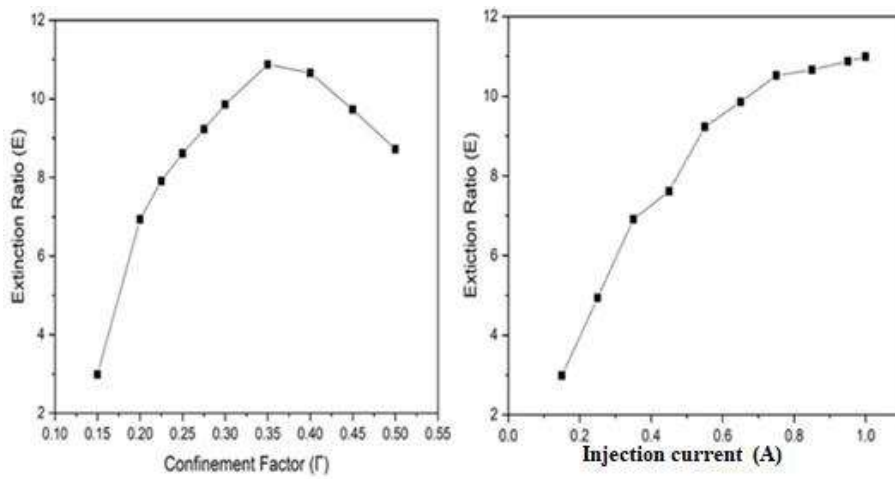


Figure 8: Relationship between confinement factor, injection current and extinction ratio at 10 Gbps data rate.

In telecommunications and optical systems, the extinction ratio (ER) is a measure of the contrast or ratio of power between the "on" and "off" states of an optical signal which considered as an important factor in evaluating the performance of the system at a particular data rate.

The performance of the NAND gate is verified using the Extinction Ratio (ER) as shown in Figure 7, by adjusting the coupling coefficient of the X-coupler. According to this, ER ratio increases if the coupling coefficient is smaller than 0.5. The ER is decreased-when the coupling coefficient lies between 0.5 and 0.9. The NAND logic operation will not function correctly, after the coupling coefficient approaches one. The coupling coefficient selected for the current work is 0.5 in order to achieve an appropriate NAND gate logical operation at a high data rate of 40 Gbps. Moreover, both the confinement factor and injection current varied independently and the extinction ratio based on the output results is shown in Figure. 8. The confinement factor and the injection current of 0.35 and 0.95 A, respectively, produced an excellent extinction ratio of 15.323 dB. The same high extinction ratio can be maintained for the high-speed data rate of 10 Gbps to 40 Gbps. Similarly, the important parameters such as the Extinction Ratio (ER) and Bit Error Rate (BER) were calculated and listed in Table 3.

Table 3: Calculated parameters of the designed NAND logic system

Sl. No	Parameters	Metrics
1	Extinction ratio	15.323 dB
2	Bit error rate (BER)	4.27×10^{-26}

Table 4: Comparison of NAND gate designs

Sl. no.	Author name and year	Title	Optical components used	Data rate (Gbps)	Extinction ratio (dB)
1	Heydarian <i>et al.</i> , 2022	Design and analysis of an all-optical NAND logic gate using a photonic crystal semiconductor optical amplifier based on the Mach-Zehnder interferometer structure	SOA	80	7.1
2	Mukherjee <i>et al.</i> , 2019	All-optical logic gate NAND using semiconductor optical amplifiers with simulation	PC-SOA	80	16.2
3	Oliveira <i>et al.</i> , 2019	New design of all-optical logic universal NAND gate formed by NOT (A AND B) gates using Michelson Interferometer based on semiconductor optical amplifier	Two SOA	10	13.0
4	Yu <i>et al.</i> , 2014	All-optical decision gate with extinction ratio improved scheme using a SOA-DBR laser	SOA- MI	10	-
5	Mehra <i>et al.</i> , 2012	All optical universal logic Gates Design and Simulation using SOA	SOA- DBR Laser	10	24
6	Mehra <i>et al.</i> , 2012	SOA based all-optical NAND gates and their comparison	Two SOA	40	8.75
7	Nakarmi <i>et al.</i> , 2012	Demonstration of all-optical NAND gate using single-mode Fabry-Pérot laser diode	SOA- filter	80	9.73
			SOA- MZI	80	11.09
			Fabry Perot laser diode	10	14.6

We deduce from the comparison table that the majority of research on the design of all-optical NAND gates for optoelectronic integrated circuits has a data rate of 10 Gbps. If the data rate rises, the extinction ratio may decline. With a single SOA and filter combination, the NAND gate in the proposed work is created with a high data rate of 40 Gbps and an enhanced extinction ratio of 15.323 dB.

CONCLUSION

A unique all-optical NAND gate using a single TWSOA has been developed and implemented in this study, and by numerical simulation, a high ER of 15.323 dB at a data rate of 10 Gbps to 40 Gbps is achieved. Additionally, the functionality of all-optical NAND gate is examined in various scenarios. By adjusting the input data, SOA, CW laser, or optical filter parameters, the maximum extinction ratio for the NAND gate was achieved. Calculated values for the ER and BER were 15.323 dB and 4.27×10^{-26} respectively.

Conflict of interest

The authors declare that there is no conflict of interest.

Acknowledgement

The authors acknowledge the Department of Electronics and Communication Engineering, Government College of Engineering Tirunelveli for providing software facility for the successful completion of the proposed work.

REFERENCES

- Agrawal G.P. (1997). *Fiber-optic Communication Systems*, 2nd edition. John Wiley & Sons, Inc., USA.
- Desurvire E. (1994). *Erbium Doped Fiber Amplifiers*. John Wiley & Sons, Inc., USA.
- Dailey J.M., Ibrahim S.K., Manning R.J., Webb R.P., Lardenois S., Maxwell G.D. & Poustie A.J. (2009). 42.6 Gbit/s fully integrated all-optical XOR gate. *Electronics Letters* **45**(20): 1047–1049.
- Durhuus T., Mikkelsen B., Joergensen C., Lykke Danielsen S. & Stubkjaer K.E. (1996). All-optical wavelength conversion by semiconductor optical amplifiers. *Journal of Lightwave Technology* **14**(6): 942–954.
DOI: <https://doi.org/10.1109/50.511594>
- Eisenstein G. (1989). Semiconductor optical amplifiers. *IEEE Circuits and Devices Magazine* **5**(4): 25–30.
DOI: <https://doi.org/10.1109/101.29899>
- Heydarian K., Nosratpour A. & Razaghi M. (2022). Design and analysis of an all-optical NAND logic gate using a photonic crystal semiconductor optical amplifier based on the Mach–Zehnder interferometer structure. *Photonics and Nanostructures-Fundamentals and Applications* **49**: 100992.
DOI: <https://doi.org/10.1016/j.photonics.2022.100992>
- Ibrahim T.A., Grover R., Kuo L.C., Kanakaraju S., Calhoun L.C. & Ho P.T. (2003). All-optical AND/NAND logic gates using semiconductor microresonators. *IEEE Photonics Technology Letters* **15**(10): 1422–1424.
DOI: <https://doi.org/10.1109/LPT.2003.818049>
- Ishikawa H. (2008). Ultrafast all-optical signal processing devices. In: *Ultrafast All-Optical Signal Processing Devices*. John Wiley & Sons, Inc., USA.
DOI: <https://doi.org/10.1002/9780470758694>
- Kim J.-Y., Kang J.-M., Kim T.-Y. & Han S.-K. (2006a). All-optical multiple logic gates with XOR, NOR, OR, and NAND functions using parallel SOA-MZI structures: theory and experiment. *Journal of Lightwave Technology* **24**(9): 3392–3399.
DOI: <https://doi.org/10.1109/JLT.2006.880593>
- Kim J.-Y., Kang J.-M., Kim T.-Y. & Han S.-K. (2006b). 10 Gbit/s all-optical composite logic gates with XOR, NOR, OR and NAND functions using SOA-MZI structures. *Electronics Letters* **42**(5): 303–304.
DOI: <https://doi.org/10.1049/el:20063501>
- Liou K.-Y., Koren U., Burrows E.C., Zyskind J.L. & Dreyer K. (1997). A WDM access system architecture based on spectral slicing of an amplified LED and delay-line multiplexing and encoding of eight wavelength channels for 64 subscribers. *IEEE Photonics Technology Letters* **9**(4): 517–519.
DOI: <https://doi.org/10.1109/68.559407>
- Manimaran P. & Madhan M.G. (2020). Bandwidth characteristics of TWSOA based inline detector configurations for near infrared communications. *Optical and Quantum Electronics* **52**(1): 32.
DOI: <https://doi.org/10.1007/s11082-019-2143-y>
- Mehra R. & Tripathi J.K. (2012). All optical universal logic gates design and simulation using SOA. *IJCEM International Journal of Computational Engineering and Management* **15**: 41–45.
- Mehra R., Jaiswal S. & Dixit H. K. (2012). SOA based all-optical NAND gates and their comparison. 2012 *Third International Conference on Computer and Communication Technology*, 23-25 November, Allahabad, India, pp. 175–177.
DOI: <https://doi.org/10.1109/ICCCT.2012.42>

- Mukherjee K. & Raja A. (2020). Three Input NAND gate using semiconductor optical amplifier. *2020 IEEE VLSI Device Circuit and System (VLSI DCS 2020)*, Kolkata, India, 18–19 July, pp. 142–145.
- Mukherjee K., Raja A. & Maji K. (2019). All-optical logic gate NAND using semiconductor optical amplifiers with simulation. *Journal of Optics* **48**(3): 357–364.
DOI: <https://doi.org/10.1007/s12596-019-00555-9>
- Nakarmi B., Rakib-Uddin M., Hoai T. Q. & Won Y. H. (2010). Demonstration of all-optical NAND gate using single-mode Fabry–Pérot laser diode. *IEEE Photonics Technology Letters* **23**(4): 236–238.
DOI: <https://doi.org/10.1109/LPT.2010.2098863>
- Nakazawa M., Kimura Y. & Suzuki K. (1989). Efficient Er³⁺-doped optical fiber amplifier pumped by a 1.48 μm InGaAsP laser diode. *Applied Physics Letters* **54**(4): 295–297.
- Oliveira J.M., Silva H.A.B.D., Oliveira L.A.D., Sousa F.B.D., Oliveira J.E.D., Sousa F.M.D. & Costa M.B.C. (2019). New design of all-optical logic universal NAND gate formed by NOT (A AND B) gates using Michelson interferometer based on semiconductor optical amplifier. *Journal of Computational and Theoretical Nanoscience* **16**(7): 2712–2719.
DOI: <https://doi.org/10.1166/jctn.2019.8236>
- Obermann K., Koltchanov I., Petermann K., Diez S., Ludwig R. & Weber H. G. (1997). Noise analysis of frequency converters utilizing semiconductor-laser amplifiers. *IEEE Journal of Quantum Electronics* **33**(1): 81–88.
DOI: <https://doi.org/10.1109/3.554895>
- Porzi C., Guina M., Bogoni A. & Potì L. (2008). All-optical NAND/NOR logic gates based on semiconductor saturable absorber etalons. *IEEE Journal of Selected Topics in Quantum Electronics* **14**(3): 927–937.
DOI: <https://doi.org/10.1109/JSTQE.2008.919754>
- Sabella R. & Lugli P. (1999). High speed optical communications. In: *High Speed Optical Communications*, pp. 207–232. Springer, USA.
DOI: <https://doi.org/10.1007/978-1-4615-5275-8>
- Ye X., Ye P. & Zhang M. (2006). All-optical NAND gate using integrated SOA-based Mach-Zehnder interferometer. *Optical Fiber Technology* **12**(4): 312–316.
DOI: <https://doi.org/10.1016/j.yofte.2005.12.001>
- Yu L.-Q., Lu D. & Zhao L.-J. (2014). All-optical decision gate with extinction ratio improved scheme using an SOA-DBR laser. *IEEE Photonics Technology Letters* **26**(21): 2126–2129.
DOI: <https://doi.org/10.1109/LPT.2014.2349274>

RESEARCH ARTICLE

Geotechnical Engineering

Effect of degree of saturation on pullout resistance of soil nailing in lateritic soil

KASN Fernando¹ and NH Priyankara^{2*}

¹ State Engineering Corporation of Sri Lanka, No:130 W A D Ramanayake Mawatha, Colombo 00200, Sri Lanka.

² Department of Civil and Environmental Engineering, Faculty of Engineering, University of Ruhuna, Hapugala, Galle, 80000, Sri Lanka.

Submitted: 05 May 2022; Revised: 29 August 2022; Accepted: 28 October 2022


Abstract: Soil nailing is a technique used to reinforce and strengthen the existing ground conditions. This is done by installing closely spaced, passive, structural inclusions known as nails into the soil, and these nails help to improve the overall shear strength of the soil. The nail pullout resistance is the shear stress at the grout-soil interface. The soil nail pullout resistance depends on many parameters. Among the factors influencing the soil nail pullout resistance, the degree of saturation of the soil is an important factor. The pullout resistance may decrease during intense rainfall as the degree of saturation of soil mass changes with the moisture content of the soil. However, verification of pullout tests on soil nail is not conducted under extreme conditions. Hence, the measured pullout resistance may not be a safe parameter for design. As such, in this research study, the effect of the degree of saturation on pullout resistance was studied by conducting a series of laboratory tests using a laboratory pullout box. A specially designed waterproof cap was used to apply back pressure to saturate the soil within the pullout box. Variations of earth pressures close to the grouted nail were observed during the tests. It is evident from the results that the higher the degree of saturation, the lower the pullout resistance. Maximum pullout resistance was observed when the degree of saturation was near the optimum moisture of the soil. When the soil is sufficiently dry, lower pullout resistance was observed due to low bond strength between the grout surface and surrounding dry soil.

Keywords: Degree of saturation, earth pressure, laboratory model setup, pullout resistance, soil nailing.

INTRODUCTION

Soil nailing is an in-situ reinforcement technique that is installed to stabilize soil masses, such as cut and fill slopes, deep excavations, retaining structures, tunnels, etc. The technique used in soil nailing is to reinforce the soil with slender elements such as reinforcing bars, which are called nails; these reinforcing bars are installed into pre-drilled holes and then grouted. These nails are installed at an inclination of 10 to 20 degrees to the horizontal. At present, soil nailing has been widely used to stabilize existing natural slopes as well as cut slopes in Sri Lanka.

Both internal and external failure modes must be considered in the design of soil nailing systems. The internal failure mode consists of pullout failure, tensile failure, and facing failure. Among these, pullout resistance is the key factor in the current soil nailing design (Su *et al.*, 2007). Usually, field pullout tests are carried out during the construction stage to verify the design values. There are many factors affecting the soil nail pullout resistance, such as soil type, soil dilatancy, soil shear strength, soil density, grouting pressure, drilling method, degree of saturation, overburden pressure, and matric suction (Burland, 2002; Lazarte *et al.*, 2003; Gurbarsud, 2010; Su *et al.*, 2010; Gurbarsud *et al.*, 2013; Kalehsar *et al.*, 2021; Najafi *et al.*, 2021). Among the factors influencing the soil nail pullout resistance, the degree of saturation of the soil is important, especially for permanent soil-nailed structures. This is because the degree of soil saturation of the soil mass changes with the variation in ground water levels and weather conditions, and the pullout resistance may drop to a low level during intense rainfall (Su *et al.*,

* Corresponding author (nadeej@cee.ruh.ac.lk;  <https://orcid.org/0000-0002-8775-7246>)



This article is published under the Creative Commons CC-BY-ND License (<http://creativecommons.org/licenses/by-nd/4.0/>). This license permits use, distribution and reproduction, commercial and non-commercial, provided that the original work is properly cited and is not changed in anyway.

2007; Zhang *et al.*, 2009). However, the verification of field pullout tests is rarely conducted under extreme saturated conditions. As such, the measured pullout resistance in the field is overestimated by the design value.

Only a few researchers have studied the influence of the degree of saturation on soil nail pullout resistance (Hong *et al.*, 2003; Junaideen *et al.*, 2004; Chu & Yin, 2005; Pradhan *et al.*, 2006; Su *et al.*, 2007). These researchers found that the soil nail pullout resistance decreased with the increase in the degree of saturation of soil. Schlosser and Buhar (1991) found that the maximum pullout force was reduced by more than half, when the moisture content increased from the optimum water content to the saturated moisture content. Based on laboratory pullout tests on cement grouted nails in loosely compacted Completely Decomposed Granite fill (CDG), Pradhan *et al.* (2006) found that only the nail–soil interface adhesion was reduced under the high degree of saturation. It was reported that the pullout box used by Chu and Yin (2005), to study the effect of soil saturation on pullout resistance, was simple and it was difficult to achieve a high degree of saturation owing to leakage problems. In addition, in most of the laboratory pullout tests, the overburden pressures were applied to the soil after the soil-nails had been installed, whereas in real-life situations the overburden pressure existed prior to the installation of the soil-nails. As such, in order to overcome these shortcomings and to meet the demand for more comprehensive study on the soil nail pullout resistance, an innovative pullout box was designed and constructed at the Hong Kong Polytechnic University (Su *et al.*, 2007). As a result of their research study, the effects of saturation of CDG and overburden pressure on pullout resistance were reported.

However, very few studies have been conducted related to soil nailing in the Sri Lankan context. Generally, the peak shear strength parameters of the soil are used for soil nailing design. However, the effect of soil saturation on the soil nailing design is neglected. In this study, the effect of the degree of saturation of soil on the pullout resistance was studied using a specially fabricated laboratory model setup. A specially designed waterproof front cap and a special tubing arrangement were used to apply the back water pressure to achieve the required degree of saturation. In addition, the variation of earth pressure near the grouted nail during soil nail installation and during pullout tests was studied.

MATERIALS AND METHODS

Pullout box

The effect of the degree of saturation on the pullout resistance of the soil nailing system was evaluated using a laboratory model setup, as shown in Figure 1. One nail was tested at a time to avoid the effects of soil disturbance during the pullout of other nails (Harshani & Priyankara, 2018). The internal dimensions of the model setup used for the study were 600 mm in length, 460 mm in width, and 600 mm in height; these dimensions were sufficient to avoid the boundary effect (Yin & Su, 2006). An additional extension chamber, 280 mm in length, 130 mm in width, and 130 mm in height, was attached to the end of the box, covering the tail of the soil nail, as illustrated in Figure 2. With this chamber, no cavity was developed at the nail tip, and the test length of the soil nail remained constant during the pulling out. A waterproof front cap was provided by means of a triaxial cell at the nail head for the saturation process. Overburden stress was applied using a floor-mounted portal frame and two hydraulic jacks, as depicted in Figure 1. A photograph of the model setup in the laboratory is shown in Figure 3.

Instrumentation and calibration

Five Earth Pressure Sensors (EPS) were installed in the pullout box to monitor the variation of the earth pressure around the soil nail (Figure 2). EPS were used to evaluate the effect of dilation on the resistance to soil nail pullout. The EPS were calibrated initially with an Arduino circuit and a breadboard (Figure 4). Known weights were applied to the pressure pad, and the corresponding analog readings were recorded separately for each pressure sensor. A piece of metal with a cross-sectional area equal to that of the pressure pad was used to place the weights to ensure even application of the weights to the pressure pad. The five sensors showed a similar variation; hence, the average fitted curve was used to obtain the pressure values (Fernando, 2020).

Overburden pressure was applied by using a portal frame with two hydraulic jacks (Figure 1). The applied overburden pressure was measured by using a proving ring attached to the portal frame. A steel plate was placed

above the soil surface to achieve uniform deformation of the soil across the pullout box, and two dial gauges were used to measure the vertical deformation.

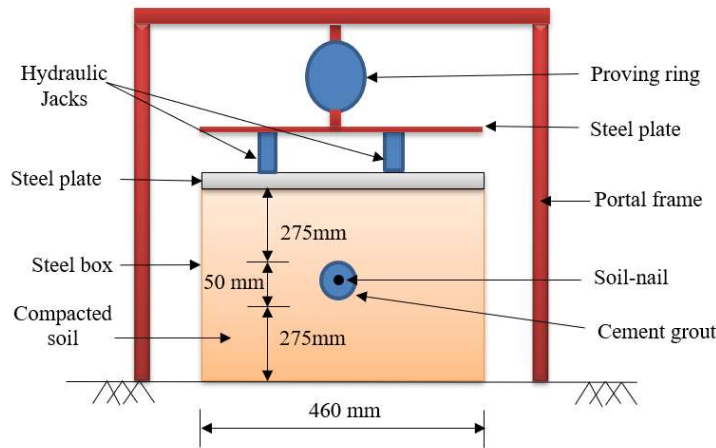


Figure 1: A schematic diagram of the model setup

A hydraulic pullout jack was used to apply the pullout force to the grouted soil nail, and the jack was connected to the nail at the nail head. Hydraulic pressure was applied to the nail in the form of suction so that the nail was pulled out by the jack. A dial gauge fixed at the nail head was used to measure the horizontal displacement of the nail when the pullout force was applied.

Materials

The commonly available lateritic soil was used in this study. The engineering properties of the lateritic soil are given in Table 1. Based on the sieve analysis test results, lateritic soil basically consists of sand, and the soil can be classified as Silty Sand (SM) according to the Unified Soil Classification System (USCS). To determine the degree of saturation of the test specimens, the saturated moisture content of the soil was determined by allowing lateritic soil to saturate over a period of time, and moisture content was measured daily until it became a constant value.

Table 1: Engineering properties of lateritic soil

Property	Value
Specific gravity, G_s	2.41
Maximum dry unit weight, $\gamma_{d(max)} \left(\frac{kN}{m^3} \right)$	17.15
Optimum moisture content, ω_{opt} (%)	17.6
Liquid limit, LL (%)	53
Plastic limit, PL (%)	44
Saturated moisture content (%)	39.5
Gravel content (%)	0
Sand content (%)	71
Fine content (%)	29

Test Procedure

The general test procedure for soil filling, installation of EPS, applying vertical stress, drilling, grouting, saturation, and nail pullout can be listed as follows:

- The soil was compacted in the pullout box using a rammer to 90% of the maximum dry unit weight. The soil was compacted into layers with a thickness of 50 mm. The amount of soil required for compaction was calculated, and the corresponding amount of water added to the soil.

- Five earth pressure sensors were installed at different levels during the compaction, as shown in Figure 2. Three EPS were installed at the nail head, middle, and tail and placed 40 mm above the grouted nail. To investigate the change of overburden stress over depth during pullout tests, two additional EPS were installed 175 mm above and below the grouted nail (EPS-T and EPS-B), as shown in Figure 2.

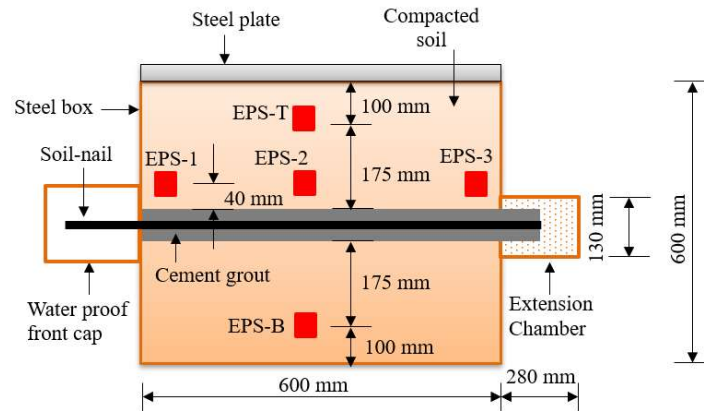


Figure 2: Arrangement of extension chamber, waterproof front cap and instrumentation

- A constant overburden stress of about 48 kPa was applied using two hydraulic jacks (Figure 1 and Figure 3). Both hydraulic jacks were jacked up and down at the same time using a specially fabricated handle to ensure even application of the overburden stress. The applied force was measured by using a proving ring attached to the portal frame. A steel plate above the hydraulic jacks distributes the load uniformly to the jacks. After jacking, the overburden stress was kept constant throughout the experiment.



Figure 3: Arrangement of the model setup

- The setup was kept for 24 hours from the application of overburden stress until the soil achieved equilibrium (i.e., EPS readings became constant). A horizontal hole of diameter 50 mm was then drilled using a hand auger (Figure 5). An Arduino setup and a computer were used for the real-time recording of EPS. A steel nail of diameter 10 mm was placed centrally in the drilled hole with the use of centralizers.

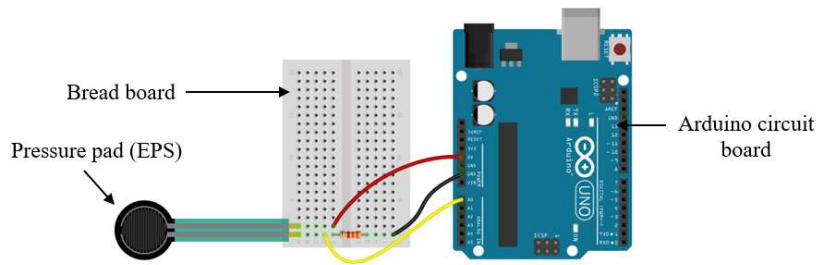


Figure 4: Arduino Circuit arrangement used for calibration

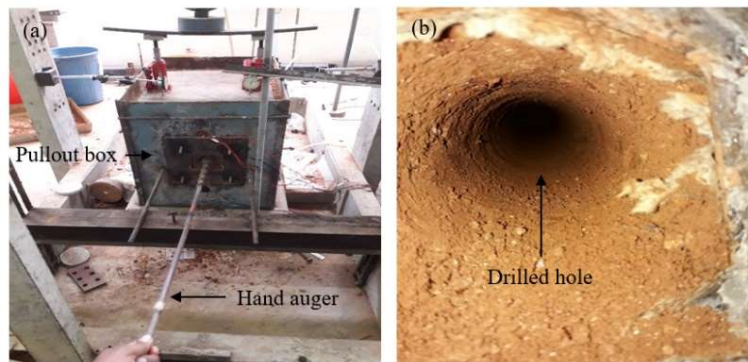


Figure 5: Drilling process (a) drilling a hole using a hand auger; (b) drilled hole

- After the placement of the nail within the drilled hole, grouting was done using a pressure grouting cylinder, as stated in Harshani and Priyankara (2018). A schematic diagram of the grouting device used in this study is shown in Figure 6. Commercially available ordinary Portland cement was used to prepare the grout. The water: cement ratio was kept at 0.5, and the cement was mixed with water and admixture for a period of 20 minutes using a mechanical mixer. Admixture was used to make the grout flowable, permeable, non-shrinkage, and non-segregate cement slurry. The admixture was added at a rate of 0.5% by weight of cement (Harshani & Priyankara, 2018). Grouting pressure was applied using a compressor and kept constant at 60 kPa throughout all the laboratory experiments.
- Saturation was started three days after the grouting once the grouted nail had acquired adequate strength. The nail head was covered with a waterproof front cap (Figure 2). The waterproof front cap was fixed to a steel plate, which was connected to the pullout box using bolts. To saturate the soil, water flowed into the pullout box through plastic tubes connected to a hole in the side plate. This inlet was divided into 4 lines using T-joints, and 7 openings were provided around the soil nail to facilitate the saturation process, as shown in Figure 7. The openings of the tubes were covered with filter paper to avoid clogging by fine particles. A vacuum pump was used to pump out air from the voids within the soil. A vacuum was applied by connecting the vacuum pump to the valve at the front of the pullout box (near the nail head). Under this suction pressure, the water rose to the top and filled the waterproof front cap. Then, using the air compressor, back-water pressure of about 30 kN/m² was applied to the waterproof front cap, which helped to saturate the soil, as shown in Figure 8. The same procedure was repeated, at different time intervals, to achieve different degrees of saturation. Generally, back water pressure was applied in 5-10-minute intervals. A photograph of the pullout box after the application of back pressure is illustrated in Figure 9. Soil samples were collected adjacent to the grouted nail after the pullout test to determine the moisture content of the soil surrounding the grouted nail.

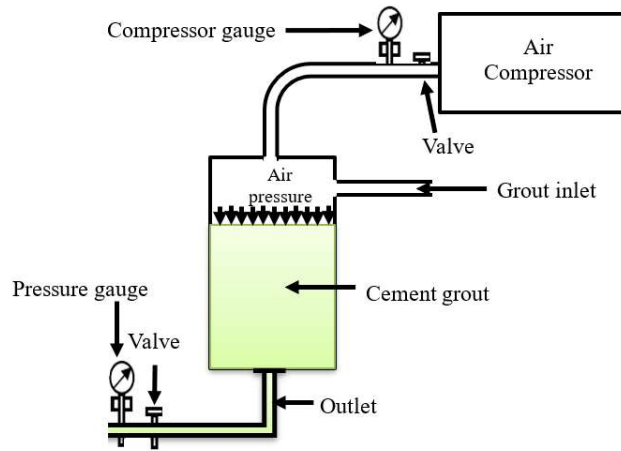


Figure 6: A schematic diagram of grouting device

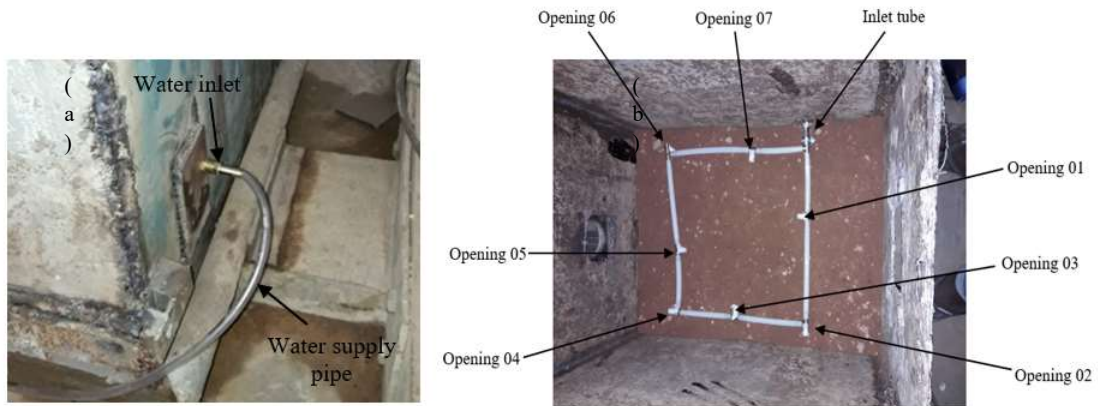


Figure 7: Water tube arrangement in the saturation process (a) water inlet to the pullout box; (b) tube arrangement to saturate the soil (top view)

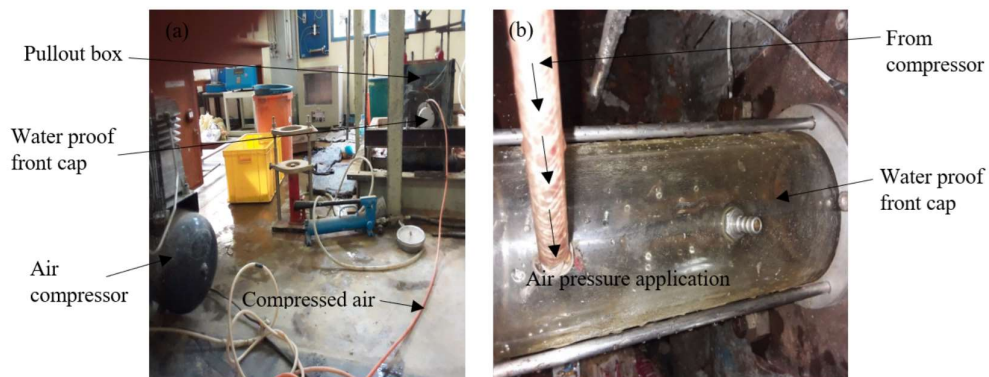


Figure 8: Application of back-water pressure using a compressor (a) complete setup (b) enlarged view of back pressure application



Figure 9: Saturated pullout box after application of back-water pressure

- After the saturation procedure was completed, a pullout test was conducted to determine the pullout resistance of the soil nail. The waterproof front cap was removed, and the nail head was secured to the pullout device with a steel rod that had been additionally welded. The dial gauge was fixed to the end of the nail, and suction was applied to the jack to pull out the nail. The test was conducted under the force control method. Horizontal displacement corresponding to the pullout force was measured using a dial gauge. EPS were used to measure the variation in the overburden stress during the test, which was then recorded in real-time using the Arduino circuit arrangement. A recording software called ‘CoolTerm’ was used for the real-time recording of earth pressure. The complete experimental setup is shown in Figure 10.



Figure 10: Complete experimental setup

RESULTS AND DISCUSSION

Variation of earth pressure

The variations in earth pressure during the application of overburden stress, drilling, grouting, saturation, and nail pullout are presented in this section.

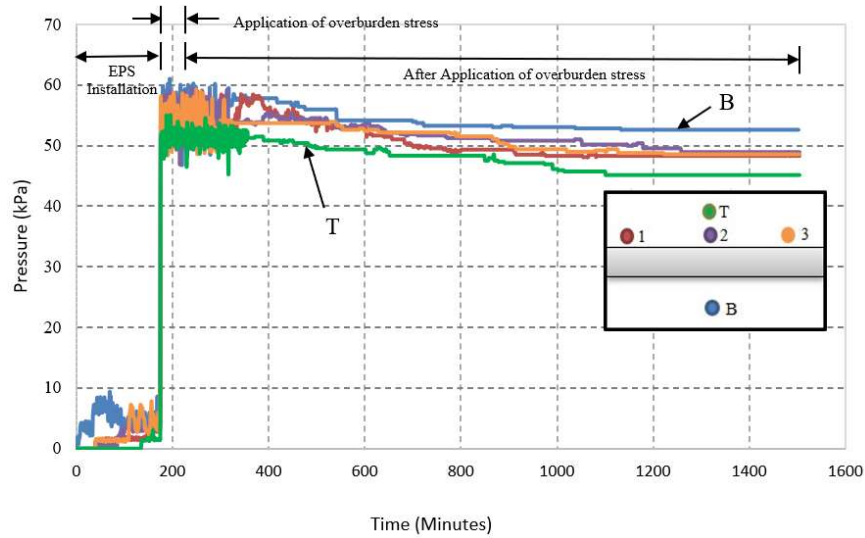


Figure 11: Typical variation of earth pressure during installation and application of the overburden pressure ($S_r = 82\%$)

During the installation of EPS and application of overburden pressure

Figure 11 depicts the earth pressure response against time during the installation of the EPS and the application of the overburden pressure. Since the observed responses are typical for all the experiments, only the results with $S_r = 82\%$ (where $S_r =$ degree of saturation) are presented. Small fluctuations in EPS readings were observed during the installation of earth pressure sensors due to soil filling in the pullout box. A significant increment in the earth pressure was observed during the application of the overburden stress. There was a large fluctuation in the earth pressure readings at the initial stage after the application of the overburden stress. This fluctuation was caused by the movement of soil particles that come into contact with the EPS and by the application of different soil weights above the EPS. After approximately 21 h, there was a negligible change in the measured earth pressures, indicating that the vertical stress in the soil was constant and reflected the applied overburden stress. Based on Figure 11, it can be seen that the earth pressure measured by the EPS generally agreed with the applied overburden stress of 44.77 kN/m^2 . However, there was a slight difference between the calculated and observed values owing to the variation in the soil density during compaction.

During drilling and grouting

During the process of drilling a hole to install the soil nail, the stress in the soil increases due to the outward pushing of the soil by the drill bit. This behaviour is clearly illustrated in Figure 12; when the drill bit reached the section with the EPS, the earth pressure increased slightly. The earth pressure at Point 1 (i.e., nail head) increased prior to Point 2 (i.e., middle) and Point 3 (i.e., nail tail), and when the drilling progressed further, the earth pressure at Point 2 and Point 3 increased (Figure 12). After the drill bit passed the section of the EPS, the earth pressure dropped significantly due to the release of surrounding stress. There was no significant change in the earth pressure at Point 'B' since the sensor was away from the drill hole. Initially, the earth pressure at points 1, 2 and 3 was approximately 48 kPa , and this increased to approximately 58 kPa at the start of drilling. That is an increment of about 10 kPa . Then there was a sudden drop of nearly 38 kPa , reducing the resultant value of the three sensors to approximately 30 kPa due to the release of surrounding soil stress. Similar behaviour was observed at point 'T', where the earth pressure increased by 5 kPa during drilling and reduced by 10 kPa during the release of stress. This clearly indicates that the soil disturbance during drilling spread only in the upward direction.

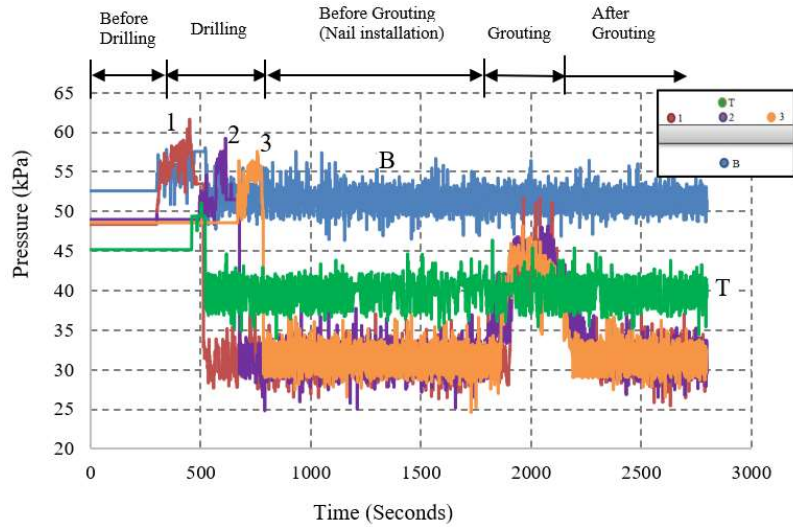


Figure 12: Typical variation in earth pressure during drilling the hole, nail installation and pressure grouting ($S_r = 82\%$)

During the soil nail installation, there was no significant variation of earth pressure in any of the sensors. Grouting was done for nearly 6 min, and during this period, the earth pressure again increased by approximately 15 kPa. However, once the grouting process was completed, the earth pressure dropped to nearly 30 kPa, which means the earth pressure released after grouting was almost 15 kPa. Since the water: cement ratio of the grout was 0.5, the grout contains a significant amount of water. Hence, during pressure grouting, the water in the grout is absorbed by the surrounding soil. As a result, the grout hardens rapidly.

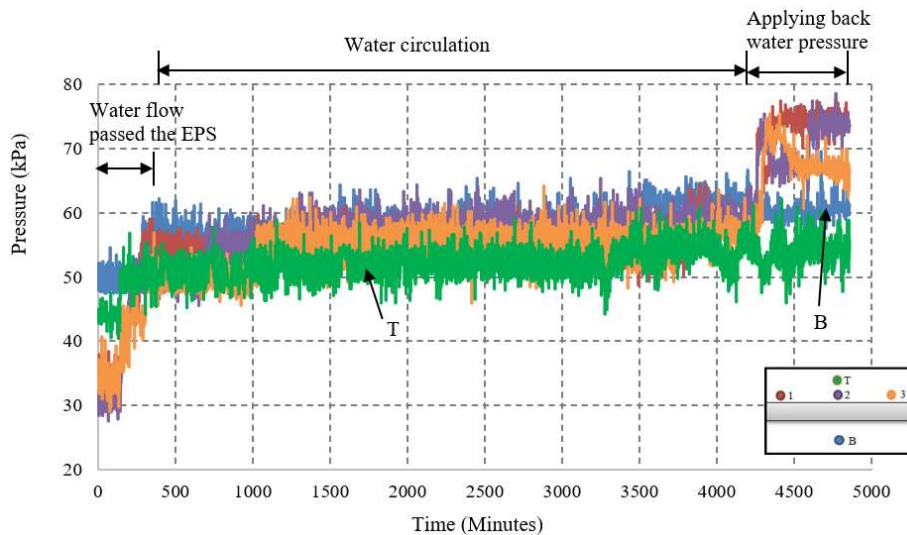


Figure 13: Variation in earth pressure during saturation ($S_r = 82\%$)

During saturation

Saturation was initiated three days after grouting by allowing the grout to harden so that the grouted nail had acquired sufficient strength. The variation of earth pressure during the saturation process is illustrated in Figure 13. Immediately after saturation started, the earth pressure values of all the sensors showed a gradual increment.

The earth pressures in EPS-B and EPS-T showed a sudden increment at first and then continued to increase slowly throughout the saturation period. The earth pressure near the soil nail (EPS-1, EPS-2, and EPS-3) indicated a significant increase in earth pressure when the water flowed passed the sensors. Because of the application of back-water pressure when the waterproof front cap was filled with water, there was a significant increase in earth pressure again near the soil nail. The increase in earth pressure near the nail head (EPS-1) was slightly higher than that of the other two sensors since it was the closest sensor to the waterproof front cap, which applied the back water pressure. After three days of saturation, the water began to fill the waterproof front cap continuously so that the back pressure was applied for a longer time interval than on the previous occasions. This caused the earth pressure values of EPS-1, EPS-2, and EPS-3 to increase significantly because of the continuous back water flow around the nail. It required 2.3 days, 3.3 days, and 8 days to achieve 68%, 82%, and 98% degrees of saturation of the soil within the pullout box, respectively.

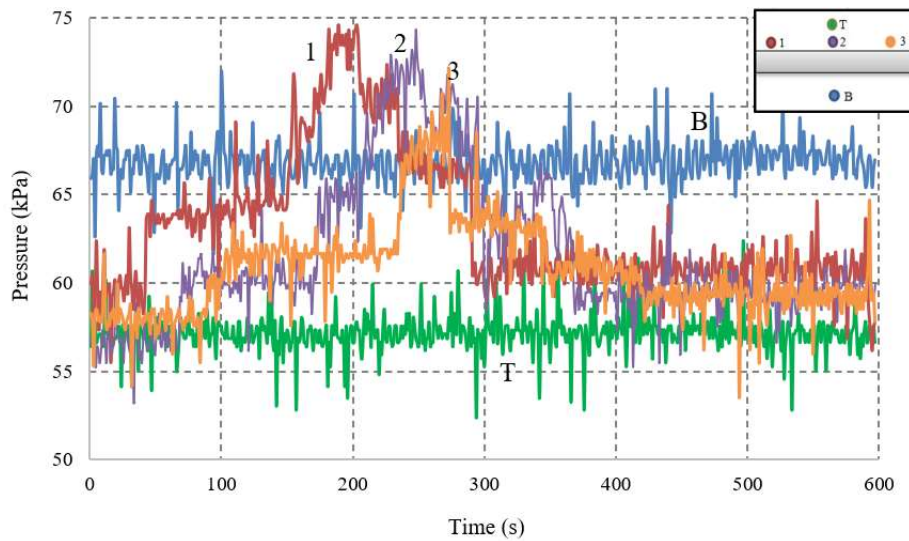


Figure 14: Typical variation in earth pressure during pullout test ($S_r = 82\%$)

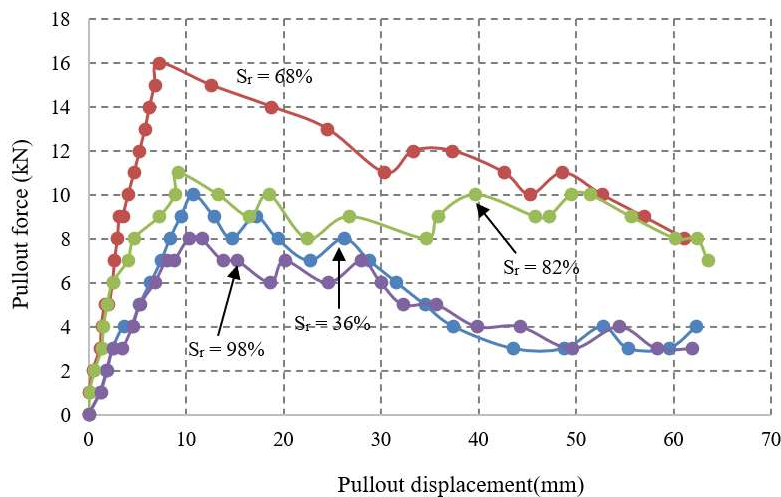


Figure 15: Relationship between pullout force and pullout displacement under different degrees of saturation of the soil

During the pullout test

During the pulling out of the grouted nails, the readings of EPS-1, EPS-2, and EPS-3 increased to their peak values and then decreased with the displacement of the soil nail (Figure 14). The peak value of EPS-1 was higher than that of EPS-2 and EPS-3. This was due to the stress transfer from the nail surface to the soil from the head of the nail to the tail. It is worth noting that the greatest shear displacement was mobilized near the nail head, which decreased towards the nail tail. Earth pressures at EPS-B and EPS-T did not change significantly during the pullout of the nail. Hence, it is evident that the earth pressure changed significantly at or near the soil-grouted nail interface during the pullout test. This behaviour can be identified as dilation of the soil as earth pressure increases during shearing, which depends on soil suction, soil density, and interface roughness. Since soil density and interface roughness remain constant during the pullout, it is evident that soil suction may cause an increase in soil dilatancy. A similar relationship between soil suction and dilatancy was reported by Ng and Zhou (2005). Therefore, it can be concluded that soil dilation is one of the key influencing parameters in the pullout resistance of the soil nail.

Pullout force-displacement behaviour

The relationship between the pullout force and the pullout displacement for different degrees of saturation under constant overburden pressure is shown in Figure 15. Regardless of the saturation level, all the curves exhibit the same pullout force-displacement behaviour. As shown in the pullout force-displacement curves, the average pullout force increased rapidly to reach its peak value and then decreased gradually with displacement.

The analysis of the pullout force-displacement behaviour is illustrated in Table 2. The displacement at the peak pullout force was less than 12 mm in all the experiments. When the soil moisture content was less than the optimum moisture content ($\omega_{opt} < 17.6\%$), the displacement rate per pullout force, up to the peak value, was 1.0 mm/force. When the soil moisture content was more than the optimum moisture content, the displacement rate per pullout force up to the peak value was approximately 0.5 mm/force. From this, it can be concluded that the rate of displacement per force decreases when the moisture content is greater than the optimum moisture content.

Table 2: Pullout force-displacement behaviour

Moisture content (%)	Degree of saturation (%)	Peak pullout force (kN)	Displacement at peak pullout force (mm)
14.22	36	10	10.75
26.86	68	16	7.24
32.39	82	11	9.10
38.71	98	8	11.55

However, when the degree of saturation was more than 80%, the pullout force initially increased at a rapid rate of 0.5 mm/force with the pullout displacement to nearly 90% of the peak pullout value, and then it continued to increase at a slower rate of 1.5 mm/force until it reached the peak pullout force. In contrast to the above, the opposite behaviour can be observed when the soil is fully saturated. The pullout force initially increased at a rate of 0.6 mm/force until 50% of the peak pullout value was reached, and then it continued to increase at a slower rate of 1.2 mm/force until the peak pullout force was reached. The above explanation clearly illustrates that the rate of displacement per pullout force is highly dependent on the degree of saturation. Furthermore, it can be noted that a maximum displacement of around 63 mm was achieved due to the limitations of the apparatus.

Variation of peak pullout force with the degree of saturation

The variation of peak pullout force over the degree of saturation is illustrated in Figure 16. The shape of the peak pullout force curve versus the degree of saturation was very similar to the compaction curve, where the peak pullout force increases with the degree of saturation until it reaches an optimum moisture content and then decreases when the moisture content is greater than the optimum moisture content. On the contrary, displacement at peak pullout force decreases until the maximum peak pullout force is reached, as shown in Figure 17. The peak pullout force reaches its maximum value when the moisture content is near the optimum moisture content, i.e.,

$S_r = 49\%$. When the soil is on the dry side of its optimum moisture content, water is absorbed by the soil due to higher matric suction. This may cause more contraction of the cement grout, thus reducing the bond strength between the grouted nail surface and the surrounding soil. As such, the peak pullout force is less on the dry side of the soil than that at the optimum moisture content.

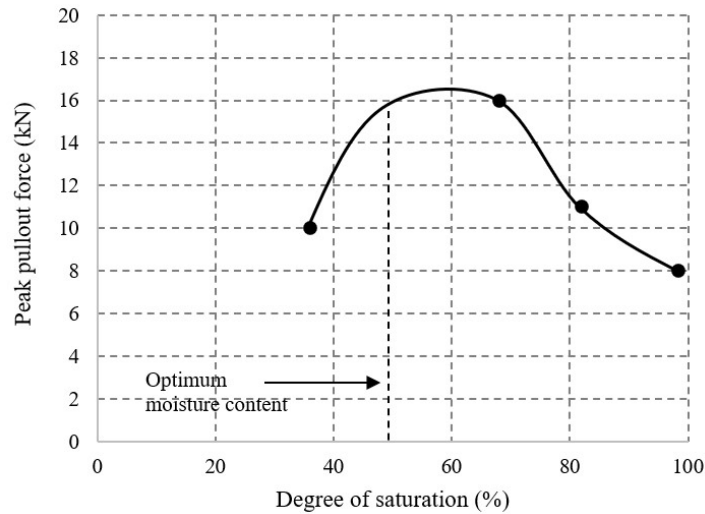


Figure 16: Variation of the peak pullout force over different degrees of saturation

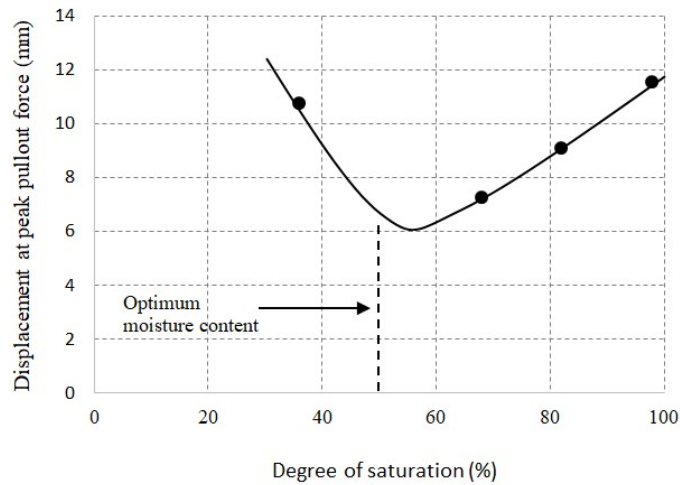


Figure 17: Variation displacement at peak pullout force versus degree of saturation

It is generally believed that when the soil is dry due to higher matric suction, the soil has a higher pullout resistance. However, it was observed that when $S_r = 36\%$, the soil had a lower pullout resistance than that of the others. If the soil is very dry, water within the cement grout is absorbed by the soil due to a higher matric suction. This will lead to the contraction of the cement grout and reduce the bond strength between the grout surface and surrounding soil, resulting in a low peak pullout force. When the moisture content of the soil is more than the optimum moisture content, the apparent cohesion of the soil decreases. As a result, the pullout resistance decreases with an increase in soil moisture content above the optimum value.

Failure mechanism

To determine the failure mechanism of grouted nails during pullout, the surface of the grouted nails was investigated after the tests. Figure 18 illustrates the photographs of the grouted nails after the pullout tests. Even though the hole diameter was only 50 mm, it can be seen that the average diameter of the grouted nail was more than the hole diameter (Table 3), indicating the effect of the grouting pressure. Harshani and Priyankara (2018) reported that the pullout resistance increases with the increase of grouting pressure due to the increase in the diameter of the grouted nail under high grouting pressure. Further, it was observed that the diameter of the grouted nail at the centre was more than that of the nail head and nail tail, irrespective of the degree of saturation. This implies the grouting pressure is concentrated more at the centre than at the nail head and tail. However, the average grouted nail diameter was the same, irrespective of the degree of saturation.

According to the shearing planes illustrated in Figure 18, at different degrees of saturation, the shearing plane had migrated from the interface between the grouted nail and the surrounding soil further into the soil when the soil became saturated. When the soil is fully saturated, a noticeable thick layer of the soil had adhered to the grouted nail surface. This implies the migration of the shearing plane from the grouted nail-soil interface to the soil owing to the decrease of the soil matric suction.

Table 3: Average nail diameter

Degree of saturation (%)	Average nail diameter (mm)
36	55.21
68	55.70
82	54.07
98	55.25

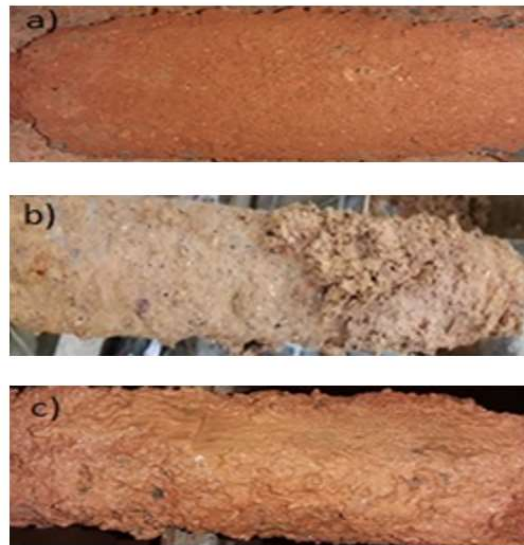


Figure 18: Nail surfaces after pullout test for different degrees of saturation at (a) $S_r = 36\%$; (b) $S_r = 82\%$; (c) $S_r = 98\%$

CONCLUSION

To determine the effect of the degree of saturation of soil on pullout resistance, a series of laboratory tests were conducted using a pullout box by varying the soil moisture content. A specially designed waterproof front cap was used to apply backwater pressure to saturate the soil within the pullout box. Variations in earth pressure near

the grouted nail surface were observed during the experiments. Based on the laboratory experimental results discussed above, the following conclusions were drawn:

1. The peak pullout force is highly dependent on the degree of saturation of the soil. The higher the degree of saturation (wet side of the optimum moisture content), the lower the pullout resistance. Similarly, when the soil is sufficiently dry (dry side of the optimum moisture content), water within the cement grout is absorbed by the soil due to higher matric suction, thus reducing the bond strength between the grout surface and surrounding soil. This results in a low pullout resistance.
2. The highest peak pullout force occurs when the moisture content of the soil is close to the optimum moisture content. Similarly, it can be concluded that the highest peak pullout force is within the degree of saturation of soil between 45% and 70%.
3. During the pullout test, the minimum displacement occurs when the moisture content of the soil is near the optimum moisture content. This indicates that the minimum displacement corresponds to the highest peak pullout force.
4. The rate of displacement per pullout force is highly dependent on the degree of saturation of the soil, where the rate of displacement per pullout force decreases when the moisture content is greater than the optimum moisture content.
5. The shearing plane migrated further into the soil from the grouted nail-soil interface when the degree of saturation was high, i.e., more than the optimum moisture content.
6. The stresses within the soil medium near the soil nail interface vary significantly during the grouted nail installation process and during the pullout test. The earth pressure variation near the soil nail interface during the pullout tests indicated that there is a significant effect of soil dilatancy on the pullout resistance of soil nails. Further, soil dilatancy depends on the matric suction of the soil.

It should be noted that the number of tests was limited in this study, and more soil nail pullout tests with more degrees of saturation should be performed to accurately examine the effect of the degree of saturation on pullout resistance. Furthermore, it is necessary to measure the matric suction during the pullout tests to analyse the effect of matric suction on pullout resistance.

REFERENCES

- Burland J.B. (2002). *Reliability of soil nailed slopes in Hong Kong. (Internal Report)* Geotechnical Engineering Office, Hong Kong, pp. 4–12.
- Chu L.M & Yin J.H. (2005). Laboratory Pullout testing study of soil nails in a completely decomposed granite soil. *Geotechnical Testing Journal* **28**: 1–15.
- Fernando K.A.S.N. (2020). The effect of degree of saturation on pullout resistance. *B.Sc. thesis*, University of Ruhuna, Galle, Sri Lanka.
- Gurpersaud N. (2010). The influence of matric suction on the pullout capacity of grouted soil nails. *M.Sc. thesis*, Carleton University, Canada.
- Gurpersaud N., Vanapalli S.K. & Sivathayalan S. (2013). Semi-empirical method for estimation of pullout capacity of grouted soil nails in saturated and unsaturated soil environments. *Journal of Geotechnical and Geoenvironmental Engineering* **39**(11): 1934–1943.
DOI: [https://doi.org/10.1061/\(ASCE\)GT.1943-5606.0000883](https://doi.org/10.1061/(ASCE)GT.1943-5606.0000883)
- Harshani R.G.F. & Priyankara N.H. (2018). Influence of grouting pressure on pullout resistance of soil nail. *Proceedings of 7th International Symposium on Advances in Civil and Environmental Engineering Practices for Sustainable Development*, ACEPS-2019, Galle, pp. 28–33.
- Hong Y.S., Wu C.S. & Yang S.H. (2003). Pullout resistance of single and double nails in a model sandbox. *Canadian Geotechnical Journal* **40**(5): 1039–1047.
DOI: <https://doi.org/10.1139/t03-048>
- Junaideen S.M., Tham L.G., Law K.T., Lee C.F. & Yue Z.Q. (2004). Laboratory study of soil nail interaction in loose, completely decomposed granite. *Canadian Geotechnical Journal* **41**(2): 274–286.
DOI: <https://doi.org/10.1139/t03-094>
- Kalehsar R.I., Khodaei M., Dehghan A.N. & Najafi N. (2021). Numerical modelling of effect of surcharge load on the stability of nailed soil slopes. *Model Earth Systems and Environment* **6**: 1–12.
- Lazarte C. A., Baecher G. B. & Withiam J. L. (2003). New directions in LRFD for soil nailing design and specifications. *Proceedings of the International Workshop on Limit State Design in Geotechnical Engineering Practice, LSD 2003*. World Scientific.
DOI: https://doi.org/10.1142/9789812704252_0008

- Najafi N., Kalehsar R.I., Khodaei M., Dehghan A.N. & Karroubi K. (2021). Effect of installation angle on pullout resistance of nails in soil slopes. *SN Applied Sciences* **3**: 1–13.
DOI: <https://doi.org/10.1007/s42452-021-04705-2>
- Ng C.W.W. & Zhou R.Z.B. (2005). Effect of soil suction on dilatancy of an unsaturated soil, *Proceedings of 16th International Conference on Soil Mechanics and Geotechnical Engineering: Geotechnology in Harmony with the Global Environment, ICSMGE*, volume 2, Osaka, Japan, pp. 559–562.
- Pradhan B., Tham L., Yue Z., Junaideen S. & Lee C. (2006). Soil–nail pullout interaction in loose fill materials. *International Journal of Geomechanics* **6**(4): 238–247.
DOI: [https://doi.org/10.1061/\(ASCE\)1532-3641\(2006\)6:4\(238\)](https://doi.org/10.1061/(ASCE)1532-3641(2006)6:4(238))
- Schlosser F. & Buhan P. (1991). Theory and design related to the performance of reinforced soil structures. In: Performance of Reinforced Soil Structures, *Proceedings of the International Reinforced Soil Conference Organized by the British Geotechnical Society*, pp. 1–14. Thomas Telford Publishers, London, UK.
- Su L., Chan T., Shiu Y., Cheung T. & Yin J. (2007). Influence of degree of saturation on soil nail pullout resistance in compacted completely decomposed granite fill. *Canadian Geotechnical Journal* **44**(11): 1314–1328.
DOI: <https://doi.org/10.1139/T07-056>
- Su L.J., Yin J. H. & Zhou W.H. (2010). Influence of overburden pressure and soil dilation on soil nail pullout resistance. *Computers and Geotechnics* **37**(4): 555–564.
DOI: <https://doi.org/10.1016/j.compgeo.2010.03.004>
- Zhang L.L., Zhang L.M. & Tang W.H. (2009). Uncertainties of field pullout resistance of soil nails. *Journal of Geotechnical and Geoenvironmental Engineering* **135**(7): 966–972.
DOI: [https://doi.org/10.1061/\(ASCE\)GT.1943-5606.0000014](https://doi.org/10.1061/(ASCE)GT.1943-5606.0000014)

RESEARCH ARTICLE

Polymer Solar Cells

Efficiency boost of inverted polymer solar cells using electrodeposited n-type Cu₂O electrons selective transport layers (ESTLs)

WTMAPK Wanninayake¹, DGKK Namawardana¹, RMG Wanigasekara¹, KMDC Jayathilaka¹, RP Wijesundera^{1*}, W Siripala¹ and MI Malik²

¹ Department of Physics and Electronics, Faculty of Science, University of Kelaniya, Dalugama, Kelaniya 11600, Sri Lanka.

² Third World Center for Science and Technology, H.E.J. Research Institute of Chemistry, International Center for Chemical and Biological Sciences (ICCBS), University of Karachi, Karachi 75270, Pakistan.

Submitted: 20 June 2022; Revised: 17 October 2022; Accepted: 28 October 2022

Abstract: Polymer solar cells (PSCs) have attracted tremendous interest as suitable candidates for harnessing solar energy in the recent years. The inherent optoelectronic properties of the inorganic transition metal oxide, negative type cuprous oxide (n-Cu₂O), makes it an attractive candidate to improve the performance of PSCs when incorporated as the electron selective transport layers (ESTLs) in the device. In this study, inverted PSCs were fabricated on stainless steel (SS) substrates with n-Cu₂O as the ESTL. The n-Cu₂O films were prepared by electrodeposition method, followed by annealing under ambient conditions. The active layer material was prepared as bulk heterojunction blend using regioregular poly(3-hexylthiophene) (P3HT) and phenyl-C61-butyric acid methyl ester (PCBM). Poly-(4,3-ethylene dioxathiophene):poly(styrenesulphonate) (PEDOT:PSS) was used as the hole transport layer (HTL) and the final device structure was SS/n-Cu₂O/P3HT:PCBM/PEDOT:PSS/Au. Annealing of the n-Cu₂O ESTL in air was optimized observing the photoactive performance of the device. Optoelectronic performance of the devices was characterized using spectral response and dark and light current-voltage (I-V) measurements. n-Cu₂O ESTL- incorporated devices have absorbed more photons in the short wavelength region of 450–600 nm with the annealing of n-Cu₂O ESTL due to the reduction of electron-hole recombination. The performance of the devices was significantly increased after incorporating pre-annealed n-Cu₂O ESTL at 175 °C for 30 min in air. The maximum power conversion efficiency (PCE) was 0.35%.

Keywords: ESTL, inverted PSCs, n-Cu₂O, P3HT-PCBM, polymer solar cells.

INTRODUCTION

Solar energy has become the most promising renewable and green energy source due to its free availability and environmentally friendly. Much work has been carried out worldwide to extract solar energy as an alternative for fossil fuels (Dang *et al.*, 2011; Bansal *et al.*, 2014). Various types of solar cells such as inorganic, dye sensitized and perovskite based solar cells were employed in this task; at present, inorganic solar cells play the dominant role with highest reported power conversion efficiencies. However, large scale fabricating process of silicon solar cells is associated with a high production cost and, in addition, inorganic materials have caused environmental issues (Fu *et al.*, 2017; Liu *et al.*, 2017). Therefore, the polymer solar cells (PSCs) have received the attention of academia and industry over their conventional counterparts, owing to advantages such as their potential to be low cost, efficient and environmentally friendly, and their solution processability (Reisdorffer *et al.*, 2012). The most widely used combination of a small molecule and a conjugated polymer system in PSCs is a bulk heterojunction blend of [6,6]-phenyl-C61-butyric acid methyl ester (PCBM) and regioregular poly(3-hexylthiophene) (rr-P3HT). The power conversion efficiency (PCE) of bulk heterojunction solar cells of over 10% has been achieved through remarkable progress in the past few decades (Wanwong *et al.*, 2020; Zheng *et al.*, 2020).

The indium-tin-oxide (ITO) coated glass slides are the most popular substrate for fabricating the devices. However, the active layer of such solar cells is more prone to oxidation and degradation due to the diffusion of

* Corresponding author (palitha@kln.ac.lk;  <https://orcid.org/0000-0002-3223-5969>)



This article is published under the Creative Commons CC-BY-ND License (<http://creativecommons.org/licenses/by-nd/4.0/>). This license permits use, distribution and reproduction, commercial and non-commercial, provided that the original work is properly cited and is not changed in anyway.

oxygen and moisture through pinholes. Furthermore, one of the very common hole transport materials, poly-(4,3-ethylene dioxythiophene): poly(styrene sulfonate) (PEDOT: PSS) interfacial layer directly contacts the ITO glass and can react with ITO substrates, leading to a degradation of the anode performance. Since indium is an expensive material, the production cost of the ITO is high and ITO is not an ideal substrate for fabricating solar cell devices (Chen *et al.*, 2009). Therefore, the major disadvantage of the conventional structure of PSCs is the lack of long-term stability when exposed to the environment. This has inspired the emergence of inverted PSC devices as an alternative, with high air resistive and more stable high work function metals (Ag, Au) as the top electrodes. The inverted PSCs consists of a conductive metal substrate as the cathode, an active layer, a hole transport layer (HTL), and a top metal anode (Galagan *et al.*, 2011; Chang *et al.*, 2013).

Development of the PSCs for higher PCE can be achieved by tuning the architecture of the inverted structure such as inserting an electron selective transport layers (ESTLs) in the device. The free electrons released diffuse through the acceptor material and are collected by the ESTL and ultimately injected to the cathode (Kietzke, 2007). Furthermore, the ESTLs in the inverted PSCs play key roles including create an electron selective and transport intermediate layer, block the reverse holes flowing from the donor polymer to the cathode, adjust the energy gap between the active layer and the cathode, and avoid the chemical and physical reactions between the active layer and the cathode (Yang *et al.*, 2005).

In the recent years, tremendous work has been implemented to improve the performances of ESTLs using many semiconducting metal oxides (MOs) such as zinc oxide (ZnO), zinc tin oxide (ZTO), titanium sub-oxide (TiO_x), aluminum oxide (Al_2O_3), and niobium pentoxide (Nb_2O_5) in inverted PSCs (Li *et al.*, 2009; Huang *et al.*, 2010; Zhou *et al.*, 2010; Sun *et al.*, 2011; Wiranwetchayan *et al.*, 2011; Oo *et al.*, 2012). However, cuprous oxide (Cu_2O) has not been tested so far in the reported research, even though Cu_2O provides many suitable inherent semiconducting properties for an ESTL (Wanninayake *et al.*, 2015; Iqbal *et al.*, 2018). Cuprous oxide is a nontoxic, low cost and direct band gap (2 eV) semiconducting material. It is generally considered as a p-type material due to a stoichiometry defect of copper ion vacancies (Maake *et al.*, 2020). However, n-type Cu_2O (n- Cu_2O) films can be obtained by tuning the material growth condition in the device fabrication. In this work, we fabricated inverted structured P3HT/PCBM based solar cells on SS substrates with n- Cu_2O ESTL and demonstrate the optoelectronic properties of the PSCs.

MATERIALS AND METHODS

Materials

Poly(3-hexylthiophene) (P3HT) (>99%) was purchased from Sigma Aldrich, USA. [6,6]-phenyl-C61-butyric acid methyl ester (PCBM) (>99%) was purchased from Sigma Aldrich, Netherlands. Mono-chloro-benzene (MCB) (>99.5%) was purchased from Sigma Aldrich, Germany. Poly(3,4-ethylenedioxythiophene) polystyrene sulfonate (PEDOT: PSS) (1.3 wt.%, conductive grade) was purchased from Sigma Aldrich, USA. Copper acetate (>99%) was purchased from Sisco Research Laboratories, India. Sodium acetate (anhydrous, $\geq 99.0\%$) was purchased from Sigma Aldrich, Germany. 304 Grade Stainless steel (SS) was purchased from Sri Lanka.

Fabrication of devices

Polished SS substrates ($20 \times 25 \text{ mm}^2$ size) were cleaned ultrasonically with detergent and rinsed in deionized water, acetone, methanol, and isopropyl alcohol sequentially, air drying at each step. Cupric acetate (1.0 g) and 4.1 g of sodium acetate were dissolved in 500 mL deionized water to prepare an aqueous solution containing 0.01 M $(\text{CH}_3\text{COO})_2\text{Cu}$, 0.1 M CH_3COONa and magnetically stirred for 15 min at room temperature. n- Cu_2O thin films were electrodeposited on SS substrates at -200 mV vs. Ag/AgCl for 30 min in the previously prepared $(\text{CH}_3\text{COO})_2\text{Cu}$ bath using Hokuto Denko Potentiostat/Galvanostat HAB 151. Temperature of the bath was maintained at 55 °C while magnetically stirring at 50 rpm. Then the thin films were annealed at 100°C, 150 °C, 175 °C, 200 °C for 30 min to prepare four different sample series including reference sample. P3HT (10 mg) and PCBM (10 mg) were mixed in 1 mL of MCB to prepare a 20 mg/mL solution and the solution was magnetically stirred for 12 h at 55 °C. This solution was spin coated on top of the annealed n- Cu_2O coated SS substrates at 3000 rev/min to grow a thin film. The samples were annealed at 140 °C for 30 min. Conductive grade, 1.3 wt.% dispersion of PEDOT:PSS was mixed with ethylene glycol (EG) (10 wt.%) as a dopant. The prepared PEDOT:PSS

was blade coated and subsequently annealed at 120 °C for 15 min to grow the Hole Transport Layer (HTL). Finally, Gold (Au) spots were deposited on the PEDOT:PSS layer by sputter coating to produce the SS/n-Cu₂O/P3HT:PCBM/PEDOT:PSS/Au structure. Also, the reference device was fabricated following the above procedure without Cu₂O ESTL. The schematic diagrams of fabricated devices are shown in Figure 1.

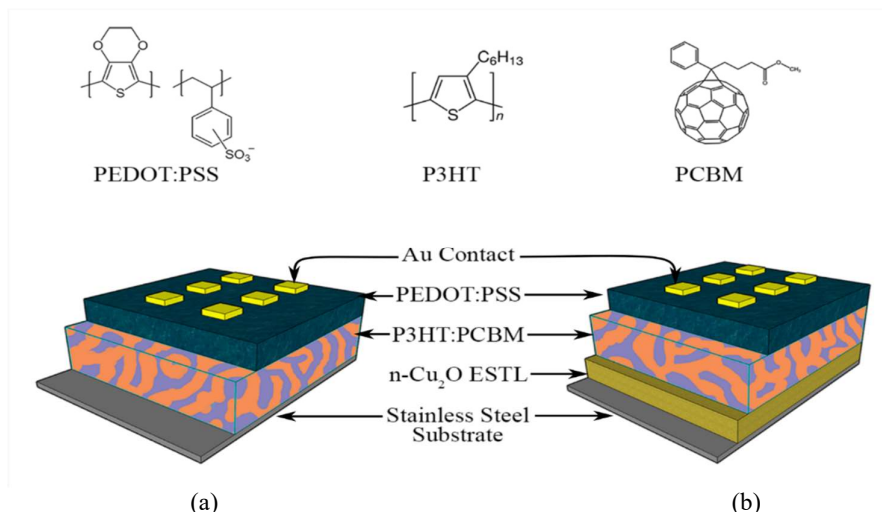


Figure 1: Schematic diagram of cross section of top illuminated inverted PSCs on SS substrates (a) without, and (b) with n-Cu₂O ESTL

Device characterization

The layer structures of the fabricated solar cells were analysed using a scanning electron microscope (FEG-SEM Hitachi S-4800). The crystallinity studies of the thin layers were performed by XRD (Bruker D8 Advance ECO X-ray diffractometer) with a Cu/K α source at a rate of 0.2° per minute. Recorded range of the X-ray spectra were from 0°–80°. Open circuit voltage (V_{oc}), short circuit current (I_{sc}), current density (J_{sc}), power conversion efficiency (PCE) and fill factor (FF) of fabricated devices were measured using Keithley 2100 multimeter under 1 sun illumination (AM 1.5G, 1000 Wm⁻²) of ScienceTech SciSun-300 solar simulator. I-V characteristics of the devices were obtained using Gamry series G300 potentiostat/Galvanostat. Spectral responses of the cells were measured using a computer-controlled system consisting of Stanford Research-SR 830 DSP lock-in amplifier, ScienceTech 9010 (200 - 1200 nm) monochromator and a Stanford Research-SR 540 chopper.

RESULTS AND DISCUSSION

Morphological characterization

The SEM images of the inverted structure of the fabricated SS/n-Cu₂O/P3HT:PCBM/PEDOT:PSS/Au devices are shown in the Figure 2. Figures 2(a) and 2(b) presents the SEM images at two different resolutions of a same sample. Figures 2(c) represents cross section of the electrodeposited n-Cu₂O layer (n-Cu₂O ESTL) on the SS substrate. The SEM images depicts that electrodeposition method is convenient to obtain a uniform and densely packed n-Cu₂O ESTL on the SS substrate. It is evident that the film is polycrystalline and its grain sizes are in the range of 1–2 μ m. The SEM results of the P3HT/PCBM active layer show the homogeneity of the surface of the active layer deposited on the thin layer of n-Cu₂O. The crucial factors behind this homogenous growth of the active layer are the proper adhesive properties and surface roughness between the n-Cu₂O ESTL and the active layer under the electrodeposition and spin coating technique, respectively. The interface having better contacts between the layers is essential for the exciton separation and the transportation of separated electrons or holes, which will lead to high performance inverted solar cells.

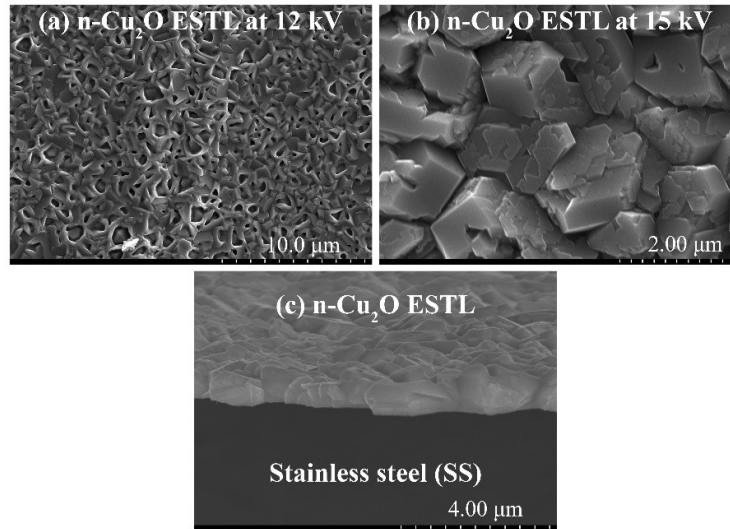


Figure 2: SEM images of (a) electrodeposited n-Cu₂O ESTL at 12KV; (b) electrodeposited n-Cu₂O ESTL at 15KV; (c) cross section: n-Cu₂O ESTL on SS substrate

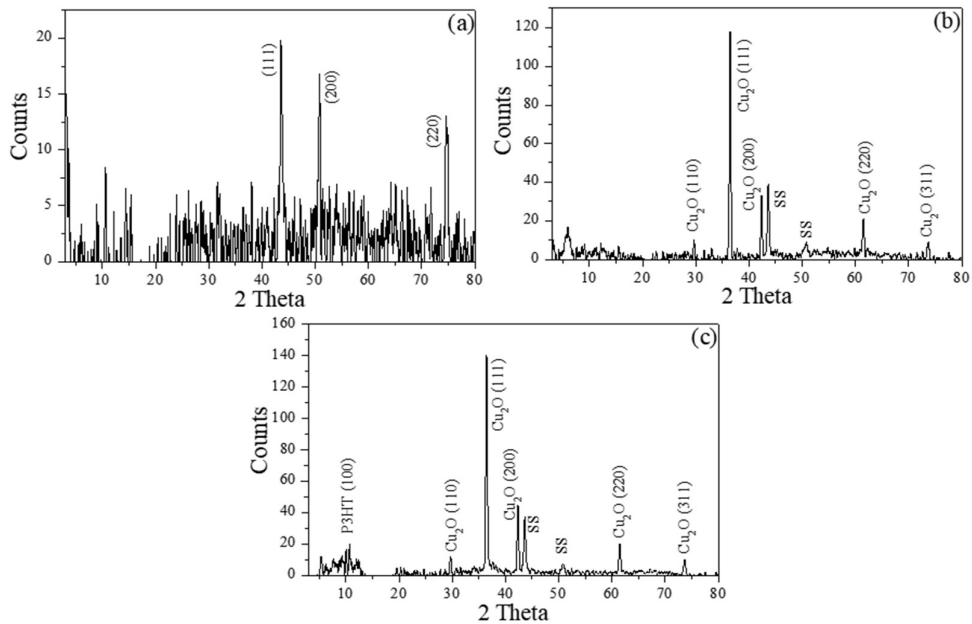


Figure 3: XRD patterns of (a) SS substrate; (b) electrodeposited and annealed (at 175 °C) n-Cu₂O ESTL on SS substrate; (c) SS/ n-Cu₂O ESTL/ P3HT:PCBM

Structural characterization

Figure 3 shows the X-ray diffraction (XRD) patterns of SS substrate, electrodeposited with annealed n-Cu₂O ESTL on SS substrate and cross section of SS/n-Cu₂O ESTL/P3HT:PCBM device. Diffraction pattern of SS substrate shows the peaks corresponding to diffraction from the planes (111), (200) and (220) confirming the austenite phase of Fe-C system (Quan & He, 2015). The XRD pattern of electrodeposited and annealed Cu₂O thin film on SS substrate shows five peaks corresponding to the planes (110), (111), (200), (220) and (311) of Cu₂O

in addition to the SS peaks indicating deposited Cu₂O is polycrystalline in nature (Gre^z *et al.*, 2012). Also, there are no additional peaks present corresponding to any impurity. Furthermore, it can be observed that the intensity of (111) diffraction peak is higher when compared with the other peaks. In the XRD pattern of SS/n-Cu₂O ESTL/P3HT:PCBM, a broad peak at 2θ 5.37 degree can be observed due to the reflection plane (100) of thiophene rings in P3HT chain. This is a peak additional to the peaks of Cu₂O and SS crystal structures. The P3HT:PCBM blend is originally amorphous but, annealing of the film leads to a phase separation between P3HT and PCBM regions enabling the crystallization of P3HT (Sahare *et al.*, 2015).

Spectral response

Spectral responses of the fabricated devices are shown in Figure 4. All the devices, with and without n-Cu₂O ESTL have shown responses in the visible wavelengths of the electromagnetic spectrum. However, the n-Cu₂O ESTL incorporated devices have absorbed more photons in the short wavelength region of 450-600 nm and the best device has been fabricated using the annealing treatment at 175 °C for 30 minutes. This could be attributed to the reduction of electron-hole recombination due to the fast transfer of electrons from PCBM layer to SS substrate. The annealing treatment has improved the photo absorption of the devices, but after the optimum annealing temperature at 175 °C, the photo absorption has declined. The enhanced photo absorption of n-Cu₂O ESTL could be due to the improved nanoscale crystallinity or grain boundary elimination and reduced defects when subjected to annealing treatment. However, at high temperature, n-Cu₂O tends to transform to the positive type (p-type) p-Cu₂O. This can be the reason for the reduction of the photo absorption of the ESTL at the higher temperatures beyond 175 °C.

All the devices exhibit a band edge at the 680 nm level, indicating a band gap energy of 1.82 eV. Lower energy photons are not absorbed due to the higher energy level differences between the HOMO and LUMO levels of the P3HT. Once the threshold energy 1.82 eV is achieved, the photons are absorbed causing a photocurrent. However, the higher energy photons transmit through the active material without absorption. This decrease in absorption causes lower photo-response in the higher energy region.

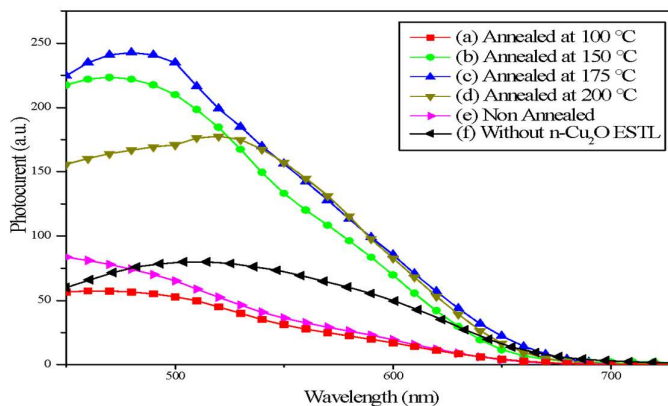


Figure 4: Spectral response curves of fabricated devices: n-Cu₂O ESTL annealed at (a) 100 °C; (b) 150 °C; (c) 175 °C; (d) 200 °C; (e) non annealed and (f) without n-Cu₂O ESTL

Band diagram of the device

Figure 5 shows the schematic diagram of energy levels and the transport directions of electrons and holes in a fabricated inverted structure of solar cell consisting of a n-Cu₂O ESTL and a P3HT:PCBM active layer. The conduction band (CB) of n-Cu₂O ESTL is lower than the lowest unoccupied molecular orbitals (LUMOs) of P3HT and PCBM, allowing electrons to transport efficiently from LUMO energy level of PCBM to the CB of n-Cu₂O ESTL. Furthermore, the valence band edge of n-Cu₂O ESTL is much lower than the highest occupied molecular orbitals (HOMOs) of both P3HT and PCBM; hence the n-Cu₂O ESTL block the reverse flow of holes from the polymer donor to the SS cathode by creating an energy barrier at the P3HT/Cu₂O interface. Also, it prevents the

electrons flowing back to the acceptor and reduces the charge combinations. It can be seen that the n-Cu₂O ESTL can assist in extracting and collecting electrons in the PCBM acceptor.

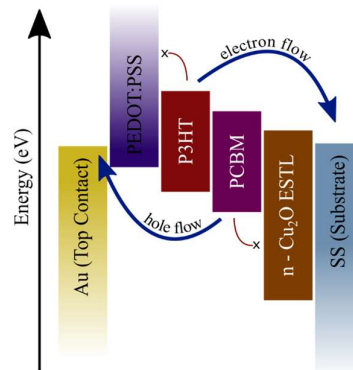


Figure 5: Band diagram of n-Cu₂O ESTL incorporated P3HT:PCBM solar cell

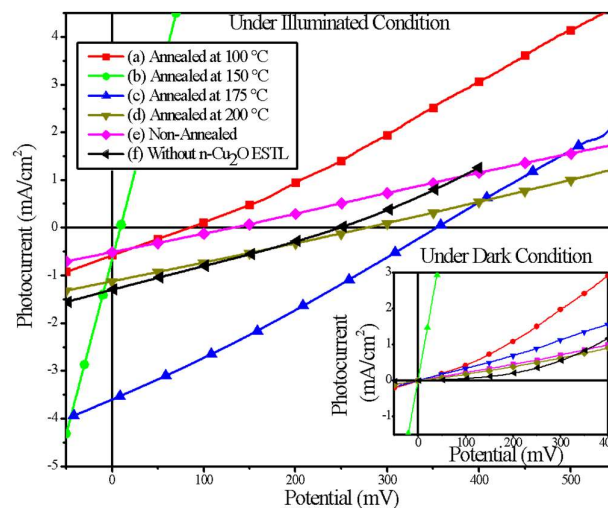


Figure 6: Dark and light J–V curves of the fabricated devices: n-Cu₂O ESTL annealed at (a) 100 °C; (b) 150 °C; (c) 175 °C; (d) 200 °C; (e) non annealed and (f) without Cu₂O ESTL

J-V characteristics

Aforementioned improvements have led to the enhancement of J_{sc} and PCE of the annealed n-Cu₂O ESTL devices. Figure 6 depicts the J–V characteristics of SS/n-Cu₂O/P3HT:PCBM/PEDOT:PSS/Au devices before and after the thermal annealing treatment. Also, the J–V characteristic of the reference device (without annealing and without n-Cu₂O ESTL) was obtained for the comparison purposes. The electrical parameters of all the devices are summarized in Table 1. The J_{sc} has decreased from 1.3 mA/cm² to 0.5 mA/cm² after adding n-Cu₂O ESTL in the device. However, it is clear that the J_{sc} was drastically increased to 3.6 mA/cm² after annealing the n-Cu₂O ESTL at 175 °C. Furthermore, the J_{sc} values were enhanced to 0.6 mA/cm² and 0.7 mA/cm² after annealing the devices at 100 °C, and 150 °C, respectively. However, in the devices consisting of further annealed (more than 200 °C) n-Cu₂O ESTL, the J_{sc} has started to decrease. It can be noticed that the variation of the J_{sc} has similar trend with spectral response. Therefore, pre-annealing of n-Cu₂O ESTL may have optimized the crystallinity, grain boundary condition and defects condition, leading to the J_{sc} enhancement. The FF values have slightly decreased from

26.47% to 25.19% after incorporating the n-Cu₂O ESTL. However, the FF has improved to 27.45% with annealing the devices at 175 °C. The FF explains the combination of the series resistance (R_s) and shunt resistance (R_{sh}) of the device. R_s represents the sum of contact resistance on the front/back surfaces and the ohmic resistances. Shunt resistance is mainly due to the imperfections on the device surface (Zhang *et al.*, 2011; Sun *et al.*, 2017). The n-Cu₂O ESTL may have significant influence on the resistance of the device. However, the thermal annealing has improved the FF of the devices as shown in Table 1 and it may be due to the reduced resistance with grain boundary elimination.

Table 1: Performance of fabricated PSCs

Sample	J_{sc} (mAcm ⁻²)	V_{oc} (mV)	FF (%)	PCE (%)
Without n-Cu ₂ O ESTL	1.3	246	26.47	0.08
Non-annealed n-Cu ₂ O ESTL	0.5	132	25.19	0.02
n-Cu ₂ O ESTL annealed 100 °C	0.6	84	24.94	0.01
n-Cu ₂ O ESTL annealed 150 °C	0.7	9	25.45	0.001
n-Cu ₂ O ESTL annealed 175 °C	3.6	354	27.45	0.35
n-Cu ₂ O ESTL annealed 200 °C	1.1	277	25.57	0.08

The V_{oc} of fabricated solar cells declined from 246 mV to 132 mV in the presence of n-Cu₂O ESTL. However, the V_{oc} values were drastically enhanced to 354 mV after the thermal annealing at 175 °C. The V_{oc} of PSCs relied on the energy difference between the HOMO level of the donor (P3HT) and the LUMO level of the acceptor (PCBM). This study reveals that the energy difference between the HOMO and LUMO levels of P3HT and PCBM can be tuned by adding pre-annealed n-Cu₂O ESTL. However, it is clearly noticed that the n-Cu₂O ESTL and thermal annealing treatment have significant influence on the V_{oc} . Subsequently, the improved J_{sc} , spectral responses, FF and V_{oc} enhanced the power conversion efficiency (PCE) from 0.08% to 0.35%.

CONCLUSION

In this study, n-Cu₂O ESTL was incorporated to the inverted device to be the structure of SS/n-Cu₂O/P3HT:PCBM/PEDOT:PSS/Au. However, the performance of the solar cells decreased in the presence of n-Cu₂O ESTL. This may be due to the increased internal resistance. The devices fabricated with n-Cu₂O ESTL annealed at four different temperatures: 100 °C, 150 °C, 175 °C and 200 °C, the PCE increased from 0.08 to 0.35% in the cells annealed at 175 °C. The improved performance can be attributed to enhanced photo response, and J_{sc} . The photoresponse spectrum improved significantly after the presence of n-Cu₂O ESTL due to the enhanced electron transferability. The pre-annealing treatment of n-Cu₂O ESTL may have tuned the crystallinity, grain boundary condition and defects condition which led to the J_{sc} increment. The XRD peaks indicate that the deposited Cu₂O is pure and polycrystalline in nature. Also, the SEM shows uniformity of the annealed n-Cu₂O ESTL.

Acknowledgements

This work was financially supported by the National Science Foundation (NSF), Sri Lanka through the research grant NSF-PSF/ICRP/2017EA&ICT/02.

REFERENCES

- Bansal A., Sekhon J.S. & Verma S.S. (2014). Scattering efficiency and LSPR tunability of bimetallic Ag Au and Cu nanoparticles. *Plasmonics* **9**(1): 143–150.
DOI: <https://doi.org/10.1007/s11468-013-9607-x>
- Chang Y.M., Chen C.P., Ding J.M., Leu C.Y., Lee M.J. & Chen R.D. (2013). Top-illuminated organic solar cells fabricated by vacuum-free and all-solution processes. *Solar Energy Materials and Solar Cells* **109**: 91–96.
DOI: <https://doi.org/10.1016/j.solmat.2012.09.020>
- Chen L.M., Hong Z., Li G. & Yang Y. (2009). Recent progress in polymer solar cells: manipulation of polymer: fullerene morphology and the formation of efficient inverted polymer solar cells. *Advanced Materials* **21**(14-15): 1434–1449.
DOI: <https://doi.org/10.1002/adma.200802854>
- Dang M.T., Hirsch L. & Wantz G. (2011). P3HT: PCBM best seller in polymer photovoltaic research. *Advanced Materials* **23**(31): 3597–3602.

- DOI: <https://doi.org/10.1002/adma.201100792>
- Fu L., Li C., Li Y., Chen S., Long Y. & Zeng R. (2017). Simultaneous determination of iodide and bromide using a novel LSPR fluorescent Ag nanocluster probe. *Sensors and Actuators B: Chemical* **240**: 315–321.
DOI: <https://doi.org/10.1016/j.snb.2016.08.151>
- Galagan Y., Rubingh J.E.J., Andriessen R., Fan C.C., Blom P. W., Veenstra S.C. & Kroon J.M. (2011). ITO-free flexible organic solar cells with printed current collecting grids. *Solar Energy Materials and Solar Cells* **95**(5): 1339–1343.
DOI: <https://doi.org/10.1016/j.solmat.2010.08.011>
- Grez P., Herrera F., Riveros G., Ramírez A., Henríquez R., Dalchiele E. & Schrebler R. (2012). Morphological structural and photoelectrochemical characterization of n-type Cu₂O thin films obtained by electrodeposition. *Physica Status Solidi(a)* **209**(12): 2470–2475.
DOI: <https://doi.org/10.1002/pssa.201228286>
- Huang J.H., Wei H.Y., Huang K.C., Chen C.L., Wang R.R., Chen F.C., Ho K.C. & Chu C.W. (2010). Using a low temperature crystallization process to prepare anatase TiO₂ buffer layers for air-stable inverted polymer solar cells. *Energy and Environmental Science* **3**(5): 654–658.
DOI: <https://doi.org/10.1039/b922373h>
- Iqbal K., Ikram M., Afzal M. & Ali S. (2018). Efficient low-dimensional nanocomposite bilayer CuO/ZnO solar cell at various annealing temperatures. *Materials for Renewable and Sustainable Energy* **7**(2): 1–7.
DOI: <https://doi.org/10.1007/s40243-018-0111-2>
- Kietzke T. (2007). Recent advances in organic solar cells. *Advances in Optoelectronics* **2007**: 1687–1702.
DOI: <https://doi.org/10.1155/2007/40285>
- Li C.Y., Wen T.C., Lee T.H., Guo T.F., Lin Y.C. & Hsu Y.J. (2009). An inverted polymer photovoltaic cell with increased air stability obtained by employing novel hole/electron collecting layers. *Journal of Materials Chemistry* **19**(11): 1643–1647.
DOI: <https://doi.org/10.1039/b815523b>
- Liu D., Li L. & You T. (2017). Superior catalytic performances of platinum nanoparticles loaded nitrogen-doped graphene toward methanol oxidation and hydrogen evolution reaction. *Journal of Colloid and Interface Science* **487**: 330–335.
DOI: <https://doi.org/10.1016/j.jcis.2016.10.038>
- Maake P.J., Bolokang A.S., Arendse C.J., Vohra V., Iwuoha E.I. & Motaung D.E. (2020). Metal oxides and noble metals application in organic solar cells. *Solar Energy* **207**: 347–366.
DOI: <https://doi.org/10.1016/j.solener.2020.06.084>
- Oo T.Z., Chandra R.D., Yantara N., Prabhakar R.R., Wong L.H., Mathews N. & Mhaisalkar S.G. (2012). Zinc tin oxide (ZTO) electron transporting buffer layer in inverted organic solar cell. *Organic Electronics* **13**(5): 870–874.
DOI: <https://doi.org/10.1016/j.orgel.2012.01.011>
- Quan C. & He Y. (2015). Properties of nanocrystalline Cr coatings prepared by cathode plasma electrolytic deposition from trivalent chromium electrolyte. *Surface and Coatings Technology* **269**: 319–323.
DOI: <https://doi.org/10.1016/j.surfcoat.2015.02.001>
- Reisdorffer F., Haas O., Le Rendu P. & Nguyen T.P. (2012). Cosolvent effects on the morphology of P3HT: PCBM thin films. *Synthetic Metals* **161**(23–24): 2544–2548
DOI: <https://doi.org/10.1016/j.synthmet.2011.08.005>
- Sahare S., Veldurthi N., Datar S. & Bhave T. (2015). Photon assisted conducting atomic force microscopy study of nanostructured additives in P3HT: PCBM. *RSC advances* **5**(124): 102795–102802.
DOI: <https://doi.org/10.1039/C5RA20266C>
- Sun B., Zhou D., Wang C., Liu P., Hao Y., Han D., Feng L. & Zhou Y. (2017). Copper (II) chloride doped graphene oxides as efficient hole transport layer for high-performance polymer solar cells. *Organic Electronics* **44**: 176–182.
DOI: <https://doi.org/10.1016/j.orgel.2017.02.020>
- Sun Y., Seo J.H., Takacs C.J., Seifert J. & Heeger A.J. (2011). Inverted polymer solar cells integrated with a low-temperature-annealed sol-gel-derived ZnO film as an electron transport layer. *Advanced Materials* **23**(14): 1679–1683.
DOI: <https://doi.org/10.1002/adma.201004301>
- Wanninayake A.P., Gunashekar S., Li S., Church B.C. & Abu-Zahra N. (2015). Performance enhancement of polymer solar cells using copper oxide nanoparticles. *Semiconductor Science and Technology* **30**(6): 064004.
DOI: <https://doi.org/10.1088/0268-1242/30/6/064004>
- Wanwong S., Sangkhun W., Kumnorkaew P. & Wootthikanokkhan J. (2020). Improved performance of ternary solar cells by using BODIPY triads. *Materials* **13**(12): 2723.
DOI: <https://doi.org/10.3390/ma13122723>
- Wiranwetchayan O., Liang Z., Zhang Q., Cao G. & Singjai P. (2011). The role of oxide thin layer in inverted structure polymer solar cells. *Materials Sciences and Applications* **2**(12): 1697–1701.
DOI: <https://doi.org/10.4236/msa.2011.212226>
- Yang X., Loos J., Veenstra S.C., Verhees W.J., Wienk M.M., Kroon J.M., Michels M.A.J. & Janssen R.A.J. (2005). Nanoscale morphology of high-performance polymer solar cells. *Nano Letters* **5**(4): 579–583.
DOI: <https://doi.org/10.1021/nl048120i>
- Zheng B., Huo L. & Li Y. (2020). Benzodithiophenedione-based polymers: recent advances in organic photovoltaics. *NPG Asia Materials* **12**: 3.

DOI: <https://doi.org/10.1038/s41427-019-0163-5>

Zhang S., Chen Z., Xiao L., Qu B. & Gong Q. (2011). Organic solar cells with 2-Thenylmercaptan/AU self-assembly film as buffer layer. *Solar Energy Materials and Solar Cells* **95**(3): 917–920.

DOI: <https://doi.org/10.1016/j.solmat.2010.11.021>

Zhou Y., Cheun H., Potscavage Jr W.J., Fuentes-Hernandez C., Kim S.J. & Kippelen B. (2010). Inverted organic solar cells with ITO electrodes modified with an ultrathin Al₂O₃ buffer layer deposited by atomic layer deposition. *Journal of Materials Chemistry* **20**(29): 6189–6194.

DOI: <https://doi.org/10.1039/c0jm00662a>

RESEARCH ARTICLE

Marine Geology

Identification of depositional features in the Albian and Aptian sections over the hydrocarbon exploration block M2 on the Mannar Basin, Sri Lanka

TM Munasinghe¹, U Premarathne^{1*} and DA Weerasinghe²

¹ Department of Oceanography and Marine Geology, Faculty of Fisheries and Marine Sciences and Technology, University of Ruhuna, Wellamadama, Matara, Sri Lanka.

² Petroleum Resources Development Secretariat, Level 06, Ceylinco House, No. 69, Janadhipathi Mawatha, Colombo 01, Sri Lanka.

Submitted: 18 March 2022; Revised: 17 November 2022; Accepted: 25 November 2022

Abstract: The Mannar Basin extends over 45,000 km² off the western coast of Sri Lanka. It has evolved due to the multiphase rifting between Indo-Lanka landmasses during the Barremian-Paleocene time. The sediment thickness of the basin ranges from about 4 to 10 km. The northern part of the basin is a targeted area for hydrocarbon exploration in Sri Lanka. Though two natural gas discoveries were made in 2011, the basin remains a frontier due to lack of well penetration and 3D seismic coverage. As a result, the depositional features of sediment in the basin are little known. This study focuses on identifying paleo depositional features in the Albian and Aptian strata using 650 km² 3D seismic data from the Mannar Basin. Root Mean Square (RMS) amplitude was used to characterize the depositional features in three-time windows on IHS Kingdom software (v.8.3). The results show the existence of a multi-level paleo submarine fan system in the Albian and Aptian strata. They are located relatively close to the western coastline compared to the fan system in the Eocene strata. The deposition of this paleo submarine fan system has taken place in a shelf marine environment and has been influenced by relatively high sea levels during the Albian and Aptian compared to the relatively low sea levels in the Paleocene and Eocene.


Keywords: Depositional features, Mannar Basin, RMS amplitude, seismic data, Sri Lanka.

INTRODUCTION

The Mannar Basin extends over 45,000 km² off the western coast of Sri Lanka. It lies in water depths ranging from 20 m in the northern part to more than 3,000 m towards the southern part of the basin. A major portion of the basin lies in deep-water (> 400 m) depths.

The Mannar Basin is a pericratonic failed rift basin (Curry, 1984). It has evolved due to the multiphase breakup of the Gondwana (Desa *et al.*, 2006; Lal *et al.*, 2009; Gibbons *et al.*, 2013). The first phase of rifting began due to the extension between Africa and Antarctica in the Late Jurassic, while the second phase started with the breakup of East Gondwana in the Early Cretaceous (Baillie *et al.*, 2002). The basin entered into a thermal sag phase in the early Paleocene and it remains as a passive margin ever since (Baillie *et al.*, 2002; Premarathne, 2015; Premarathne *et al.*, 2016). The formation and evolution of the basin have been addressed in detail by Baillie *et al.* (2002), Lal *et al.* (2009), Premarathne *et al.* (2016), Ratheesh-Kumar *et al.* (2020), Singh & Rao (2021), Premarathne and Ranaweera (2021).

The stratigraphic thickness of the basin varies roughly from 4 to 10 km. The oldest sediment overlain by the crystalline basement is thought to be Late Jurassic in age (Premarathne *et al.*, 2016). Information on the basin's stratigraphy and tectonic history comes mainly from seismic data and hydrocarbon exploration wells. Since 1981, five exploration wells have been drilled in the Mannar Basin (well locations in Figure 1). Out of them, Dorado and Barracuda drilled in the M2 exploration block in the Mannar Basin in 2011, penetrated natural gas-bearing sandstones in Maastrichtian and Campanian strata, respectively (Figure 2B and 2C). This finding confirmed the occurrence of an active petroleum system in the basin. Campanian sandstone penetrated by the Dorado-North well, which was drilled 2.5 km north of Dorado, has higher porosity (~20%) indicating very good

* Corresponding author (premarat@yahoo.com;  <https://orcid.org/0000-0003-4934-1618>)



This article is published under the Creative Commons CC-BY-ND License (<http://creativecommons.org/licenses/by-nd/4.0/>). This license permits use, distribution and reproduction, commercial and non-commercial, provided that the original work is properly cited and is not changed in anyway.

reservoir potential (Bandara & Premarathne, 2021). The last well, named Wallago drilled in the M2 block in 2013 ended up as a dry hole. The Petroleum system of the basin has been addressed in detail by Premarathne *et al.* (2015), and Galushkin & Dubinin (2020).

Albian and older sediment have not been penetrated by hydrocarbon exploration wells drilled so far in the Mannar Basin in Sri Lanka (Premarathne, 2015). However, some wells drilled in the Indian portion of the Mannar Basin and the Cauvery Basin, both on the Sri Lankan and Indian sides, have penetrated the Albian section (Rao *et al.*, 2010; Premarathne, 2015). Recent to Late Cretaceous stratigraphy in the northern part of the Cauvery and Mannar Basins have been addressed in detail by Premarathne (2015), and Premarathne *et al.* (2016), respectively.

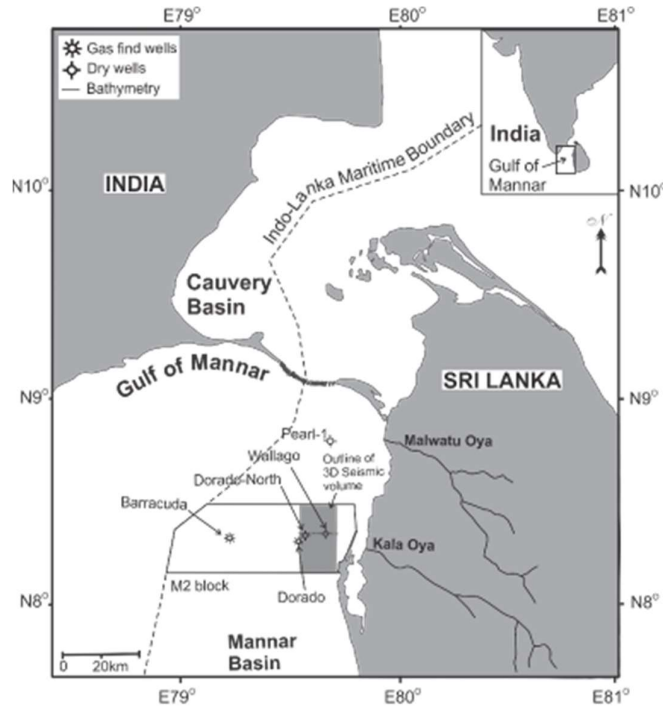


Figure 1: Locations of exploration wells and the 3D seismic coverage over the M2 block in the Mannar Basin (modified after Dushyendra *et al.*, 2022). Dashed line across the 3D seismic coverage (gray color rectangle) shows the location of the seismic profile in Figure 3.

The formation of hydrocarbon reservoirs and seals in a shelf marine environment, among other factors, depends on sea-level changes (Bjørlykke, 2010; Miller *et al.*, 2011). Ramkumar *et al.* (2011) discuss the Barremian–Danian sea level changes in the Indian portion of the Cauvery Basin. However, there is only a handful of studies on the relation between the relative sea level changes and depositional features in these stratigraphic intervals on the Sri Lankan side of the Cauvery and Mannar Basins due to the lack of well penetration and 3D seismic coverage. Among them, Dushyendra *et al.* (2022) discuss the depositional features in the Eocene and Paleocene sections in the M2 block (Figure 1) in the Mannar Basin, while Bandara *et al.* (2019) discuss that in sandstones intercalated with igneous rocks (Figure 2D) in the same block. Reuter *et al.* (2021) discuss the role of sea-level and climate changes in the assembly of Sri Lankan biodiversity using Miocene limestone in Sri Lanka. The objectives of this study were to identify the depositional features in the Albian and Aptian sections close to the coastal line under the M2 exploration block and then to compare them with the depositional features interpreted in the Paleocene and Eocene sediments in the M2 block by Dushyendra *et al.* (2022). This information will be useful to understand the change in the relative sea level and the deposition of reservoir facies in shelf marine environment in the Mannar Basin.

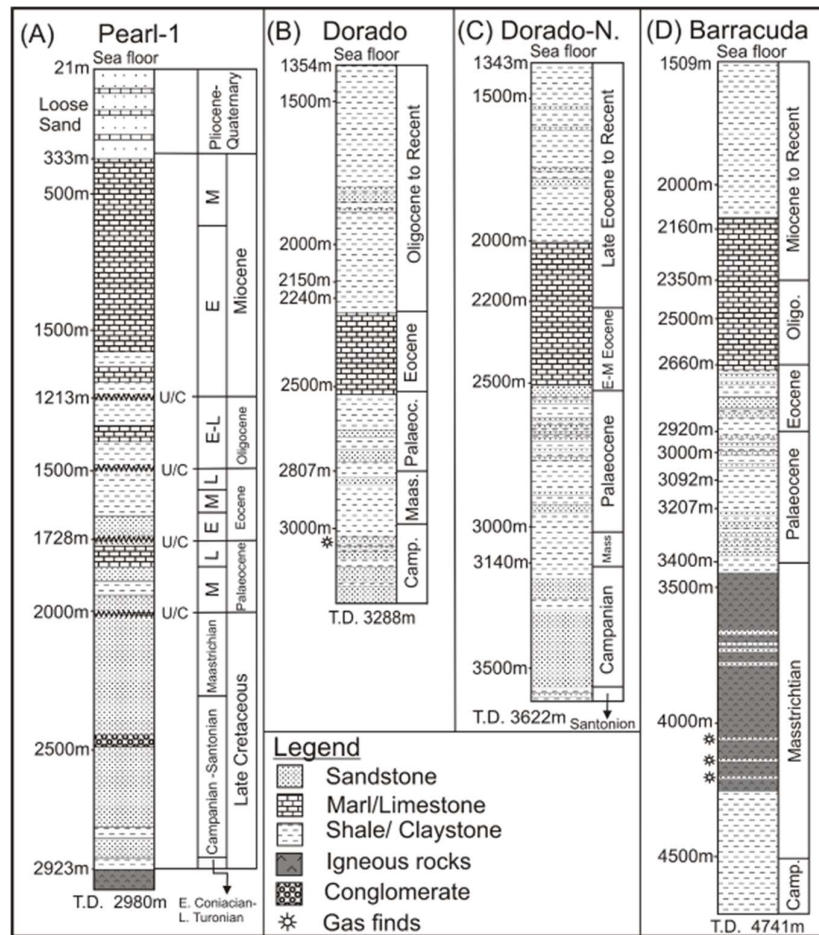


Figure 2: Generalised stratigraphic sections of the wells (a) Pearl-1; (b) Dorado; (c) Dorado-North and (d) Barracuda (modified after Premarathne *et al.*, 2015). Oligo. = Oligocene; Palaeoc. = Palaeocene; Maas. = Maastrichtian; Camp. = Campanian; E = Early; M = Middle; L = Late; U/C = unconformity; T.D. = total depth

MATERIALS AND METHODS

Data, software and hardware

650 km² of post-stacked time migrated three dimensional (3D) seismic data, acquired over the M2 exploration block in the Mannar Basin (Figure 1) were obtained from the Petroleum Resources Development Secretariat of Sri Lanka (PRDS), the regulator of Sri Lanka’s upstream petroleum industry. IHS Kingdom Suite (v. 8.3), on a workstation at the PRDS, was used for data analysis and interpretation. Some data from unpublished reports held at PRDS were also used for this study.

Because of the relatively thick (> 700 m) section of basalts interbedded with Maastrichtian sediments (Premarathne & Ranaweera, 2021) (Figure 2D), the quality of seismic data acquired and processed in 2012 was not clear below the Paleocene level. Therefore, the original data set has been broadband reprocessed in 2015. The reprocessing has significantly improved the seismic data compared to the previous data set due to the low frequency boost up and the reduction of high frequency random noise. This has improved the continuity of reflectors below basalts, offering better quality and greater interpretation confidence. Also, reprocessing helps in the identification of broad reservoir heterogeneities but has not improved the fault geometry significantly.

Data interpretation

In this study, three reflectors corresponding to the boundaries between the Early and Late Cretaceous (Albian Top), Albian and Aptian (Aptian top), and the crystalline basement (Basement) were interpreted using their seismic continuity and seismic to well correlation (Figure 3). Albian and Aptian top horizons were picked based on well correlation. In addition, three more horizons, one 60 ms below the Albian top horizon, and two, 120 ms and 450 ms below the Aptian top horizon were interpreted (seismic profiles in Figures 4, 5, 6 and 7). Lateral continuity and terminations of the reflectors were interpreted using on laps, down laps, top laps, and truncations.

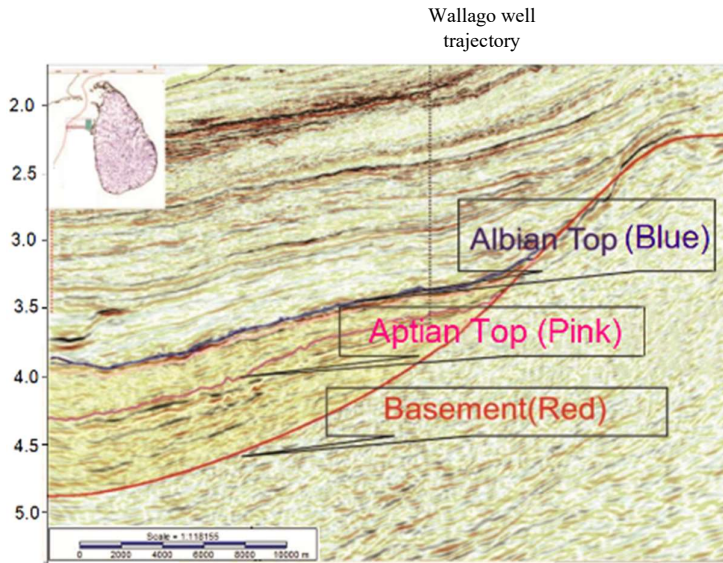


Figure 3: An E-W regional seismic profile (dashed line crossing the seismic coverage shown in Figure 1) showing the interpreted horizons.

Seismic attributes

The Root Mean Square (RMS) amplitude (Kenney & Keeping, 1962) (equation 1) was used in this study. It is a commonly used physical attribute calculated for a particular time window of stacked data. It demarcates the boundaries between different facies type and depositional environments. One of the weaknesses of the RMS amplitude attribute is that it is sensitive to noise as it squares every value within the time window. IHS Kingdom Suite was used to calculate the RMS amplitude.

$$xRMS = \sqrt{\frac{1}{n} \sum_{i=1}^n x_i^2} \quad \dots(1)$$

Where, xRMS is Root Mean Square amplitude and *n* is number of amplitudes, *x*₁, *x*₂, *x*₃..... *x*_{*n*}.

RMS amplitude was calculated for three time windows, a 60 ms window in the Albian section starting from the Albian top horizon and a 120 ms and 450 ms time windows in the stratigraphic interval below the Aptian top horizon (Figure 4). These intervals were denoted as +0.06 Albian Top (+0.06 ALT), +0.12 Aptian Top (+0.12 APT), and +0.45 Aptian Top (+0.45 APT), respectively. The positive (+) sign indicates that the time intervals are located below the Albian or Aptian top horizons.

RMS amplitude data from the three time windows were converted to RMS amplitude maps using the IHS Kingdom software. They were used to interpret depositional features in the time window. The same notation that refers to each time interval was used to refer to the RMS amplitude maps generated for the respective time intervals.

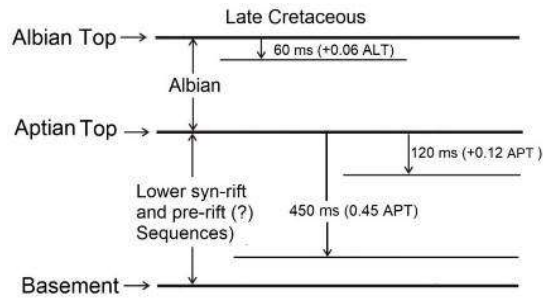


Figure 4: Relative positioning of the six (6) horizons interpreted and three time windows used to calculate RMS amplitude and create RMS amplitude maps (not to scale).

RESULTS AND DISCUSSION

Interpretation of horizons

Albian and Aptian top horizons appear as bright and continuous reflectors that could be easily mapped throughout the 3D seismic volume (Figure 3). They can be interpreted as a high amplitude, and acoustically hard (peak) events.

Depositional marine environments can be classified as shoreface/nearshore, shelf, and slope environments with increasing inferred paleo-water depths (Sahoo *et al.*, 2014). In seismic data, shelfal sandstones are characterized by moderate to high amplitude and continuous reflectors (Sahoo *et al.*, 2014). Accordingly, it can be thought that the top part of the Albian and Aptian stratigraphic sections have been deposited in a shelfal marine environment and they could be rich in sandstone. Albian sediments penetrated by most exploration wells drilled on the Sri Lankan side of the Cauvery Basin is bounded on top by an unconformity (Premarathne *et al.*, 2015). However, such information is not available for the Albian strata in the Sri Lankan portion of the Mannar Basin since no well has reached this stratigraphic interval.

Below the Albian section exist the bottom-most syn-rift sediment and probably pre-rift sediment overlain by the crystalline basement. Premarathne *et al.* (2016) think that the oldest sediment overlain by the crystalline basement could be Late Jurassic in age. The maximum thickness of the stratigraphic section below the Aptian top in the study areas is around 550 ms (Figure 3).

The crystalline basement (below the red line in Figure 3), is composed of metamorphic rocks. It is characterized by variable amplitude reflections, with poor to low continuity. The interpreted sedimentary sequence wedges towards the east and abuts against the basement creating a three-way closure (Figure 3).

Interpretation of RMS amplitude maps

Relatively high amplitudes areas (bright spots) on seismic profiles appear in red and yellow colours in RMS amplitude maps, while relatively low amplitude areas appear in green and blue colours (+0.06 ALT, +0.12 APT, and +0.45 APT in Figures 5, 6, and 7, respectively). Note that the three RMS amplitude maps are not colour-normalized because each map required different colour intensities to highlight the depositional features appearing in them. The dark/ black coloured areas on the right in each RMS amplitude map indicate that respective reflectors do not extend to that area. The interface between coloured and dark coloured areas indicates the margin where each reflector terminates (truncations) against the crystalline basement.

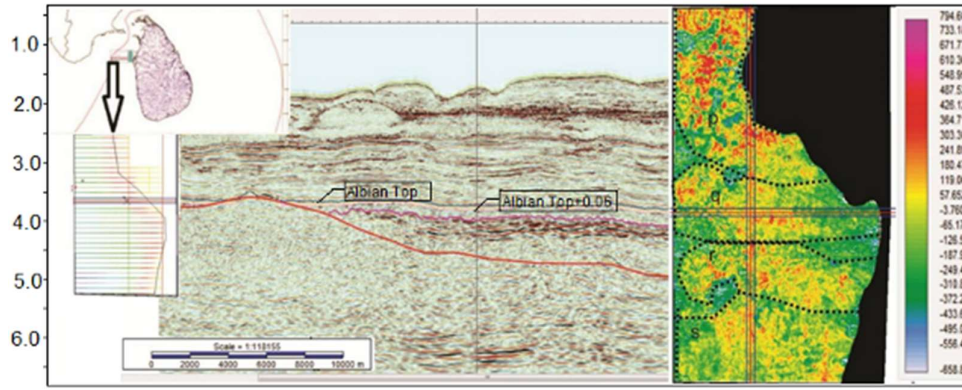


Figure 5: +0.06 ALT RMS amplitude map. p, q, r, and v, indicate the paleo submarine fan system. The seismic profile on the left side indicates the interpreted Albian top and +0.06 ALT horizons in peach and pink colours, respectively.

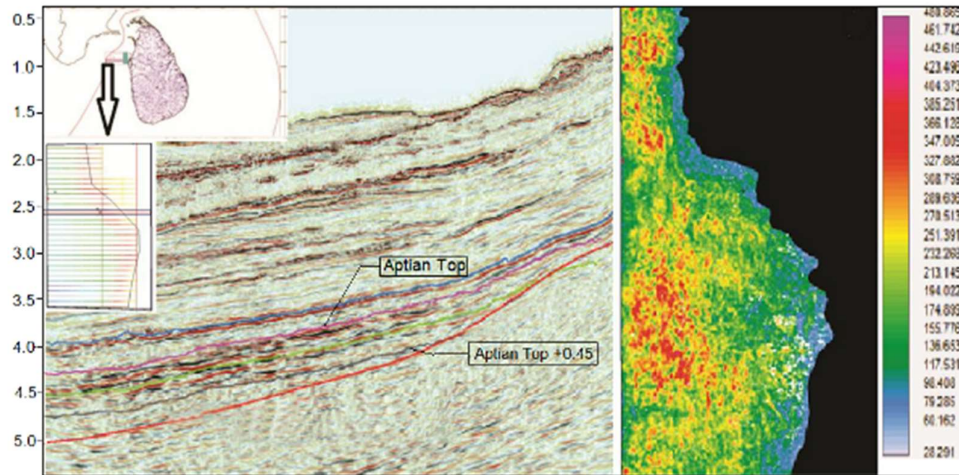


Figure 6: +0.12 APT RMS amplitude map. t, u, and v, indicate the paleo submarine fan system. The seismic profile on the left side indicates the interpreted Aptian top and +0.12 APT horizons in pink and peach colours, respectively.

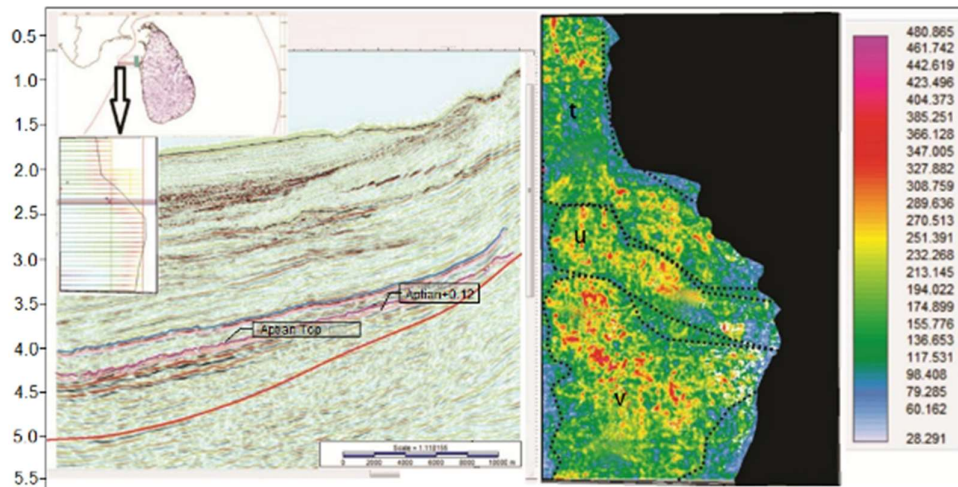


Figure 7: +0.45 APT RMS Amplitude map. The seismic profile on the left side indicates the interpreted Aptian top (pink) and +0.45 APT horizons in pink and gray colours, respectively.

However, such a distinct depositional feature cannot be related to the +0.45 APT RMS amplitude map, though it has a relatively high amplitude areas at its center. The time interval used to calculate the RMS amplitude in the +0.45 APT map is much larger compared to the other two time windows. This interval has considered the amplitude data in a 450 ms time window where the maximum thickness of the sediment package between the Aptian top horizon and the crystalline basement is about 550 ms (see Figure 3). Therefore, the +0.45 APT RMS amplitude map includes RMS amplitude data from almost the entire stratigraphic section.

John *et al.* (2010) think that the relatively high amplitude zones in RMS amplitude maps could be due to higher acoustic impedance contrast generated by the intercalation of sand and clay/silt. However, a higher acoustic impedance contrast can be generated by the intercalation of other lithologies and their pore fluids.

Interpretation with previous work

Dushyendra *et al.* (2022) have interpreted the depositional features in the Eocene and Paleocene sections in the M2 block using the same seismic attribute used in this study, but on a much larger seismic coverage (1850 km²). Their study has unraveled the existence of a multi-level Eocene and Paleocene submarine fan system emerging from the west coast of Sri Lanka and a northeast-southwest trending deep water channel system in the Eocene section (Figures 8 and 9). The Eocene fan systems are located relatively distant (~18 km) from the coastline (Figure 8), while the Albian and Aptian fan systems interpreted in this study occur relatively closer to the coastline (Figures 5, 6, and 9). Such a distinct fan system is not visible in the Paleocene (Figure 9).

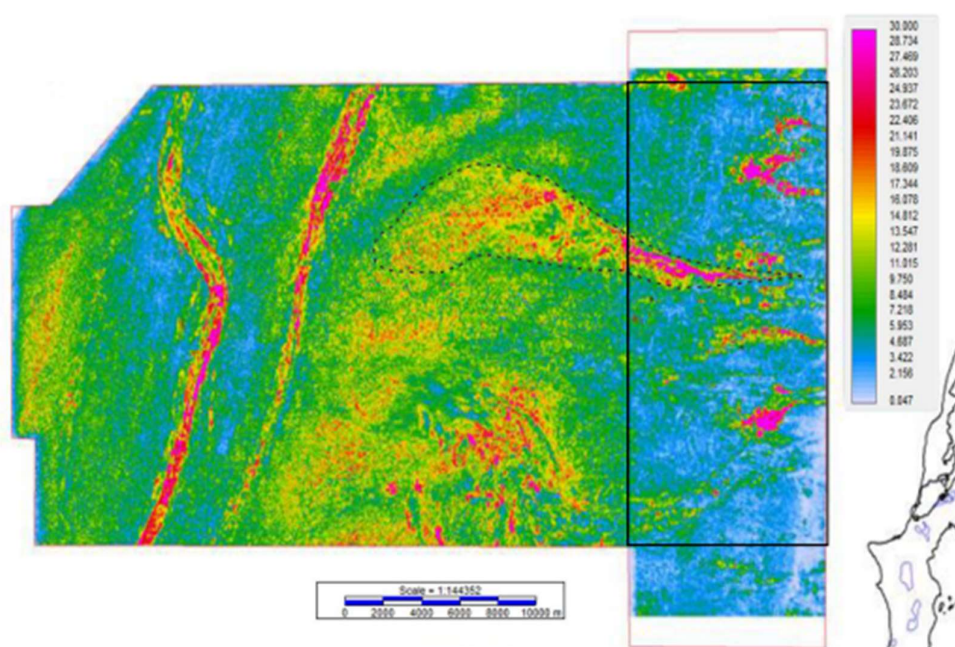


Figure 8: RMS Amplitude map showing submarine fan and channel systems in the Eocene section. RMS Amplitude has been calculated for a 50 millisecond time interval between the Paleocene-Eocene reflector and a horizon 50 milliseconds above it (after Dushyendra *et al.*, 2022). The rectangle indicates the seismic data coverage of this study.

The rate of sedimentation on continents and their margins are controlled by the relative sea level, which results from the combined effect of eustatic sea-level and tectonic subsidence or upliftment (Miller *et al.*, 2011). Eustatic sea levels in the Cretaceous are relatively higher compared to that in the Paleocene and Eocene (Vail *et al.*, 1977; Haq *et al.*, 1987; Kominz *et al.*, 2008). The Collision of the Indian and Eurasian tectonic plates in the Early Eocene created regional upliftment and the Himalayan orogeny (Torsvik *et al.*, 2002). As a result, an erosional unconformity in the Eocene section can be observed in many of the hydrocarbon exploration wells drilled in the Cauvery and Mannar Basin (Sasthri *et al.*, 1981; Premarathne, 2015; Premarathne *et al.*, 2016). Based on these

observations, it could be thought that there had been high relative sea levels in the Mannar Basin in the Albian and Aptian compared to that during the Eocene, which agrees well with the Paleo submarine fan system located distant to the coastline in the Eocene compared to the Albian and Aptian.

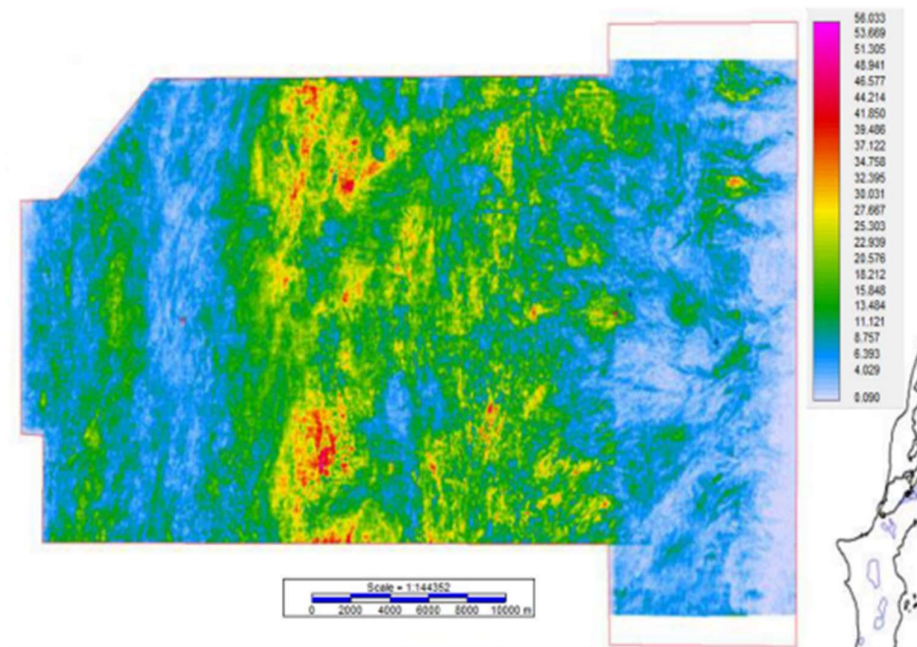


Figure 9: RMS Amplitude map showing submarine fan and channel systems in the Paleocene section. RMS Amplitude has been calculated for a 100 millisecond time interval between the Cretaceous-Paleocene reflector and a horizon 100 milliseconds above it (after Dushyendra *et al.*, 2022).

The absence of a fans system in the Paleocene could be related to the low sea levels, sediment starvation or the presence of an erosional unconformity. Around 500 m thick Paleocene stratigraphic section in the Dorado-North and Barracuda wells (Figures 2C and 2D) rules out the notion of sediment starvation. However, the relatively thin Paleocene stratigraphic interval bounded on top by an unconformity (Paleocene Eocene boundary) is seen in the stratigraphic section of the Pearl-1 well (Figure 2A). Baillie *et al.* (2002) are of the opinion that the rifting between indo-Lanka landmasses, which ceased at the end of the Cretaceous period, created regional upliftment. This is enunciated as an unconformity in some regional wells (e.g. Figure 2A). On the other hand, the relative sea level curve that Ramkumar *et al.* (2004) developed for the Barremian-Danian strata of the Cauvery Basin indicates relatively high sea levels in the Albian and Aptian compared to that in the Danian. Hence the absence of Paleocene submarine fan system could be related to the non-deposition and/or erosion due to low relative sea levels.

CONCLUSIONS

A distinct paleo submarine fan system and a distributary channel system in between the fans occur in the Albian and Aptian close to the western coastline under the M2 exploration block in the Mannar Basin, Sri Lanka. They have been deposited in a shelf marine environment. The formation of these fans has been influenced by the sea level, which was relatively high during the Albian and Aptian compared to the Paleocene and Eocene.

Acknowledgements

Authors are thankful to Mr. Saliaya Wickramasooriya, former Director General of the Petroleum Resources Development Secretariat (PRDS), for providing seismic data and data interpretation facility, Mrs. Preeni Withanage, Director (Benefits), and other staff of the PRDS for numerous support and words of encouragement.

REFERENCES

- Baillie P., Shaw R., Liyanaarachi D. & Jayaratne M. (2002). A New Mesozoic sedimentary Basin, Offshore Sri Lanka. *Proceedings of the EAGA 64th Conference & Exhibition*, 27–30 May. Florence, Italy.
- Bandara W.G.S.S., Weerasinghe D. & Premarathne U. (2019). Distribution of sandstones in between igneous rocks in the M2 block of the Mannar Basin, offshore Sri Lanka, based on seismic attribute analysis. *Proceedings of the 35th annual technical sessions of Geological Society of Sri Lanka*, Kandy, Sri Lanka, pp 3.
- Bandara M. & Premarathne U. (2021). Reservoir potential of the Campanian sandstone in the Dorado-North well on the Mannar Basin, offshore Sri Lanka. *Journal of the Geological Society of Sri Lanka* **22**(2): 27–37.
DOI: <https://doi.org/10.4038/jgssl.v22i2.72>
- Bjørlykke K. (2010). *Petroleum Geoscience: From Sedimentary Environments to Rock Physics*, pp. 507. Springer Science and Business Media, Inc., New York, USA.
DOI: <https://doi.org/10.1007/978-3-642-02332-3>
- Curray J.R. (1984). Sri Lanka: is it a Mid-Plate Platelet? *Journal of NARA* **31**: 30–50.
- Desa M., Ramana M.V. & Ramprasad T. (2006). Seafloor spreading magnetic anomalies south off Sri Lanka. *Marine Geology* **229** (3–4): 227–240.
DOI: <https://doi.org/10.1016/j.margeo.2006.03.006>
- Dushyendra A., Premarathne U. & Weerasinghe D. (2022). Revelation of depositional features in the Paleocene and Eocene in the Mannar basin using amplitude analysis of a 3D data set. *International Journal of Oil, Gas and Coal Technology* **31**(01): 38–50.
DOI: <https://doi.org/10.1504/IJOGCT.2022.10047417>
- Galushkin Y.I. & Dubinin E.P. (2020). Thermal history and extension of the lithosphere in the Mannar Basin and realization its hydrocarbon potential, offshore Sri Lanka. *Marine and Petroleum Geology* **119**: 104477.
DOI: <https://doi.org/10.1016/j.marpetgeo.2020.104477>
- Gibbons A.D., Whittaker J.M. & Müller R.D. (2013). The breakup of East Gondwana: Assimilating constraints from Cretaceous ocean basins around India into a best-fit tectonic model. *Journal of Geophysical Research: Solid Earth* **118**: 808–822.
DOI: <https://doi.org/10.1002/jgrb.50079>
- Haq B.U., Hardenbol J. & Vail P.R. (1987). Chronology of fluctuating sea levels since the Triassic (250 Ma ago to present). *Science* **235**: 1156–1167.
DOI: <https://doi.org/10.1126/science.235.4793.1156>
- John R.O., Adujo A.A. & Taiwo A.O. (2010). Applications of 3-D structural interpretation and seismic attribute analysis to hydrocarbon prospecting over X-Field, Niger-Delta. *International Journal of Basic and Applied Sciences* **10**: 28–40.
DOI: <https://doi.org/10.1007/s12517-017-3078-x>
- Kenney J.F. & Keeping E.S. (1962). Root mean square. In: *Mathematics of Statistics*, 3rd edition, pp. 59–60. D. Van Nostrand Co., Princeton, USA.
- Kominz M., Browning J.V., Miller K.G., Sugarman P.J., Mizintseva S. & Scotese C.A. (2008). Late Cretaceous to Miocene sea-level estimates from the New Jersey and Delaware coastal plain coreholes: an error analysis. *Basin Research* **20**(2): 211–226.
DOI: <https://doi.org/10.1111/j.1365-2117.2008.00354.x>
- Lal N.K., Siawal A. & Kaul A.K. (2009). Evolution of East Coast of India—a plate tectonic reconstruction. *Journal of Geological Society of India* **73**: 249–260.
DOI: <https://doi.org/10.1007/s12594-009-0081-1>
- Miller K., Mountain G., Wright J. & Browning J. (2011). A 180-million-year record of sea level and ice volume variations from continental margin and deep-sea isotopic records. *Oceanography* **24**(2): 40–53.
DOI: <https://doi.org/10.5670/oceanog.2011.26>
- Premarathne U., Suzuki N. & Ratnayake N.P. (2015). Modelling of hydrocarbon generation, migration and accumulation in the northern part of the Mannar Basin, offshore Sri Lanka. *Journal of Geological Society of Sri Lanka* **17**: 139–158.
- Premarathne U. (2015). Petroleum Potential of the Cauvery Basin, Sri Lanka. *Journal of the Geological Society of Sri Lanka* **17**: 41–52.
- Premarathne U., Suzuki N., Ratnayake N.P. & Kularathne C.W. (2016). Burial and thermal history modelling of the Mannar Basin, Offshore Sri Lanka. *Journal of Petroleum Geology* **39**(2): 193–214.
DOI: <https://doi.org/10.1111/jpg.12640>
- Premarathne U. & Ranaweera L.V. (2021). Contemporaneous Deccan type continental flood basalt magmatism in the Mannar Basin, offshore Sri Lanka. *Island Arc Journal* **31**(1): e12409.
DOI: <https://doi.org/10.1111/iar.12409>
- Ramkumar M., Stüben D. & Berner Z. (2011). Barremian–Danian chemostratigraphic sequences of the Cauvery Basin, India: Implications on scales of stratigraphic correlation. *Gondwana Research* **19**(1): 291–309.
DOI: <https://doi.org/10.1016/j.gr.2010.05.014>
- Rao M.V., Chidambaram L., Bharktya D. & Janardhanan M. (2010). Integrated analysis of Late Albian to Middle Miocene sediments in Gulf of Mannar shallow waters of the Cauvery Basin, India: A sequence stratigraphic approach.

- Proceedings of the 8th Biennial International Conference and Exposition on Petroleum Geophysics*, 1–3 February, Hyderabad, India.
- Ratheesh-Kumar R.T., Dharmapriya P.L., Windley B.F., Xiao W.J. & Jeevan U. (2020). The tectonic 'Umbilical Cord' linking India and Sri Lanka, and the tale of their failed rift. *Journal of Geophysical Research: Solid Earth* **125**(5): e2019JB018225.
DOI: <https://doi.org/10.1029/2019JB018225>
- Reuter M., Harzhauser M. & Piller W.E. (2021). The role of sea level and climate changes in the assembly of Sri Lankan biodiversity: A perspective from the Miocene Jaffna Limestone. *Gondwana Research* **91**: 152–165.
DOI: <https://doi.org/10.1016/j.gr.2020.12.014>
- Sahoo T.R., Browne G.H. & Hill M.G. (2014). Seismic attribute analysis and depositional elements in the Canterbury Basin. *Proceedings of the Geotechnical Petroleum Forum*, Wellington, New Zealand.
- Sastri V.V., Venkatachala S.B.S. & Narayananthe V. (1981). Evolution of the east coast of India. *Palaeogeography, Palaeoclimatology, Palaeoecology* **36**: 23–54.
DOI: [https://doi.org/10.1016/0031-0182\(81\)90047-X](https://doi.org/10.1016/0031-0182(81)90047-X)
- Singh A. & Rao G.S. (2021). Crustal structure and subsidence history of the Mannar basin through potential field modelling and backstripping analysis: Implications on basin evolution and hydrocarbon exploration. *Journal of Petroleum Science and Engineering* **206**: 1090000.
DOI: <https://doi.org/10.1016/j.petrol.2021.109000>
- Torsvik T.H., Carlos D., Mosar M., Cocks L.R.M. & Malme T. (2002). Global reconstructions and North Atlantic paleogeography 440 Ma to recent. In: *Batlas-Mid Norway Plate Reconstruction Atlas with Global and Atlantic Perspective* (ed. E.A. Eide), pp. 18–39. Geological Survey of Norway, Trondheim, Norway.
- Vail P.R., Mitchum R.M. Jr., Todd R.G., Widmier J.M., Thompson S., Sangree J.B., Bubb J.N. & Hatlelid W.G. (1977). Seismic stratigraphy and global changes of sea level. In: *Seismic Stratigraphy-Application to Hydrocarbon Exploration, AAPG Memoir 26* (ed. C.E. Payton), pp. 49 – 212.

RESEARCH ARTICLE

Agriculture and Food Science

Study on compositional changes of king coconut (*Cocos nucifera* var. *aurantiaca*) water and kernel during maturation and evaluation of optimum quality characteristics targeting commercial applications

MD Jayasinghe*, MMNP Gunasekara, MGDS Perera, KDSM Karunarathna, GU Chandrasiri and IGN Hewajulige

Industrial Technology Institute (ITI), 363, Bauddhaloka Mawatha, Colombo 07, Sri Lanka.

Submitted: 21 March 2022; Revised: 05 October 2022; Accepted: 25 November 2022


Abstract: King coconut (*Cocos nucifera* var. *aurantiaca*) is a tropical nut with notable nutritional and medicinal values. King coconut water (KCW) and king coconut kernel (KCK) are sweet and refreshing. They undergo several changes during maturation. The objective of this study was to assess the physico-chemical changes of KCW and KCK with maturity. Three different maturity stages (6, 7, and 8 months) of the variety *aurantica*, known locally as 'Nawasi Thembili' were studied for several physico-chemical parameters. Whole nut weight (g), nut-circumference (cm), colour (water/kernel) (*L), nut-water volume (mL), kernel weight (g), and kernel thickness (mm) were assessed as physical parameters, while pH, total soluble solids (°Brix), titratable acidity (as % ascorbic acid), total sugars (g/100g; g/100mL), and minerals (mg/L; mg/kg) were analysed as chemical attributes. Sugars were estimated using Agilent 1260 HPLC and ICP-MS was used to measure the mineral profile. Results revealed that all the tested physical parameters of KCW and KCK increased significantly ($p < 0.05$) with maturity. The pH, TSS, total sugars, and acidity of KCW increased significantly ($p < 0.05$), while mineral content decreased significantly ($p < 0.05$) with maturity. However, the TSS and minerals of KCK decreased significantly ($p < 0.05$) with maturity and a higher sucrose content was reported in KCK compared to KCW at later maturity. The Ca^{+2} and Mg^{+2} were prominent in both KCW and KCK. The study concluded that the physico-chemical characteristics varied widely with the maturity of king coconuts. The selection of optimum harvest maturity to match the preferred attributes of intended applications is suggested.

Keywords: Harvest maturity, kernel, king coconut water, physico-chemical changes.

INTRODUCTION

King coconut (*Cocos nucifera* var. *aurantiaca*) is a tropical nut that belongs to the Family Arecaceae. It is endemic to Sri Lanka with unique flavour characteristics compared to green coconut. King coconut cultivation in Sri Lanka has been estimated as 2.20 million palms (Department of Census and Statistics, 2005), and has contributed Rs. 600 Mn of foreign exchange in 2020 (CDA, 2020). The nut consists of four distinct parts; exocarp (outermost skin), mesocarp (middle fibrous part), endocarp (hard-shell), and endosperm (water and kernel), where the endosperm is extensively used in industrial applications (Prades *et al.*, 2012a). The nut develops through the nuclear, cellular, and helobial stages; the endosperm is developed at the nuclear stage, while the embryo cavity is liquid-filled by the 'Cellularization Process' (Lopes & Larkins, 1993). Several compositional changes take place within the nut during maturation with distinct quality attributes at each harvesting stage (Yong *et al.*, 2009).

The king coconut water (liquid endosperm) and kernel are considered as the main edible parts, which possess a high economic value. King coconut water is a popular functional beverage with nutritional properties such as moderate concentrations of sugars, vitamins, minerals, and amino acids with therapeutic values (DebMandal & Mandal, 2011). The kernel is a delicate spongy material, which offers versatile market potential arising from claims on antioxidants and plant growth hormonal properties. However, it is evident that king coconut kernel is underutilized while king coconut water is extensively used for commercial scale productions such as bottled/packed king coconut water mainly for the export market (Perera *et al.*, 2015). Therefore, king coconut

* Corresponding author (maheshika@iti.lk.com;  <https://orcid.org/0000-0003-1162-6132>)



This article is published under the Creative Commons CC-BY-ND License (<http://creativecommons.org/licenses/by-nd/4.0/>). This license permits use, distribution and reproduction, commercial and non-commercial, provided that the original work is properly cited and is not changed in anyway.

kernel needs attention to identify potential opportunities for further commercialization (Kalina & Navaratne, 2018).

In terms of distribution, king coconut palms are mainly concentrated in the Gampaha, Kalutara, Kurunegala, and Galle districts, commonly in home gardens. King coconuts are mainly characterized by the orange-coloured pericarp compared with green coconuts. The major king coconut varieties are categorized as 'Typica' known locally as (*Ran Thembili*, *Gon Thembili*) and 'Aurantiaca' known locally as (*Nawasi Thembili*, *Rathran Thembili*, *Bothal Thembili*). The Aurantiaca varieties have been widely utilized as a beverage due to its higher nut water yield and sweet taste (Perera et al., 2014). '*Nawasi Thembili*' is the commonly grown king coconut variety in Sri Lanka and the availability of '*Rathran Thembili*' (characteristic pink coloured epicarp) and '*Bothal Thembili*' (bottle shaped nuts) are comparatively low (Ekanayake et al., 2010). Therefore, '*Nawasi Thembili*' is widely used for commercial scale productions due to its higher availability along with optimum quality characteristics (Perera et al., 2015).

A wide range of commercial applications such as fresh nut exports, bottled king coconut water, and kernel-incorporated functional beverages and confectionaries have raised a critical requirement of evaluating optimum quality characteristics of king coconuts based on maturity (EDB, 2019). It is demanded by the local industrialists with the aim of marketing the 'authentic' taste of Sri Lankan king coconuts as well as maintaining their product consistency within batches. Therefore, it is important to study the exact patterns of variations with maturity and to match optimum quality characteristics of edible king coconut components compatible with intended uses. Since, very limited research data is available on the nutritional and functional properties of king coconut water and kernel, it is vital to conduct comprehensive scientific research studies, for a better understanding. Therefore, this research study aimed to evaluate the compositional changes of king coconut water and kernel in relation to maturity as an effective approach to identify the optimum harvesting stage for specific industrial applications.

MATERIALS AND METHODS

Sample collection and preparation

A total of 60 nuts (n=20, 5 palms) were harvested of the variety '*Nawasi Thembili*' from a commercial king coconut cultivation in the Western Province, Sri Lanka at three maturity stages (6, 7, and 8 months after nut set) based on the 'Leaf Counting Method' recommended by the Coconut Research Institute (CRI), Sri Lanka. The three specific maturity stages were selected targeting industrial applications based on the preliminary research data and the 'Maturity Charts' developed by the Industrial Technology Institute (ITI), Sri Lanka. Based on the CRI guidelines, the 7 months old bunch was selected at the 14th leaf counted from the uppermost tender leaf of the tree, and bunches of 6 months and 8 months maturity were selected as bunches at the 13th leaf and 15th leaf, respectively (Ranasinghe & Wimalasekara, 2002). Bunches were immediately transported to the post-harvest technology laboratory of the ITI, Sri Lanka.

Each nut was split using a curved knife, in the laboratory to remove the king coconut water. The water was filtered through a muslin cloth into a clean plastic container. The soft, spongy coconut kernel was scooped out using a spoon from the nutshell avoiding excessive scraping. The mature kernel was cut into small pieces using a sharp stainless-steel knife and ground using mortar and pestle. The king coconut water and kernel samples at each maturity stage were composited separately into sealed containers, and stored at 4 ± 0.1 °C for further analysis.

Physico-chemical analyses

Physical parameters

Whole nut circumference, whole nut weight, nut water volume, kernel weight, kernel thickness, colour of king coconut water, and kernel were measured as physical parameters. The whole nut circumference was measured at the maximum girth of the individual nut using a measuring tape and all weights and water volumes were measured using a calibrated top loading balance and measuring cylinder, respectively. The thickness of the kernel was measured using a digital vernier caliper (MITUTOYO, 500-197-20, Japan). Colour was measured using the CIE Lab Space method (KONICA MINOLTA CR-410, Japan) and expressed as Lightness (*L value) (Brainard,

2003). As chemical parameters, pH was measured using a calibrated pH meter (EUTECH pH 510 Model, USA) at 25 °C, and TSS was measured using a hand-held refractometer (Atago, S-28, Japan). The pH of king coconut kernels was measured with a solution of 10 g of sample blended with 50 mL of distilled water. The TSS content was measured via extracting the juice out of the kernel by pressing using a cotton wool/cloth. Titratable acidity of the king coconut kernel estimated by the standard method using 0.1M NaOH with phenolphthalein indicator (ISO 750:998).

Analyses of total sugar content

Total sugar content was measured according to a modified method of ISO 10504 (2013); ‘Starch derivatives - Determination of the composition of glucose syrups, fructose syrups and hydrogenated glucose syrups’ using HPLC chromatographic system equipped with quaternary gradient pump and Refractive Index Detector (Agilent 1260 Infinity, USA). In this study, Hydrogen (H⁺) based cation exchange HPLC column was used as the modification, instead of using Calcium (Ca²⁺) column as depicted in the standard. The modified method was optimized by an in-house accredited laboratory at ITI, Sri Lanka, and validated for linearity, sensitivity, and selectivity parameters. Chromatographic separation was achieved on an analytical column/stationary phase (7.8 mm × 300 mm, 5 µm) (Phenomenex, Rezex ROA Organic Acid H⁺ 8%, USA), and a guard column (4.6 mm × 12.5 mm, 5 µm) (Phenomenex, Rezex, USA). The mobile phase was 0.005N H₂SO₄ with a flow rate of 0.4 mL/min for the analysis. Samples were micro-filtered (0.45 µm) and a volume of 10.0 µL was injected into an auto-sampler with a total run time of 30 min.

Analytical grade reagents (≥ 99% purity) of glucose, fructose, and sucrose (Sigma Aldrich, USA) were used to prepare the standard sugar solutions to generate a multi-point calibration curve for the quantification of sugars in the sample. Peaks were identified as Retention Time (R_T), as shown by the respective peaks of standard sugar solutions and quantified as area under the curve using a programmed software (OpenLab CDS, ChemStation Edition C.01.09) coupled with HPLC. The total sugar content of king coconut water and kernel was expressed as g/100 mL and g/100g on wet basis, respectively.

Analyses of mineral content

The mineral content (K⁺, Na⁺, Mg⁺², Ca⁺², and Fe⁺²) was measured using an Inductively Coupled Plasma Mass Spectrometer (ICP-MS) (Agilent 7900, Japan) based on the method described in Marasinghe *et al.* (2019). Approximately 10 mL of king coconut water and 1 g of king coconut kernel were digested separately at 180 °C for 30 min, using a microwave digester (MAS 5, CEM, USA) with added 10 mL of ultra-pure > 69% nitric acid. Digested king coconut water and kernel were filtered using Whatman No. 542 filter paper and diluted using deionized water up to 25 mL and 50 mL, respectively prior to mineral analysis. Mineral concentrations of digested and blank samples were analysed under standard operating conditions of ICP-MS.

Proximate analyses

King coconuts at 7 months of maturity, were used for proximate analysis covering both king coconut water and kernel according to standard AOAC analytical methods as follows. Moisture AOAC 2012 (934.01), Crude Protein AOAC 2012 (2001.11), Crude Fat AOAC 2012 (2003.05), Total Ash AOAC 2012 (942.05), Crude Fiber: AOAC 2012 (978.10). All reagents were analytical grade chemicals (Sigma Aldrich, USA).

Sensory analyses

The king coconut water and kernel samples at three different maturities were tested for quality attributes comprised of colour, flavour, taste (sweetness), texture (softness), and overall acceptance. Ten trained panellists from the ITI, Sri Lanka, scored the samples using a 7-point hedonic scale (1- Strongly Dislike, 7- Strongly Like) based on their preference (Gunathilake, 2012).

Statistical analysis

The experiment was conducted as a complete randomized design and the data were analysed at a 95% confidence interval using one-way ANOVA. The mean comparison was done by Tukey's family error rate test using SPSS 10 statistical package. The mean and standard deviations of data were calculated using EXCEL 2010.

RESULTS AND DISCUSSION

Physical parameters of whole king coconut

The general appearance of the whole nut and the pared nuts at each tested maturity stage of the variety '*Nawasi Thembili*' are given in Figure 1. The outer pericarp of the selected king coconuts was observed as bright orange in colour and poor kernel development was observed at the 6-month maturity stage.



Figure 1: The appearance of king coconut (whole nut) and pared nut at different maturity stages

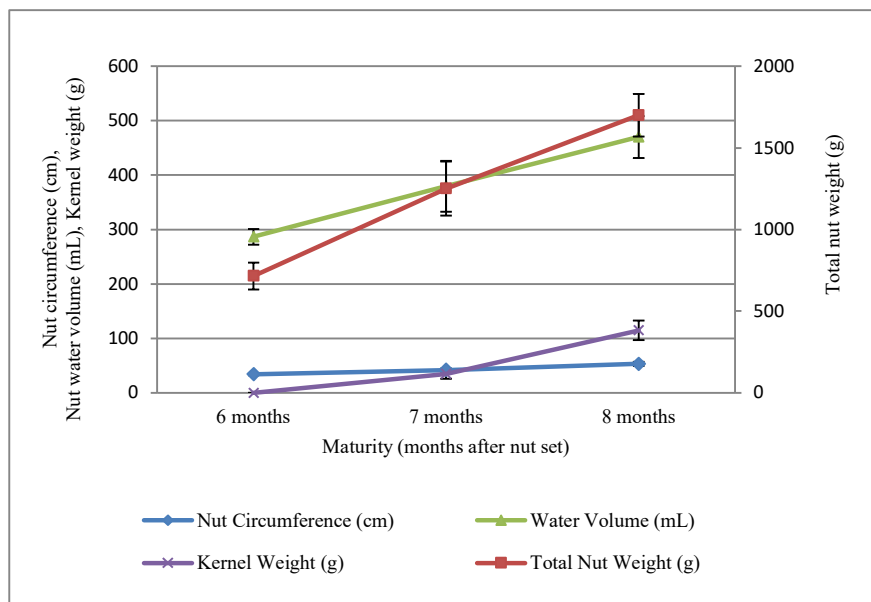


Figure 2: Changes in physical parameters of king coconuts (whole nut) at different maturity stages

As given in Figure 2, total nut weight, kernel weight, nut water volume, and the nut circumference of the whole nut increased significantly ($p < 0.05$) with maturity. The kernel thickness at the 7 month maturity was 2.97 ± 0.21 mm; this increased significantly ($p < 0.05$) to 5.34 ± 0.13 mm at the 8 month stage of maturity. The kernel at 7 month maturity was soft/smooth and became thick/hard at 8 month of maturity. The colour (*L) of king coconut water decreased significantly ($p < 0.05$) as 18.23 ± 0.07 , 18.08 ± 0.09 and 17.72 ± 0.07 at the stages of 6, 7, and

8 months of maturity, respectively. A significant turbidity development was observed at the 8 months of maturity in king coconut water. The colour (*L) of king coconut kernel increased significantly ($p < 0.05$) with maturity. The lightness value (*L) of the kernel varied from 51.86 ± 2.34 at 7 months of maturity to 75.20 ± 2.28 at 8 months of maturity.

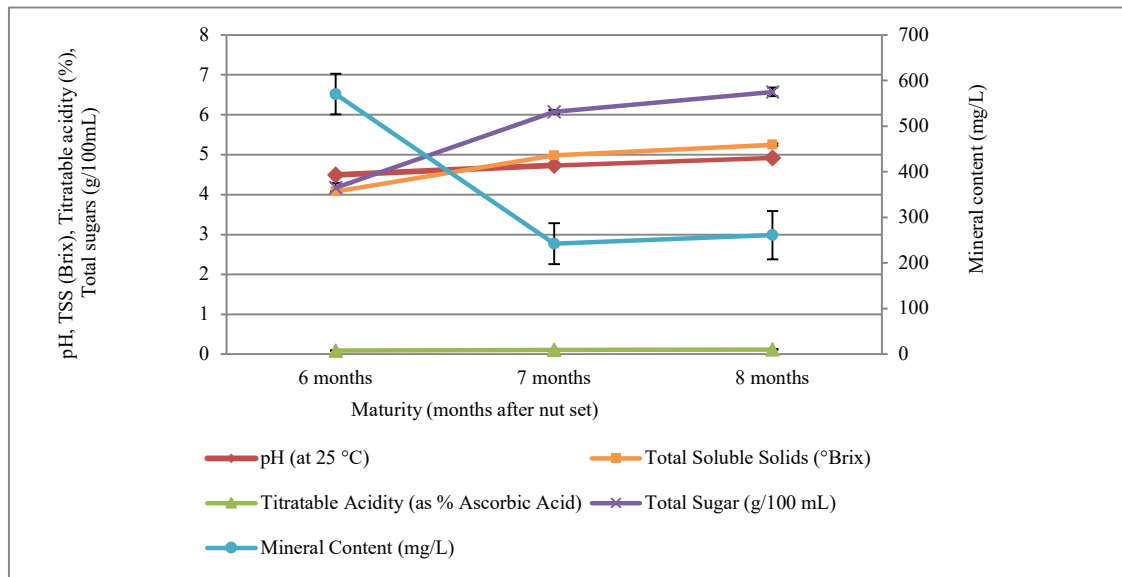


Figure 3: Changes in physico-chemical parameters of king coconut water at different maturity stages

The kernel weight was the highest at the 8 months maturity after fruit set; this is further supported by the significant increase ($p < 0.05$) in total nut weight from 7 to 8 months of maturity. The mean nut water volume at 6, 7, and 8 month stages of maturity varied as 287 ± 15 mL, 380 ± 47 mL, and 470 ± 39 mL, respectively; the nut water volume increased in a decreasing pattern along with a gradual increase of kernel development towards the later maturity stages. The nut circumference increased significantly ($p < 0.05$) as 34.2 ± 1.7 cm, 41.5 ± 2.7 cm, and 53.1 ± 3.8 cm at 6,7 and 8 months of maturity, respectively. The chemical parameters of king coconut water and the kernel are given in Figure 3 and Figure 4, respectively.

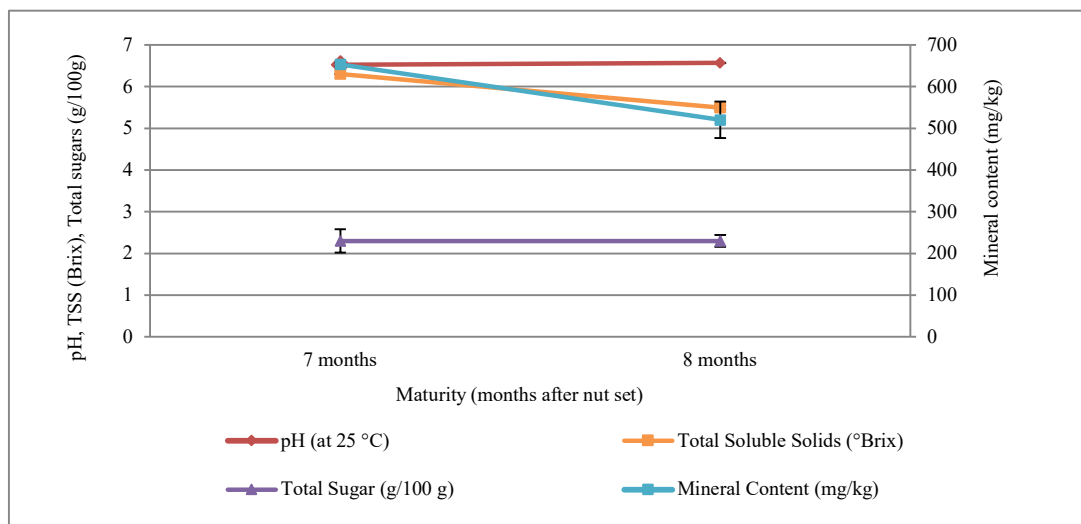


Figure 4: Changes in physico-chemical parameters of king coconut kernel at different maturity stages

According to statistical analysis, all the tested physico-chemical parameters of king coconut water were significantly varied ($p < 0.05$) with maturity, where pH, TSS, total sugars, and acidity increased significantly ($p < 0.05$) with maturity. However, mineral content and the TSS of the kernel decreased significantly ($p < 0.05$) during maturation, while changes in pH and total sugars were non-significant. Several researchers have found interesting relationships and patterns of physico-chemical variations (Tan *et al.*, 2014; Kannangara *et al.*, 2018) in king coconut water and kernel with maturity, similar to the findings reported in this study.

The low kernel content at 6 months of maturity and the gradual development at the of 7–8 months of maturity is in agreement with by Janick and Paull (2008), who reported that the king coconut shell initially contains clear sweet liquid and the tender young kernel begins to develop as a thin layer inside the endocarp/shell at the stage of 5 months of maturity. Furthermore, Jackson *et al.* (2004) and Chikkasubbanna *et al.* (1990) reported that the liquid endosperm exerts pressure inside the nut during maturation due to increased water holding capacity with the initiation of kernel development, and is partially replaced by the kernel to release the excess pressure.

Changes in total sugars

Total sugars play a vital role in the quality and sensory attributes of king coconut water and kernel, which directly affects its marketability. According to Figure 5, glucose and fructose were the most prominent sugar types present in immature king coconut water, and found to increase significantly ($p < 0.05$) during 7–8 months of maturity. HPLC peaks for trace sugars were not observed in the chromatograms in this study. However, the presence of trace sugars may not be detected in the present study due to low sensitivity. Therefore, it is suggested to follow LC-MS technology with enhanced sensitivity for better identification of trace sugars. Later initiation of sucrose at 8 months of maturity may influence the sweet taste of king coconut water. In contrast, king coconut kernel has shown a significant increase ($p < 0.05$) in sucrose compared to glucose and fructose throughout maturation. Therefore, young king coconut water at 7–8 months of maturity could be considered as a good source of invert sugars (glucose and fructose), while the mature kernel is rich in sucrose. The present work has shown that the sweet taste in both king coconut water and kernel could be achieved at 7 months of maturity.

The detection of individual sugar forms seems to be effective in selecting the optimum harvesting stage as given in Figure 5. However, the Aurantiaca (intermediate) varieties have shown the highest sugar contents of 5–7 % with a sweet taste for water and kernel, according to other research findings, (Kwiatkowski *et al.*, 2008). Therefore, it is important to select an intermediate maturity level of 7 months for optimum sweetness in king coconut water when it is used as a beverage, and the 7–8 months of maturity would be optimum when utilizing king coconut kernel for industrial uses such as kernel incorporated functional beverages, chewing confectionaries, table desserts, fruit leathers, and snacks.

Several research studies have shown that reducing sugars (glucose and fructose) predominate in young coconuts, and the mature kernel is rich in non-reducing sugars mainly as sucrose (Jackson *et al.*, 2004; Appaiah *et al.*, 2015). Furthermore, it was reported that the glucose and fructose concentrations steadily increase with the maturation of king coconut water and starts to decline with the increase of sucrose at later mature stages (Halim *et al.*, 2018).

The total sugars in king coconut water fluctuated, starting from a value of 4.18 ± 0.12 g/100 mL and increased gradually to 6.08 ± 0.05 g/100 mL, and 6.58 ± 0.11 g/100 mL at 7–8 months of maturity (Figure 5), followed by a value of 5.86 ± 0.14 g/100 mL, which is a decreasing pattern at later maturity (*unpublished data*). In contrast, the increasing pattern of total sugars in coconut kernel can be seen and lately dominated by proteins and lipids. The basic ion composition of king coconut water warrants its utilization as a rehydration beverage. It could serve as a source of electrolytes and for numerous biological applications as an essential component in studying cellular function, enzyme activation, gene expression, and metabolism of amino acids, lipids, and carbohydrates (Radenahmad *et al.*, 2009).

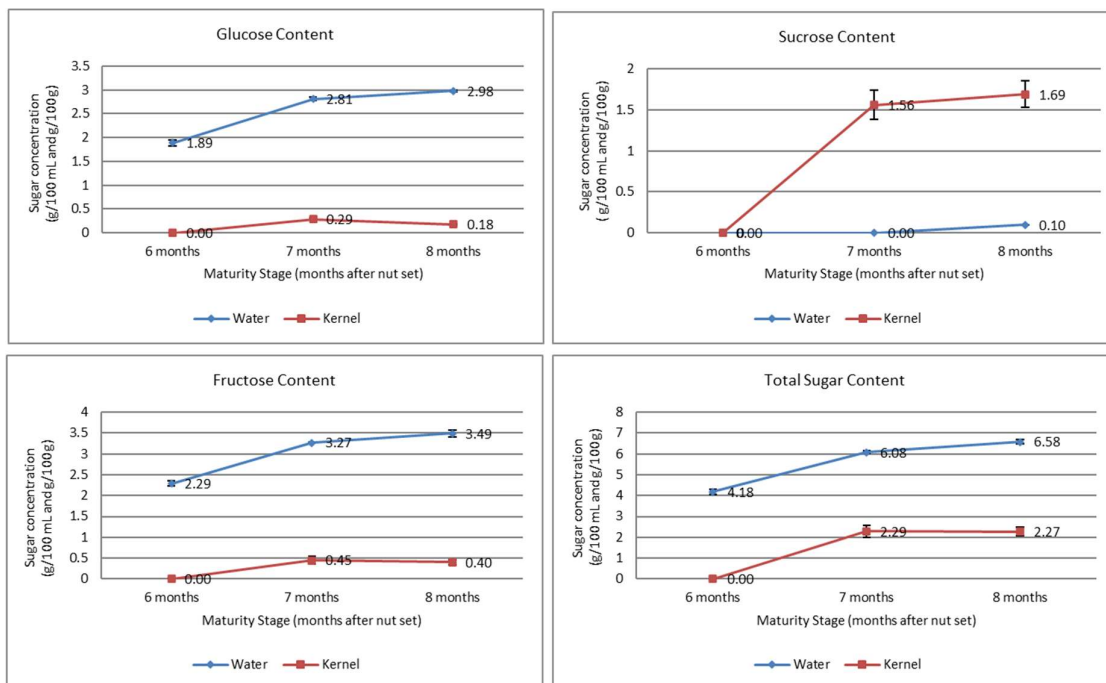


Figure 5: Changes in sugar contents of king coconut water and king coconut kernel at different maturity stages

Changes in mineral content

The total mineral content of king coconut water significantly decreased ($p < 0.05$) during 6 to 8 months period of maturity (Table 1). However, the total mineral content of king coconut kernel was significantly higher ($p < 0.05$) compared to the value of king coconut water at 8 months of maturity. According to Table 1, a recognizable movement of minerals from king coconut water to the kernel occurs with maturity. It appears that minerals in king coconut water might have been deposited in the kernel during maturation. However, total mineral content in the whole nut has significantly increased ($p < 0.05$) up to 7 months of maturity and significantly decreased ($p < 0.05$) at the stage of 8 months of maturity.

Table 1: Changes in mineral content of king coconut water and kernel with maturity

Minerals (mg/L; mg/kg)	6 Months		7 Months		8 Months	
	Water	Kernel	Water	Kernel	Water	Kernel
K ⁺	0.30 ± 0.00 ^a	n/d	0.25 ± 0.07 ^a	0.35 ± 0.07 ^A	0.25 ± 0.07 ^a	0.35 ± 0.07 ^A
Na ⁺	13.8 ± 2.55 ^a	n/d	13.00 ± 1.98 ^a	49.5 ± 2.69 ^A	10.2 ± 3.11 ^a	58.3 ± 6.93 ^A
Mg ⁺²	93.2 ± 9.62 ^a	n/d	45.5 ± 8.34 ^b	347.5 ± 9.19 ^A	45.4 ± 6.79 ^b	353.0 ± 42.43 ^A
Ca ⁺²	463 ± 32.53 ^a	n/d	183.5 ± 34.65 ^b	256 ± 2.83 ^A	205 ± 49.5 ^b	105 ± 5.66 ^B
Fe ⁺²	0.05 ± 0.00 ^a	n/d	0.05 ± 0.001 ^a	0.05 ± 0.01 ^B	0.05 ± 0.00 ^a	3.5 ± 2.55 ^A
Total	570.35 ± 45.35 ^b	n/d	242.30 ± 38.11 ^a	653.40 ± 11.42 ^A	260.9 ± 44.23 ^a	520.15 ± 44.8 ^B
Whole Nut	570.35 ± 45.35 ^c		895.70 ± 33.35 ^a		781.05 ± 3.89 ^b	

† Data is expressed as mean ± SD, n=20, The n/d refers to 'not detected' since no kernel development was observed at 6 months of maturity. The significance *($p < 0.05$) between maturity levels are denoted by lower- and upper-case letters within a row for king coconut water and kernel, respectively.

As shown in Table 1, Ca⁺² is the most prominent mineral followed by Mg⁺² in king coconut water, while Mg⁺² is the highly prominent mineral in the kernel. However, Fe⁺² and K⁺ were also detected in trace amounts in

the nut water and kernel. King coconut water and kernel can be considered as good sources of Ca^{+2} , Mg^{+2} , and Na^+ . Furthermore, it is evident that the total mineral content in the average nut water volume varied as 163.40 ± 13.51 mg, 91.95 ± 18.56 mg, and 122.62 ± 14.21 mg for the 6, 7, and 8 months of maturity, respectively. Moreover, total mineral content in an average weight of kernel varied as 22.61 ± 8.56 mg and 59.60 ± 6.45 mg at 7 and 8 months of maturity, respectively. This result confirms the pattern of deposition of chemical constituents from nut water to kernel with maturity. Overall, results indicated that all the tested physico-chemical parameters varied significantly between king coconut water and kernel with the stage of maturity. Although the present study has focused mainly on the presence of electrolytes (Na^+ , Ca^{+2} , and Mg^{+2} , K^+ and Fe^{+2}), it is evident from the reviewed literature that coconut water contains a variety of inorganic ions such as chlorides (Cl^-), phosphates (PO_4^{-3}), and sulfates (SO_4^{-2}) (Richter *et al.*, 2005).

The majority of studies have shown that K^+ is the predominant mineral followed by Na^+ , Ca^{+2} , and Mg^{+2} in king coconut water (Gunathilake, 2012; Marapana *et al.*, 2017). In contrast, the present study indicates that Ca^{+2} and Mg^{+2} as the minerals occurring in the highest concentrations in king coconut water and the kernel, respectively. Several research studies reported different values for mineral concentrations present in king coconut water as shown in Table 2. It has been discussed that minerals present in king coconut water may depend on various factors such as, variety, soil properties, cultivation practices, fertilizer, and manure applications in king coconut palm orchards (Prades *et al.*, 2012b).

Table 2: Mineral concentrations present in king coconut water reported by different authors

Na^+ (mg/L)	K^+ (mg/L)	Mg^{+2} (mg/L)	Ca^{+2} (mg/L)	Fe^{+2} (mg/L)	Cl^- (mg/L)	References
87 ± 4.9	214 ± 26.2	42 ± 3.1	100 ± 4.2	–	–	Gunathilake, 2012
–	1900–2500	45–55	100–200	–	1200–600	Marapana <i>et al.</i> , 2017
105	312	30	29	0.14	183	Jayasinghe & Bandaranayake, 2005
105	250	–	–	–	–	Athauda <i>et al.</i> , 2015

Note: – not reported (data are not available or not given in the research article)

Selection of optimum harvest maturity for intended applications

The physico-chemical attributes of king coconut water and kernel, for different maturity stages, are given in Table 3, based on the local and international coconut standards (FAO, 2003; 2005) and data available in the literature (Burns *et al.*, 2020). This can help to identify the optimum maturity or harvesting stages of king coconut for any intended use or application. Since the present study has proven that there is a recognizable impact of maturity on physico-chemical attributes of king coconut water and kernel, it is advisable to match the best harvest maturity with the desired characteristics to experience a prime quality.

Table 3: Optimum harvesting stages of king coconut for the use of different applications

Application	Critical parameters	Optimum harvest maturity	References
Water based:			
Fresh nut exports	pH, TSS, Sugars	7 months	Ranasinghe & Wimalasekara, 2002
Saline water	Minerals (Na^+ , K^+ , Ca^{+2} , Mg^{+2})	6 months	Athauda <i>et al.</i> , 2015; Kailaku <i>et al.</i> , 2015; Kalina & Navaratne, 2018
Functional drink	Sugars (Sucrose)	7 months	Gunathilake, 2012; Marapana <i>et al.</i> , 2017; Segura-Badilla <i>et al.</i> , 2020
Culture media	pH, TSS, Sugars, Minerals	8 months	Baque <i>et al.</i> , 2011; Tharmila <i>et al.</i> , 2011; Naik <i>et al.</i> , 2020
Kernel-based:			
Source of antioxidants	pH, TSS, Sugars, Minerals	8 months	Kalina & Navaratne, 2019
Ready to eat desserts	Sugars	7 months	Kalina & Navaratne, 2018
Functional foods	pH, TSS, Sugars	8 months	Solangi & Iqbal, 2011

[†] Maturity is given as time in months after nut set or pollination

The sensory results of king coconut water and kernel at the maturity of stage 7 months was ranked with the highest score compared to other stages of maturity [Figures 6(a) and 6(b)]. Therefore, 7 months of maturity was selected

as the optimum stage with desired quality characteristics. As a result of the highest consumer preference for king coconut water and kernel at 7 months maturity, the study was further extended for the estimation of proximate composition for a better understanding of its nutritional values.

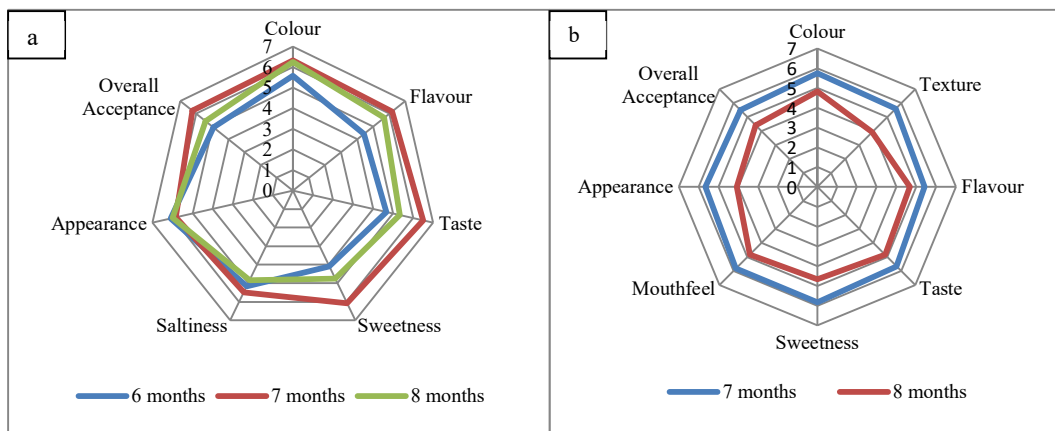


Figure 6: Sensory properties at different maturity stages of (a) king coconut water, and (b) king coconut kernel

This study was further extended to investigate the proximate/nutritional properties and physico-chemical attributes of the variety ‘*Nawasi Thembili*’ at 7 months of maturity (Table 4), which is the preferred maturity for consumption. The physico-chemical characteristics of king coconut water and kernel are highly dependent on variety, agronomic practices, and climatic conditions (Solanghi *et al.*, 2011). Total soluble solids present in king coconut water, which is mainly considered as sugars, were reported as increasing up to 7 - 8 months of maturity, and subsequently decreased in mature nuts with the formation of sucrose (Pue *et al.*, 1992; Richter *et al.*, 2005). This finding was evident by the absence of sucrose at the initial stages and the presence at 8 months of maturity in the present study.

According to Prades *et al.* (2012a), the maturity stage of 6 -7 months was identified as the most frequently used and most palatable stage when used as a beverage. Furthermore, varieties with high sugar contents could be selected depending on the preferred use as fermentation, concentrated juices, etc. Though the pH, TSS, and sugar content are known to be the most influencing parameters on organoleptic properties of king coconut water, it was proven that minerals, volatiles (aromatic), polyols (small peptides) play a vital role in preserving the characteristic flavour and sensory attributes of king coconut water (Prades *et al.*, 2012a).

Though king coconut water is more often cited in the literature, very limited research studies are available on king coconut kernel. King coconut kernel has been identified as a valuable source for several applications as reported by Arditti *et al.* (2008), and kernel extracts could be used in the orchid tissue culture process as an effective source of seed germination. Furthermore, it was reported that the kernel is a good source of antioxidants, oil, purine substances, and plant growth hormones with several nutraceutical properties (Zakaria *et al.*, 2006).

The present research work indicated that the physico-chemical composition of king coconut water and kernel widely varies with maturity and the specific applications derived from king coconut water and kernel should be matched with the precise stage of maturity with the most preferred attributes. However, the composition of king coconut is highly liable to be changed by a wide array of factors, such as selection of variety and cultivar, the effect of agronomy, climatic condition, and cultivation area; these should be thoroughly considered when focusing on optimal utilization.

Table 4: The nutritional and chemical composition of king coconut water and kernel

Nutritional and chemical parameters	King coconut water	King coconut kernel
Proximate composition (wet basis):		
Water (%)	94.46 ± 0.11	89.59 ± 0.34
Carbohydrates (%)	4.95 ± 0.14	6.60 ± 1.19
Protein (%)	0.08 ± 0.01	0.43 ± 0.09
Fat (%)	0.03 ± 0.01	1.80 ± 0.09
Crude fibre (%)	0.02 ± 0.01	0.46 ± 0.06
Ash (%)	0.44 ± 0.03	0.62 ± 0.03
Physico-chemical attributes:		
pH (at 25 °C)	4.73 ± 0.07	6.53 ± 0.13
TSS (Brix)	5.0 ± 0.1	6.3 ± 0.2
Total sugars (% wet basis)		
Glucose	2.81 ± 0.04	0.30 ± 0.01
Fructose	3.27 ± 0.01	0.45 ± 0.01
Sucrose	n/d*	1.56 ± 0.02
Acidity (%)	0.106 ± 0.004	-
Mineral content (mg/L; mg/kg)		
Na ⁺	13.0 ± 1.98	49.5 ± 2.69
K ⁺	0.25 ± 0.07	0.35 ± 0.07
Ca ⁺²	183.5 ± 34.65	256 ± 2.83
Mg ⁺²	45.5 ± 8.34	347.5 ± 9.19
Fe ⁺²	0.05 ± 0.001	0.05 ± 0.001

* Data is expressed as mean ± SD, n=20, proximate composition and physico-chemical properties of king coconut variety 'Nawasi' at 7-month maturity is given; acidity is expressed as % of ascorbic acid; n/d* is 'not detected'

CONCLUSION

The study concluded that king coconut water at 6 months of maturity is optimum when used as isotonic beverages with the highest electrolyte concentration. King coconut water at 7 months of maturity is optimal when used as 'fresh nut exports' as well as when sold in local retail markets with the highest sweetness. King coconut kernel at the stage of 7 months of maturity is best for use as ready-to-eat dishes/desserts with a smooth soft texture. Kernel at the stage of 8 months of maturity is optimum to produce kernel-based functional beverages and confectionaries with a hard texture and higher sugar content. Therefore, it is advisable to select the optimum harvest maturity compatible with intended applications for better utilization and satisfaction.

Conflict of interest statement

The authors declare that there are no conflicts of interest regarding the publication of this work.

Acknowledgments

The financial assistance provided by the funded project (FP 128) of the Ministry of Science Technology and Research, Sri Lanka is gratefully acknowledged. The authors would like to acknowledge Mr. Anura Amarathunga, Senior Laboratory Attendant, Industrial Technology Institute for the support given throughout the project.

REFERENCES

- AOAC (2012). Official methods of analysis of AOAC International, *Crude Protein in Feeds, Cereal Grains, and Forages*. 2001.11. 19th edition, Washington DC, USA.
- AOAC (2012). Official methods of analysis of AOAC International, *Crude Fat in Feeds, Cereal Grains, and Forages*. 2003.05. 19th edition, Washington DC, USA.
- AOAC (2012.) Official methods of analysis of AOAC International, *Determination of Crude Fiber in Animal Feeds*. 978.10. 19th edition, Washington DC, USA.
- AOAC (2012). Official methods of analysis of AOAC International, *Determination of Ash in Animal Feeds*. 942.05. 19th edition, Washington DC, USA.

- AOAC (2012). Official methods of analysis of AOAC International, *Moisture in Animal Feeds*. 934.01. 19th edition, Washington DC, USA.
- Appaiah P., Sunil L., Kumar P.P. & Krishna A.G. (2015). Physico-chemical characteristics and stability aspects of coconut water and kernel at different stages of maturity. *Journal of Food Science and Technology* **52**(8): 5196–5203.
DOI: <https://doi.org/10.1007/s13197-014-1559-4>
- Arditti J. (2008). *Micropropagation of Orchids*, 2nd edition. Blackwell Publishing: Oxford, UK.
- Athauda L.K., Kasturiratne A., de Silva A.P. & Wickremasinghe A.R. (2015). King coconut water, tender coconut water, Gatorade and ORS: which rehydrates athletes best? *Proceedings of the Sri Lanka Medical Association, Anniversary Academic Sessions* **60**(1): 197.
DOI: <https://doi.org/10.4038/cmj.v60i3.8188>
- Baque M.A., Shin Y.K., Lee E.J. & Paek K.Y. (2011). Effect of light quality, sucrose and coconut water concentration on the microporpagation of Calanthe hybrids (Bukduseong "Hyesung and Chunkwang" Hyesung). *Australian Journal of Crop Science* **5**(10): 1247.
- Brainard D. (2003). Color appearance and color difference specification. In: *The Science of Color*, 2nd edition, pp. 191–216. Elsevier Science Publishers Ltd., UK.
DOI: <https://doi.org/10.1016/B978-044451251-2/50006-4>
- Burns D.T., Johnston E.L. & Walker M.J. (2020). Authenticity and the potability of coconut water-a critical review. *Journal of AOAC International* **103**(3): 800–806.
DOI: <https://doi.org/10.1093/jaoacint/qs2008>
- Chikkasubbanna V., Jayaprasad K.V., Subbaiah T. & Poonacha N.M. (1990). Effect of maturity on the chemical composition of tender coconut (*Cocos nucifera* L. var. Arsikere Tall) water. *Journal of Indian Coconut* **20**: 10–13.
- Coconut Development Authority (CDA) (2020). *Export data - export performance 2018-2020. Sri Lanka*. Available at https://www.cda.gov.lk/web/images/pdf/export_perfo/2020/DEC_TI.pdf. Accessed 19 March 2021.
- De Carvalho J.M., Maia G.A., De Figueiredo R.W., De Brito E.S. & Rodrigues S. (2007). Development of a blended non-alcoholic beverage composed of coconut water and cashew apple juice containing caffeine. *Journal of Food Quality* **30**(5): 664–681.
DOI: <https://doi.org/10.1111/j.1745-4557.2007.00149.x>
- DebMandal M. & Mandal S. (2011). Coconut (*Cocos nucifera* L.: Arecaceae): in health promotion and disease prevention. *Asian Pacific Journal of Tropical Medicine* **4**(03): 241–247.
DOI: [https://doi.org/10.1016/S1995-7645\(11\)60078-3](https://doi.org/10.1016/S1995-7645(11)60078-3)
- Department of Census and Statistics (2005). *Progress of Coconut Cultivation 1962–2004*. Department of Census and Statistics, Sri Lanka. Available at http://repo.statistics.gov.lk/bitstream/handle/1/208/152_33.pdf. Accessed 19 March 2021.
- EDB (2019). *Industry Capability Report, Food and Beverage Sector*. Export Development Board, Colombo. Available at <https://www.srilankabusiness.com/ebooks/industry-capability-report-food-beverages-2021.pdf>. Accessed on 12.10.2019.
- Ekanayake G.K., Perera S.A.C.N., Dassanayake P.N. & Everard J.M.D.T. (2010). Varietal classification of new coconut (*Cocos nucifera* L.) forms identified from Southern Sri Lanka. *COCOS* **19**: 41–45.
DOI: <https://doi.org/10.4038/cocos.v19i1.4749>
- FAO/WHO Codex Alimentarius. *General Standard for Fruit Juices and Nectars (CODEXSTAN247-2005)*. Codex Alimentarius, Rome
- FAO/WHO Codex Alimentarius. *Standard for Aqueous Coconut Products, Coconut Milk and Coconut Cream (CODEX STAN240-2003)*. Codex Alimentarius, Rome.
- Gunathilake K.D.P.P. (2012). Optimum physico-chemical and processing parameters for the preservation of king coconut water. *CORD* **28**(1): 8–8.
DOI: <https://doi.org/10.37833/cord.v28i1.104>
- Halim H.H., Williams Dee E., Pak Dek M.S., Hamid A.A., Ngali A., Saari N. & Jaafar A.H. (2018). Ergogenic attributes of young and mature coconut (*Cocos nucifera* L.) water based on physical properties, sugars and electrolytes contents. *International Journal of Food Properties* **21**(1): 2378–2389.
DOI: <https://doi.org/10.1080/10942912.2018.1522329>
- Ismail I., Singh R. & Sirisinghe R.G. (2007). Rehydration with sodium-enriched coconut water after exercise-induced dehydration. *Southeast Asian Journal of Tropical Medicine and Public Health* **38**(4): 769.
- ISO10504:2013 (2013). *Starch Derivatives -Determination of the Composition of Glucose Syrups, Fructose Syrups and Hydrogenated Glucose Syrups - Method using High-performance Liquid Chromatography*. International Organization for Standards, Geneva, Switzerland.
- ISO750:1998 (1998). *Fruit and Vegetable Products; Determination of Titratable Acidity*. International Organization for Standards, Geneva, Switzerland.
- Jackson J.C., Gordon A., Wizzard G., McCook K. & Rolle R. (2004). Changes in chemical composition of coconut (*Cocos nucifera*) water during maturation of the fruit. *Journal of the Science of Food and Agriculture* **84**(9): 1049–1052.
DOI: <https://doi.org/10.1002/jsfa.1783>
- Janick J. & Paull R.E. (2008). *The Encyclopedia of Fruit and Nuts*. CABI, Wallingford, UK.
DOI: <https://doi.org/10.1079/9780851996387.0000>

- Jayasinghe K.P. & Bandaranayake C.K. (2005). An analysis of genetic diversity in king coconut, *Cocos nucifera*, Var. Aurantiaca using SSR markers. Available at <http://repository.wyb.ac.lk/handle/1/545>. Accessed on 25 May 2021.
- Kailaku S., Nur Alam Syah A., Risfaheri R., Setiawan B. & Sulaeman A. (2015). Carbohydrate-electrolyte characteristics of coconut water from different varieties and its potential as natural isotonic drink. *International Journal on Advanced Science, Engineering and Information Technology* **5**(3): 174–177.
DOI: <https://doi.org/10.18517/ijaseit.5.3.515>
- Kalina S. & Navaratne S.B. (2018). Developing an edible food product from tender coconut mesocarp and analyzing its sensory parameters. *The Pharma Innovation Journal* **7**(10): 62–66.
- Kalina S. & Navaratne S.B. (2019). Analysis of antioxidant activity and texture profile of tender-young and king coconut (*Cocos nucifera*) Mesocarps under different treatments and the possibility to develop a food product. *International Journal of Food Science* **2019**: Article ID 7470696
DOI: <https://doi.org/10.1155/2019/7470696>
- Kannangara A.C., Chandrajith V.G.G. & Ranaweera K.K.D.S. (2018). Comparative analysis of coconut water in four different maturity stages. *Journal of Pharmacognosy and Phytochemistry* **7**(3): 1814–1817.
- Kwiatkowski A., Clemente E., Scarcelli A. & Vida J.B. (2008). Quality of coconut water ‘in natura’ belonging to green dwarf fruit variety in different stages of development, in plantation on the northwest area of Parana, Brazil. *Journal of Food, Agriculture and Environment* **6**(1): 102–105.
- Lopes M.A. & Larkins B.A. (1993). Endosperm origin, development, and function. *The Plant Cell* **5**(10): 1383–1399.
DOI: <https://doi.org/10.1105/tpc.5.10.1383>
- Marapana R.A., Chandrasekara C.M. & Aponso M.M. (2017). Nutrient fortified king coconut water as an isotonic thirst quenching beverage for sports men and women. *International Journal of Chemical Studies* **5**(5): 1494–1498.
- Marasinghe S.S.K., Marikkar J.N., Yalagama C., Wimalasiri S., Seneviratne G., Weerasooriya R., & Liyanage R. (2019). Comparison of inter-varietal differences in chemical composition and nutritional properties of coconut testa flour. *Journal of the National Science Foundation of Sri Lanka* **47**(3): 349–356.
DOI: <https://doi.org/10.4038/jnsfsr.v47i3.8699>
- Naik M., Sunil C.K. & Rawson A. (2020). Tender coconut water: A review on recent advances in processing and preservation. *Food Reviews International* **38**: 1–22.
DOI: <https://doi.org/10.1080/87559129.2020.1785489>
- Perera S.A., Dissanayaka H.D., Herath H.M., Meegahakumbura M.G. & Perera L. (2014). Quantitative characterization of nut yield and fruit components in indigenous coconut germplasm in Sri Lanka. *International Journal of Biodiversity* **2014**: Article ID 740592.
DOI: <https://doi.org/10.1155/2014/740592>.
- Perera S.A.C.N., Ekanayake G.K. & Herath H.M.N.B. (2015). An investigation of the tender nut potential of diverse coconut (*Cocos nucifera* L.) varieties/forms in Sri Lanka. *CORD* **31**(1): 7.
DOI: <https://doi.org/10.37833/cord.v31i1.69>
- Prades A., Dornier M., Diop N & Pain J.P. (2012a). Coconut water uses, composition and properties: a review. *Fruits* **67**(02): 87–107.
DOI: <https://doi.org/10.1051/fruits/2012002>
- Prades A., Dornier M., Diop N. & Pain J.P. (2012b). Coconut water preservation and processing: a review. *Fruits* **67**(3): 157–171.
DOI: <https://doi.org/10.1051/fruits/2012009>
- Pue A.G., Rivu W., Sundarrao K., Kaluwin C. & Singh K. (1992). Preliminary studies on changes in coconut water during maturation of the fruit. *Science in New Guinea* **18**(2): 81–84.
- Radenahmad N., Saleh F., Sawangjaroen K., Rundorn W., Withyachumnarnkul B. & Connor J.R. (2009). Young coconut juice significantly reduces histopathological changes in the brain that is induced by hormonal imbalance: A possible implication to postmenopausal women. *Histology and Histopathology* **24**: 667–674.
- Ranasinghe C.S. & Wimalasekara R. (2002). Technical guidelines to enhance shelf life of tender king coconut for the export. Available at <https://core.ac.uk/download/pdf/52172742.pdf>. Accessed 20 March 2021.
- Richter E.M., Jesus D.P., Muñoz R.A., Lago C.L. & Angnes L. (2005). Determination of anions, cations, and sugars in coconut water by capillary electrophoresis. *Journal of the Brazilian Chemical Society* **16**(6A): 1134–1139.
DOI: <https://doi.org/10.1590/S0103-50532005000700008>
- Segura-Badilla O., Lazcano-Hernández M., Kammar-García A., Vera-López O., Aguilar-Alonso P., Ramírez-Calixto J. & Navarro-Cruz A.R. (2020). Use of coconut water (*Cocos nucifera* L) for the development of a symbiotic functional drink. *Heliyon* **6**(3): e03653.
DOI: <https://doi.org/10.1016/j.heliyon.2020.e03653>
- Solangi A.H. & Iqbal M.Z. (2011). Chemical composition of meat (kernel) and nut water of major coconut (*Cocos nucifera* L.) cultivars at coastal area of Pakistan. *Pakistan Journal of Botany* **43**(1): 357–363.
- Tan T.C., Cheng L.H., Bhat R., Rusul G. & Easa A.M. (2014). Composition, physicochemical properties and thermal inactivation kinetics of polyphenol oxidase and peroxidase from coconut (*Cocos nucifera*) water obtained from immature, mature and overly-mature coconut. *Food Chemistry* **142**: 121–128.

DOI: <https://doi.org/10.1016/j.foodchem.2013.07.040>

Tharmila S., Jeyaseelan E.C. & Thavaranjit A.C. (2011). Preliminary screening of alternative culture media for the growth of some selected fungi. *Archives of Applied Science Research* **3**(3): 389–393.

Yong J.W., Ge L., Ng Y.F. & Tan S.N. (2009). The chemical composition and biological properties of coconut (*Cocos nucifera* L.) water. *Molecules* **14**(12): 5144–5164.

DOI: <https://doi.org/10.3390/molecules14125144>

Zakaria Z.A., Reezal I., Mat Jais A.M., Somchit M.N., Sulaiman M.R., Marmin A.H.I., Sidek H., Husin S.H., Rahim M.H.A. & Abdul Rahman L. (2006). The anti-inflammatory, anti-pyretic and wound healing activities of *Cocos nucifera* L. (MATAG types) fresh juice and kernel extract in experimental animals. *Journal of Pharmacology and Toxicology* **1**: 516–526.

DOI: <https://doi.org/10.3923/jpt.2006.516.526>

RESEARCH ARTICLE

Analytical Chemistry

Fluoride analysis in aqueous solutions - a comparison of two colorimetric methods

A Fernando, S Liyanage and AT Cooray*

Department of Chemistry, University of Sri Jayewardenepura, Gangodawila, Nugegoda, 10250, Sri Lanka.

Submitted: 03 January 2022; Revised: 19 June 2022; Accepted: 23 December 2022

Abstract: Fluoride is beneficial for human health only in a narrow concentration range. Over the years, many analytical techniques have been developed to quantify fluoride in a variety of sample matrices. In this research, fluoride concentrations of twenty (20) natural water samples determined by SPADNS (SPA) and Eriochrome Cyanine R (ECR) colorimetric methods were evaluated to ascertain whether these methods can produce comparable fluoride concentrations. According to the paired t test for comparing individual differences, the two datasets are different at 95% confidence level suggesting that the two analytical methods produce statistically different fluoride concentrations for the analysed water samples. The potential interferences of Al^{3+} , Ca^{2+} , and Mg^{2+} on the fluoride analysis was evaluated using 0.85 mg L^{-1} fluoride standard solutions spiked with various amount of the above-mentioned metal ions. The highest interference was observed with Al^{3+} ions, which underestimated the fluoride concentration by 26% and 23% for ECR and SPA methods respectively at 20.0 mg L^{-1} Al^{3+} concentrations. The minimum interference was observed for Ca^{2+} ions which underestimated the fluoride concentration by 8% and 7% for ECR and SPA methods respectively at 100.0 mg L^{-1} Ca^{2+} concentrations. Acid distillation resulted in the samples spiked with Ca^{2+} and Mg^{2+} ions in the range of 0.50 to 100.0 mg L^{-1} reaching the theoretical concentration of 0.85 mg L^{-1} . Acid distillation also worked well for the Al^{3+} -fortified samples, except for Al^{3+} concentration at 20 mg L^{-1} . The efficiency of the acid distillation method was also tested with three (03) natural water samples. The fluoride concentration increased significantly after the acid distillation; however, even after the acid distillation, statistically comparable fluoride concentrations were not observed.

Keywords: Acid distillation, Eriochrome Cyanin R, fluoride, SPADNS, t test.

INTRODUCTION

Fluoride is a ubiquitous anion in natural waters and fluorine is the 13th most abundant element in the Earth's crust that contain approximately 0.6 g/kg (García & Borgnino, 2015) of fluorine. Fluoride rich minerals gradually weathers and releases fluoride ions into ground and surface water (Rafique *et al.*, 2015). Fluoride is beneficial for human health as it promotes the growth of healthy bones and teeth (Edmunds & Smedley, 2013; Prasad *et al.*, 2018). Various dietary components help absorption of fluorides from the gastrointestinal tract and the absorbed fluoride is distributed throughout the body. According to World Health Organization (WHO), fluoride is beneficial only in the narrow concentration range of 0.5 to 1.5 mg L^{-1} in drinking water (Amini *et al.*, 2008; Edmunds & Smedley, 2013; García & Borgnino, 2015). Higher concentrations of fluoride cause serious health effects such as dental and skeletal fluorosis, brain damage and chronic kidney diseases (Edmunds & Smedley, 2013; Kanduti *et al.*, 2016). The hypo-mineralization of teeth commonly known as dental fluorosis develops at fluoride concentrations above 1.5 mg L^{-1} (O Mullane *et al.*, 2016; Akuno *et al.*, 2019). The excessive accumulation of fluoride in bones leads to development of skeletal fluorosis at fluoride concentrations above 10 mg L^{-1} (Mohammadi *et al.*, 2017). Skeletal fluorosis causes painful damages to bones and joints leading to abnormalities in bone structure. Brain damage due to hypocalcemia is caused by binding of calcium with fluoride (Mohammadi *et al.*, 2017). A fluoride concentration of approximately 1.0 mg L^{-1} in drinking water effectively promotes the growth of healthy teeth and bones without harmful effects on health (Edmunds & Smedley, 2013; García & Borgnino, 2015).

* Corresponding author (atcooray@sjp.ac.lk;  <https://orcid.org/0000-0002-4876-4224>)



This article is published under the Creative Commons CC-BY-ND License (<http://creativecommons.org/licenses/by-nd/4.0/>). This license permits use, distribution and reproduction, commercial and non-commercial, provided that the original work is properly cited and is not changed in anyway.

Because of the very narrow concentration range of fluoride that differentiate between its adverse and beneficial effects on human health, quantification of fluoride in drinking water is important to ensure good quality water (Dissanayake, 2005; De Silva *et al.*, 2020). Fluoride in different sample matrices has been quantified by a variety of analytical methods including gravimetric (Shell & Craig, 1954), volumetric (Banerjee, 1955; Abramović *et al.*, 1992), polarographic (Bond & O'Donnell, 1968), potentiometric (Frant & Ross, 1968; Harwood, 1969; De Silva *et al.*, 2020; Stonebridge *et al.*, 2020), colorimetric (Mesdaghinia *et al.*, 2010; Karimi *et al.*, 2018; Prasad *et al.*, 2018) and chromatographic (Szmagara & Krzyszcak, 2019) methods. The analytical methods based on flow injection analysis have also been reported in literature (Shimada *et al.*, 2005; van Staden & Stefan-van Staden, 2010). A good review of the recent developments in fluoride analytical techniques has been done by Yahyavi and coworkers (Yahyavi *et al.*, 2016). The popular SPADNS colorimetric method recommended for the analysis of fluoride in water and wastewater by the American Public Health Association (APHA) is based on the reaction between fluoride and zirconium - SPADNS dye lake (Eaton *et al.*, 2005). The bright-red SPADNS solution is mixed with colourless zirconyl solution in an acid medium to produce dark-red zirconyl - SPADNS complex. In the presence of fluoride ions, zirconyl-SPADNS complex breaks down to form stable ZrF_6^{2-} . The working fluoride concentration range of the SPADNS method is up to 1.6 mgL^{-1} (Eaton *et al.*, 2005). The SPADNS method has been used to determine the fluoride concentration in aqueous samples (Patel *et al.*, 1999; Rafati *et al.*, 2013; Somasundaram *et al.*, 2015; Karimi *et al.*, 2018), and in food and beverages (Marier & Rose, 1966). The SPADNS method is usually carried out in 0.7 M HCl because at this pH, the reaction between Zr(IV) and SPADNS dye is very rapid and also eliminate interferences from alkalinity, Fe(III) and chloride ions (Bellack & Schouboe, 1958). The Eriochrome Cyanine R (ECR) based colorimetric method was once a popular colorimetric method for fluoride analysis (Megregian, 1954; Dixon, 1970; Lenarczyk & Marczenko, 1986). Currently it is used in certain types of field portable photometers that uses powder-pillow reagents for fluoride analysis (Gül *et al.*, 2014). The ECR method has been used to determine the fluoride concentration in aqueous samples (Sarma, 1964; Dixon, 1970; Lenarczyk & Marczenko, 1986) and in urine (Megregian, 1954; Rowley & Farrah, 1962). According to the literature, Zr: ECR ratio of 1:4 is favourable in the analysis and maintaining an acidity higher 0.1 M HCl is important to prevent other metal ions such as Fe(III), Al(III) and Pb(II) reacting with Eriochrome Cyanine R to produce coloured complexes (Megregian, 1954).

The quantification of fluoride in different sample matrices can be analytically challenging because fluoride is present as free and complex bound fluoride in samples. The quantification of total fluoride requires the breakdown of complex bound fluoride to free fluoride. It has been reported that Ca^{2+} , Fe^{3+} , Al^{3+} , and Mg^{2+} can significantly interfere with fluoride analysis by forming strong metal-fluoro complexes (Devine & Partington, 1975; Nicholson & Duff, 1981; Frenzel & Brätter, 1986; Patel *et al.*, 1999). The potentiometric method uses strong metal chelating ligands such as (cyclohexylenedinitrilo)tetraacetic acid (CDTA) to breakdown metal-fluoro complexes in total fluoride measurements (De Silva *et al.*, 2020). In addition, higher concentrations of OH^- , Cl^- and PO_4^{3-} also interfere due to the poor selectivity (Devine & Partington, 1975; Frenzel & Brätter, 1986; Patel *et al.*, 1999). It is generally recommended to perform acid distillations of the sample prior to the analysis to eliminate or at least to reduce matrix interferences. The classical Willard and Winter distillation method to separate fluoride from the sample matrix involves acid distillation with a strong non-volatile acid such as H_2SO_4 . It is a slow and lengthy process which takes about 80 minutes per sample (Patnaik, 2010). Moreover, this method requires extreme care and a strict temperature control to prevent liberation of hazardous HF gas to the environment. As a result, almost all the fluoride analyses in natural waters reported in the literature have been carried without the distillation step (Chandrajith *et al.*, 2012; Jayawardana *et al.*, 2012; Karimi *et al.*, 2018). Every analytical method has its own advantages, limitations, and interferences. Therefore, depending on the sample matrix, different analytical methods will produce fluoride concentrations that may be statistically comparable or incomparable to each other. Often, a single analytical method has been used in fluoride analyses (Msonda *et al.*, 2007; Jayawardana *et al.*, 2012; Yeşilnacar *et al.*, 2016; Yadav *et al.*, 2019); however, it is not uncommon to use two or more techniques to analyse fluoride and to use pooled data as a single data set for interpretation (Chandrajith *et al.*, 2012). The combination of fluoride concentration data obtained from two or more analytical techniques as a single data set for interpretation may be problematic if the methods produce statistically incomparable data.

The main objective of this research is to statistically evaluate comparability of the fluoride concentrations determined by two colorimetric methods: SPADNS and ECR methods. In addition, the effect of Ca^{2+} , Mg^{2+} and Al^{3+} on the accuracy of the methods was evaluated with the use of 0.85 mg L^{-1} standard fluoride solutions

fortified with the above-mentioned metal ions. Finally, the acid distillation method was evaluated as an intervention to overcome the interferences from the above-mentioned metal ions.

MATERIALS AND METHODS

All calibration standards and other reagents were prepared using analytical grade chemicals and 18.2 M Ω deionized water. Twenty (20) natural water samples were collected from different geographical areas of Sri Lanka in pre-cleaned polyethylene bottles and stored at 4 °C in a refrigerator. The conductivity and pH of the samples were measured using a DDSJ-308A conductivity meter and a MP103 pH meter, respectively. The concentrations of Ca, Mg, and Al were determined using a Thermo Scientific iCE 3000 series Atomic Absorption Spectrometer in flame and graphite modes. The concentration of anions: Cl⁻, PO₄³⁻, and SO₄²⁻ were determined using a Metrohm 930 Compact IC Flex instrument. The instrument uses a Metrosep Supp 5–250/4.0, 250 × 4.0 mm separation column in the suppressed conductivity mode. The eluent was a mixture of 3.2 mmol L⁻¹ Na₂CO₃, and 1.0 mmol L⁻¹ NaHCO₃ and the eluent flow rate was 0.70 mL min⁻¹ at 35 °C. The sample injection loop was 20 μ L.

The fluoride concentration in water samples were determined by two analytical methods: Eriochrome Cyanine R- based photometric (ECR), and SPADNS (SPA) colorimetric methods. In the ECR method, a field portable photometer and power-pillow reagents were used as in the case fluoride is determined in the field. The method uses 10.0 mL of the sample, Palintest YAP179 reagent and a YSI 9500 photometer. The YSI 9500 photometer gives a direct concentration readout and it is with an internal calibration in a linear range up to 1.5 mg L⁻¹ of fluoride. It operates at wavelengths of 445 ± 5 nm, 495 ± 5 nm, 555 ± 5 nm, 570 ± 5 nm, 605 ± 5 nm and 655 ± 5 nm. According to Megregian (1954), Zirconium–Eriochrome Cyanine R Lake dye has a maximum absorbance between 525 to 530 nm; however, due to the limited availability of wavelengths in photometers, the fluoride analysis by ECR was carried out at 555 ± 5 nm. Most of the direct read field portable photometers are capable of analysing more than dozens of water quality parameters and the wavelength selection for a particular analysis is automated based on the selection of the water quality parameter. The YSI 9500 photometer use cylindrical 20 mm outer diameter optical glass cells with 10.0 mL internal volume as the sample holder. The photometer was used with manufacturer's default calibration which was corrected using standard fluoride solutions of 0.20, 0.60, and 1.00 mg L⁻¹ concentrations. The experiment was triplicated. The zirconyl-acid reagent for the SPADNS method was prepared using zirconyl chloride octahydrate and concentrated hydrochloric acid. The SPADNS reagent was prepared using sulphanic acid azochromotrop and distilled water. Then equal volumes of zirconyl-acid reagent and SPADNS reagent were mixed to prepare the zirconyl-SPADNS reagent. The calibration curve was prepared in the range from 0.0 to 1.40 mg L⁻¹. The method is explained in detail in APHA (2005) (Eaton *et al.*, 2005). The absorbance was recorded at 570 nm with a Thermo Fisher Scientific GENESYS 10S UV-Vis Spectrophotometer. Samples were diluted with deionized water when necessary. All the analyses were carried out in triplicate. The performance of the calibration was evaluated with a different set of standard fluoride solutions of 0.20, 0.60, and 1.00 mg L⁻¹ concentrations that was used to evaluate the performance of the YSI 9500 photometer. The experiment was triplicated.

The interference of Ca²⁺, Mg²⁺ and Al³⁺ on the determination of fluoride by the above-mentioned analytical methods was assessed as follows. Three series of 0.85 mg L⁻¹ fluoride solutions were prepared with variable amounts of Ca²⁺, Mg²⁺ and Al³⁺ ions in the solution. The Mg²⁺, Ca²⁺ and Al³⁺ solutions were prepared using analytical grade MgSO₄, CaCl₂ and Al₂(SO₄)₃. The first and second series of fluoride solutions contained Mg²⁺, and Ca²⁺ in the concentration range from 0.50 to 100.0 mg L⁻¹. The third series contained Al³⁺ in the concentration range from 0.10 to 20.0 mg L⁻¹. The solutions were kept for 24 h to attain equilibrium and then analysed for fluoride. All the analyses were triplicated.

The fluoride was separated from the matrix using the acid distillation method as described in detail in APHA (2005) with minor modifications (Eaton *et al.*, 2005). Three (03) natural water samples and several 0.85 mg L⁻¹ fluoride solutions containing Ca²⁺, Mg²⁺ and Al³⁺ were analysed by the ECR and SPA methods before and after acid distillation. All the analysis was triplicated. The triplicate measurements obtained using the two methods were statistically compared to determine whether they are the same or different. The standard deviation of the triplicate measurements was very small or zero for most of the results because triplicate measures produced the

same or very close values. Therefore, paired t test for comparing individual differences were used even though all the experiments were triplicated. The t calculated (t_{cal}) values were compared with the t tabulated (t_{tab}) values at 95% confidence level.

RESULTS AND DISCUSSION

The default internal calibration of the YSI 9500 photometer (ECR method) and the calibration of the SPANDS (SPA) method were re-evaluated with a different set of standard fluoride solutions and the experimental data is illustrated in Table 1. The SPA method produced experimental fluoride concentrations identical to the theoretical values (expected values); however, the ECR method overestimated the fluoride concentration. The ECR method used the default calibration accompanied with the YSI 9500 photometer.

Table 1: The evaluation of calibration using the standard fluoride solutions

Theoretical fluoride concentration (mg/L)	Fluoride concentration reported by the methods mg L ⁻¹	
	ECR	SPA
0.20	0.21	0.20
0.60	0.63	0.60
1.00	1.06	1.00

The fluoride concentration and other physico-chemical characteristics of the natural water samples are shown in Table 2. The percentage standard deviation of the triplicate measurements was always within $\pm 5\%$ and therefore, standard deviations of triplicate measurements (errors) were not included in fluoride concentrations. According to the SPADNS (SPA) method, the fluoride concentration varied between 0.13 to 3.36 mg L⁻¹. In addition, the Ca, Mg and Al concentrations were in the range of 0.19 to 120.8 mg L⁻¹, 3.51 to 59.06 mg L⁻¹ and 0.05 to 6.55 mg L⁻¹, respectively. The chloride and sulphate concentrations were in the range of 8.8 to 601.5 mg L⁻¹ and 1.46 to 298.3 mg L⁻¹, respectively. The phosphate concentration of the samples was very low except in samples #9, #11 and #12 with concentrations of 0.44, 0.27 and 1.12 mg L⁻¹, respectively.

Table 2: The fluoride concentration and other physico-chemical characteristics of natural water samples

Sample no.	pH	EC $\mu\text{S cm}^{-1}$	Fluoride mg L ⁻¹		Concentration mg L ⁻¹					
			SPA	ECR	Ca ²⁺	Mg ²⁺	Al ³⁺	Cl ⁻	SO ₄ ²⁻	PO ₄ ³⁻
1	8.16	634.3	0.66	0.56	5.39	59.06	0.26	63.5	24.3	N/D
2	8.27	471.6	0.93	0.76	5.32	14.64	0.41	18.5	28.4	N/D
3	7.65	743.5	0.62	0.57	1.41	30.05	0.23	81.1	23.3	N/D
4	8.02	793.8	0.13	0.10	3.23	5.50	4.19	23.5	31.2	N/D
5	7.04	363.2	0.26	0.22	42.29	15.27	1.04	96.5	29.6	N/D
6	8.02	793.8	2.63	2.43	4.77	3.83	0.05	23.2	31.2	N/D
7	8.14	856.3	1.08	0.92	0.19	4.75	0.09	111.7	52.2	N/D
8	7.02	126.0	0.21	0.21	22.21	31.44	6.55	18.3	1.5	N/D
9	7.55	363.2	0.55	0.48	15.12	20.97	0.16	107.6	18.4	0.44
10	7.29	237.6	0.21	0.22	30.91	26.28	4.74	15.1	5.5	N/D
11	7.36	254.0	0.57	0.47	39.18	31.57	0.66	27.9	8.4	0.27
12	7.07	1,500.0	1.24	1.09	0.09	7.21	0.06	365.8	42.4	1.12
13	7.80	353.0	0.36	0.35	43.21	28.86	1.55	27.4	10.7	N/D
14	8.22	401.0	0.60	0.60	9.85	30.34	0.53	31.2	22.2	N/D
15	7.89	891.0	0.60	0.50	8.10	32.62	0.55	328.3	58.5	N/D
16	7.56	1,810.0	1.11	1.16	93.93	34.13	0.08	601.5	298.3	N/D
17	7.33	630.0	0.69	0.57	120.8	50.77	1.89	12.8	5.5	N/D
18	7.26	570.1	3.36	2.87	7.91	3.51	0.10	8.8	4.0	N/D
19	8.00	1,087.0	0.92	0.77	15.63	15.43	1.20	382.2	58.0	N/D
20	7.15	58.4	0.86	0.71	23.26	31.00	2.18	12.1	5.1	N/D

N/D: not detected

A brief description of the natural water samples analysed in this study is given in Table 3.

Table 3: Details of the natural water samples analysed in the study.

Sample no.	Sample location	Source of water
1	Kurunegala	Bore well
2	Eheliyagoda	Bore well
3	Dambulla	Bore well
4	Raththota	Spring
5	Horton Plains	Waterfall
6	Trincomalee	Bore well
7	Puttalam	Bore well
8	Nuwara Eliya	Spring
9	Badulla	Bore well
10	Rathnapura	Waterfall
11	Matara	Bore well
12	Embilipitiya	Bore well
13	Kalupahana	Waterfall
14	Kohuwala	Bore well
15	Matale	Spring
16	Galle	Bore well
17	Negambo	Bore well
18	Polonnaruwa	Reservoir
19	Daagonna	Bore well
20	Vavuniya	Bore well

The ion chromatographic (IC) method was also used to obtain the concentration of fluoride ions; however, the fluoride data produced by the IC method was not used in this study due to the appearance of the negative dead volume peak close to the fluoride peak in some of the chromatograms. This issue is documented in literature. The overlap of the dead volume peak with fluoride peak distorts the original shape of the fluoride peak, making it is difficult to integrate. This may lead to inaccurate fluoride concentrations reported by the IC method (Roden & Tallman, 1982; Saari-Nordhaus *et al.*, 1994).

According to the experimental data, higher fluoride concentrations were mostly (85 %) produced by the SPA method except for the samples #10, and #16. Samples #8 and #14 produced identical values from the two methods. There is a strong correlation ($r^2 = 0.99$) between fluoride concentrations determined by the SPA and ECR methods as shown in Figure 1. These two analytical methods are based on the same working principle, where a metal-dye complex breakdown in the presence of fluoride ions due to the formation of much stable metal-fluoro complexes. As a result, it can be expected that SPA and ECR methods are subjected to similar matrix interferences.

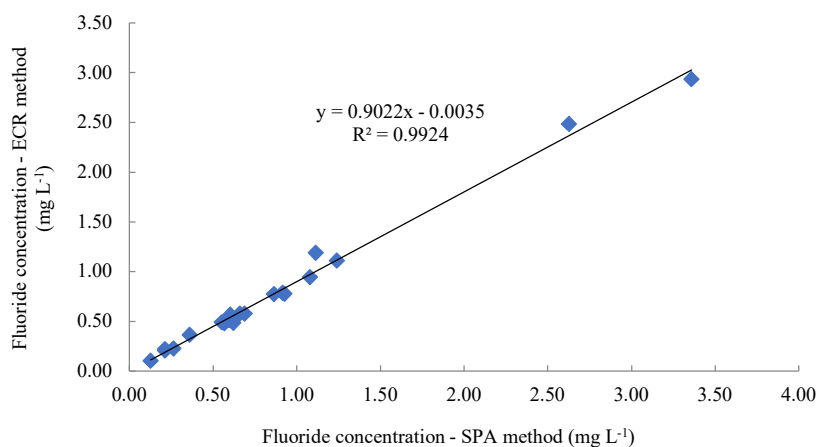


Figure 1: A graphical comparison of the fluoride concentrations determined by the SPA and ECR methods. The solid line represents the linear regression curve

The paired t test for comparing individual differences was applied to the two datasets to determine whether they are the same or different at 95 % confidence level. The calculated t value is 4.16 and the tabulated t value is 2.086, making $t_{\text{cal}} > t_{\text{tab}}$. Therefore, it can be concluded that the two datasets are different, and the two analytical methods have generated two statistically different fluoride concentrations for the twenty natural water samples. Correlation analysis showed that the fluoride concentration determined by the SPA method negatively correlated with the concentration of Al^{3+} (-0.465), Mg^{2+} (-0.449), and Ca^{2+} (-0.172) and the fluoride concentration determined by the ECR method negatively correlated with that of Al^{3+} (-0.465), Mg^{2+} (-0.440) and Ca^{2+} (-0.147). The negative correlation with metal ions is most likely due to the formation of metal-fluoro complexes. The correlation also strongly agrees with the studies done with the standard fluoride solutions spiked with metal ions and a summary of data is given in Table 4.

It was assumed that the observed differences in fluoride concentration measured by the SPA and ECR methods are most likely due to the presence of various amounts of Mg^{2+} , Ca^{2+} and Al^{3+} in water samples. In order to investigate the validity of this hypothesis, 0.85 mg L⁻¹ standard fluoride solutions were spiked with different amounts of Mg^{2+} , Ca^{2+} and Al^{3+} and then analysed for the fluoride concentration using the above-mentioned colorimetric methods. The experimental data are summarized in Table 4.

A careful look at the experimental data reveals that both ECR and SPA methods produce fluoride concentrations statistically comparable to the true value only at very low Mg^{2+} , Ca^{2+} and Al^{3+} concentrations. The highest interference was observed with Al^{3+} ions, which underestimated the fluoride concentration obtained using ECR, and SPA methods by 26%, and 23% respectively at 20.0 mg L⁻¹ Al^{3+} concentration when compared to the theoretical value. In contrast, the interference was minimum with Ca^{2+} ions. It underestimated the fluoride concentration by a maximum of 8% at 100.0 mg L⁻¹ Ca^{2+} concentration for the ECR method. The percentage underestimation was 7% for the SPA method at 100.0 mg L⁻¹ Ca^{2+} concentration. There is a pronounced underestimation of the fluoride concentration even at low concentrations of Mg^{2+} . The interferences caused by metal ions on the determination of fluoride is mainly due to the formation of stable metal-fluoro complexes that are not easily decomplexed to release free fluoride ions that need to be determined by the analytical methods. The metal-fluoro complexes such as AlF_4^- ($K_f = 1.26 \times 10^{19}$), $\text{CaF}_2(\text{s})$ ($K_f = 2.50 \times 10^{10}$) and $\text{MgF}_2(\text{s})$ ($K_f = 1.58 \times 10^8$) are stable (Stumm *et al.*, 1996) and the method using ion selective electrode for fluoride analysis use strong metal chelating agents such as CDTA to decomplex metal-fluoro complexes (De Silva *et al.*, 2020). However, in colorimetric methods such as SPADNS and Eriochrome Cyanine R methods, decomplexation of metal-fluoro complexes is determined by the relative stabilities of these complexes and ZrF_6^{2-} . Therefore, interferences caused by metal ions at higher concentrations are non-negligible for the determination of fluoride by colorimetric methods. In addition to making complexes with fluoride ions, certain metal ions such as Fe(III) make stable complexes with the Eriochrome cyanine R and SPADNS dyes and the metal-dye complexes absorb light at different wavelengths making the colorimetric method more complicated (Langmyhr & Stumpe, 1965, Hulanicki *et al.*, 1983). Moreover, dissolved organic compounds such as fulvic and humic acids can interfere with colorimetric method by either complexing with the Zr(IV) or producing a colour that overlaps with the analytical wavelengths.

The observed interferences from Ca^{2+} , Mg^{2+} and Al^{3+} cannot be used as it is to explain the experimental data given for natural water samples in Table 1. The matrix of natural water samples is more complicated than fluoride standard solutions due to the presence of organic matter, and a variety of cations and anions that could interfere with fluoride analysis. In general, natural water samples containing high concentrations of Ca^{2+} , Mg^{2+} and Al^{3+} resulted in significantly different fluoride concentrations reported by SPA and ECR methods. Some of the examples to support this observation include samples #1, #11, #15, and #19. It should be noted that, this statement cannot be generalized for all the samples because there are deviations from this observation such as in samples #6 and #20 where significantly different fluoride concentrations were reported by the ECR and SPA methods even though the Ca^{2+} , Mg^{2+} , and Al^{3+} concentrations are comparatively lower.

To determine the efficiency of the acid distillation method to overcome the interferences by Ca^{2+} , Mg^{2+} and Al^{3+} ions on the determination of fluoride by the ECR, and SPA methods, standard fluoride samples spiked with these metal ions were analysed for fluoride ions before and after the acid distillation step. The experimental data are given in Table 4.

Table 4: Fluoride concentration of the 0.85 mg L⁻¹ standard fluoride solutions spiked with the selected metal ions before and after the acid distillation (AD) step

Metal ion concentration (mg L ⁻¹)	Fluoride concentration mg L ⁻¹			
	ECR		SPA	
	Before AD	After AD	Before AD	After AD
Mg ²⁺				
0.5	0.82	0.87	0.79	0.88
10.0	0.79	0.87	0.77	0.88
60.0	0.78	0.83	0.76	0.88
100.0	0.67	0.82	0.73	0.87
[Ca ²⁺]				
0.5	0.86	0.87	0.83	0.88
10.0	0.83	0.87	0.82	0.88
60.0	0.81	0.87	0.82	0.88
100.0	0.78	0.83	0.79	0.87
[Al ³⁺]				
0.5	0.82	0.86	0.81	0.88
8.0	0.71	0.82	0.73	0.86
20.0	0.63	0.76	0.65	0.83

AD: Acid distillation

The experimental data showed that the measured fluoride concentration of the standard solutions spiked with Ca²⁺, Mg²⁺ and Al³⁺ increased after the acid distillation. With acid distillation, the samples spiked with Ca²⁺ and Mg²⁺ in the range of 0.50 to 100.0 mg L⁻¹ reached their theoretical concentration of 0.85 mg L⁻¹. Acid distillation also worked well for the Al³⁺-spiked standard solutions except at 20 mg L⁻¹. The efficiency of the acid distillation method was also tested with three (03) natural water samples and the experimental data is shown in Table 5. The fluoride concentration of the natural water samples determined by the analytical methods also increased significantly after the acid distillation as observed for the fluoride standard solutions. It should be noted that even after the acid distillation, the fluoride concentration from the two methods were not statistically comparable.

Table 5: Effect of acid distillation on natural water samples

Sample ID	Metal concentration (mg L ⁻¹)			Fluoride concentration (mg L ⁻¹)			
	Mg ²⁺	Ca ²⁺	Al ³⁺	ECR		SPA	
				Before AD	After AD	Before AD	After AD
A	30.45	10.72	0.65	0.08	0.08	0.04	0.09
B	31.57	39.18	0.66	0.47	0.59	0.51	0.71
C	7.20	0.09	0.06	1.09	1.29	1.19	1.49

AD: Acid distillation

It has been well documented that, high concentrations of organic matter, Fe³⁺, Al³⁺, Ca²⁺, Mg²⁺, Cl⁻, OH⁻, SO₄²⁻ and PO₄³⁻ can either underestimate or overestimate the fluoride concentration (Eaton *et al.*, 2005). The ECR colorimetric method has higher interferences from Fe³⁺, PO₄³⁻ and Al³⁺ ions than the SPADNS method (Megregian, 1954). It can be assumed that a specific analytical method determines free fluoride and a fraction of complex bound fluoride. The extent of complex-bound fluoride analysed by a method will depend on the chemistry of the method. The SPANDS, ECR and IC colorimetric methods use the kinetics of ligand exchange to free complex-bound fluorides (Megregian, 1954; Banerjee, (1955); Devine & Partington, 1975; Lenarczyk & Marczenko, 1986; Hatsis & Lucy, 2001) and the potentiometric method depends on strong metal chelating ligands to free complex-bound fluorides (Nicholson & Duff, 1981; De Silva *et al.*, 2020). It is almost impossible to obtain statistically comparable fluoride concentrations using different analytical techniques if the sample matrix is complicated. This is mainly due to the unique set of interferences encountered by an analytical technique at a given sample matrix. As a result, careful attention must be paid when fluoride concentrations determined by different techniques are pooled together as a single dataset for interpretations.

The fluoride concentrations determined by the two methods produced slightly different concentrations for 0.85 mg/L fluoride standard solutions in the absence of metals ions: Ca²⁺, Mg²⁺ and Al³⁺. The SPA method accurately determined the fluoride concentration as 0.85 mg/L; however, the ECR method determined it as 0.87 mg/L which differed from the theoretical value by 0.02 mg/L. This difference could have been negligible if the

random error of the repeated measurements were large for the SPA and ECR methods. However, the random error of the repeated measurements was very small for both methods and the percentage standard deviation of the triplicate measurements were always within $\pm 5\%$. As a result, whatever the differences in fluoride concentrations determined by the two techniques have to be caused by systematic and gross errors. The probability of having gross errors in the experimental data is small because all the analyses were done with utmost care. The best method to identify systematic errors in an analytical method is by the method validation using standard reference materials (SRMs). Due to the unavailability of a suitable SRM, method validation was not done for both SPA and ECR methods. However, the SPA method was performed as described by APHA (2005) (Eaton *et al.*, 2005) and the ECR method was performed as described in the User Manual of YSI 9500 photometer. The differences observed in the fluoride concentrations by the two analytical methods could have been caused by the instruments used in the experiment. The SPA method used a sophisticated spectrophotometer to measure the absorbance while the ECR method used a photometer for the same purpose. Spectrophotometers have high-end optics, light sources, and detectors to accurately measure the absorbance or emission at a given wavelength. Photometers, in contrast, use filters instead of monochromators to isolate wavelengths. Often, because of the availability of limited number of wavelengths for analysis by the light sources, the analysis is not carried out using the optimum wavelengths suitable for analysis. As a result, concentrations of analytes obtained by spectrophotometers are more accurate than photometers.

There are a few limitations to this study. A more accurate picture of the two analytical methods can be obtained by analysing more samples from a wide variety of natural sources. Unfortunately, the number of samples had to be limited to 20 due to the limited availability of YAPI 79 reagent. In addition, interferences from Fe^{2+} , Fe^{3+} and PO_4^{3-} need to be investigated. Most importantly interference from different combinations of cations and anions such as phosphate has to be investigated using standard fluoride solutions.

CONCLUSIONS

In this research, SPADNS (SPA) and Eriochrome Cyanin R (ECR) colorimetric methods were used to determine fluoride concentrations in twenty natural water samples. The fluoride concentration data were statistically evaluated by the paired t test for comparing individual differences to determine whether the two datasets are statistically the same or different at 95 % confidence level. According to the t test, the two datasets are different suggesting that the two analytical methods produce statistically different fluoride concentrations for the same water samples. However, there is a very strong correlation between the fluoride concentrations determined by the SPA and ECR methods with a correlation coefficient (r^2) of 0.99. It was assumed that the different fluoride concentrations were produced due to the presence of interfering chemical species in the test samples. The potential interferences by Al^{3+} , Ca^{2+} , and Mg^{2+} on the fluoride analysis were evaluated using 0.85 mg L^{-1} fluoride standard solutions spiked with various amount of these metal ions. The highest interference was observed with Al^{3+} ions, which underestimated the fluoride concentration obtained using ECR and SPA methods by 26 % and 23 % respectively at 20.0 mg L^{-1} Al^{3+} concentrations. The interference was minimum for Ca^{2+} ions. The presence of Ca^{2+} underestimated the fluoride concentration by 8 % at 100.0 mg L^{-1} concentration. After acid distillation, the fluoride standard solution spiked with Ca^{2+} and Mg^{2+} in the range of 0.50 to 100.0 mg L^{-1} reached its theoretical concentration of 0.85 mg L^{-1} . Acid distillation also worked well for the Al^{3+} - fortified samples, except for the Al^{3+} concentration of 20 mg L^{-1} . The efficiency of the acid distillation method was also tested with three (03) natural water samples. The fluoride concentration increased significantly after the acid distillation; however, even after the acid distillation, statistically comparable fluoride concentrations were not observed. Currently colorimetric methods are hardly used to determine fluoride concentrations in aqueous samples due to interferences from many common cations and anions present in natural systems. Furthermore, colorimetric methods are time consuming and also suffer from poor sensitivity if 1.0 cm cuvettes are used to measure the absorbance. It is always better if acid digestion is carried out before the sample analysis if the concentration of interfering ions such as Ca^{2+} , Mg^{2+} and Al^{3+} are present at elevated concentrations. In addition, for large scale environmental studies, it would be better if fluoride concentrations determined using colorimetric methods are statistically compared with other standard methods for fluoride analysis that include ion chromatography and ion selective electrode methods.

Supplementary data

All the necessary analytical data is included in the manuscript. Addition experimental data can be requested through the corresponding author.

Conflict of interest

The authors declare that they have no known competing financial interest or personal relationship that could have appeared to influence the work reported in this paper.

Acknowledgement

This project was fully funded by the Department of Chemistry, Faculty of Applied Sciences, University of Sri Jayawardenepura. The authors thank the staff of Instrument Centre at the Faculty of Applied Sciences, University of Sri Jayawardenepura for their assistance during the analysis.

REFERENCES

- Abramović B.F., Gaál F.F. & Cvetković S.D. (1992). Titrimetric determination of fluoride in some pharmaceutical products used for fluoridation. *Talanta* **39**: 511–515.
DOI: [https://doi.org/10.1016/0039-9140\(92\)80173-B](https://doi.org/10.1016/0039-9140(92)80173-B)
- Akuno M., Nocella G., Milia E. & Gutierrez L. (2019). Factors influencing the relationship between fluoride in drinking water and dental fluorosis: a ten-year systematic review and meta-analysis. *Journal of Water and Health* **17**: 845–862.
DOI: <https://doi.org/10.2166/wh.2019.300>
- Amini M., Mueller K., Abbaspour K.C., Rosenberg T., Afyuni M., Möller K.N., Sarr M. & Johnson C.A. (2008). Statistical modeling of global geogenic fluoride contamination in groundwaters. *Environmental Science and Technology* **42**: 3662–3668.
DOI: <https://doi.org/10.1021/es071958y>
- Banerjee G. (1955). Rapid titrimetric determination of microgram amounts of fluoride ion with spadns-thorium lake. *Analytica Chimica Acta* **13**: 409–414.
DOI: [https://doi.org/10.1016/S0003-2670\(00\)87967-2](https://doi.org/10.1016/S0003-2670(00)87967-2)
- Bellack E. & Schouboe P. (1958). Rapid photometric determination of fluoride in water. Use of sodium 2-(p-sulfophenylazo)-1,8-dihydroxynaphthalene-3,6-disulfonate-zirconium lake. *Analytical Chemistry* **30**: 2032–2034.
DOI: <https://doi.org/10.1021/ac60144a050>
- Bond A. & O'donnell T. (1968). Polarographic microdetermination of fluoride. *Analytical Chemistry* **40**: 1405–1407.
DOI: <https://doi.org/10.1021/ac60266a032>
- Chandrajith R., Padmasiri J., Dissanayake C. & Prematilaka K. (2012). Spatial distribution of fluoride in groundwater of Sri Lanka. *Journal of the National Science Foundation of Sri Lanka* **40**(4): 303–309.
DOI: <https://doi.org/10.4038/jnsfsr.v40i4.5044>
- De Silva S.M., Deraniyagala S., Walpita J.K., Jayaweera I., Diyabalanage S. & Cooray A.T. (2020). Masking ability of various metal complexing ligands at 1.0 mM concentrations on the potentiometric determination of fluoride in aqueous samples. *Journal of Analytical Methods in Chemistry* **2020**: 6683309
DOI: <https://doi.org/10.1155/2020/6683309>
- Devine R. & Partington G. (1975). Interference of sulfate ion on SPADNS [sodium 2-(p-sulfophenylazo)-1, 8-dihydroxynaphthalene-3, 6-disulfonate] colorimetric determination of fluoride in wastewaters. *Environmental Science and Technology* **9**: 678–679.
DOI: <https://doi.org/10.1021/es60105a005>
- Dissanayake C. (2005). Of stones and health: medical geology in Sri Lanka. *Science* **309**: 883–885.
DOI: <https://doi.org/10.1126/science.1115174>
- Dixon E. (1970). Determination of microgram amounts of fluoride with zirconium and solochrome cyanine R. *Analyst* **95**: 272–277.
DOI: <https://doi.org/10.1039/an9709500272>
- Eaton A.D., Clesceri L.S., Greenberg A.E. & Franson M.A.H. (2005). Standard methods for the examination of water and wastewater. *American Public Health Association* **21**: 1600.
- Edmunds W.M. & Smedley P.L. (2013). Fluoride in natural waters. In: *Essentials of Medical Geology* (ed. O. Selinus). Springer, Dordrecht, Netherlands.
DOI: https://doi.org/10.1007/978-94-007-4375-5_13
- Frant M. & Ross J.W. (1968). Use of a total ionic strength adjustment buffer for electrode determination of fluoride in water supplies. *Analytical Chemistry* **40**: 1169–1171.

- DOI: <https://doi.org/10.1021/ac60263a005>
- Frenzel W. & Brätter P. (1986). Fluoride ion-selective electrode in flow injection analysis: Part 2. Interference studies. *Analytica Chimica Acta* **187**: 1–16.
DOI: [https://doi.org/10.1016/S0003-2670\(00\)82893-7](https://doi.org/10.1016/S0003-2670(00)82893-7)
- García M.G. & Borgnino L. (2015). Chapter 1. *Fluoride in the Context of the Environment*. Royal Society of Chemistry EBooks, Apr. 2015.
DOI: <https://doi.org/10.1039/9781782628507-00003>
- Gül A., Uzel N., Özkul A., Erkmen B., Düzel S. & Gül G. (2014). Effects of some physicochemical properties of water on histopathological and hematological picture of fish inhabiting Emet Stream. *International Journal of Fisheries and Aquatic Studies* **2**: 65–71.
- Harwood J.E. (1969). The use of an ion-selective electrode for routine fluoride analyses on water samples. *Water Research* **3**: 273–280.
DOI: [https://doi.org/10.1016/0043-1354\(69\)90024-4](https://doi.org/10.1016/0043-1354(69)90024-4)
- Hatsis P. & Lucy C.A. (2001). Effect of temperature on retention and selectivity in ion chromatography of anions. *Journal of Chromatography A* **920**: 3–11.
DOI: [https://doi.org/10.1016/S0021-9673\(00\)01226-7](https://doi.org/10.1016/S0021-9673(00)01226-7)
- Hulanicki A., Glab S. & Ackermann G. (1983). Compleximetric indicators: characteristics and applications. *Pure and Applied Chemistry* **55**: 1137–1230.
DOI: <https://doi.org/10.1351/pac198355071137>
- Jayawardana D.T., Pitawala H.M.T.G.A. & Ishiga H. (2012). Geochemical assessment of soils in districts of fluoride-rich and fluoride-poor groundwater, north-central Sri Lanka. *Journal of Geochemical Exploration* **114**: 118–125.
DOI: <https://doi.org/10.1016/j.gexplo.2012.01.004>
- Kanduti D., Sterbenk P. & Artnik B. (2016). Fluoride: a review of use and effects on health. *Materia Socio-medica* **28**: 133.
DOI: <https://doi.org/10.5455/msm.2016.28.133-137>
- Karimi A., Radfard M., Abbasi M., Naghizadeh A., Biglari H., Alvani V. & Mahdavi M. (2018). Fluoride concentration data in groundwater resources of Gonabad, Iran. *Data in Brief* **21**: 105–110.
DOI: <https://doi.org/10.1016/j.dib.2018.09.062>
- Langmyhr F.J. & Stumpe T. (1965). Complex formation of iron (III) with eriochrome cyanine r. *Analytica Chimica Acta* **32**: 535–543.
DOI: [https://doi.org/10.1016/S0003-2670\(00\)88980-1](https://doi.org/10.1016/S0003-2670(00)88980-1)
- Lenarczyk L. & Marczenko Z. (1986). Spectrophotometric determination of fluoride using ternary complex of zirconium with Eriochrome Cyanine R and cetylpyridinium ions. *Microchemical Journal* **34**: 115–120.
DOI: [https://doi.org/10.1016/0026-265X\(86\)90109-8](https://doi.org/10.1016/0026-265X(86)90109-8)
- Marier J. & Rose D. (1966). The fluoride content of some foods and beverages—a brief survey using a modified Zr-SPADNS method. *Journal of Food Science* **31**: 941–946.
DOI: <https://doi.org/10.1111/j.1365-2621.1966.tb03273.x>
- Megregian S. (1954). Rapid spectrophotometric determination of fluoride with zirconium-eriochrome cyanine R Lake. *Analytical Chemistry* **26**: 1161–1166.
DOI: <https://doi.org/10.1021/ac60091a018>
- Mesdaghinia A., Vaghefi K.A., Montazeri A., Mohebbi M.R. & Saeedi R. (2010). Monitoring of fluoride in groundwater resources of Iran. *Bulletin of Environmental Contamination and Toxicology* **84**: 432–437.
DOI: <https://doi.org/10.1007/s00128-010-9950-y>
- Mohammadi A.A., Yousefi M., Yaseri M., Jalilzadeh M. & Mahvi A.H. (2017). Skeletal fluorosis in relation to drinking water in rural areas of West Azerbaijan, Iran. *Scientific Reports* **7**: 1–7.
DOI: <https://doi.org/10.1038/s41598-017-17328-8>
- Msonda K.W.M., Masamba W.R.L. & Fabiano E. (2007). A study of fluoride groundwater occurrence in Nathenje, Lilongwe, Malawi. *Physics and Chemistry of the Earth, Parts A/B/C* **32**: 1178–1184.
DOI: <https://doi.org/10.1016/j.pce.2007.07.050>
- Nicholson K. & Duff E. (1981). Fluoride determination in water: an optimum buffer system for use with the fluoride-selective electrode. *Analytical Letters, Part A: Chemical Analysis* **14**: 887–912.
DOI: <https://doi.org/10.1080/00032718108055488>
- O' Mullane D., Baez R., Jones S., Lennon M., Petersen P., Rugg-Gunn A., Whelton H. & Whitford G.M. (2016). Fluoride and oral health. *Community Dental Health* **33**: 69–99.
- Patel R., Patel K. & Naik M. (1999). Zr (iv)-spadns flow analysis procedure for determination of fluoride in surface and groundwater. *International Journal of Environmental Studies* **56**: 745–756.
DOI: <https://doi.org/10.1080/00207239908711235>
- Patnaik P. (2010). *Handbook of Environmental Analysis: Chemical Pollutants in Air, Water, Soil, and Solid Wastes*. CRC Press, Florida, USA.
DOI: <https://doi.org/10.1201/b10505>
- Prasad N., Pushpaangeli B., Ram A. & Maimanuku L. (2018). Fluoride concentration in drinking water samples in Fiji. *Australian and New Zealand Journal of Public Health* **42**(4): 372–374.

- DOI: <https://doi.org/10.1111/1753-6405.12787>Rafati L., Mokhtari M., Fazelinia F., Momtaz S. & Mahvi A.H. (2013). Evaluation of ground water fluoride concentration in Hamadan Province west of IRAN (2012). *Iranian Journal of Health Sciences* **1**(3): 71–76.
DOI: <https://doi.org/10.18869/acadpub.jhs.1.3.71>
- Rafique T., Naseem S., Ozsvath D., Hussain R., Bhangar M.I. & Usmani T.H. (2015). Geochemical controls of high fluoride groundwater in Umarkot Sub-District, Thar Desert, Pakistan. *Science of The Total Environment* **530-531**: 271–278.
DOI: <https://doi.org/10.1016/j.scitotenv.2015.05.038>
- Roden D.R. & Tallman D.E. (1982). Determination of inorganic selenium species in groundwaters containing organic interferences by ion chromatography and hydride generation/atomic absorption spectrometry. *Analytical Chemistry* **54**: 307–309.
DOI: <https://doi.org/10.1021/ac00239a037>
- Rowley R. & Farrah G. (1962). Diffusion method for determination of urinary fluoride. *American Industrial Hygiene Association Journal* **23**: 314–318.
DOI: <https://doi.org/10.1080/00028896209342873>
- Saari-Nordhaus R., Nair L.M. & Anderson Jr J.M. (1994). Elimination of matrix interferences in ion chromatography by the use of solid-phase extraction disks. *Journal of Chromatography A* **671**: 159–163.
DOI: [https://doi.org/10.1016/0021-9673\(94\)80234-3](https://doi.org/10.1016/0021-9673(94)80234-3)
- Sarna P. (1964). Spectrophotometric determination of fluoride by zirconium-eriochrome cyanine R. *Analytical Chemistry* **36**: 1684–1685.
DOI: <https://doi.org/10.1021/ac60214a067>
- Shell H. & Craig R. (1954). Determination of silica and fluoride in fluorosilicates. *Analytical Chemistry* **26**: 996–1001.
DOI: <https://doi.org/10.1021/ac60090a012>
- Shimada K., Shimoda T., Kokusen H. & Nakano S. (2005). Automatic microdistillation flow-injection system for the spectrophotometric determination of fluoride. *Talanta* **66**: 80–85.
DOI: <https://doi.org/10.1016/j.talanta.2004.09.026>
- Somasundaram S., Ravi K., Rajapandian K. & Gurunathan D. (2015). Fluoride content of bottled drinking water in Chennai, Tamilnadu. *Journal of Clinical and Diagnostic Research* **9**(10): ZC32–ZC34.
DOI: <https://doi.org/10.7860/JCDR/2015/14691.6594>
- Stonebridge J., Baldwin R., Thomson N.R. & Ptacek C. (2020). Fluoride-selective electrode as a tool to evaluate the degradation of PFAS in groundwater: a bench-scale investigation. *Groundwater Monitoring and Remediation* **40**: 73–80.
DOI: <https://doi.org/10.1111/gwmmr.12374>
- Stumm W., Morgan J.J. & Drever J.I. (1996). Aquatic chemistry. *Journal of Environmental Quality* **25**: 1162.
DOI: <https://doi.org/10.2134/jeq1996.00472425002500050033x>
- Szmagara A. & Krzyszczyk A. (2019). Monitoring of fluoride content in bottled mineral and spring waters by ion chromatography. *Journal of Geochemical Exploration* **202**: 27–34.
DOI: <https://doi.org/10.1016/j.gexplo.2019.03.008>
- Van Staden J.F. & Stefan-Van Staden R.I. (2010). Application of porphyrins in flow-injection analysis: A review. *Talanta* **80**: 1598–1605.
DOI: <https://doi.org/10.1016/j.talanta.2009.10.016>
- Yadav S., Bansal S.K., Yadav S. & Kumar S. (2019). Fluoride distribution in underground water of district Mahendergarh, Haryana, India. *Applied Water Science* **9**: 1–11.
DOI: <https://doi.org/10.1007/s13201-019-0935-7>
- Yahyavi H., Kaykhaii M. & Mirmoghaddam M. (2016). Recent developments in methods of analysis for fluoride determination. *Critical Reviews in Analytical Chemistry* **46**: 106–121.
DOI: <https://doi.org/10.1080/10408347.2014.985814>
- Yeşilnacar M.İ., Yetiş A.D., Dülgergil Ç.T., Kumral M., Atasoy A.D., Doğan T.R., Tekiner S.İ., Bayhan I. & Aydoğdu M. (2016). Geomedical assessment of an area having high-fluoride groundwater in southeastern Turkey. *Environmental Earth Sciences* **75**: 162.
DOI: <https://doi.org/10.1007/s12665-015-5002-6>

RESEARCH ARTICLE

Natural Products

Natural α -glucosidase inhibitors from selected medicinal plants in Malaysia

SY Liew^{1,6}, Y Sivasothy², NN Shaikh³, K Javaid³, DM Isa⁴, VS Lee⁴, MI Choudhary^{3,5} and K Awang^{4,6*}

¹ Chemistry Division, Centre for Foundation Studies in Science, Universiti Malaya, 50603 Kuala Lumpur, Malaysia.

² School of Pharmacy, Monash University Malaysia, Jalan Lagoon Selatan, 47500 Bandar Sunway, Selangor Darul Ehsan, Malaysia.

³ H. E. J. Research Institute of Chemistry, International Center for Chemical and Biological Sciences, University of Karachi, Karachi-75270, Pakistan.

⁴ Department of Chemistry, Faculty of Science, Universiti Malaya, 50603 Kuala Lumpur, Malaysia.

⁵ Department of Biochemistry, Faculty of Science, King Abdulaziz University, Jeddah-214412, Saudi Arabia.

⁶ Centre for Natural Products Research and Drug Discovery (CENAR), Universiti Malaya, 50603 Kuala Lumpur, Malaysia.


Submitted: 13 May 2022; Revised: 11 October 2022; Accepted: 23 December 2022

Abstract: The most prevalent subtype of diabetes is Type 2 Diabetes Mellitus which results from an abnormal postprandial increase in blood glucose. Inhibition of the carbohydrate-hydrolysing enzymes (alpha-glucosidase and alpha-amylase) in the human digestive organs can control blood glucose levels, making it an important strategy in the management of Type 2 Diabetes Mellitus. A majority of the oral synthetic drugs which have been developed to treat Type 2 Diabetes Mellitus are expensive and have undesirable side effects. As a result, plant-derived remedies have become preferred alternatives as they are easily available, affordable and less harmful. Angustine (**1**) the major constituent in *Nauclea subdita* (Korth.) Steud., and (*E*)-labda-8(17),12-dien-15,16-dial (**2**) and zerumin A (**3**) of *Alpinia pahangensis* Ridley were evaluated for their α -glucosidase inhibitory activity. (*E*)-Labda-8(17),12-dien-15,16-dial (**2**) ($IC_{50} = 39.7 \mu M$) was identified as the most potent inhibitor among all three, followed by angustine (**1**) ($IC_{50} = 48.1 \mu M$) and zerumin A (**3**) ($IC_{50} = 53.3 \mu M$). Enzyme kinetic studies indicated that angustine (**1**) was a mixed-type inhibitor, while (*E*)-labda-8(17),12-dien-15,16-dial (**2**), and zerumin A (**3**) were non-competitive inhibitors. Molecular docking and molecular dynamics (MD) simulation studies were performed to predict the key interactions between the ligands and the target protein, IAGM (complex of acarbose with glucoamylase from *Aspergillus awamori*). The results of the study of binding interaction energy suggested that angustine (**1**) has the potential to be used as a natural drug lead in the treatment of type 2 diabetes mellitus.

Keywords: α -glucosidase, *Alpinia pahangensis*, angustine, (*E*)-labda-8(17),12-dien-15,16-dial, molecular docking, *Nauclea subdita*.

INTRODUCTION

Diabetes mellitus (D.M.) is a chronic metabolic disorder which has become a global health problem. According to the World Health Organization (WHO) Global Report on Diabetes, 422 million adults were estimated to live with diabetes in 2014, almost quadruple compared to 108 million in 1980 (WHO, 2016). This drastic rise was due to the increase in type 2 diabetes mellitus (T2DM) (WHO, 2016). Postprandial hyperglycaemia is one of the earliest signs of T2DM, which results from insufficient insulin secretion (Sun *et al.*, 2016). α -Glucosidase plays an important role in catalysing the hydrolysis of carbohydrates *i.e.*, cleavage of the terminal non-reducing 1-4 linked α -D-glucose residues and the release of α -D-glucose (Simpson *et al.*, 2012). Inhibition of this enzyme is a validated strategy to treat and prevent T2DM by decreasing postprandial hyperglycaemia (Sun *et al.*, 2016). The current clinical α -glucosidase inhibitors (acarbose, voglibose, and miglitol) are widely used for the treatment of T2DM (Liu *et al.*, 2016). However, they are reported to cause many adverse effects, such as diarrhoea, flatulence, and adverse gastrointestinal symptoms (Sivasothy *et al.*, 2016; Sun *et al.*, 2016). Hence, it is of interest to identify effective natural plant-derived α -glucosidase inhibitors devoid of side effects.

* Corresponding author (khalijah@um.edu.my;  <https://orcid.org/0000-0001-5971-6570>)



This article is published under the Creative Commons CC-BY-ND License (<http://creativecommons.org/licenses/by-nd/4.0/>). This license permits use, distribution and reproduction, commercial and non-commercial, provided that the original work is properly cited and is not changed in anyway.

Nauclea subdita (Korth.) Steud. and *Alpinia pahangensis* Ridley are two medicinal plants from Malaysia with the latter being endemic to the state of Pahang. *N. subdita* has traditionally been used to treat many ailments such as fever, pain, dental caries, oral septic, malaria, dysentery, diarrhoea, and central nervous system-related diseases (e.g. epilepsy) (Aisiah et al., 2019). *A. pahangensis* on the other hand has only been reported to have been used by the tribal natives of Pahang to relieve flatulence (Phang et al., 2013). Previous study has reported that the ethanol extract of *Nauclea subdita* is able to decrease the blood glucose level of mice with 25.45% at the dosage of 250 mg/20 g body weight. (Diana, 2017). Besides, pahangensin A, a bis-labdane diterpene isolated from *A. pahangensis* has shown to exhibit stronger inhibitory effects towards α -amylase and α -glucosidase in comparison to acarbose (Loo et al., 2019).

Phytochemical investigation of the bark of *N. subdita* and the rhizomes of *A. pahangensis* by our group has yielded indole alkaloids and labdane diterpenes respectively as the major class of secondary metabolites in these medicinal plants (Sivasothy et al., 2013a; 2013b; 2014; Liew et al., 2014). In addition, a large number of plants and plant derived constituents, for example, terpenes, alkaloids, flavonoids, and phenols have been known to exhibit anti-diabetic activities (Sivasothy et al., 2016; Tran et al., 2020) With regard to this, although *N. subdita* and *A. pahangensis* have never been reported to be traditionally used to treat diabetes, it would be worthwhile to investigate their potential as a source of α -glucosidase inhibitors since the bark of *N. subdita* and the rhizomes of *A. pahangensis* are rich in alkaloids and terpenoids, respectively. Hence, in the present paper, the α -glucosidase inhibitory activity of the major compounds, an indole alkaloid from *Nauclea subdita* (Korth.) Steud. and two labdane diterpenes from *Alpinia pahangensis* Ridley, along with their enzyme kinetic and molecular docking studies, are reported.

MATERIALS AND METHODS

General experimental procedures and plant materials

The general procedures were the same as those previously described (Liew et al., 2014; Sivasothy et al., 2013b). *Nauclea subdita* (Korth.) Steud. (Rubiaceae), and *Alpinia pahangensis* Ridley. (Zingiberaceae) were collected from Perak and Pahang (Malaysia), respectively. Their voucher specimens KL 5254, and KU 001, respectively) were deposited in the Herbarium of the Department of Chemistry, Universiti Malaya, Kuala Lumpur, Malaysia.

Extraction, isolation, and characterization of compounds 1-3

Compounds **1-3** were extracted, purified, and characterized according to previously described methods (Sivasothy et al., 2013b; Liew et al., 2014).

α -glucosidase inhibitory assay

The inhibition of the α -glucosidase enzyme (E.C.3.2.1.20 from *Saccharomyces cerevisiae*) was measured spectrophotometrically at 37 °C with the addition of 0.5 mM substrate (*p*-nitrophenyl α -D-glucopyranoside), 50 mM of phosphate saline buffer (pH 6.8) to a 96-well plate, followed by the addition of the test samples (20 μ L/well), prepared in 70% DMSO. The reaction was initiated with the addition of the enzyme (0.2 units/mL), prepared in 50 mM sodium phosphate buffer containing 100 mM NaCl. Standard drug acarbose was used as the positive control. The absorbance at 400 nm, due to the hydrolysis of the substrate by α -glucosidase, was observed continuously with a multi-plate spectrophotometer (Spectra Max, Molecular Devices, U.S.A.). Measurements were carried out in triplicate for each experiment (Sivasothy et al., 2013b; Liew et al., 2014). The percentage of inhibition was calculated according to the following formula:

$$\text{Inhibitory activity (\%)} = (\text{OD Control} - \text{OD Test sample}) / \text{OD Control} \times 100$$

Enzyme kinetics

Enzyme kinetic studies were performed to evaluate the mechanism of inhibition and therapeutic potential of the active compounds. The inhibitory potential of the active compounds, as well as their inhibition types, were inferred from the Lineweaver-Burk plot, secondary replot of the Lineweaver-Burk plot, and the Dixon plot. The

Lineweaver-Burk plot is the plot of reciprocal of the rate of reaction against the reciprocal of the concentrations of substrate, while the secondary replot of the Lineweaver-Burk plot was used to study the inhibitory effect of the compounds on K_m and V_{max} . The K_i values were determined by plotting the slope of each line against different inhibitory concentrations. The reciprocal of the rate of reaction, plotted against various inhibitor concentrations, represented as the Dixon plot, and reconfirmed the K_i values. Kinetic parameters were calculated using the GraFit software, where [I] and [S] are the total concentrations of the inhibitor and substrate, respectively. K_m is the Michaelis constant, and $K_{m\ app}$ is the apparent Michaelis constant. V_{max} is the maximum reaction velocity, and $V_{max\ app}$ is the apparent maximum reaction velocity of the α -glucosidase enzyme with the substrate *p*-nitrophenyl α -D-glucopyranoside. K_i and K_i' are the inhibition constants of the inhibitors (Sivasothy *et al.*, 2013b; Liew *et al.*, 2014).

Molecular docking

α -Glucosidase from *Aspergillus awamori* has a 24% sequence similarity with its human counterpart. Interestingly relatively high sequence similarity of 34% to 59% in the C-terminal of the enzyme (*i.e.*, the catalytic domain). In humans and *Aspergillus awamori*, α -glucosidase enzymes show almost similar pH, substrate specificity and inhibitor sensitivity. In the enzyme of both the species, the modification in residues such as arginine, tryptophan or cysteine adversely affects the enzymatic activity. Hence, to identify the inhibitors against human α -glucosidase, *Aspergillus awamori* α -glucosidase is used as a model (Faridmoayer & Scaman, 2004).

Crystal structure of α -glucosidase with PDB ID 1AGM, 2.4 Å resolution was used as the target protein. The water and ligand molecules were removed from the original crystal structure and modified according to the CHARMM force field with partial charge Momany-Rone (Momany & Rone, 1992). Short minimizations of the structures were performed with a root mean square (RMS) gradient tolerance of 0.1000 kcal/(mol \times Angstrom), satisfied in Discovery Studio 2.5 (Accelrys Discovery Studio, 2009). The ligands were obtained from PubChem compound (<http://www.ncbi.nlm.nih.gov/pccompound>), and optimized based on functional B3LYP, the basis set of 6-31G* (d,p) in Gaussian 09 before being minimized using the same protocol employed for the target protein. AUTODOCK VINA (Trott & Olson, 2010) program was used for rigid docking of the ligands into the binding site (ARG52, ASP53, LEU174, GLU176, ARG301, and GLU395) of the target protein.

Molecular dynamics (MD) simulations and binding free energy calculations

Since compounds **1** and **2** were found to be more active as compared to compound **3**, they were selected along with acarbose for MD simulation using PMEMD. CUDA (Götz *et al.*, 2012; Le Grand *et al.*, 2013; Salomon-Ferrer *et al.*, 2013) from AMBER 12 on GPUs Quadro 2000D produced by NVIDIA, which speeds up the simulation wall time required to obtain the trajectory files from each simulation. Prior to that the ligands were sent to the RESP ESP charge derive server to generate the general force field parameters (GAFF), and to build the force field library (Vanquelf *et al.*, 2011). The structures of the protein-ligand complex were solvated in a cubic box of TIP3P water (Jorgensen *et al.*, 1983), extending at least 10 Å in each direction from the solute and the force field 12 (ff12SB). To neutralize the counter ion, Na⁺ ions were added to the protein-ligand complex, and the cut-off radius was kept to 20 Å to compute the non-bonded interactions. All simulations were performed under periodic boundary conditions (Weber *et al.*, 2000), and long-range electrostatic were treated based on the Particle-Mesh-Ewald (PME) methods (Darden *et al.*, 1993; Essmann *et al.*, 1995). The SHAKE algorithm and Langevin dynamics were applied to constrain the bonds that involved hydrogen, and to control the temperature (Weber *et al.*, 2000). The temperature of each system was gradually increased from 0 to 310.15 K, over a period of 60 ps of NVT dynamics. Later on, 300 ps of NPT equilibration at 310.15 K, and 1 atmosphere pressure, followed by 10,000 ps of NPT-MD simulation were carried out. The trajectories were analysed using the PTRAJ module of the amber package.

The binding free energy of each complex was estimated, based on the MM-PBSA (Molecular Mechanics Poisson-Boltzmann Surface Area; Kollman *et al.*, 2000), and MM-GBSA (Molecular Mechanics Generalized Born Solvent Area; Chong *et al.*, 1999) protocols from 6–10 ns of the trajectories. A total of 500 snapshots were collected from each range, and the complex interaction energy profiles were generated by decomposing the total

binding free energies into residue-residue interaction pairs by the MM-GBSA decomposition process in the *mm_pbsa* program of AMBER 12.

RESULTS AND DISCUSSION

α -Glucosidase inhibitory assay

Angustine (**1**), (*E*)-labda-8(17),12-dien-15,16-dial (**2**), and zerumin A (**3**) (Figure 1) were evaluated for *in vitro* α -glucosidase inhibitory activity. Compounds **1** ($IC_{50} = 48.1 \pm 2.5 \mu M$), **2** ($IC_{50} = 39.7 \pm 1.09 \mu M$), and **3** ($IC_{50} = 53.3 \pm 2.94 \mu M$) demonstrated significantly high inhibitory activity as compared to the standard inhibitor drug, acarbose ($IC_{50} = 840 \pm 1.73 \mu M$). Results are summarized in Table 1, and Figure 2.

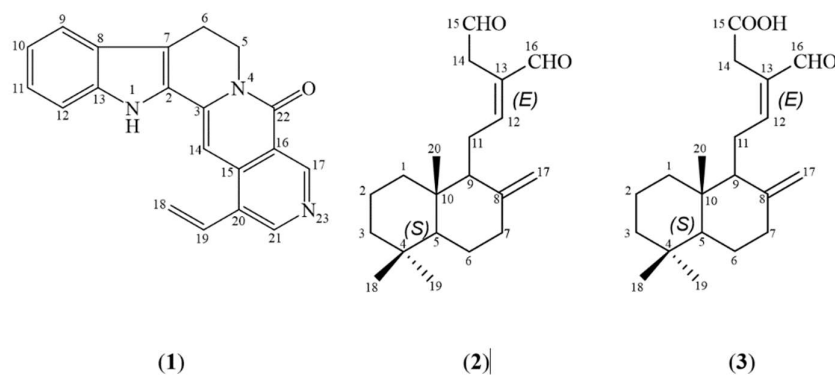


Figure 1: The structures of angustine (**1**), (*E*)-labda-8(17),12-dien-15,16-dial (**2**), and zerumin A (**3**)

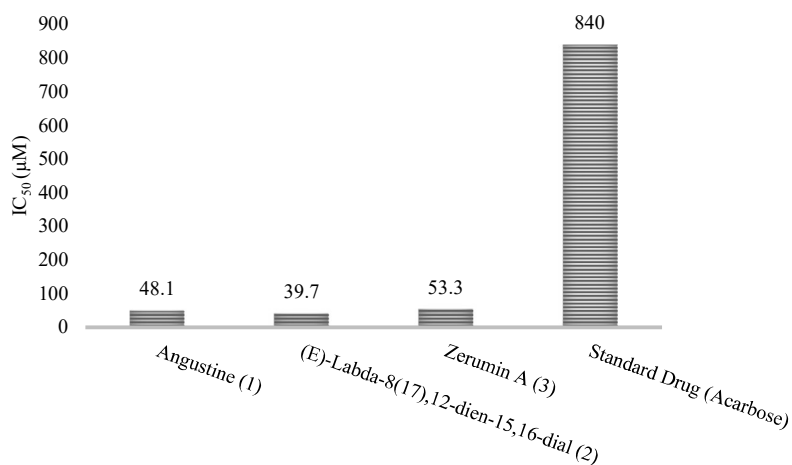


Figure 2: Inhibition of α -glucosidase by angustine (**1**), (*E*)-labda-8(17),12-dien-15,16-dial (**2**), and zerumin A (**3**)

Table 1: Results of molecular docking of α -glucosidase with compounds **1-3** AutodockVina

Receptor	Ligands	$IC_{50} \pm SEM$ (μM)	Binding affinity (kcal/mol)
α -Glucosidase	Angustine (1)	48.1 ± 2.5	-9.5(-6.5)
	(<i>E</i>)-Labda-8(17),12-dien-15,16-dial (2)	39.7 ± 1.09	-7.2(-6.0)
	Zerumin A (3)	53.3 ± 2.94	-7.8(-6.6)
	Standard (Acarbose)	840 ± 1.73	-9.8(-9.1)

IC_{50} Values expressed as SEM (standard error of mean), where n=3

Enzyme kinetics

The mechanism of inhibition of the most potent compounds and their interactions with the amino acid residues were evaluated. Compounds **1**, **2**, and **3** with K_i values 46, 55, and 34 μM , respectively, inhibited the α -glucosidase enzyme in a concentration dependent manner. Kinetic studies of compound **1** revealed a mixed-type inhibition, whereas compound **2** was found to inhibit α -glucosidase in a non-competitive type manner with no change in enzyme K_m , which showed that the binding of the enzyme to the substrate was not affected by the inhibitor, and it only reduced the enzyme concentration. Compound **3** was also identified as a non-competitive inhibitor. The standard α -glucosidase inhibitor drug (Acarbose) with a K_i value of 700 μM showed a competitive mode of inhibition, indicating that acarbose interacts with the amino acid residues of the active site of the enzyme (Table 2, Figures 3-5).

Table 2: Kinetic parameters of inhibition of α -glucosidase enzyme by compounds 1-3

Compounds	V_{\max} ($\mu\text{mol}/\text{min}^{-1}$)	$V_{\max\text{app}}$ ($\mu\text{mol}/\text{min}^{-1}$)	K_m (mM)	K_{mapp} (mM)	K_i (μM)	Type of inhibition
Angustine (1)	43	44	1.74	1.13	46	Mixed-type
(<i>E</i>)-Labda-8(17),12-dien-15,16-dial (2)	58.4	1.54	1.29	0.73	55	Non-Competitive
Zerumin A (3)	72.9	34	2.23	2.34	34	Non-Competitive
Standard (Acarbose)	43	41	0.8	1.38	700	Competitive

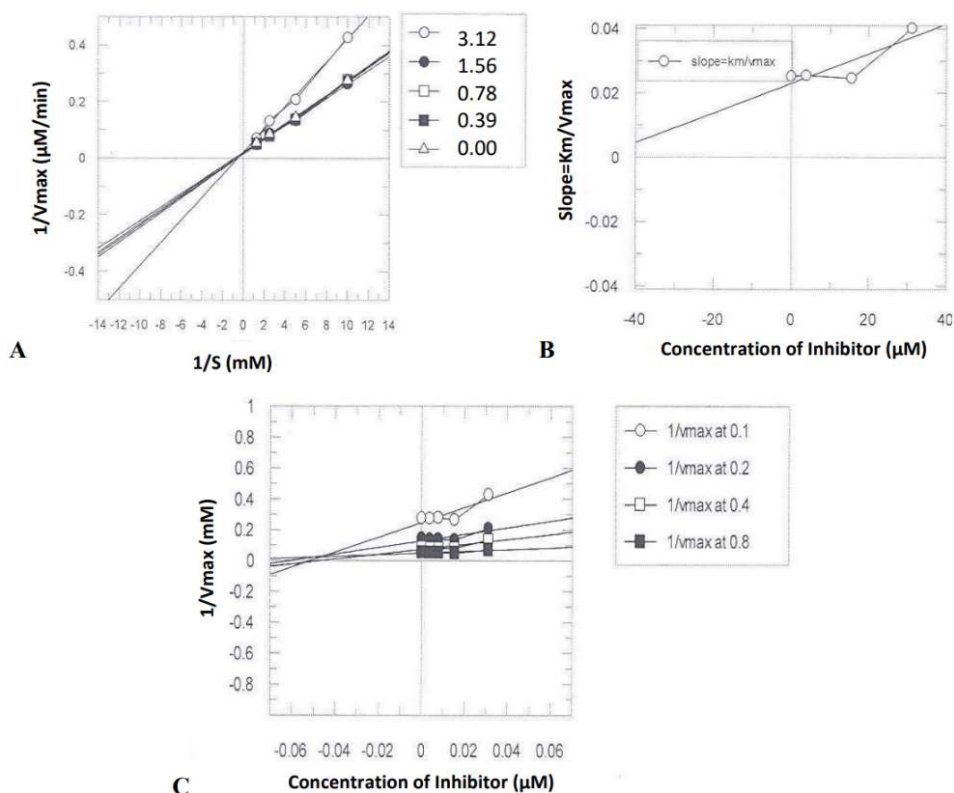


Figure 3: Inhibition of α -glucosidase by angustine (**1**).
 A. Lineweaver-Burk plot (reciprocal of rate of reaction versus reciprocal of substrate in the absence, and presence of 12.5, 6.25, 3.12, 1.56, 0.78, and 0.39 μM of compound **1**); B. Secondary replot of Lineweaver-Burk plot (slopes of each line versus different concentrations of compound **1**); C. Dixon plot (reciprocal of rate of reaction versus different concentrations of compound **1**)

Binding affinity with protein targets from the *in silico* molecular docking study

Docking studies were performed to gain insight into the preferable binding conformation of the ligands with the target protein. The results with the rigid docking indicated that the ligands were active with negative binding affinity range (kcal/mol) of possible binding poses of -9.5 – (-6.5), -7.2 – (-6.0), -7.8 – (-6.6), and -9.8 – (-9.1) kcal/mol, respectively, as shown in Table 1. The lower the value of the binding affinity, the stronger is the interaction between the receptor and peptides, therefore indicating that the peptides are in their most stable conformation (Spratt & Greenwood, 2000). The MD simulation complexes of 10 ns trajectory were visualized using discovery studio, as depicted in Figure 6. In the representation, ligands A) Angustine, B) (*E*)-labda-8(17), 12-dien-15,16-dial, and C) acarbose which have been illustrated in blue, red, and yellow respectively, were observed with important amino acid residue(s) that contributed negative value(s) in the 3 Å region. A close view of the interactions has shown that the green dotted lines represent the hydrogen bonds. Several hydrogen bonds were observed between acarbose at A:ARG52:HH12 - ACR:O1D, A:ARG52:HH12 - ACR:O2D, A:ARG52:HH22 - ACR:O2D, ACR:H43 - A:GLU176:OE1, ACR:H45 - A:GLU177:OE2, ACR:H39 - A:GLU176:OE1, and ACR:H41 - A:GLU176:OE1. Only one hydrogen bond was observed for (*E*)-labda-8(17), 12-dien-15,16-dial (2) at A:SER406:H-(*E*)-labda:O16, whereas none was found in Angustine (1).

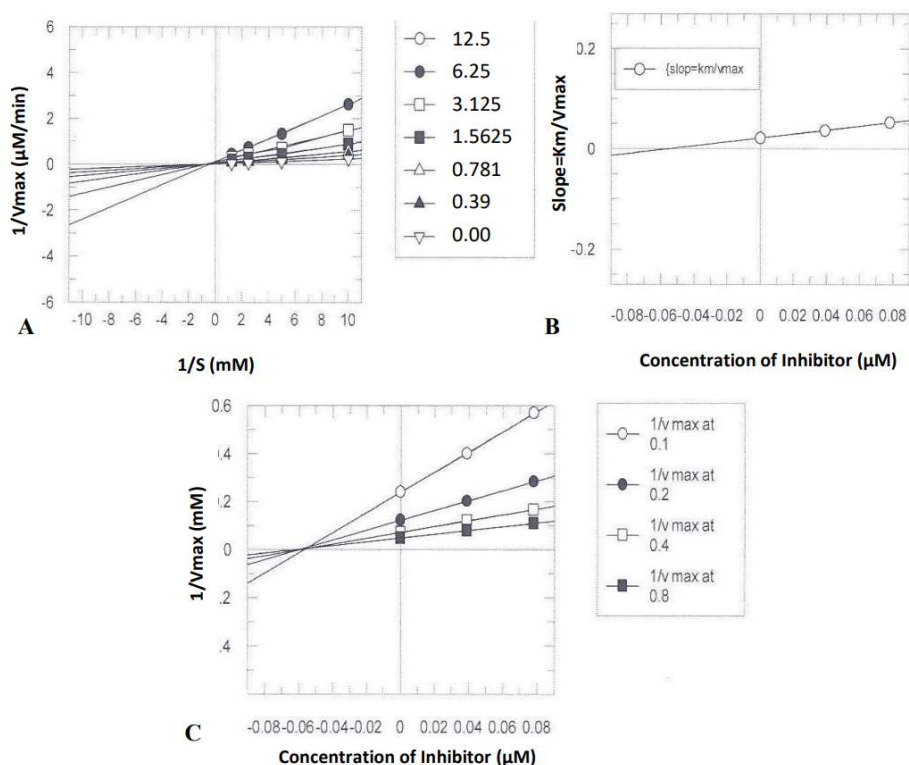


Figure 4: Inhibition of α -glucosidase by (*E*)-labda-8(17), 12-dien-15,16-dial (2).

A. Lineweaver-Burk plot (reciprocal of rate of reaction *versus* reciprocal of substrate both in the absence, and presence of 12.5, 6.25, 3.12, 1.56, 0.78, and 0.39 μM of compound 2); B. Secondary replot of Lineweaver-Burk plot (slopes of each line *versus* different concentrations of compound 2); C. Dixon plot (reciprocal of rate of reaction *versus* different concentrations of compound 2)

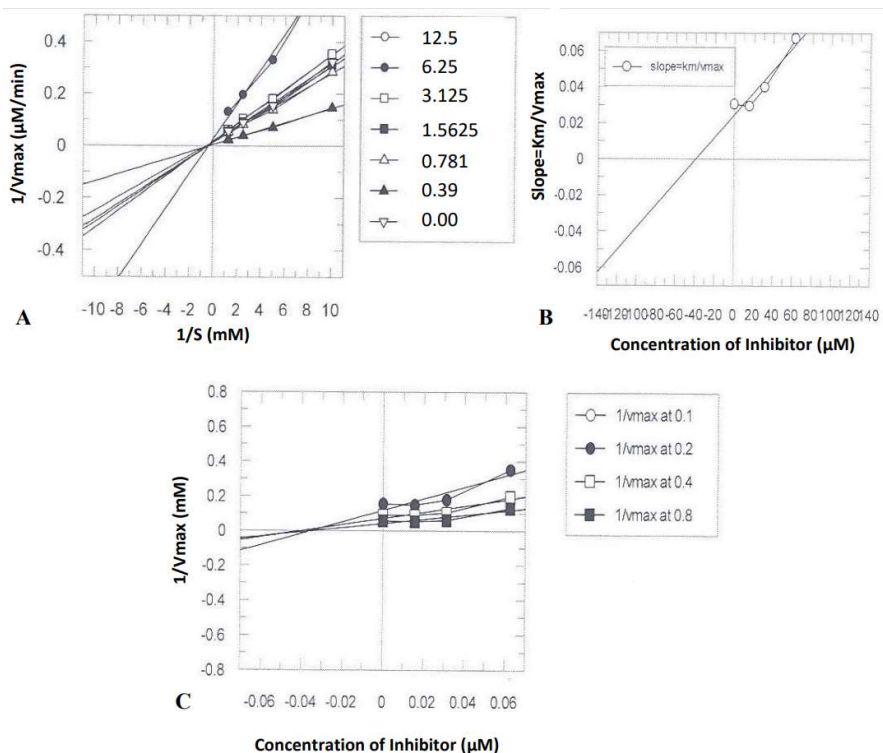


Figure 5: Inhibition of α -glucosidase by zerumin A (**3**)
 A. Lineweaver-Burk plot (reciprocal of rate of reaction *versus* reciprocal of substrate both in the absence, and presence of 12.5, 6.25, 3.12, 1.56, 0.78, and 0.39 μM of compound **3**); B. Secondary replot of Lineweaver-Burk plot (slopes of each line *versus* different concentrations of compound **3**); C. Dixon plot (reciprocal of rate of reaction *versus* different concentrations of compound **3**)

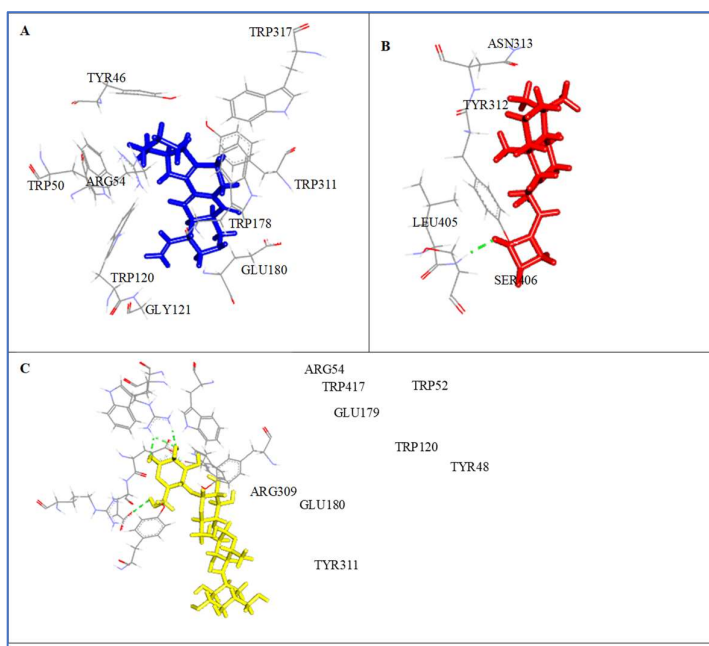


Figure 6: Interaction between α -glucosidase and the ligands with 3 Å region with hydrogen bonds. **A** angustine (**1**) (blue), **B** (*E*)-labda-8(17),12-dien-15,16-dial (**2**) (red), and **C** acarbose (yellow) at 10 ns simulation time.

Dynamics conformational changes of the protein-ligand complex

The trajectory stability was monitored, and confirmed by the analysis of the root mean squared deviations (RMSD) of all of the C α -atoms in Figure 7. Based on the docking results, the top-ranked conformations of ligands were selected for further studies in the MD simulation(s). The RMSD values fluctuated upon reaching a maximum of about 2.52 Å, 2.50 Å, and 2.77 Å for angustine (**1**), (*E*)-labda-8(17),12-dien-15,16-dial (**2**), and acarbose at 6 ns, 9 ns and 6 ns, respectively. During the simulation time, angustine (**1**) was observed to oscillate steadily within a small range as compared to the other two ligands.

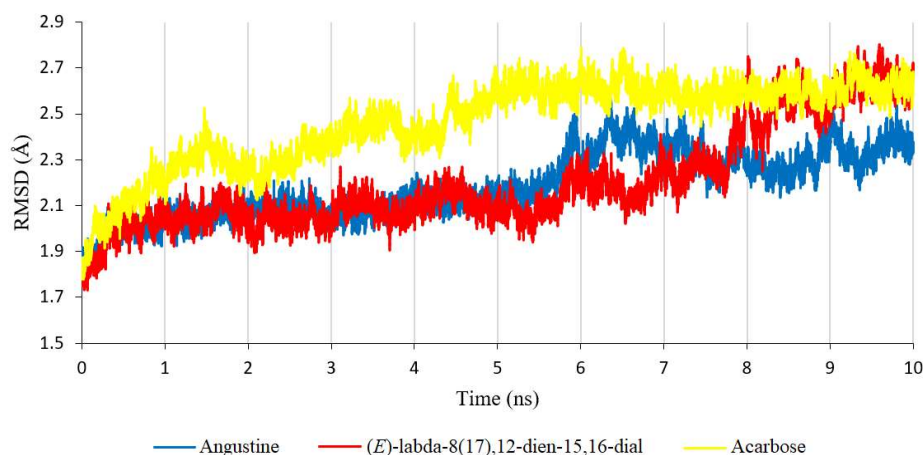


Figure 7: Root mean squared deviations (RMSD) of all C α -atoms of α -glucosidase with angustine (**1**) (blue), (*E*)-labda-8(17),12-dien-15,16-dial (**2**) (red), and acarbose (yellow) against simulation

Table 3: MM-PBSA/GBSA calculation during 6–10 ns of the MD simulations for α -glucosidase and selected ligands **1** and **2**

Method	Contribution	Energy in each contribution (kcal/mol) from 6–10 ns		
		Angustine (1)	(<i>E</i>)-Labda-8(17),12-dien-15,16-dial (2)	Standard (Acarbose)
MM	ELE	-5.60 ± 1.65	-3.21 ± 2.11	-66.51 ± 9.59
	VDW	-38.59 ± 2.04	-21.62 ± 1.93	-24.80 ± 4.04
	GAS	-44.19 ± 2.52	-24.83 ± 2.97	-91.32 ± 8.32
PBSA	PB _{SUR}	-4.93 ± 0.15	-4.21 ± 0.19	-5.01 ± 0.37
	PB _{CAL}	33.43 ± 3.41	21.30 ± 3.68	86.15 ± 8.69
	PB _{SOL}	28.50 ± 3.35	17.09 ± 3.57	81.15 ± 8.61
	PB _{ELE}	27.83 ± 3.26	18.09 ± 3.43	19.64 ± 8.90
	PB _{TOT}	-15.69 ± 3.35	-7.74 ± 3.05	-10.17 ± 6.70
GBSA	GB _{SUR}	-2.79 ± 0.10	-1.90 ± 0.16	-3.10 ± 0.24
	GB _{CAL}	23.40 ± 1.61	14.04 ± 1.93	88.19 ± 7.16
	GB _{SOL}	20.61 ± 1.59	12.13 ± 1.85	85.09 ± 7.13
	GB _{ELE}	17.79 ± 1.11	10.83 ± 1.46	21.68 ± 4.84
	GB _{TOT}	-23.58 ± 2.13	-12.70 ± 1.77	-6.23 ± 3.47

Note: ELE accounts for the electrostatic interaction, VDW denotes the Van der Waals interactions, GAS accounts for the addition ELE + VDW + INT being the binding enthalpic contributions in vacuo, PB_{SUR} accounts for the non-polar contribution to solvation, PB_{CAL} is the polar contribution of solvation, PB_{SOL} for the PB_{SUR} + PB_{CAL}, PB_{ELE} denotes the PB_{CAL} + ELE addition, and PB_{TOT} accounts for the total binding free energy calculated by the MM-PBSA method.

Binding free energy of the complex

The contribution of energies and the binding free energy of each complex are tabulated in Table 3. The calculations from MM-GBSA between 6 and 10 ns were approximate to the experimental value with a lower standard error of the mean, whereas the MM-PBSA protocol did not give any good correlation. Angustine (**1**) showed a lower GB_{TOT} value of -23.58 kcal/mol, as compared to (*E*)-labda-8(17),12-dien-15,16-dial (-12.70 kcal/mol) (**2**), and acarbose (-6.23 kcal/mol) during 6-10 ns of simulation with α -glucosidase. The main contribution of energy was from the Van der Waal's forces, rather than the electrostatic forces, for both angustine (**1**), and (*E*)-labda-8(17),12-dien-15,16-dial (**2**), while it was *vice versa* for the binding of acarbose. For a protein-ligand complex, properties which are calculated based on the MM-GBSA protocol are more often reported in the literature as they provide better correlations with the experimental results.

Important amino acid residues involved in binding of the complex

Binding free energies of each complex were analysed to investigate the important amino acid residues that showed strong interactions with the target proteins. Figure 8 illustrates the results of this analysis by plotting the decomposed energies against significant amino acid residues of each complex. The positive and negative values indicate the unfavourable and favourable contributions respectively. Residues which contribute to a large relative energy (< -1 kcal/mol) were considered as the key amino acid residues of the complex, while residues TRP50, TRP175, GLU 177, ARG301, and TYR307 were identified to have a significant contribution to the binding energy of angustine (**1**) with negative energy values of -1.08, -1.37, -1.07, -2.06, and -2.98 kcal/mol, respectively. TYR46, TRP117, and TYR307 were identified as important amino acid residues for (*E*)-labda-8(17),12-dien-15,16-dial (**2**) with the energy contributions of -1.5, -1.1, and -1.91 kcal/mol, respectively. Acarbose forms contact with important amino acids of PRO44, ARG52, TRP117, GLU176, ARG301, and TYR307 with energy values of -1.32, -7.03, -1.26, -1.25, -1.27 and -1.03 kcal/mol, respectively.

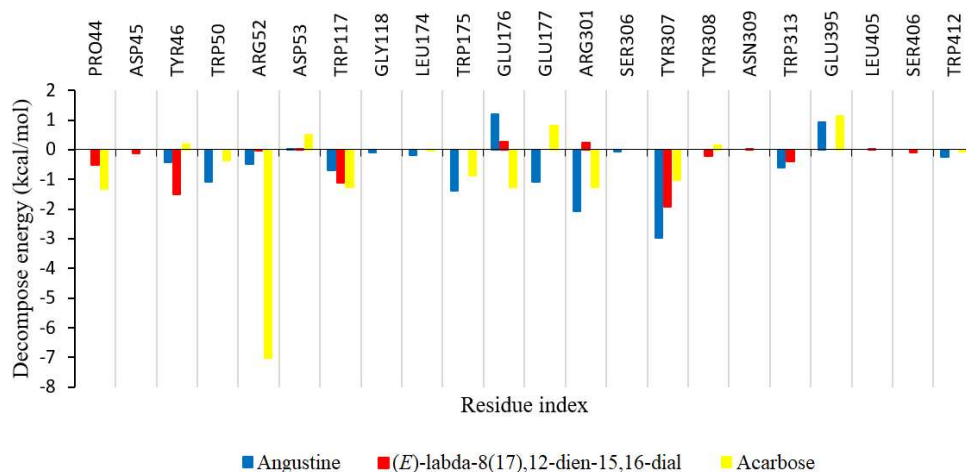


Figure 8: Decomposition of binding free energy on a per residue within 3 Å, including binding site region of α -glucosidase during 6-10 ns simulations

Since angustine (**1**) and (*E*)-labda-8(17),12-dien-15,16-dial (**2**) have better binding activities as compared to acarbose, the best conformations of angustine (**1**), and (*E*)-labda-8(17),12-dien-15,16-dial (**2**) were generated from their respective docking experiments and selected to perform the MD simulation to study their binding mechanisms and compared with acarbose. MD simulation was not performed for zerumin A (**3**), as it exhibited a lower activity as compared to other the two ligands. The RMSD values showed angustine (**1**) to be better in stability over simulation time. The MM-GBSA calculations revealed that angustine (**1**) had the lowest energy value as compared to the other two ligands, thus indicating it to be the most stable with the most favourable binding. Therefore, the kinetic study for angustine (**1**) showed a good correlation with the experimental results,

and thus it was identified as a potent α -glucosidase inhibitor. The analyses of the decomposed energy during 6–10 ns were carried out, however, for long-term MDs simulations at least 100 ns will be needed to explore in more detail to gain accurate details for the new drug discovery, design, and development. From our observation, ARG52 and ARG301 were identified as the key residues which bind with angustine (**1**) and acarbose, as they contributed to the negative value of the decomposed energy and were present at the binding site, which similarly found in the Xray complexes. ARG52 has a negative energy of -7.03 kcal/mol since it is able to form three hydrogen bonds with acarbose as compared to -0.47 kcal/mol for angustine (**1**). This indicated that ARG52 may have played a crucial role in binding with the ligands acarbose, and angustine (**1**). SER406 showed an energy value of -0.1 kcal/mol with (*E*)-labda-8(17),12-dien-15,16-dial (**2**), whereby this amino acid was apparently involved in the formation of the hydrogen bond.

CONCLUSION

This study involved the biochemical assay and study of kinetic patterns, molecular docking, the inhibitory aspects and binding modes of three natural compounds as α -glucosidase inhibitors. Through this study, potent natural α -glucosidase inhibitors were identified. Kinetic studies indicated that the compounds with electron donating groups take part in binding with the amino acid residues of the enzyme, α -glucosidase. This idea can be used for rational drug design toward the development of more effective inhibitors for therapeutic purposes. These lead molecules need to be further investigated *in-vivo* as anti-diabetic agents. From the knowledge of the binding conformation between the ligands and the target protein resulting from the molecular docking and MD simulation, angustine (**1**) was identified as a potential lead α -glucosidase inhibitor.

Acknowledgement

This work was supported by the Universiti Malaya Research Grant (BK005-2018).

Conflicts of Interest

The authors declare no conflict of interest.

REFERENCES

- Accelrys Discovery Studio (2009). Discovery Studio (Version Version 2.5.5). Accelrys Inc., San Diego, CA, USA.
- Aisiah S., Prajitno A., Maftuch M. & Yuniarti A. (2019). The potential of bangklaf leaf (*Nauclea subdita* [Korth.] Steud.) extract as antibacterial in catfish *Pangasius hypophthalmus* culture **12**(6): 2093–2102.
- Chong L.T., Duan Y., Wang L., Massova I. & Kollman P.A. (1999). Molecular dynamics and free-energy calculations applied to affinity maturation in antibody 48G7. *Proceedings of the National Academy of Sciences of the United States of America* **96**(25): 14330–14335.
- Darden T., York D. & Pedersen L. (1993). Particle mesh Ewald: An N log(N) method for Ewald sums in large systems. *The Journal of Chemical Physics* **98**(12): 10089–10092.
DOI: <http://dx.doi.org/10.1063/1.464397>
- Diana L.R. (2017). Uji aktivitas antidiabetes ekstrak etanol 70% daun taya (*Nauclea Subdita* (Korth) Steud) terhadap mencit putih (*Mus Musculus* L.) dengan induksi aloksan. *Indonesia Natural Research Pharmaceutical Journal* **2**(2): 79–87.
- Essmann U., Perera L., Berkowitz M.L., Darden T., Lee H. & Pedersen L.G. (1995). A smooth particle mesh Ewald potential. *The Journal of Chemical Physics* **103**(19): 8577–8593.
- Faridmoayer A. & Scaman C.H. (2004). An improved purification procedure for soluble processing alpha-glucosidase I from *Saccharomyces cerevisiae* overexpressing CWH41. *Protein Expression and Purification* **33**(1): 11–18.
DOI: <http://dx.doi.org/10.1016/j.pep.2003.09.013>
- Götz A. W., Williamson M.J., Xu D., Poole D., Le Grand S. & Walker R.C. (2012). Routine microsecond molecular dynamics simulations with AMBER on GPUs. 1. Generalized born. *Journal of Chemical Theory and Computation* **8**(5): 1542–1555.
DOI: <http://dx.doi.org/10.1021/ct200909j>
- Jorgensen W.L., Chandrasekhar J., Madura J.D., Impey R.W. & Klein M.L. (1983). Comparison of simple potential functions for simulating liquid water. *The Journal of Chemical Physics* **79**(2): 926–935.
DOI: <http://dx.doi.org/10.1063/1.445869>
- Kollman P.A. et al. (15 authors) (2000). Calculating structures and free energies of complex molecules: combining molecular mechanics and continuum models. *Accounts of Chemical Research* **33**(12): 889–897.

- DOI: <http://dx.doi.org/10.1021/ar000033j>
- Le Grand S., Götz A.W. & Walker R.C. (2013). SPFP: Speed without compromise—A mixed precision model for GPU accelerated molecular dynamics simulations. *Computer Physics Communications* **184**(2): 374–380.
DOI: <http://dx.doi.org/10.1016/j.cpc.2012.09.022>
- Liew S.Y., Looi C.Y., Paydar M., Cheah F.K., Leong K.H., Wong W.F., Mustafa M.R., Litaudon M. & Awang K. (2014). Subditine, a new monoterpenoid indole alkaloid from bark of *Nauclea subdita* (Korth.) Steud. induces apoptosis in human prostate cancer Cells. *PLoS ONE* **9**(2): e87286.
DOI: <http://dx.doi.org/10.1371/journal.pone.0087286>
- Liu D. *et al.* (13 authors) (2016). Design, synthesis and biological evaluation of 3'-benzylated analogs of 3'-epineponkoranol as potent α -glucosidase inhibitors. *European Journal of Medicinal Chemistry* **110**: 224–236.
DOI: <http://dx.doi.org/10.1016/j.ejmech.2016.01.029>
- Loo K.Y., Leong K.H., Sivasothy Y., Ibrahim H. & Awang K. (2019). Molecular insight and mode of inhibition of α -glucosidase and α -amylase by pahangensin A from *Alpinia pahangensis* Ridl. *Chemistry and Biodiversity* **16**(6): e1900032.
DOI: <http://dx.doi.org/10.1002/cbdv.201900032>
- Momany F.A. & Rone R. (1992). Validation of the general purpose QUANTA $\text{\textcircled{R}}$ 3.2/CHARMm $\text{\textcircled{R}}$ force field. *Journal of Computational Chemistry* **13**(7): 888–900.
DOI: <http://dx.doi.org/10.1002/jcc.540130714>
- Phang C.W., Malek S.N. & Ibrahim H. (2013). Antioxidant potential, cytotoxic activity and total phenolic content of *Alpinia pahangensis* rhizomes. *BMC Complementary and Alternative Medicine* **13**: 243.
DOI: <http://dx.doi.org/10.1186/1472-6882-13-243>
- Salomon-Ferrer R., Götz A.W., Poole D., Le Grand S. & Walker R.C. (2013). Routine microsecond molecular dynamics simulations with AMBER on GPUs. 2. explicit solvent particle mesh Ewald. *Journal of Chemical Theory and Computation* **9**(9): 3878–3888.
DOI: <http://dx.doi.org/10.1021/ct400314y>
- Simpson B.K., Nollet L.M.L., Toldrá F., Benjakul S., Paliyath G. & Hui Y.H. (2012). *Food Biochemistry and Food Processing*, 2nd edition. John Wiley & Sons, New York, USA.
- Sivasothy Y., Ibrahim H., Paliany A.S., Alias S.A. & Awang K. (2013a). Pahangensin A and B, two new antibacterial diterpenes from the rhizomes of *Alpinia pahangensis* Ridley. *Bioorganic and Medicinal Chemistry Letters* **23**(23): 6280–6285.
DOI: <https://doi.org/10.1016/j.bmcl.2013.09.082>
- Sivasothy Y., Ibrahim H., Paliany A.S., Alias S.A., Md Nor N.R. & Awang K. (2013b). A new bis-labdanic diterpene from the rhizomes of *Alpinia pahangensis*. *Planta Medica* **79**(18): 1775–1780.
DOI: <http://dx.doi.org/10.1055/s-0033-1351075>
- Sivasothy Y., Loo K.Y., Leong K.H., Litaudon M. & Awang K. (2016). A potent alpha-glucosidase inhibitor from *Myristica cinnamomea* King. *Phytochemistry* **122**: 265–269.
DOI: <http://dx.doi.org/10.1016/j.phytochem.2015.12.007>
- Sivasothy Y., Zachariah C.C.K., Leong K.H., John S.K.S., Ibrahim H. & Awang K. (2014). A novel heptacyclic diterpene from *Alpinia pahangensis* Ridley, a wild ginger endemic to Malaysia. *Tetrahedron Letters* **55**(45): 6163–6166.
DOI: <https://doi.org/10.1016/j.tetlet.2014.08.115>
- Spratt B.G. & Greenwood B.M. (2000). Prevention of pneumococcal disease by vaccination: does serotype replacement matter? *The Lancet* **356**(9237): 1210–1211.
DOI: [http://dx.doi.org/10.1016/S0140-6736\(00\)02779-3](http://dx.doi.org/10.1016/S0140-6736(00)02779-3)
- Sun S., Kadouh H.C., Zhu W. & Zhou K. (2016). Bioactivity-guided isolation and purification of α -glucosidase inhibitor, 6-*O-D*-glycosides, from Tinta Cão grape pomace. *Journal of Functional Foods* **23**: 573–579.
DOI: <http://dx.doi.org/10.1016/j.jff.2016.03.009>
- Tran N., Pham B. & Le L. (2020). Bioactive compounds in anti-diabetic plants: from herbal medicine to modern drug discovery. *Biology* **9**(9): 252.
DOI: <http://dx.doi.org/10.3390/biology9090252>
- Trott O. & Olson A.J. (2010). AutoDock Vina: improving the speed and accuracy of docking with a new scoring function, efficient optimization and multithreading. *Journal of Computational Chemistry* **31**(2): 455–461.
DOI: <http://dx.doi.org/10.1002/jcc.21334>
- Vanqualef E., Simon S., Marquant G., Garcia E., Klimerak G., Delepine, J.C., Cieplak P. & Dupradeau F.Y. (2011). R.E.D. Server: a web service for deriving RESP and ESP charges and building force field libraries for new molecules and molecular fragments. *Nucleic Acids Research* **39**(Issue Suppl. 2): W511–W517.
- Weber W., Hünenberger P.H. & McCammon J.A. (2000). Molecular dynamics simulations of a polyalanine octapeptide under Ewald boundary conditions: influence of artificial periodicity on peptide conformation. *The Journal of Physical Chemistry B* **104**(15): 3668–3675.
DOI: <http://dx.doi.org/10.1021/jp9937757>
- WHO (2016) *Global Report on Diabetes*. World Health Organization, Geneva, Switzerland.

RESEARCH ARTICLE

Plant Pathology

Molecular and phenotypic characterization of *Colletotrichum plurivorum* and *Colletotrichum musae* causing banana anthracnose disease in the Central Province of Sri Lanka

WMS Kurera^{1,2}, NKB Adikaram^{1,3*}, DMD Yakandawala³, SS Maharachchikumbura⁴, L Jayasinghe¹ and K Samarakoon¹

¹ National Institute of Fundamental Studies, Hantana Road, Kandy 20000, Sri Lanka.

² Postgraduate Institute of Science, University of Peradeniya, Peradeniya 20400, Sri Lanka.

³ Department of Botany, Faculty of Science, University of Peradeniya, Peradeniya 20400, Sri Lanka.

⁴ School of Life Science and Technology, University of Electronic Science and Technology of China, Chengdu, 611731, China.

Submitted: 21 November 2021; Revised: 30 July 2022; Accepted: 26 August 2022

Abstract: Most of the commercial banana cultivars in Sri Lanka are susceptible to anthracnose disease. *Colletotrichum musae* has been known as the causal agent of banana anthracnose for decades and the pathogen has been identified using morphological characteristics. Molecular analyses based on multigene phylogenetics are now standard protocols to identify *Colletotrichum* species. The present study was aimed at identifying *Colletotrichum* species causing banana anthracnose by molecular and phenotypic characterization. Thirty-seven isolates were obtained from ripened bananas showing anthracnose symptoms, collected from different locations in the Central Province of Sri Lanka. Of them, 36 were preliminarily identified as *Colletotrichum* based on conidial morphology. The remaining isolate did not sporulate during the entire study period. Ten isolates taken for molecular studies consisted of eight with orange/white aerial mycelia and orange conidial masses, one with a white to greyish colony and blackish clusters of ascospores, and one with a white to faint pink colour colony. DNA extracted from each isolate was subjected to multi-gene DNA sequence analysis using ITS, TUB, GAPDH and GS loci. Based on phylogenetic analyses, eight isolates were identified as *Colletotrichum musae*, and the other two as *C. plurivorum* and *C. siamense*. The vegetative morphology of *C. plurivorum* differed considerably from *C. musae* and *C. siamense*. Slight differences in colony morphology were observed among the *C. musae* isolates. Freshly harvested healthy bananas were artificially inoculated with isolates of *C. musae* or *C. plurivorum* and produced typical anthracnose lesions within a week. The *Colletotrichum siamense* isolate failed to develop anthracnose symptoms. This is the first report of *C. plurivorum* causing banana anthracnose.

Keywords: *Colletotrichum gloeosporioides* species complex, *Colletotrichum orchidearum* species complex, *C. plurivorum*, molecular phylogeny, pathogenicity.

INTRODUCTION

Bananas are among the most produced, traded and consumed fruits globally. More than 1000 varieties of bananas exist in the world. The most traded variety is the Cavendish banana. In 2020, the amount of bananas produced worldwide reached approximately 119.83 million tonnes (FAO, 2022).

Colletotrichum species comprise important plant pathogens that cause anthracnose disease in many economically important crops worldwide. Anthracnose is by far the most destructive postharvest disease in all banana-producing and marketing countries of the world (Abayasekara *et al.*, 2013), causing serious damage to fruit quality and drastically reducing shelf life and marketability.

Colletotrichum musae (Berkeley & M.A. Curtis) Arx was known as the causal agent of banana anthracnose disease for decades. The identification was mainly based on the host specificity and morphological characters. *Colletotrichum* infects immature banana fruits long before harvest in the field. The fungus is abundant in transition

* Corresponding author (nimal.ad@nifs.ac.lk;  <https://orcid.org/0000-0001-8570-1241>)



leaves and diseased crop debris, including flower parts, and the last bunch bract (de Lapeyre de Bellaire *et al.*, 2008), serving as major sources of the primary inoculum. Conidia, disseminated by rain and wind, adhere to the surface of the developing fruit, germinate producing germ-tubes, and form appressoria on the tip of germ-tubes. Infection pegs that emerge from appressoria penetrate the cuticle and epidermal cell wall of the host tissue. The fungus remains quiescent for long periods (Swinburne, 1983) and progressive lesion development takes place only with the commencement of fruit ripening, during storage or marketing. The typical anthracnose lesions in ripe bananas are dark, circular, sunken and numerous with salmon-pink conidia masses (Adikaram *et al.*, 2010). Quiescent infections are rather difficult to be controlled than wound infections (Abayasekara *et al.*, 2013; Wanigasekara *et al.*, 2014). Young fruits are usually free from visible symptoms. *Colletotrichum musae* is also associated with other diseases of bananas such as crown rot (Indrakeerthi & Adikaram, 2011), blossom-end rot and tip rot (Meredith, 1965).

Colletotrichum siamense Prihast., L. Cai & K.D. Hyde was identified as a pathogen causing anthracnose in bananas in Turkey using partial sequences of GAPDH, ACT and CHS-1 (Uysal & Kurt, 2020), India (Kumar *et al.*, 2017) and Brazil (Vieira *et al.*, 2017). *Colletotrichum gloeosporioides* (Penz.) Penz. & Sacc. (Cannon *et al.*, 2008) was reported as a causal agent of banana anthracnose in Ecuador (Riera *et al.*, 2019). In Malaysia, while 92% of isolates were identified as *C. gloeosporioides* (Penz.) Penz. & Sacc, only 8% of the isolates were *C. musae* (Sakinah *et al.*, 2014). *Colletotrichum scovillei* Damm, P.F. Cannon & Crous (Zhou *et al.*, 2017), *C. fruticola* Prihast., L. Cai & K.D. Hyde, *C. cliviicola* Damm & Crous, *C. siamense*, *C. karstii* You L. Yang, Zuo Y. Liu, K.D. Hyde & L. Cai, and *C. musae* (Huang *et al.*, 2021) were quite recently reported as causing banana anthracnose in China.

Most of the commercial banana cultivars in Sri Lanka are susceptible to the pathogens causing anthracnose disease. Popular banana cultivars of Sri Lanka include, ‘Ambon’ (*Musa acuminata*, AAA), ‘Anamalu’ (*Musa acuminata*, AAA), ‘Embul’ (*M. acuminata* x *M. balbisiana*, AAB), ‘Kolikuttu’ (*M. acuminata* x *M. balbisiana*, AAB), ‘Puwalu’ (*M. acuminata* x *M. balbisiana*, AAB) and, ‘Suwandal’ (*M. acuminata* x *M. balbisiana*, AAB) (Anthony *et al.*, 2004; Nazriya *et al.*, 2007; Abayasekara *et al.*, 2013).

Due to the global importance of *Colletotrichum* as a plant pathogenic genus, accurate diagnosis is essential to improve biosecurity and disease management strategies (Cannon *et al.*, 2012). However, cultural and morphological characteristics alone are insufficient to identify or differentiate *Colletotrichum* at the species level. Therefore, a polyphasic approach involving morphological and molecular methods and pathogenicity tests is needed for accurate species-level identification of *Colletotrichum* spp. Molecular analyses based on multigene phylogenetics, and pathogenicity assays are now the standard protocols to identify *Colletotrichum* species.

In spite of the establishment of molecular-based species-level identification of *Colletotrichum*, the identity of *Colletotrichum* species causing anthracnose disease in banana has not been performed. Therefore, the objectives of the present study were to, (i) collect banana fruits showing anthracnose disease symptoms from locations within the Central Province of Sri Lanka, irrespective of the cultivar, and to isolate *Colletotrichum* spp. from diseased fruits, (ii) characterize isolates morphologically and by performing a phylogenetic analysis of a sample of ten selected isolates, and complete species level identification, and (iii) confirm their pathogenicity. The present study identified the *Colletotrichum* species causing banana anthracnose in the Central Province (CP) of Sri Lanka using both morphological and molecular markers and pathogenicity tests.

MATERIALS AND METHODS

Collection of diseased fruits and isolation of fungi

Ripe fruits of banana cultivars, ‘Anamalu’ (*Musa acuminata*, AAA), ‘Emban’ (*M. acuminata*, AAA), ‘Kolikuttu’ (*M. acuminata* x *M. balbisiana*, AAB), ‘Puwalu’ (*M. acuminata* x *M. balbisiana*, AAB), and ‘Seeni’ (*M. acuminata* x *M. balbisiana*, ABB), showing characteristic symptoms of anthracnose disease were collected from fruit stalls and markets in different locations within the Central Province (CP), Sri Lanka in 2020. Diseased fruits were brought in sealed polythene bags to the laboratory at the National Institute of Fundamental Studies (NIFS), Kandy.

Peel segments ($0.5 \times 0.5 \text{ cm}^2$), cut from the advancing margins of anthracnose lesions, were surface sterilized in 1% NaOCl (Clorox[®], USA) for 1–3 min and rinsed twice in sterile distilled water (SDW). After removing the excess liquid by placing on sterile filter paper, tissue segments were aseptically transferred onto PDA (Himedia Lab, India) plates (4 segments per plate) in replicates of four plates per specimen. The plates were incubated at room temperature (RT, 25 °C). After 7 d, the mycelium that emerged from each of the tissue segment was sub-cultured on PDA.

Preparation of mono-conidial cultures

The mycelia scraped from 7 d old cultures, was suspended separately in 10 mL SDW. After shaking vigorously to release conidia, the suspensions were filtered through a muslin cloth. The concentration of conidia in the filtrate was adjusted to $5 \times 10^6/\text{mL}$. A loopful of each conidia suspension was streaked on Tap Water Agar (2 %, Himedia Lab, India). Following 12 to 18 h of incubation, a small piece of agar with a single germinated conidium located by moving the objective lens ($\times 25$) of the light microscope (Euromax BB.1153 PLi model) along the streak line, was transferred onto fresh PDA. Single spore isolates were sub-cultured and used for molecular studies (Johnston & Booth, 1983).

DNA extraction

Ten isolates, labelled C-1 to C-10, were used for molecular studies (Table 1) of which 8 were selected randomly from among 35 cultures showing pink to orange conidial masses. The two remaining isolates had contrasting colony morphologies compared with the first 35 isolates. DNA extraction was performed using Promega Wizard[®] Genomic DNA Purification Kit (Promega Corporation, USA). Mycelia were scraped using a sterile inoculation loop, from fresh cultures grown on PDA at 25 °C for 7 to 10 d for DNA extraction, which was performed according to the manufacturer's protocol with modifications i.e., addition of 20 μL proteinase K, after cooling to RT, following the addition of cell lysis solution (20 μL), nuclei lysis solution (20 μL) and incubating for 1 h at 65 °C. Finally, the DNA sample was stored at -20 °C in the freezer.

Table 1: The cultivars and locations from where the banana fruits were collected for obtaining the ten isolates used for DNA extraction.

Label	Collection location	Cultivar
C-1	Pilimalalawa	'Puwalu' (AAB)
C-2	Pilimalalawa	'Seeni' (ABB)
C-3	Kadugannawa	'Emban' (AAA)
C-4	Peradeniya	'Kolikuttu' (AAB)
C-5	Kandy	'Seeni' (ABB)
C-6	Kandy	'Puwalu' (AAB)
C-7	Pilimalalawa	'Seeni' (ABB)
C-8	Kadugannawa	'Anamalu' (AAA)
C-9	Kandy	'Seeni' (ABB)
C-10	Wattegama	'Kolikuttu' (AAB)

PCR amplification

Current taxonomic and phylogenetic studies on the genus *Colletotrichum* recommend the use of multiple gene regions for species-level identification (Damm *et al.*, 2012). The present study used four loci, internal transcribed spacer (ITS), glyceraldehyde-3-phosphate dehydrogenase (GAPDH), glutamine synthetase (GS) and β -tubulin (TUB), and were amplified using primer pair ITS1 and ITS4, GD92F1 and GDR1, GSF1 and GSR1 and, BT2a and BT2b, respectively (White *et al.*, 1990; Templeton *et al.*, 1992; Gardes & Bruns, 1993; Glass & Donaldson, 1995; Stephenson *et al.*, 1997; Weir *et al.*, 2012). All PCR amplifications were carried out using the Promega - 20 μl GoTaq[®] Green Master Mix, 0.2 μM each forward and reverse primers and 5 μL of unquantified DNA template. PCR reaction was performed using a thermal cycler (Applied Biosystems Veriti). The thermal cycler

was programmed to perform the PCR reactions using an initial denaturation at 95 °C for 4 min, 35 cycles of denaturation at 95 °C for 30 s and annealing at 52 °C, 60 °C, 54 °C and, 55 °C for ITS, GAPDH, GS and TUB2, respectively, for 30 s, extension at 72 °C for 45 s and a final extension at 72 °C for 7 min (Weir *et al.*, 2012).

The amplified PCR products were separated by electrophoresis in 1% agarose gel, stained with ethidium bromide, and visualized with a UV transilluminator. The PCR products were sequenced with the same primers (Applied Biosystems, 3500 genetic analyzer).

Phylogenetic analyses

Sequenced data of the four gene regions of each strain were visualized, and ambiguous bases were edited manually using MEGA6 software v. 6.0 (Tamura *et al.*, 2013). Sequences derived in this study were deposited in GenBank and the Accession numbers obtained are given in Supplementary Tables 1 and 2. These sequences were subjected to a similarity-based search using the NCBI, BLASTn programme. Initial blast results showed that the isolates belonged to two species complexes, the *C. gloeosporioides* and the *C. orchidearum* species complex. Hence, two different datasets were used to estimate two phylogenies, the *C. gloeosporioides* species complex tree based on combined ITS + GAPDH + TUB + GS regions, and the *C. orchidearum* species complex tree based on combined ITS + GAPDH. A Maximum Likelihood (ML) analysis was conducted using raxmlGUI v. 1.3 (Silvestro & Michalak, 2012). The optimal ML tree search was performed with 1000 separate runs, employing the default algorithm of the programme from a random starting tree for each run. The ultimate tree was chosen amongst suboptimal trees from each run by examining likelihood scores under the GTR + GAMMA substitution model. The resulting phylogenetic tree (Table 3) was visualized in FigTree v. 1.2.2 (Rambaut & Drummond, 2008).

Colony and reproductive morphology of isolates

Suspensions of conidia were prepared from 7–10 d old mono-conidial cultures of *Colletotrichum* isolates as described previously. Drops of conidia of each isolate were mounted on microscope slides and examined under a light microscope and photographed (Olympus BX53 with DP 74 Digital Camera & cellSens software ver. 2.1, Olympus, Japan). The dimensions of 50 randomly selected conidia from each drop were measured. The average width and length were calculated.

Appressoria were produced in fungal hyphae using a slide culture technique (Sutton, 1968). A few Petri plates were poured with a thin layer of PDA. Square pieces (10 mm²) of PDA were cut and placed in the centre of empty sterile Petri plates. The four edges of each agar piece were inoculated with conidia taken from a sporulating culture and a sterile cover slip was placed over the inoculated agar. After 7 d, the appressoria formed on the underside of the cover slip were examined (Prihastuti *et al.*, 2009) under a light microscope, and their morphology, dimensions and other features were recorded and photographed (Olympus BX53 with DP 74).

Pathogenicity test

Conidial suspensions of *C. musae* (C-1 to C-4 & C-7 to C-10) and *C. siamense* (C-6) were prepared by suspending the mycelium scraped from 14 d old cultures in SDW and filtering through a muslin cloth. The concentration of conidia was adjusted to approximately 1×10⁶/mL. Since isolate C-5 did not produce conidia, a suspension of ascospores was prepared. Clusters of perithecia, carefully picked from a 14 d old culture, were crushed and suspended in 10 mL SDW. The suspension was vigorously shaken on a Vortex mixer to force the release of ascospores and the suspension was filtered through a muslin cloth. The concentration of ascospores was adjusted to approximately 1×10³/mL. Seven drops (20 µL) of conidia or ascospores from each isolate were separately applied on to the surface of freshly harvested, mature fruits of bananas cv. ‘Emban’ (AAA) in triplicates, along the long axis, leaving a 2 cm space between each drop. A set of bananas, similarly treated with drops (20 µL) of SDW, was maintained as a control. Inoculated and control fruits were arranged in trays lined with moistened tissues and covered with glass plates, and incubated at 26–28 °C. The fruits were observed daily for disease development. Once the symptoms appeared, the pathogen was re-isolated on PDA and compared with the original isolate used for inoculation.

RESULTS AND DISCUSSION

Collection of diseased bananas and isolation of fungi

A total of 37 isolates were collected from diseased banana fruits belonging to a range of cultivars. Thirty-six isolates (97.3%) produced oblong conidia and yellow/orange or pale orange conidiomata, which were tentatively identified as belonging to the genus *Colletotrichum* using colony and conidial morphology. The remaining isolate did not produce any conidia.

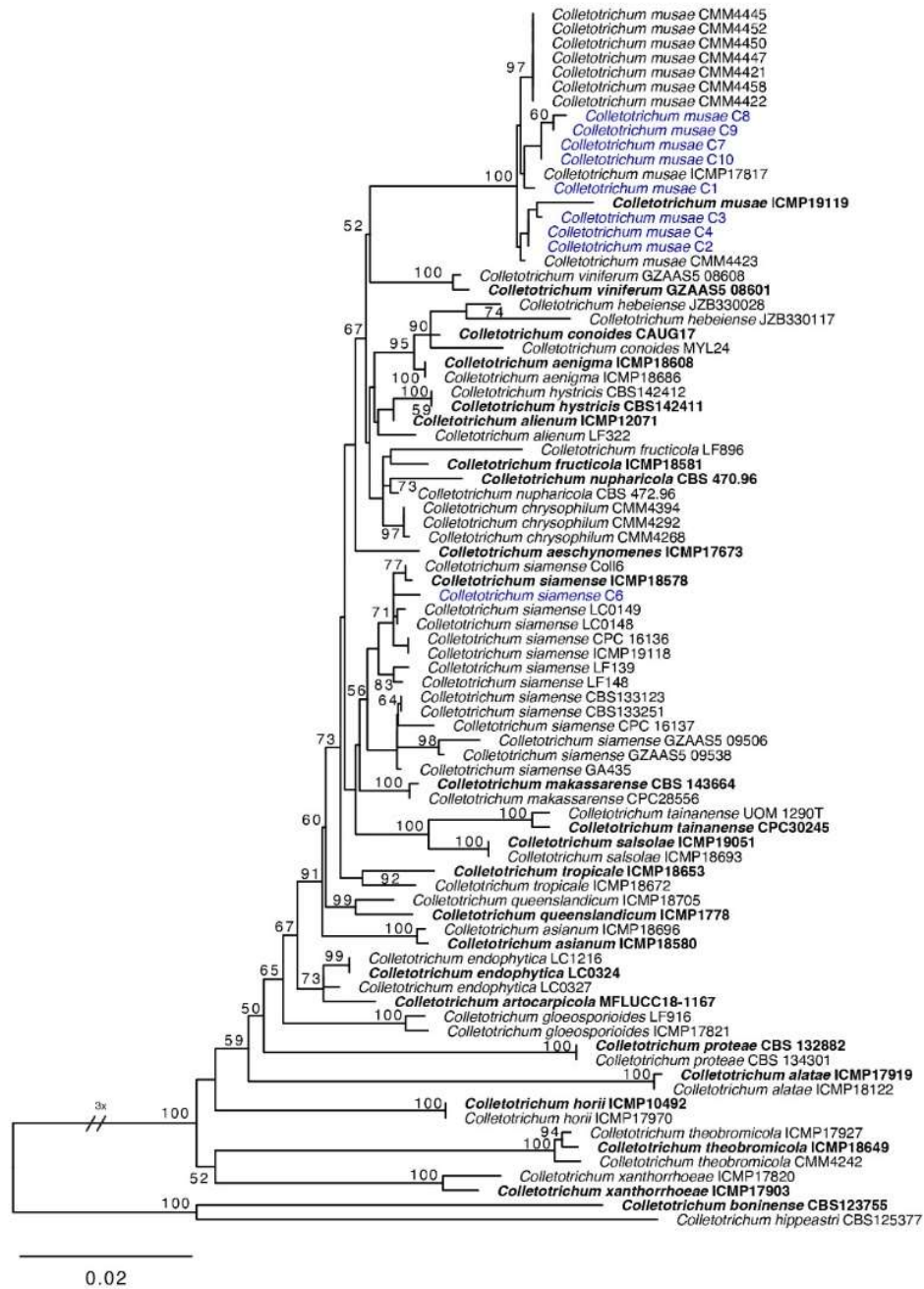


Figure 1: Phylogenetic relationships in the *Colletotrichum gloeosporioides* species complex based on combined ITS+GAPDH+GS+TUB loci. The isolates derived from the present study are in blue. Type strains are in bold.

Molecular identification of isolates

Ten isolates, C-1 to C-10 (Table 1), were used for molecular studies. The combined GAPDH + GS + ITS + TUB dataset for the *C. gloeosporioides* species complex comprised 84 strains, including two out-group taxa from the *C. boninense* species complex (*Colletotrichum boninense* Moriwaki, Toy. Sato & Tsukib. strain CBS 123755 and *Colletotrichum hippeastri* Yan L. Yang, Zuo Y. Liu, K.D. Hyde & L. Cai strain ICMP 17920). The concatenated data matrixes comprised 2409 characters (GAPDH: 276, GS: 868, ITS: 564, and TUB: 701). The ML analysis for 1,000 bootstrap replicates yielded a tree with the likelihood value of ln: -18432.224367.

Based on the phylogenetic tree (Figure 1), the isolates C-1, C-2, C-3, C-4, C-7, C-8, C-9, and C-10 were identified as *C. musae* and one strain (C-6) clustered with the strains of *C. siamense*. Both *C. musae* and *C. siamense* belong to the *C. gloeosporioides* species complex. *Colletotrichum musae*, while showing its prominence as an anthracnose pathogen in bananas, is also involved in causing banana crown rot (Indrakeerthi & Adikaram, 2011).

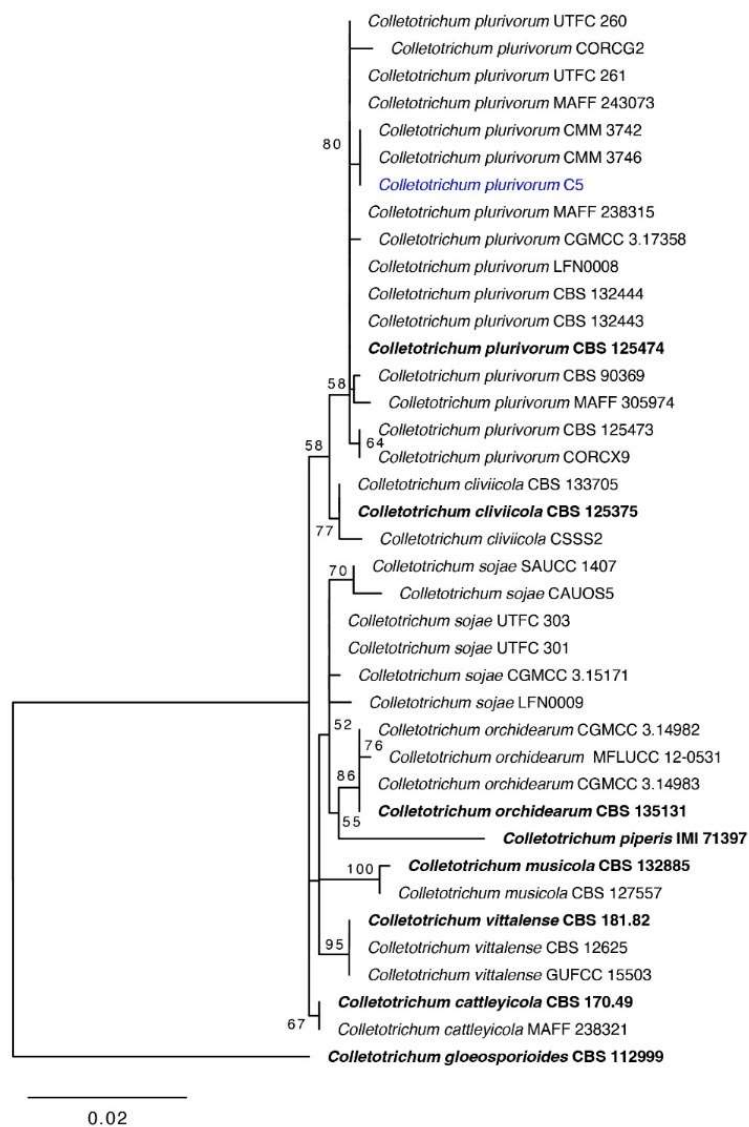


Figure 2: Phylogenetic relationships in the *Colletotrichum orchidearum* species complex based on combined ITS+GAPDH loci. The isolate derived from the present study is in blue.

The combined ITS + GAPDH dataset for the *C. orchidearum* species complex comprised 39 strains, including an out-group taxon from the *C. gloeosporioides* species complex (*C. gloeosporioides* isolate CBS 112999). The aligned data matrixes comprised 839 characters (ITS: 553 and GAPDH: 286). The ML analysis for 1,000 bootstrap replicates yielded a tree with the likelihood value of $\ln: -13321.232547$. The isolate C-5 formed a clade with reference strains of *Colletotrichum plurivorum* Damm, Alizadeh & Toy. Sato (Figure 2).

Colletotrichum plurivorum, belonging to the *C. orchidearum* species complex, was previously isolated from leaves of *Musa* sp. in Japan (Damm *et al.*, 2012), and known to be associated with the fruit rot of papaya in Taiwan (Sun *et al.*, 2019), anthracnose disease in chilli pepper (*Capsicum annuum*) in Andaman and Nicobar Islands (Sakthivel *et al.*, 2018), okra in Brazil (Batista *et al.*, 2020), and cassava in China (Liu *et al.*, 2019).

Colony and reproductive morphology

Colonies of *C. musae*, grown on PDA, produced orange to pinkish-white, cottony aerial mycelium and abundant bright orange conidial masses or conidiomata (Figure 3). The lower surface had white to greyish-orange pigmentation. The colony characteristics, texture, and pigmentation underneath, varied slightly within the eight *C. musae* isolates but pink/orange aerial mycelium was common to a majority (87.5%) of the identified isolates C1 to C-4, C-7, C-8, C-10. *Colletotrichum musae* was the fastest in colony growth on PDA among the three species, and *C. plurivorum* was the next (Table 2). The *Colletotrichum musae* isolate C-9, produced whitish to faint orange aerial mycelium and also tiny, faint orange coloured conidiomata over the centre of the colony (Figure 3).

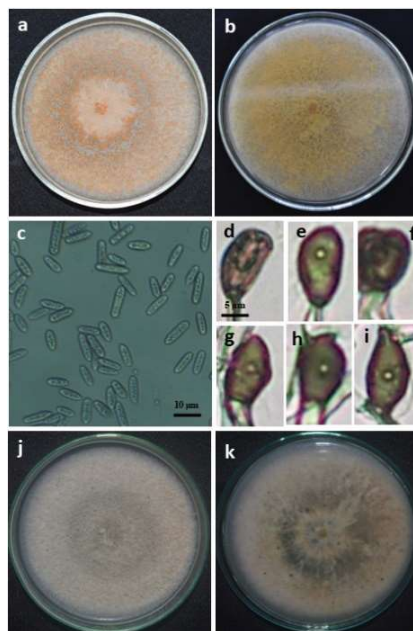


Figure 3: Colony morphology of *C. musae* isolate C-1, grown on PDA at 25 °C for 14 days, with orange aerial mycelium and conidiomata, common to seven *C. musae* isolates, C-1 to C-4, C-7, C-8 & C-10; (a) upper, and (b) lower surface, (c) conidia, and (d, e, f, g, h, i) appressoria. (j) *C. musae* isolate C-9 with slightly different colony morphology from the seven isolates, with whitish aerial mycelium and some conidiomata in the centre, upper, and (k) lower surface.

Conidia were abundant, hyaline, aseptate, guttulate, oval, elliptical or cylindrical, often with a flattened base and obtuse apex. Vegetative hyphae of all three species, grew on agar pieces in slide cultures and formed appressoria.

Each species produced appressoria of varied morphological forms. Appressoria of *C. musae* in slide cultures were medium to dark brown and irregular, the edges were entire or slightly lobed (Figure 3; Table 2).

The colony of *C. siamense* (C-6) on PDA was pale-yellow to pinkish white, circular with an irregular margin, white; aerial mycelium sparse to abundant and cottony, with pale orange conidial masses in the centre of colony. The lower surface was also pale-yellow to pinkish-white (Figure 5). Conidia hyaline, aseptate, smooth-walled, fusiform to cylindrical, both ends bluntly rounded. Appressoria single, medium to dark brown, smooth-walled, elliptical, navicular, bullet-shaped or irregular outline, with undulate or frequently lobate margin (Figure 5). These indicate that *C. siamense* shows slight differences in colony morphology compared to *C. musae*. The isolate was comparatively slow-growing (Table 2).

Colonies of *C. plurivorum* (C-5) on PDA were circular with dense, white to greyish aerial mycelium. The lower surface of the colony appeared yellowish green (Figure 4). Colony morphology was quite distinct from the other two species, *C. musae* and *C. siamense*, due to its white-to-greyish aerial mycelium containing dense, clusters of blackish ascomata spread over the colony (Figure 4). The eight *C. musae* isolates, and the single isolate of *C. siamense*, could be conveniently separated from *C. plurivorum* (Figure 4) using colony morphology (Figure 3). However, the morphological characteristics of singular isolates like *C. plurivorum* or *C. siamense* cannot be compared with species like *C. musae* with several isolates with confirmed identity in the present study.

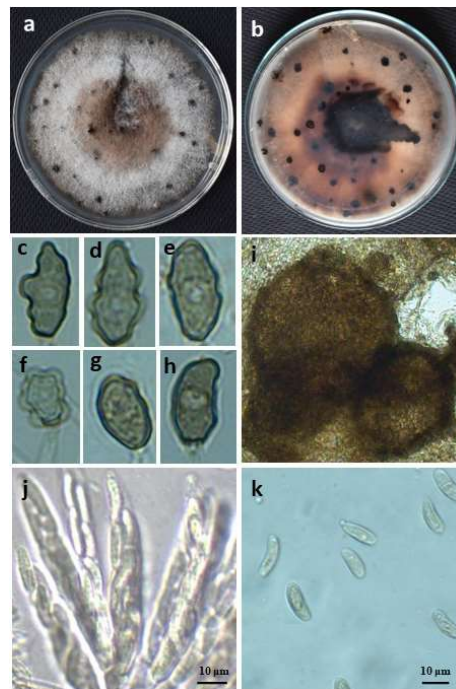


Figure 4: Colony morphology and microscopic characteristics of *Colletotrichum plurivorum*. A 14-day old culture (C-5) grown on PDA at 25 °C (a) upper surface, (b) lower surface, (c, d, e, f, g, h) appressoria produced in vegetative hyphae, (i) perithecia, (j) asci, and (k) ascospores.

Interspecific morphological variability could also be expected within individual species of *C. plurivorum* or *C. siamense*. Cultural characteristics are normally considered as less important criteria for distinguishing species within the genus *Colletotrichum* since they can be influenced by changing environmental factors and growth conditions (Cannon *et al.*, 2012). Due to these inconsistencies, morphological characteristics alone are considered insufficient to identify or differentiate *Colletotrichum* at the species level.

Appressoria of *C. plurivorum* were single, pale to medium brown with a tint of light black background and smooth-walled with varied shapes, sub-globose to globose or irregular shaped, the edge undulated, crenate or slightly lobed (Figure 4; Table 2). Ascospores formed on PDA in clusters, covered by aerial mycelium, black, globose, solitary or gregarious and 140–290 µm diameter. Individual perithecia were ostiolate, the outer wall composed of greenish-grey angular cell. Asci were cylindrical, obclavate to clavate and 8-spored; ascospores were hyaline, smooth-walled, aseptate, fusoid, with rounded ends, straight or slightly curved (Figure 4; Table 2).

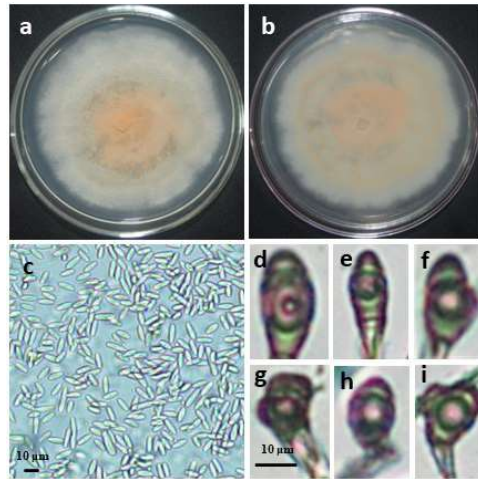


Figure 5: Colony and microscopic characteristics of *Colletotrichum siamense* (C-6) culture, grown on PDA for 14 d at 25 °C, (a) upper and (b) lower surface of the colony, (c) conidia, and (d, e, f, g, h, i) appressoria.



Figure 6: Anthracose lesions developed in ripe banana cultivar 'Emban' (AAA), 7 d after inoculation with conidia of *Colletotrichum musae* (C-1 to C-4 & C-7 to C-10), *C. siamense* (C-6) and ascospores of *C. plurivorum* (C-5).

Pathogenicity test

The banana fruits, artificially inoculated with all nine *Colletotrichum* isolates separately, developed anthracnose lesions with the commencement of ripening. The lesions gradually became darker, slightly depressed, and expanded in size with time. Pink-coloured conidial masses appeared on the surface of colonies of *C. musae* or *C. siamense*. Symptoms developed by the isolates were typical of anthracnose disease, the size of lesions, however, varied slightly among the isolates (Figure 6). *Colletotrichum siamense* (C-6), on the other hand, produced only minute superficial specks none of which developed into progressive lesions.

The isolates of *C. musae* appeared highly pathogenic on the banana cultivar ‘Emban’. The varied size of anthracnose lesions produced by *C. musae* isolates on inoculation indicates the existence of differences in virulence among isolates within the species. C-1 and C-9 appeared to be the most and the least virulent isolates of *C. musae* respectively. *Colletotrichum musae* isolate C-9 also displayed contrasting colony morphology from the rest of the *C. musae* isolates.

Table 2: Vegetative and reproductive morphology of *Colletotrichum* isolated and identified from banana fruits

Parameter	C-1 to 4 & C-7 to 10, <i>Colletotrichum musae</i>	C-5, <i>Colletotrichum plurivorum</i>	C-6, <i>Colletotrichum siamense</i>
Colony characteristics	Orange to pinkish-white, cottony mycelium with abundant yellow/orange conidial masses, the lower surface was white to greyish orange colour (Figure 3).	White to greyish, dense aerial mycelium and, black, clusters of perithecia spread over the colony (Figure 4).	Colonies yellow to pinkish-white, sparse to abundant, aerial mycelium pale orange conidiomata (Figure 5).
Average colony growth mm d ⁻¹	11.43	10.71	9.29
Conidial morphology	Hyaline, aseptate, oval to cylindrical	Isolate did not produce conidia.	Hyaline, aseptate, cylindrical to subcylindrical, spindle-shaped with obtuse ends.
Conidial dimensions (µm)	11.16 – 14.2 (12.5 ± 1.5) × 4.68 – 5.56 (5.0 ± 0.5)	-----	14.5 – 16.7 (15.8 ± 0.9) long × 4.2 – 4.9 (4.55 ± 0.35)
Perithecia, ascus, ascospore morphology & dimensions (µm)	(not produced)	Ascomata globose, irregular, solitary or gregarious, black, 150–300 µm diameter. Perithecia solitary, sub-globose, ostiolate outer wall composed of greenish grey angular cells, glabrous, 100 – 200 × 95 – 160. Asci cylindrical, obclavate to clavate 32–55 × 7.3–13, 8-spored. Ascospores hyaline, smooth-walled, aseptate, fusiform, straight or slightly curved, with rounded ends, straight or slightly curved. 14.5 – 16.7 (15.8 ± 0.9) × 4.2 – 4.9 (4.55 ± 0.35)	(not produced)
Appressoria morphology	Single, medium to dark brown, smooth-walled, oval, elliptical or heart-shaped, with undulate or slightly lobate margin.	Mostly single, pale to medium brown, smooth-walled, sub-globose to globose, the edge undulate, crenate or slightly lobed. Only a few appressoria were produced.	Single, medium to dark brown, smooth-walled, elliptical, navicular or bullet-shaped, with undulate or lobate margin.
Appressoria Dimensions (µm)	Mean ± SD = 11.5 ± 2.5 × 9.7 ± 1.5	Mean ± SD = 15.4 ± 3.0 × 8.8 ± 2.6	Mean ± SD = 12.5 ± 2.9 × 6.8 ± 1.3
Average lesion diameter of inoculated fruit (cm)	1.44 ± 0.54	1.1 ± 0.46	<i>C. siamense</i> did not develop lesions.

Banana fruits, inoculated with ascospores of the *C. plurivorum* isolate also developed fairly larger anthracnose lesions similar to suggesting a reasonably higher level of pathogenicity. The symptoms developed were quite similar to the progressive anthracnose lesions developed from natural infections. Although

C. plurivorum appeared to be moderately pathogenic to banana fruits, its association with the anthracnose disease in other fruit species is not very common.

The *C. siamense* isolate (C-6) failed to develop progressive lesions in bananas inoculated artificially. Instead, brown colored, superficial specks appeared only on the inoculation sites of the fruit peel, which did not expand into progressive lesions. The isolate (C-6) maybe a variant with an inability of forming appressoria on germ-tubes of germinating conidia, which could be a possible reason for its failure to develop anthracnose lesions. *Colletotrichum* species generally produce distinct appressoria, which facilitate the pathogen-penetration through intact fruit surface. Morphology of colonies, conidia or ascospores produced in cultures raised through re-isolation on PDA was similar to those of the *Colletotrichum* isolates used for fruit inoculation.

Two *Colletotrichum* species isolated from banana fruits in the present study were identified as belonging to the *C. gleosporioides* species complex while *C. plurivorum* belongs to the *C. orchideorum* species complex based on molecular studies. Identification of new and unknown *Colletotrichum* species associated with banana anthracnose reflects the significance of continuous investigations into *Colletotrichum* systematics, which could help reduce the risk from unknown pathogens to the country's banana fruit industry.

Accurate identification is vital since the scientific name links the knowledge concerning a species including the biology, host range, distribution, and potential risk of the pathogen, which are necessary for planning effective control strategies, biosecurity and screening new banana cultivars against anthracnose (Bhunjun *et al.*, 2021). Determination of the pathogenicity or the capability of the pathogen/s to cause host damage is also important, which usually relies upon the application of Koch's postulates for fungal plant pathogens. Similar trends have been found in the composition of *Colletotrichum* species causing anthracnose disease in other fruits, avocado (Sharma *et al.*, 2017), chilli (Diao *et al.*, 2017), and the ornamental plants, begonia (Wickramasinghe *et al.*, 2020) and anthurium (Vithanage *et al.*, 2021).

In summary, the current study represents the most comprehensive investigation of *Colletotrichum* species on banana in the CP of Sri Lanka. The study revealed that *Colletotrichum plurivorum* and *C. musae* were the causal agents of banana anthracnose in the province. *Colletotrichum musae* was the most frequently isolated pathogen. *Colletotrichum siamense* was also isolated but the pathogenicity tests showed its inability to produce typical anthracnose symptoms from artificial inoculation.

CONCLUSIONS

The study identified *Colletotrichum musae* and *C. plurivorum* as the causal agents of banana anthracnose in the CP of Sri Lanka. *Colletotrichum musae* was the most frequently found species among the isolates subjected to molecular studies. *Colletotrichum siamense* isolated in the study was not found to be pathogenic to banana fruits (Emban, AAA) making its role in banana anthracnose quite uncertain.

This is the first report of the involvement of *C. plurivorum* causing banana anthracnose anywhere in the world.

Acknowledgement

Authors gratefully acknowledge the Postgraduate Institute of Science, University of Peradeniya for part-funding of research.

Competing Interests

All authors disclose that they have no competing interest.

REFERENCES

- Abayasekara C.L., Adikaram N.K.B. & Bandara B.M.R. (2013). *Phyllosticta musarum* infection-induced defences suppress anthracnose disease caused by *Colletotrichum musae* in banana fruits cv 'Embul'. *The Plant Pathology Journal* **29**(1): 77–86.

- DOI: <https://doi.org/10.5423/PPJ.OA.06.2012.0081>
- Adikaram N., Karunanayake C. & Abayasekara C. (2010). Chapter 1: The role of pre-formed antifungal substances in the resistance of fruits to postharvest pathogens. In: *Postharvest Pathology, Plant Pathology in the 21st Century* (eds. D. Prusky & M.L. Gullino), pp. 1–11, volume 2. Springer.
DOI: https://doi.org/10.1007/978-1-4020-8930-5_1
- Anthony S., Abeywickrama K., Dayananda R., Wijeratnam S. & Arambewela L. (2004). Fungal pathogens associated with banana fruit in Sri Lanka, and their treatment with essential oils. *Mycopathologia* **157**(1): 91–97.
- Batista I.C.A., Boari A.D.J., Kauffmann C.M. & Lima Nechet K de. (2020). *Colletotrichum plurivorum* causes anthracnose on okra in Brazil. *Journal of Plant Pathology* **102**: 1331.
DOI: <https://doi.org/10.1007/s42161-020-00615-1>
- Bhunjun C.S., Phillip A. J. L., Jayawardena R.S., Promputtha I. & Hyde K.D. (2021). Importance of molecular data to identify fungal plant pathogens and guidelines for pathogenicity testing based on Koch's Postulates. *Pathogens* **10**: 1096.
DOI: <https://doi.org/10.3390/pathogens10091096>
- Cannon P.F., Buddie A.G. & Bridge P.D. (2008). The typification of *Colletotrichum gloeosporioides*. *Mycotaxon* **104**: 189–204.
- Cannon P.F., Damm U., Johnston P.R. & Weir B.S. (2012). *Colletotrichum* – Current status and future directions. *Studies in Mycology* **73**: 181–213.
DOI: <https://doi.org/10.3114/sim0014>
- Damm U., Cannon P.F., Woudenberg J.H.C. & Crous P.W. (2012). The *Colletotrichum acutatum* species complex. *Studies in Mycology* **73**: 37–113.
- De Lapeyre de Bellaire L., Chillet M., Dubois C. & Mourichon X. (2008). Importance of different sources of inoculum and dispersal methods of conidia of *Colletotrichum musae*, the causal agent of banana anthracnose for fruit contamination. *Plant Pathology* **49**: 782–790.
DOI: <https://doi.org/10.1046/j.1365-3059.2000.00516.x>
- Diao Y.Z., Zhang C., Liu F., Wang W.Z., Liu L., Cai L. & Liu X. L. (2017). *Colletotrichum* species causing anthracnose disease of chili in China. *Persoonia* **38**: 20–37.
DOI: <https://doi.org/10.3767/003158517X692788>
- Food and Agriculture Organization of the United Nations (2022). Bananas. Available at <https://www.fao.org/markets-and-trade/commodities/bananas/en/>. Accessed 05 October 2022.
- Gardes M. & Bruns T.D. (1993). ITS primers with enhanced specificity for basidiomycetes - Application to identification of mycorrhizae and rusts. *Molecular Ecology* **2**: 113–118.
DOI: <https://doi.org/10.1111/j.1365-294X.1993.tb00005.x>
- Glass N.L. & Donaldson G.C. (1995). Development of primer sets designed for use with the PCR to amplify conserved genes from filamentous ascomycetes. *Applied and Environmental Microbiology* **61**(4): 1323–1330.
- Huang R., Sun. W., Wang L., Li Q., Huang S., Tang L., Guo T., Mo J. & Hsiang T. (2021). Identification and characterization of *Colletotrichum* species associated with anthracnose disease of banana. *Plant Pathology* **70**(8): 1827–1837.
DOI: <https://doi.org/10.1111/ppa.13426>
- Indrakeerthi S.R.P. & Adikaram N.K.B. (2011). Control of crown rot of banana using *Carica papaya* latex. *Journal of the National Science Foundation of Sri Lanka* **39**(2): 155–162.
- Johnston A. & Booth C. (1983). *Plant Pathologist's Handbook*, 2nd edition, pp. 333–334. Commonwealth Mycological Institute, England.
- Kumar V.S., Nair B.A., Nair P.V.R., Annamalai A., Jaishanker R., Umamaheswaran K., Sooraj N.P. & Peethambaran C.K. (2017). First report of *Colletotrichum siamense* causing anthracnose of cliff banana in India. *Plant Disease* **101**(2): 390.
- Liu X., Shi T., Li B., Cai J., Li C. & Huang G. (2019). *Colletotrichum* species associated with cassava anthracnose in China. *Journal of Phytopathology* **167**(1): 1–9.
- Meredith D.S. (1965). Tip rot of banana fruits in Jamaica: II. *Verticillium theobromae* and *Fusarium* spp. *Transactions of the British Mycological Society* **48**(2): 327–336.
- Nazriya N.F., De Costa D.M. & Azhaar A.S. (2007). Genomic variations of *Colletotrichum musae* morphotypes infecting banana varieties of Sri Lanka. *Proceedings of the Peradeniya University Research Sessions, Sri Lanka* **12**(1): 1–2.
- Prihastuti H., Mckenzie E., Hyde K., Cai L., Mckenzie H. & Hyde E. (2009) Characterization of *Colletotrichum* species associated with coffee berries in northern Thailand. *Fungal Diversity* **39**: 89–109.
- Rambaut A. & Drummond A. (2008). FigTree: Tree figures drawing tool, version 1.2. 2. Institute of Evolutionary Biology, University of Edinburgh, UK.
- Riera N., Ramirez-Villalacis D., Barriga-Medina N., Alvarez-Santana J., Herrera K., Ruales C. & Leon-Reyes A. (2019). First report of banana anthracnose caused by *Colletotrichum gloeosporioides* in Ecuador. *Plant Disease* **103**(4): 763–763.
- Sakinah M.A.I., Suzianti I.V. & Latiffah Z. (2014). Phenotypic and molecular characterization of *Colletotrichum* species associated with anthracnose of banana (*Musa* spp.) in Malaysia. *Genetics and Molecular Research* **13**(2): 3627–3637.
- Sakthivel K., Manigundan K., Sneha S., Patel A., Charishma K., Neelam S., Gautam R.K. & Kumar A. (2018). First report of *Colletotrichum plurivorum* from the Andaman and Nicobar Islands causing anthracnose in chilli (*Capsicum annum*). *New Disease Reports* **38**: 26.
DOI: <http://dx.doi.org/10.5197/j.2044-0588.2018.038.026>

- Sharma G., Maymon M. & Freeman S. (2017). Epidemiology, pathology and identification of *Colletotrichum* including a novel species associated with avocado (*Persea americana*) anthracnose in Israel. *Scientific Reports* **7**(1): 15839.
DOI: <https://doi.org/10.1038/s41598-017-15946-w>
- Silvestro D. & Michalak I. (2012). raxmlGUI: a graphical front-end for RaxML. *Organisms Diversity and Evolution* **12**(4): 1–3.
DOI: <https://doi.org/10.1007/s13127-011-0056-0>
- Stephenson S.A., Green J., Manners J. & Maclean D.J. (1997). Cloning and characterisation of glutamine synthetase from *Colletotrichum gloeosporioides* and demonstration of elevated expression during pathogenesis on *Stylosanthes guianensis*. *Current Genetics* **31**: 447–454.
DOI: <https://doi.org/10.1007/s002940050228>
- Sun Y.C., Damm U. & Huang C.J. (2019). *Colletotrichum plurivorum*, the causal agent of anthracnose fruit rot of papaya in Taiwan. *Plant Disease* **103**(5): 1040.
- Sutton B.C. (1968). The appressoria of *Colletotrichum graminicola* and *C. falcatum*. *Canadian Journal of Botany* **46**: 873–876.
- Swinburne T.R. (1983). Quiescent infections in post-harvest diseases. In: *Postharvest Pathology of Fruits and Vegetables* (ed. C. Dennis), pp. 1 – 21. Academic Press, London, UK.
- Tamura K., Stecher G., Peterson D., Filipski A. & Kumar S. (2013). MEGA6: molecular evolutionary genetics analysis version 6.0. *Molecular Biology and Evolution* **30**(12): 2725–2729.
- Templeton M.D., Rikkerink E.H.A., Solon S.L. & Crowhurst R.N. (1992). Cloning and molecular characterization of the glyceraldehyde-3-phosphate dehydrogenase encoding gene and cDNA from the plant pathogenic fungus *Glomerella cingulata*. *Gene* **122**: 225–230.
- Uysal A. & Kurt S. (2020). First report of *Colletotrichum siamense* causing anthracnose on banana fruits in Turkey. *Journal of Plant Pathology* **102**: 967.
- Vieira. W.A.S., Lima W.G., Nascimento E.S., Michereff S.J., Câmara M.P.S. & Doyle V.P. (2017). The impact of phenotypic and molecular data on the inference of *Colletotrichum* diversity associated with *Musa*. *Mycologia* **109**(6): 912–934.
- Vithanage I.S.K., Yakandawala D.M.D., Maharachchikumbura S.S.N., Jayasinghe L. & Adikaram N.K.B. (2021). *Colletotrichum* species causing anthracnose disease in *A. andraeanum*, manifested as spathe rot also in addition to spadix rot and leaf spot. *European Journal of Plant Pathology* **161**: 837–846.
DOI: <https://doi.org/10.1007/s10658-021-02366-w>
- Wanigasekara U.W.N.P., Adikaram N.K.B. & Abayasekara C.L. (2014). Pre-harvest chemical elicitor treatment enhances induced resistance in harvested banana fruit cv. ‘Embul’ and reduces anthracnose caused by *Colletotrichum musae*. *Journal of the National Science Foundation of Sri Lanka* **42**(2): 99–108.
- Weir B.S., Johnston P.R. & Damm U. (2012). The *Colletotrichum gloeosporioides* species complex. *Studies in Mycology* **73**: 115–180.
- White T.J., Bruns T.D., Lee S.B. & Taylor J.W. (1990). Amplification and direct sequencing of fungal ribosomal RNA genes for phylogenetics. In: *PCR Protocols: A Guide to Methods and Applications* (eds. M.A. Innis, D.H. Gelfand, J.J. Sninsky & T.J. White), pp. 315–322. Academic Press, New York, USA.
DOI: <http://dx.doi.org/10.1016/B978-0-12-372180-8.50042-1>
- Wickramasinghe P., Adikaram N. & Yakandawala D. (2020). Molecular characterization of *Colletotrichum* species causing *Begonia* anthracnose in Sri Lanka. *Ceylon Journal of Science* **49**(5): 363–371.
DOI: <http://doi.org/10.4038/cjs.v49i5.7803>
- Zhou Y., Huang, J.S., Yang L.Y., Wang G.F. & Li J.Q. (2017). First report of banana anthracnose caused by *Colletotrichum scovillei* in China. *Plant Disease* **101**(2): 381.

Molecular and phenotypic characterization of *Colletotrichum plurivorum* and *Colletotrichum musae* causing banana anthracnose disease in the Central Province of Sri Lanka

Supplementary Information

Supplementary Table 1: GenBank accession numbers of isolates included in *C. gloeosporioides* species complex tree. Sequences from the present study are in bold letters

Species	Culture	GenBank Accession number	
		ITS	GAPDH
<i>Colletotrichum cattleyicola</i>	MAFF 238321	MG600759	-
<i>Colletotrichum cattleyicola</i>	CBS 170.49	MG600758	MG600819
<i>Colletotrichum cliviicola</i>	CSSS2	GU109480	GU085868
<i>Colletotrichum cliviicola</i>	CBS 125375	MG600733	MG600795
<i>Colletotrichum cliviicola</i>	CBS 133705	MG600732	MG600794
<i>Colletotrichum gloeosporioides</i>	CBS 112999	JQ005152	JQ005239
<i>Colletotrichum musicola</i>	CBS 127557	MG600737	MG600799
<i>Colletotrichum musicola</i>	CBS 132885	MG600736	MG600798
<i>Colletotrichum orchidearum</i>	CGMCC 3.14982	KX853166	KX893585
<i>Colletotrichum orchidearum</i>	CGMCC 3.14983	KX853167	KX893586
<i>Colletotrichum orchidearum</i>	MFLUCC 12-0531	KT290264	KT290263
<i>Colletotrichum orchidearum</i>	CBS 135131	MG600738	MG600800
<i>Colletotrichum piperis</i>	IMI 71397	MG600760.	MG600820
<i>Colletotrichum plurivorum</i>	CBS 90369	MG600721	MG600784
<i>Colletotrichum plurivorum</i>	CBS 125474	MG600718	MG600781
<i>Colletotrichum plurivorum</i>	CORCG2	HM585397	HM585380
<i>Colletotrichum plurivorum</i>	CBS 132443	MG600719	MG600782
<i>Colletotrichum plurivorum</i>	UTFC 260	MG600723	MG600786
<i>Colletotrichum plurivorum</i>	MAFF 243073	MG600730	MG600793
<i>Colletotrichum plurivorum</i>	CBS 125473	MG600717	MG600780
<i>Colletotrichum plurivorum</i>	MAFF 305974	MG600731	-
<i>Colletotrichum plurivorum</i>	CORCX9	HM585398	HM585381
<i>Colletotrichum plurivorum</i>	CGMCC 3.17358	KJ955215	KJ954916
<i>Colletotrichum plurivorum</i>	UTFC 261	MG600722	MG600785
<i>Colletotrichum plurivorum</i>	LFN0008	KT696336	KT696289
<i>Colletotrichum plurivorum</i>	CMM 3746	KC702981	KC702942
<i>Colletotrichum plurivorum</i>	CBS 132444	MG600720	MG600783
<i>Colletotrichum plurivorum</i>	CMM 3742	KC702980.	KC702941
<i>Colletotrichum plurivorum</i>	MAFF 238315	MG600729	MG600792
<i>Colletotrichum plurivorum</i>	C5	MT742141	MW192221
<i>Colletotrichum sojae</i>	CGMCC 3.15171	-	KC843501
<i>Colletotrichum sojae</i>	UTFC 301	MG600756	MG600817
<i>Colletotrichum sojae</i>	LFN0009	KT696354	-
<i>Colletotrichum sojae</i>	CAUOS5	KP890107	KP890138
<i>Colletotrichum sojae</i>	UTFC 303	MG600757	MG600818
<i>Colletotrichum sojae</i>	SAUCC 1407	KT362184	KT362188
<i>Colletotrichum vittalense</i>	CBS 12625	MG600735	MG600797
<i>Colletotrichum vittalense</i>	GUFCC 15503	JN390935	-
<i>Colletotrichum vittalense</i>	CBS 18182	JN390935	MG600796

Supplementary Table 2: Collection details and GenBank accession numbers of isolates included in the *C. gloeosporioides* species complex tree. Sequences from present study are in bold letters

Species	Culture	GenBank Accession numbers			
		ITS	GAPDH	TUB2	GS
<i>Colletotrichum aenigma</i>	ICMP18608	JX010244	JX010044	JX010389	JX010078
<i>Colletotrichum aenigma</i>	ICMP18686	JX010243	JX009913	JX010390	JX010079
<i>Colletotrichum aeshynomenes</i>	ICMP17673	JX010176	JX009930	JX010392	JX010081
<i>Colletotrichum alatae</i>	ICMP17919	JX010190	JX009990	JX010383	JX010065
<i>Colletotrichum alatae</i>	ICMP18122	JX010191	JX010011	JX010136	JX010449
<i>Colletotrichum alienum</i>	ICMP12071	JX010251	JX010028	JX010411	JX010101
<i>Colletotrichum alienum</i>	LF322	KJ955131	KJ954832	KJ955279	KJ954982
<i>Colletotrichum artocarpicola</i>	MFLUCC18-1167	MN415991	MN435568	MN435567	-
<i>Colletotrichum asianum</i>	ICMP18580	FJ972612	JX010053	JX010406	JX010096
<i>Colletotrichum asianum</i>	ICMP18696	JX010192	JX009915	JX010384	JX010073
<i>Colletotrichum boninense</i>	CBS123755	JQ005153	JQ005240	JQ005588	-
<i>Colletotrichum chrysophilum</i>	CMM4268	KX094252	KX094183	KX094285	KX094204
<i>Colletotrichum chrysophilum</i>	CMM4292	KX094248	KX094182	KX094284	KX094203
<i>Colletotrichum chrysophilum</i>	CMM4394	KX094239	KX094179	KX094282	KX094200
<i>Colletotrichum conoides</i>	CAUG17	KP890168	KP890162	KP890174	-
<i>Colletotrichum conoides</i>	MYL24	KY995389	KY995340	KY995473	-
<i>Colletotrichum endophytica</i>	LC0324	KC633854	KC832854	-	-
<i>Colletotrichum endophytica</i>	LC0327	KC633855	KC832846	-	-
<i>Colletotrichum endophytica</i>	LC1216	KC633853	KC832853	-	-
<i>Colletotrichum fruticicola</i>	ICMP18581	JX010165	JX010033	JX010405	JX010095
<i>Colletotrichum fruticicola</i>	LF896	J955221	KJ954922	KJ955366	KJ955071
<i>Colletotrichum gloeosporioides</i>	ICMP17821	JX010152	JX010056	JX010445	JX010085
<i>Colletotrichum gloeosporioides</i>	LF916	KJ955226	KJ954927	KJ955371	KJ955076
<i>Colletotrichum hebeiense</i>	JZB330117	MG763977	MG812555	MG812561	-
<i>Colletotrichum hebeiense</i>	JZB330028	KF156863	KF377495	KF288975	-
<i>Colletotrichum hippeastri</i>	CBS125377	JQ005230	JQ005317	JQ005664	-
<i>Colletotrichum horii</i>	ICMP10492	GQ329690	GQ329681	JX010450	JX010137
<i>Colletotrichum horii</i>	ICMP17970	JX010213	JX010000	-	-
<i>Colletotrichum hystrix</i>	CBS142411	KY856450	KY856274	KY856532	-
<i>Colletotrichum hystrix</i>	CBS142412	KY856451	KY856275	KY856533	-
<i>Colletotrichum makassarensis</i>	CBS143664	MH728812	MH728820	MH846563	-
<i>Colletotrichum makassarensis</i>	CPC28556	MH728815	MH728821	-	MH748262
<i>Colletotrichum musae</i>	C1	MT742137	MW196689	OM274079	OM274088
<i>Colletotrichum musae</i>	C10	MT742138	MW196690	OM274082	OM274091
<i>Colletotrichum musae</i>	C2	MT742139	MW196691	OM274083	OM274092
<i>Colletotrichum musae</i>	C3	MT742140	MW196692	OM274084	OM274093
<i>Colletotrichum musae</i>	C4	MT742143	MW196693	OM274080	OM274089
<i>Colletotrichum musae</i>	C7	MT742144	MW196694	OM274086	-
<i>Colletotrichum musae</i>	C8	MT742145	MW196695	OM274081	OM274090
<i>Colletotrichum musae</i>	C9	MT742146	MW196696	OM274087	OM274094
<i>Colletotrichum musae</i>	CMM4421	KX094259	KX094194	KX094297	KX094237
<i>Colletotrichum musae</i>	CMM4422	KX094244	KX094189	KX094298	KX094232
<i>Colletotrichum musae</i>	CMM4423	KX094243	KX094195	KX094294	KX094231
<i>Colletotrichum musae</i>	CMM4445	KX094241	KX094188	KX094293	KX094230
<i>Colletotrichum musae</i>	CMM4447	KX094251	KX094192	KX094296	KX094235
<i>Colletotrichum musae</i>	CMM4450	KX094245	KX094190	KX094295	KX094233
<i>Colletotrichum musae</i>	CMM4452	KX094253	KX094193	KX094291	KX094236
<i>Colletotrichum musae</i>	CMM4458	KX094249	KX094191	KX094292	KX094234
<i>Colletotrichum musae</i>	ICMP17817	JX010142	JX010015	JX01039	JX010084
<i>Colletotrichum musae</i>	ICMP19119	NG_06284	JX010050	JQ005861	JX010103
<i>Colletotrichum nupharicola</i>	CBS 470.96	JX010187	JX009972	JX010398	JX010088

<i>Colletotrichum nupharicola</i>	CBS 472.96	JX010188	JX010031	JX010399	JX010089
<i>Colletotrichum proteae</i>	CBS132882	KC297079	KC297009	KC297101	KC297032
<i>Colletotrichum proteae</i>	CBS134301	KC842385	KC842379	KC842387	KC842387
<i>Colletotrichum queenslandicum</i>	ICMP1778	JX010276	JX009934	JX010414	JX010104
<i>Colletotrichum queenslandicum</i>	ICMP18705	JX010185	JX010036	JX010412	JX010102
<i>Colletotrichum salsolae</i>	ICMP18693	JX010241	JX009917	-	-
<i>Colletotrichum salsolae</i>	ICMP19051	NR_120139	JX009916	-	-
<i>Colletotrichum siamense</i>	CPC 16136	KP703417	KP703347	KP703504	KP703758
<i>Colletotrichum siamense</i>	C6	MT742142	MW192222	OM274085	-
<i>Colletotrichum siamense</i>	CBS133123	JX145142	-	JX145193	-
<i>Colletotrichum siamense</i>	CBS133251	JX145144	-	JX145195	-
<i>Colletotrichum siamense</i>	CPC 16137	KP703418	KP703348	KP703505	KP703759
<i>Colletotrichum siamense</i>	Coll6	JX145153	-	JX145205	-
<i>Colletotrichum siamense</i>	GA435	KX620330	KX620264	KX620363	KX620295
<i>Colletotrichum siamense</i>	GZAAS5 09506	JQ247633	JQ247609	JQ247644	JQ247621
<i>Colletotrichum siamense</i>	GZAAS5 09538	JQ247632	JQ247608	JQ247645	JQ247620
<i>Colletotrichum siamense</i>	ICMP18578	JX010171	JX009924	JX010404	JX010094
<i>Colletotrichum siamense</i>	ICMP19118	JX010259	JX009974	JX010415	JX010105
<i>Colletotrichum siamense</i>	LC0148	KJ955078	KJ954779	KJ955227	KJ954929
<i>Colletotrichum siamense</i>	LC0149	KJ955079	KJ954780	KJ955228	KJ954930
<i>Colletotrichum siamense</i>	LF139	KJ955087	KJ954788	KJ955236	KJ954938
<i>Colletotrichum siamense</i>	LF148	KJ955088	KJ954789	KJ955237	KJ954939
<i>Colletotrichum tainanense</i>	UOM 1290T	MH728805	MH728819	-	MH748271
<i>Colletotrichum tainanense</i>	CPC30245	MH728805	MH728823	MH846558	MH748259
<i>Colletotrichum theobromicola</i>	CMM4242	KX094238	KX094173	KX094278	KX094197
<i>Colletotrichum theobromicola</i>	ICMP17927	JX010286	JX010024	JX010373	JX010064
<i>Colletotrichum theobromicola</i>	ICMP18649	JX010294	JX010006	JX010447	JX010139
<i>Colletotrichum tropicale</i>	ICMP18653	JX010264	JX010007	JX010407	JX010097
<i>Colletotrichum tropicale</i>	ICMP18672	JX010275	JX010020	JX010396	JX010086
<i>Colletotrichum viniferum</i>	GZAAS5 08601	JN412804	JN412798	-	JN412787
<i>Colletotrichum viniferum</i>	GZAAS5 08608	JN412802	JN412800	-	JN412784
<i>Colletotrichum xanthorrhoeae</i>	ICMP17820	JX010260	JX010008	-	-
<i>Colletotrichum xanthorrhoeae</i>	ICMP17903	JX010261	JX009927	JX010448	JX010138

RESEARCH ARTICLE

Natural Products

In-vitro wound healing potential of *Ziziphus oenoplia* (L.) Miller

WMP Samarasinghe¹, KH Jayawardana², C Ranasinghe¹, S Somaratne³ and GMKB Gunaherath^{1*}

¹ Department of Chemistry, Faculty of Natural Sciences, PO Box 21, The Open University of Sri Lanka, Nawala, Nugegoda, Sri Lanka.

² Department of Zoology, Faculty of Natural Sciences, PO Box 21, The Open University of Sri Lanka, Nawala, Nugegoda, Sri Lanka.

³ Department of Botany, Faculty of Natural Sciences, PO Box 21, The Open University of Sri Lanka, Nawala, Nugegoda, Sri Lanka.

Submitted: 15 June 2022; Revised: 22 November 2022; Accepted: 27 January 2023

Abstract: Non-healing wounds are a global health problem. Substances that enhance cell proliferation, angiogenesis, and prevention of bacterial infections accelerate the wound healing process. In this study, the wound healing potential of *Ziziphus oenoplia*, is investigated for its ability in cell proliferation, angiogenesis, and antibacterial potential. The potential of cell proliferation enhancement (mean percent wound closure) and angiogenic response (mean vascular index) of hexanes, dichloromethane, ethyl acetate, and methanol extracts of leaf and bark of *Z. oenoplia* were evaluated by scratch wound assay (SWA) using Madin-Darby Canine Kidney (MDCK) cells and chick chorioallantoic membrane (CAM) assay, respectively. The antibacterial activity of these extracts was evaluated against *Bacillus subtilis*, *Staphylococcus aureus*, *Escherichia coli*, and *Pseudomonas aeruginosa* by disc diffusion method. Enhanced cell proliferation was shown by the hexanes, dichloromethane, and ethyl acetate extracts of leaf and the hexanes extract of bark. An enhanced angiogenic response was shown by the methanol and ethyl acetate extracts of leaves and the methanol and hexanes extracts of bark. Dichloromethane extract of both leaf and bark showed considerable antibacterial activity against *P. aeruginosa* which is less susceptible to common antibiotics. SWA-directed fractionation of the hexanes extract of the leaf has resulted in the isolation and identification of an active fraction showing mean percent wound closure of 86.4% (positive control 90.2%) and mean vascular index of 34.5 (positive control 48.6). This fraction contained lupeol, α -amyirin, β -amyirin, hexacosanol, and octacosanol. The present study provides supportive evidence for the potential of wound healing enhancement of leaf and bark extracts of *Z. oenoplia*.

Keywords: Antibacterial assay, chick chorioallantoic membrane (CAM) assay, Rhamnaceae, scratch wound assay (SWA), wound healing, *Ziziphus oenoplia*.

INTRODUCTION

Non-healing wounds are a major health concern in the human population. Impairment of the natural healing process of wounds can result in a serious threat to life. Wounds are physical, chemical, or thermal injuries that result in an opening or breaking in the integrity of the skin (Singh *et al.*, 2006) or may also be defined as the disruption of the anatomical and functional integrity of living tissue (Agyare *et al.*, 2016). Wound healing is a multifaceted process governed by sequential, yet overlapping phases including hemostasis, inflammation, proliferation, and remodelling (Lindley *et al.*, 2016). Cell proliferation is a characteristic event during the proliferative phase (Heil *et al.*, 2017) while angiogenesis is a critical process involved in wound healing in order to re-establish the nutrient supply to regenerating tissue (Gerritsen, 2008). The natural wound healing process could also be delayed by microbial infections (Serra *et al.*, 2014). It is known that natural products can enhance the wound healing process through multiple cellular mechanisms (Thakur *et al.*, 2011). The scratch wound assay (cell migration assay) is a classic and commonly used *in-vitro* method for studying cell proliferation (Yarrow *et al.*, 2004). The chick embryo chorioallantoic membrane (CAM) assay is a method for evaluating angiogenic activity which can also be used as a wound healing model (Ribatt *et al.*, 1996).

Sri Lanka has rich traditional systems of medicine which have been practiced over 3000 years (Weragoda, 1980). Plants and herbal preparations are most frequently employed as therapeutics in indigenous medicine in Sri Lanka, especially in Ayurveda for curing a wide variety of diseases (Weragoda, 1980). Even though a large number of plants are being used by people in many countries including Sri Lanka for the treatment of wounds and

*Corresponding author (kbgun@ou.ac.lk;  <https://orcid.org/0000-0002-2523-5581>)



This article is published under the Creative Commons CC-BY-ND License (<http://creativecommons.org/licenses/by-nd/4.0/>). This license permits use, distribution and reproduction, commercial and non-commercial, provided that the original work is properly cited and is not changed in anyway.

burns (Krishnappa *et al.*, 2016) most of them are scientifically unexplored for their validity with pharmacological models and human subjects (Kumar *et al.*, 2007).

In continuing our studies on plants used for the enhancement of wound healing, (Bopage *et al.*, 2018) we initiated a chemical and biological investigation on *Ziziphus oenoplia* (L.) Miller (family: Rhamnaceae), commonly known as the ‘jackal jujube’ in English and ‘*Heen Eraminiya*’ in Sinhala. Various parts of *Z. oenoplia* have been used as a remedy for an array of illnesses in Ayurveda and in indigenous medicine practiced in Sri Lanka. The leaf and bark of this plant have been used for the treatment of wounds, particularly for fresh cuts (Nadkarni, 1976) while the water boiled with a few medicinal plants including *Z. oenoplia* has been used to wash chronic wounds (Kumarasinghe, 1987). Although it is not reported in literature, rural communities in Sri Lanka use crushed fresh leaves of this plant on fresh cuts on skin as a home remedy. Members of *Z. oenoplia* (L.) Miller belonging to the family Rhamnaceae, and are often trailing or ascending shrubs with curved spines, solitary or in pairs. They are distributed in forests of dry regions in India, Pakistan, Malaysia, Australia, and Sri Lanka (Wadhwa, 1996). An array of biological activities such as analgesic and antinociceptive, anthelmintic, antibacterial, anti-denaturation, antioxidant, hepatoprotective, hypoglycaemic have been shown by different parts of this plant (Shukla *et al.*, 2016; Rashmi *et al.*, 2018). The wound-healing activity of aqueous and alcoholic extracts of the fruits of this plant has been evaluated by *in-vivo* methods (Kuppast & Kumar, 2012). The angiogenic potential of ethanol extract of root of *Z. oenoplia* has been evaluated using the chorioallantoic membrane (CAM) model (Mahapatra *et al.*, 2011) while wound healing potential of several solvent extracts of root have been evaluated by a rat model (Majumder, 2012).

Compounds belonging to different chemical classes have been identified from *Z. oenoplia*. Of these, the cyclopeptide alkaloids belonging to the ziziphine series, having 13–15 membered rings, are the most abundant chemical class. The chemistry of the cyclopeptide alkaloids of genus *Ziziphus* has been reviewed (Tuenter *et al.*, 2017). Apart from several ziziphine alkaloids, betulinic acid (Nahar *et al.*, 1997), zizyotin, a terpenoid saponin (Maurya *et al.*, 1995), β -sitosterol, β -sitosteryl- β -D-glucoside, luteolin, and quercetin have been identified from bark (Singh & Singh, 2012). Several antiplasmodial ziziphine alkaloids (Suksamrarn *et al.*, 2005), an antibacterial hydroxy carboxylic acid (Prabhavathi & Vijayalakshmi, 2015), and an aliphatic hydroxy ether (Prabhavathi & Vijayalakshmi, 2016) have been reported from the root of *Z. oenoplia*. Chemical work on leaf of *Z. oenoplia* is scarce. Presence of some volatile constituents from the ethanol extract of leaf of *Z. oenoplia* has been reported (Shyamala & Manikandan, 2019).

Herein we report the *in-vitro* wound healing activity of leaf and bark extracts of *Z. oenoplia* with respect to the results of scratch wound assay (SWA), chick chorioallantoic membrane (CAM) assay and the antibacterial activity of these extracts against Gram positive bacteria, *B. subtilis* and *S. aureus* and Gram negative bacteria, *E. coli* and *P. aeruginosa* using agar disc diffusion method and the identification of a fraction exhibiting cell proliferation by SWA and proangiogenic activity by CAM assay. This fraction was found to be an inseparable mixture consisting of lupeol (1), α -amyrin (2), β -amyrin (3), hexacosanol (4) and octacosanol (5) (Figure 1). Their identities were confirmed by GC-MS analysis and $^1\text{H-NMR}$ and $^{13}\text{C-NMR}$ spectroscopic techniques. It is noteworthy that this constitutes the first report of compounds 2–5 from *Z. oenoplia*.

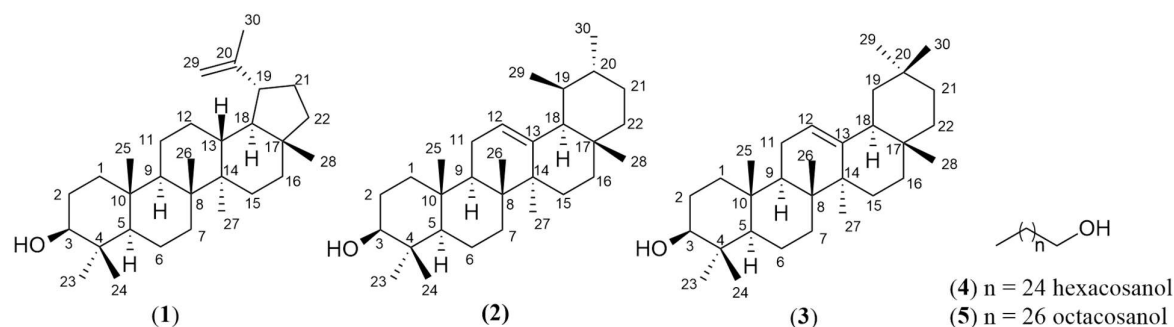


Figure 1. Chemical structures of lupeol (1), α -amyrin (2), β -amyrin (3), hexacosanol (4) and octacosanol (5)

MATERIALS AND METHODS

General

Chemicals and reagents were purchased from Merck, Sigma-Aldrich, Fluka, Himedia and Invitrogen. Silica gel 60 G (Fluka-60741) was used as solid phase, for gravity columns. Analytical Thin Layer Chromatography (TLC) was performed on pre-coated 0.25 mm thick plates of silica gel 60 F₂₅₄ (Merck). Preparative TLCs were carried out on glass plates (20 × 20 cm) coated with a 1:1 mixture of silica gel 60 G (Fluka 60760) and silica gel 60 GF₂₅₄ (Fluka 60765), 0.5 mm thickness. TLC plates were visualized by UV-illumination (254 nm and 365 nm) and spraying with anisaldehyde-sulfuric acid reagent which was made by mixing anisaldehyde (0.5 mL) with glacial acetic acid (10 mL), followed by 85 mL of methanol and concentrated sulfuric acid (5 mL). Column fractions having similar TLC patterns were combined and evaporated under reduced pressure. 1D and 2D NMR spectra were recorded in CDCl₃ with a Bruker Ascend 400 spectrometer at 400 MHz for ¹H-NMR and 100 MHz for ¹³C-NMR using residual CHCl₃ as the internal reference. GC-MS analysis was carried out using an Agilent 7890 A GC system equipped with 5975C inert XL MSD Triple-Axis Detector, and HP-5 MS fused silica capillary column with (5% Phenyl)-methylpolysiloxane stationary phase (30 m × 0.25 mm Id, × 0.25 μm film thickness). Helium (99.999%) was used as the carrier gas. Mass spectra were acquired in the EI mode at 70 eV. MDCK cell line was purchased from American Type Culture Collection (ATCC®), Manassas, Virginia, USA. Fertilized chicken eggs were purchased from Three Acre Farms PLC, Colombo 15.

Plant material

Fresh leaf and bark of *Ziziphus oenoplia* (L.) Miller was collected from Dompe area in Gampaha District (Sri Lanka, 6°56'08.8"N 80°03'03.3"E) and identified by one of the authors, Dr S. Somaratna. The voucher specimen, NSF/PSF/ICRP/2017/HS02/PT/03 was authenticated and deposited at the National Herbarium, Department of National Botanical Gardens, Peradeniya, Sri Lanka. The plant materials were chopped, and air dried at room temperature (30 °C) for the extraction.

Extraction

Both leaf (LF) and bark (BK) of *Z. oenoplia* (100 g each) were extracted sequentially with hexanes, dichloromethane, ethyl acetate, and methanol (1.0 L each for 24 h × 3) in an orbital shaker (~90 rpm) at 30±2 °C. The solvents were removed under reduced pressure at < 35 °C using a rotary evaporator and each extract was dried in a vacuum oven at 30±2 °C for 2 days and weighed.

Cell culture

Madin-Darby Canine Kidney (MDCK: ATCC®CRL-2936) cell cultures were established in the laboratory using standard *in-vitro* methods. The cells were grown in plastic tissue culture flasks (25 cm²) in Dulbecco's Modified Eagles Medium (DMEM) containing 10% Fetal Bovine Serum (10% growth medium) supplemented with antibiotics (50 IU/mL penicillin and 50 μg/mL streptomycin). MDCK cell culture was maintained at 37 °C in a 5% CO₂ humidified incubator until they reached the confluent stage of the growth.

Scratch wound assay (SWA)

The cells which grow at confluent stage were harvested and inoculated in clear bottom 24 well plates at a cell density of 2 × 10⁴ cells/well in 10% growth medium. The well plates were incubated at 37 °C for 24 h in a humidified incubator for the formation of monolayer. Scratch wound assay (SWA) was carried out in 20% DMEM solution (amount of DMEM in this solution is equivalent to 1/5th of a standard DMEM solution) which was prepared by the following procedure. DMEM powder supplemented with high glucose and L-glutamine (Sigma-Aldrich) (2.680 g) was dissolved in 1 L of 2.25% NaHCO₃ solution. At this DMEM concentration, untreated cells were found to be almost static for 24 h.

A scratch was performed on a monolayer of cells along the vertical axis of each well under the microscope (LABOMED TCM400™) using a sterile micropipette tip. The monolayer of cells with the wound (scratch) was

washed with phosphate buffered saline (PBS) (400 $\mu\text{L} \times 2$). Each test well was filled with 495 μL of 20% DMEM and 5 μL of DMSO containing an appropriate amount of the test sample was added such that its final concentration is 20 mg/L for the extracts and 10 or 5 mg/L for the fractions. A potent wound healing compound, asiaticoside (25 μM) was used as the positive control (Lee *et al.*, 2012), and 1% DMSO in 20% DMEM was used as the negative control in this experiment. Initial width of each wound was measured. The well plates were incubated for 24 h at 37 °C with 5% CO₂. Width of each wound was measured after 24 h of incubation period. Both stages of each wound were photographed under inverted tissue culture microscope equipped with a digital camera (SONY CORP.DSC-W210). Percent wound closure was calculated, and the cell proliferation enhancement is presented as the mean percent wound closure. Plant extracts which have shown >75.0% mean wound closures at 24 h are considered as wound healing active extracts.

Chick chorioallantoic membrane (CAM) assay

The chick embryo chorioallantoic membrane (CAM) assay was performed according to Talekar and co-workers (Talekar *et al.*, 2017) with a few modifications as described below. The surface of freshly laid fertilized chicken eggs was wiped with 70% ethanol and incubated at 37 °C in 60% humidity in an egg incubator for 9 days with continuous monitoring. On the 9th day, vascularized regions were identified using an egg Candler (Life Basis, LSEC001BK). A small window (1 cm²) was made in the shell above the vascularized region. Each of the plant extracts (50 μg in 10 μL DMSO) and active fractions in SWA (10 μg in 10 μL DMSO) was introduced into a sterile Whatman® No. 01 filter paper disc (diameter, 6 mm) and placed on the chicken chorioallantoic membrane in each egg. Filter paper disc containing β -sitosterol (10 μg in 10 μL DMSO) served as the positive control while filter paper disc containing 10 μL of DMSO served as the negative control (Moon *et al.*, 1999). The windows were sealed with parafilm® and incubated for further 72 h. On the 12th day of incubation, the windows were opened and the surrounding CAM area with the paper disc was photographed with a digital camera (SONY CORP.DSC-W210). The CAM assay for each plant extract and for the controls was performed in 05 replicates. Vascular index of each CAM for different extracts and controls was determined and the angiogenic response is expressed as the mean vascular index (Barnhill & Ryan, 1983).

Antibacterial assay: Kirby-Bauer disk diffusion method

The anti-bacterial activity of each plant extract was tested against two Gram positive bacterial strains; *Bacillus subtilis* (ATCC 6633) and *Staphylococcus aureus* (ATCC 25923), and two Gram negative bacterial strains, *Escherichia coli*, (ATCC 25922) and *Pseudomonas aeruginosa* (ATCC 27853) (Bacterial culture collection, Department of Microbiology, Faculty of Medicine, University of Colombo, Sri Lanka) using disk diffusion method in Petri plates (diameter, 9 cm). The pure bacterial cultures of each bacterial strain were grown on nutrient agar (NA) (Himedia- M001) plates and incubated at 37 °C during the study period.

Each culture was made into a suspension in sterilized distilled water up to a certain density, which was measured as a predetermined optical density (OD value); 0.05 OD at the wavelength (λ) = 500 nm for *Bacillus subtilis*, 0.1 OD at λ = 500 nm for *E. coli*, *S. aureus* and *P. aeruginosa*. From each suspension 100 μL aliquots were transferred to different nutrient agar plates and spread using a sterilized glass spreader to prepare a uniform lawn of each bacterial species under study.

The discs containing plant extracts for the antibacterial assay were prepared by impregnating 500 μg of each plant extract dissolved in 10 μL DMSO into sterile Whatman® No. 3 filter paper discs (diameter, 6 mm). The discs containing 10 μg of Amoxicillin (Himedia) served as the positive control (Pommerville & Alcamo, 2004) while sterile Whatman® No. 3 filter paper discs (diameter, 6 mm) treated with 10 μL of DMSO served as the negative control in this experiment. Two discs containing same plant extract, a disc of positive control and a disc of negative control were placed on each nutrient agar plate and were incubated at 37 °C for 24 h. Experiments were performed in triplicate for each extract. The diameter of the inhibition zone was measured, and the results are expressed as the mean diameter of inhibition zone with the standard deviation.

Bioactivity directed chemical investigation of hexanes extract of leaf of *Z. oenoplia*

Hexanes extract of leaf of *Z. oenoplia* (1.00 g) was subjected to column chromatography over a column of silica gel (35.0 g; Merck, 230–400 mesh) made up in hexanes. The column was eluted with hexanes containing increasing amounts of ethyl acetate and, finally, washed with methanol. Of the 99 fractions (18 mL each) collected, those having similar TLC patterns were combined to give 6 major fractions (HF₁–HF₆). Each fraction was subjected to scratch wound assay at a concentration of 10 mg/L. The fraction HF₃ (220 mg) which showed the highest mean wound closure (75.8%) in SWA, was subjected to further fractionation over a column of silica gel (8.0 g; Fluka, 220–440 mesh) made up in hexanes. The column was eluted with hexanes containing increasing amounts of dichloromethane and, finally, washed with methanol. Of the 92 fractions (7 mL each) collected, those having similar TLC patterns were combined to yield 4 major fractions (HF_{3A}–HF_{3D}). Each fraction was subjected to SWA at a concentration of 5 mg/L. The fraction HF_{3C} (42 mg) which showed the highest mean wound closure (75.8%) was subjected to preparative TLC (20 × 20 cm², thickness 0.50 mm, eluent: CH₂Cl₂) and the prominent band appeared on TLC plate was scraped off and eluted with 10% MeOH in CH₂Cl₂ to yield of HF_{3CA} (24.6 mg).

Statistical analysis

Results of all experiments are presented as mean ± standard deviation. The mean comparisons were performed using ANOVA and the Least Significant Difference (LSD) with significance level of $p \leq 0.05$. All statistical analyses were carried out using the SAS® Ver. 9.00 (2002) (SAS Institute Inc., Cary, NC, USA).

RESULTS AND DISCUSSION

Dry weights of extracts with their percentage yields, are given in Table 1.

Table 1: Dry weights and percentage yields of extracts of *Z. oenoplia*

Plant part	Weight /g (% yield) of solvent extract			
	Hexane	Dichloromethane	Ethyl acetate	Methanol
Leaf	0.935 (0.935)	1.009 (1.009)	0.743 (0.743)	2.786 (2.786)
Bark	0.321 (0.321)	0.876 (0.876)	0.524 (0.524)	3.567 (3.567)

Scratch wound assay (SWA)

The scratch wound assay (SWA) has been established as a simple and low-cost tool to obtain first insight into whether plant preparations or their secondary metabolites can enhance the formation of new tissue by unidirectional cell migration (Liang *et al.*, 2007). During the scratch wound assay, scratched cell monolayer responds to the disturbance of cell-cell contacts by increasing the concentration of growth factors and cytokines at the wound edge (Lipton *et al.*, 1971).

Microscopic images (×400) of scratched wounds of monolayer of MDCK cells treated with extracts of *Z. oenoplia*, asiaticoside (25 μM) (positive control), and 1% DMSO in 20% DMEM (negative control) at the beginning and after 24 h of the experiment are shown in Figure 2.

The wound healing activity of *Z. oenoplia* extracts is expressed in terms of mean percent wound closure within 24 h of incubation period. It is evident that the hexanes, dichloromethane and ethyl acetate extracts of leaf and the hexanes extract of bark have shown a significantly high wound closure within the specified time (Figure 3 and Supplementary Table S1). The wound healing activity shown by these extracts is almost comparable with that of positive control, a well-established wound healing compound. Because, all extracts, except the methanol extract, are highly active in SWA, it is suggested that in terms of cell proliferation, the leaf of *Z. oenoplia* consists of an array of secondary metabolites with varying polarities which assist wound healing.

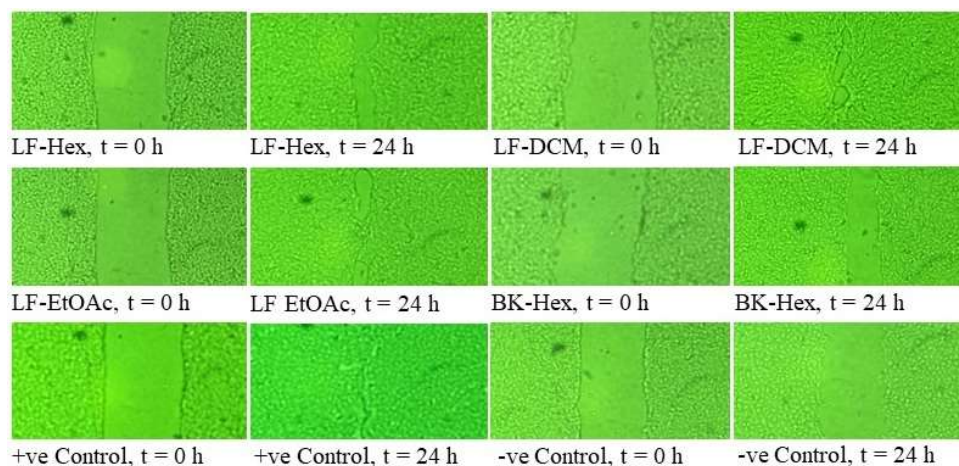


Figure 2. Microscopic images ($\times 400$) of scratched wounds of monolayer of MDCK cells at the beginning ($t = 0$ hours) and after 24 hours ($t = 24$ hours) in SWA of *Z. oenoplia* extracts, positive and negative controls. (LF = leaf, BK = bark, Hex = hexanes extract, DCM = dichloromethane extract, EtOAc = ethyl acetate extract)

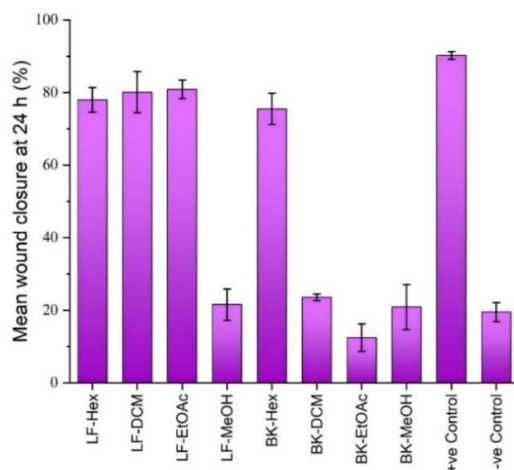


Figure 3: Mean percentage wound closure (\pm SD) at 24 hours of leaf and bark extracts of *Z. oenoplia* with positive and negative controls in SWA. (LF = leaf, BK = bark, Hex = hexanes extract, DCM = dichloromethane extract, EtOAc = ethyl acetate extract, MeOH = methanol extract)

The proliferative phase of the wound healing process is characterized by several cellular activities of keratinocytes, fibroblasts, macrophages, and endothelial cells regulated by multiple growth factors and cytokines (Werner & Grose, 2003). The proliferation and migration of epithelial cells from the cutaneous wound edges to close the wound area is termed as re-epithelization (Beldon, 2010; Rousselle *et al.*, 2019). Thus, the enhanced proliferation of MDCK cells observed in SWA resembles the re-epithelization of the wound healing process. Therefore, it is possible that the leaf and bark extractives of *Z. oenoplia* enhance the wound healing process by accelerating the re-epithelization during the proliferative phase.

Chick chorioallantoic membrane (CAM) assay

The chick chorioallantoic membrane (CAM) assay is a method to study the process of blood vessel sprouting during the wound healing in response to the angiogenic agents (Surekha *et al.*, 2013). The angiogenic response of CAM assay is generally expressed as the vascular index. It is obtained by counting all the noticeable blood vessels

such as capillaries, arterioles and venules traversing a 1 mm annulus around the filter disc provided they form an angle less than 45° with a line radiating from the centre (Barnhill & Ryan, 1983).

Images of harvested chorioallantoic membranes treated with methanol and ethyl acetate extracts of leaf, and methanol and hexane extracts of bark and positive and negative controls are shown in Figure 4.

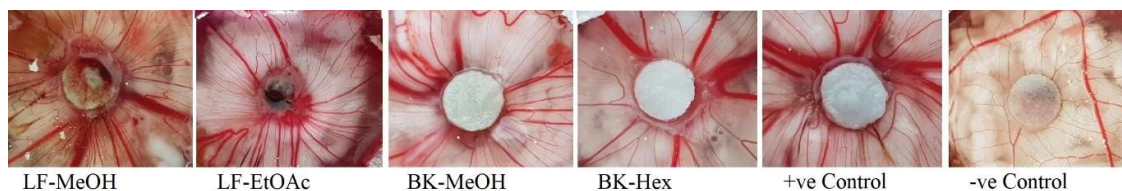


Figure 4: Images of CAM vascularization after 72 hours of incubation, treated with methanol and ethyl acetate extracts of leaf, methanol and hexane extracts of bark, β -sitosterol (positive control) (10 μ g/disc), and DMSO (negative control) (10 μ L/disc). (LF = leaf, BK = bark, Hex = hexanes extract, EtOAc = ethyl acetate extract, MeOH = methanol extract)

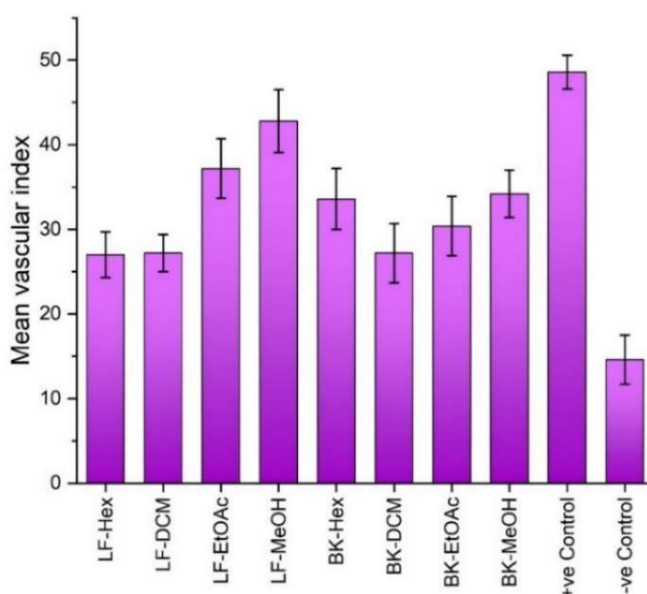


Figure 5: Mean vascular indices (\pm SD) of leaf and bark extracts of *Z. oenoplia* with controls in the CAM assay (LF = leaf, BK = bark, Hex = hexane extract, DCM = dichloromethane extract, EtOAc = ethyl acetate extract, MeOH = methanol extract)

Mean vascular indices of different extracts of *Z. oenoplia* suggest that the ethyl acetate and methanol extracts of leaf and the hexane and methanol extracts of bark has exhibited a higher angiogenic activity in comparison with rest of the extracts (Figure 5 and Supplementary Table S1).

New blood vessel formation (angiogenesis) during the proliferative stage of wound healing process is a significant event in which, replacement of damaged capillaries, reestablishment of oxygen and nutrient supply, and dilatation of vascularization occur (Bauer *et al.*, 2005). Enhanced vascularization observed in the CAM assay is a result of higher fibroblastic activity, which is necessary for the enhanced wound healing process (Theoret, 2017). Since different extracts of *Z. oenoplia* leaf and bark exhibit varying degrees of increased angiogenic response, it shows that the chemical constituents having diverse structural motifs present in these extracts of *Z. oenoplia* may be acting as proangiogenic substances.

Antibacterial assay

Results of the antibacterial assay of *Z. oenoplia* plant extracts against *Bacillus subtilis*, *Staphylococcus aureus*, *Escherichia coli*, and *Pseudomonas aeruginosa* showed that other than the dichloromethane extract against *P. aeruginosa*, they are either much less active than Amoxicillin (positive control), or inactive (Supplementary Table S2). Dichloromethane extracts of both leaf and bark showed mild antibacterial activity against all four tested bacterial strains indicating that both Gram positive (*B. subtilis*, *S. aureus*) and Gram negative (*E. coli* and *P. aeruginosa*) bacteria are sensitive to these two extracts. It is noteworthy that the activities shown by dichloromethane extracts are somewhat comparable across all four bacteria strains while the activity of Amoxicillin (positive control) against *P. aeruginosa* is distinctly less when compared with the remaining bacterial strains (Figure 6).

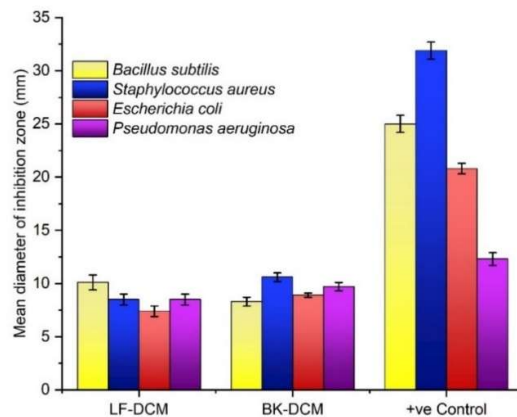


Figure 6: Antibacterial activity of dichloromethane extracts of leaf and bark of *Z. oenoplia* and the Positive control (amoxicillin) against *B. subtilis*, *S. aureus*, *E. coli*, and *P. aeruginosa*

In the treatment of wounds, acceleration of the healing process and protecting the wound from bacterial infections are the two main objectives. The open blood vessels and tissues in a wound area are a favourable place for bacterial growth. Bacterial infections delay the wound healing process. As such, in addition to enhancing cell proliferation and angiogenesis, prevention of bacterial invasion of the wound is also an essential requirement in wound healing (Rodeheaver *et al.*, 1980). *Pseudomonas aeruginosa* and *Staphylococcus aureus* are the most common bacteria isolated from chronic wounds. Hence, the compounds present in dichloromethane extracts of both leaf and bark of *Z. oenoplia* which showed relatively enhanced antibacterial activity against *P. aeruginosa* can play a vital role during the wound healing.

Table 2: Dry weights of column fractions of the hexane extract of leaves of *Z. oenoplia* and the mean percent of wound closure at 24 h of those fractions at a concentration of 10 mg/L, with negative and positive controls.

Fraction no.	Weight (g)	Mean % wound closure (\pm SD)*
HF ₁	80.0	49.1 (0.6) ^e
HF ₂	274.7	72.4 (1.0) ^c
HF ₃	220.0	75.8 (0.8) ^b
HF ₄	80.1	62.3 (0.5) ^d
HF ₅	55.4	36.4 (1.2) ^f
HF ₆	92.3	49.1 (2.8) ^e
Positive control [†]		89.5 (0.4) ^a
Negative control [‡]		20.9 (1.6) ^g

* Different letters in the same column indicate significant differences at $t = 1.98$ and $p \leq 0.05$ level. [†]Asiaticoside (25 μ M), [‡]1% DMSO in 20% DMEM

Bioactivity directed chemical investigation of hexanes extract of leaf of *Z. oenoplia*

Chemical investigation of *Z. oenoplia* extracts was initiated with the hexanes extract which showed 78.0% wound closure in SWA. Since the SWA is relatively fast and cheap, it was selected as the guiding bioassay for the chemical investigation. The 6 major fractions obtained from the silica gel column chromatographic separation of the hexanes extract of leaf of *Z. oenoplia* were subjected to SWA at a concentration of 10 mg/L. The yields and mean percent wound closure of each fraction along with the percentage wound closure of positive and negative controls are given in Table 2.

Results indicated that the fraction HF₃ to be the most active fraction (75.8% wound closure). Hence, further fractionation of fraction HF₃ was carried out. The silica gel column chromatographic separation of fraction HF₃ yielded 4 major fractions. They were subjected to SWA at a concentration of 5 mg/L. The yields and percent wound closure of these fractions, along with the mean percent wound closure of positive and negative controls are given in Table 3.

Table 3: Dry weights of column fractions of Fraction HF₃ and the mean percentage of wound closure at 24 h of those extracts of 5 mg/L concentration, with negative and positive controls.

Fraction no.	Weight (g)	Mean % wound closure (±SD)*
HF _{3A}	53.3	56.9 (1.5) ^e
HF _{3B}	34.2	73.1 (1.2) ^c
HF _{3C}	42.7	86.4 (0.9) ^b
HF _{3D}	55.7	68.4 (0.6) ^d
Positive control [†]		90.4 (0.9) ^a
Negative control [‡]		20.1 (1.5) ^f

* Different letters in the same column indicate significant difference at $t = 1.98$ and $p \leq 0.05$ level. [†] Asiaticoside (25 μ M), [‡] 1% DMSO in 20% DMEM

The results indicated that the fraction HF_{3C} was the most active fraction (86.4% wound closure) containing one major spot on TLC. A large portion of the fraction HF_{3C} (42 mg) was subjected to preparative TLC (20 × 20 cm, 0.50mm, eluent: CH₂Cl₂) and the prominent band that appeared on TLC plate was scraped off and eluted with 10% MeOH in CH₂Cl₂ to yield the 24.6 mg of HF_{3CA}. NMR spectroscopic analysis of the isolate HF_{3CA} was found to contain an inseparable mixture containing lupeol (**1**), [δ_C 150.3 (20-C), δ_H 4.68 (1H, br), 4.56 (1H, br), and 109.3, (29-CH₂), δ_H 3.18 (1H, dd, $J=5.1$ & 11.1 Hz), δ_C 79.0 (3-CH)], α -amyrin (**2**), [δ_C 139.6 (C-13), δ_H 5.12 (1H, t, $J=3.4$ Hz) and δ_C 124.4 (12-CH), δ_H 3.22 (1H, dd, $J=4.8$, 10.9 Hz) and δ_C 79.0 (3-CH)], β -amyrin (**3**), [δ_C 145.2 (C-13), δ_H 5.18 (1H, t, $J=3.4$ Hz), and δ_C 121.7 (12-CH), δ_H 3.22 (1H, dd, $J=4.8$ & 10.9 Hz, and δ_C 79.0 (3-CH)] and a fatty alcohol, [δ_H 3.60 (t, $J=6.4$ Hz) and δ_C 63.1 (1-CH₂), δ_C 29.3–29.7 (CH₂)_n, δ_C 14.1 (CH₃)] (See Supplementary material and Figures S3–S10). GC-MS analysis of this mixture showed 4 peaks in the total ion chromatogram ($t_R = 13.955$, 15.345, 17.720, and 18.211 min.) (Supplementary Figure S11) of which the first two at $t_R = 13.955$ and 15.345 min were identified as fatty alcohols, hexacosanol (**4**) and octacosanol (**5**) respectively. It is observed that ¹H-NMR and ¹³C-NMR signals of these two compounds appear at the same δ values (Hamill *et al.*, 2003; Park *et al.*, 2008; Yun-Choi *et al.*, 2003). The third peak in the GC-MS was identified as β -amyrin (**3**). Careful analysis of the remaining peak revealed that both lupeol (**1**) and α -amyrin (**2**), have been co-eluted during the GC-MS analysis. The identities of **1**, **2** and **3** were confirmed by the comparison of observed NMR data with those reported (Mahato & Kundu 1994; Burns *et al.*, 2000; Viet *et al.*, 2021). The molar ratio of lupeol (**1**), α -amyrin (**2**), β -amyrin (**3**), and the two alkanols has been determined as 1:2:2:3 by ¹H-NMR using the signals at δ 4.68, 1H (for lupeol), δ 5.12, 1H (for α -amyrin), δ 5.18, 1H (for β -amyrin), and δ 3.63, 2H (for two alkanols) and the ratio of their relative intensities (0.5: 1: 1: 3 respectively) (Supplementary Figures S4 and S5). The mean percent wound closure of the fraction, HF_{3CA} in SWA was found to be 87.5 % at 24 h at a concentration of 5 mg/L. Since the hexane extract of leaf of *Z. oenoplia* showed relatively moderate proangiogenic response in CAM assay, the fraction HF_{3CA} was subjected to CAM assay at a concentration of 10 μ g/disc and mean vascular index was found to be 34.5.

Lupeol (**1**), α -amyrin (**2**), and β -amyrin (**3**) are pentacyclic triterpenoids found in many medicinal plants. Previous studies have reported that these individual compounds have numerous biological activities. Although the wound healing potential of **1** was previously reported (Beserra *et al.*, 2018; Bopage *et al.*, 2018) such activity for compounds **2–5** have not been reported. Therefore, investigating the effect of these individual compounds and their involvement in wound healing as constituents in a mixture would be important to identify their contribution to wound healing.

CONCLUSION

Cell proliferation and angiogenesis are key events in the proliferative stage of wound healing process. Enhanced cell proliferation in SWA and higher angiogenic response in CAM assay exhibited by the different extracts of *Z. oenoplia* leaf and bark during this study suggest that these extracts are capable of accelerating the wound healing process. In addition to the acceleration of wound healing process, it is shown that these extracts are capable of prevention of bacterial infections of wounds, especially the infections caused by *P. aeruginosa*, thus facilitating the wound healing process. Bioactivity guided chemical investigation of the hexane extract of leaf of *Z. oenoplia* led to the identification of a fraction exhibiting both cell migration and angiogenic potential that consists of lupeol (**1**), α -amyrin (**2**), β -amyrin (**3**) and two alkanols hexacosanol (**4**) and octacosanol (**5**). This is the first report of the presence of compounds **2–5** from *Z. oenoplia*. Chemical investigation of the other active extracts is underway to identify chemical constituents present in those extracts that have wound healing potential.

Conflict of interest

The authors declare that they have no competing interests.

Acknowledgements

Financial assistance from the National Science Foundation (NSF) of Sri Lanka through the research grant No: NSF/PSF/ICRP/2017/HS/02 is gratefully acknowledged. We are thankful to Dr Muhammad Yar, Associate Professor, IRCBM, COMSATS University Islamabad, Lahore Campus, Pakistan, for the support of establishing CAM assay in our laboratory, Dr Nuwan Dileepa De Silva, Sri Lanka Institute of Nano Technology (SLINTEC) and Dr T.M.S.G. Tennakoon, Link Natural Products Ltd., for providing NMR data and GC-MS data, respectively, and Mr. S.B.R. Chinthaka Samarakoon, Link Natural Products Ltd. for the assistance in obtaining GC-MS data. Ms. D.U. Dhanapala, Technical officer, Department of Chemistry, The Open University of Sri Lanka, for the technical support provided at the initial stages of CAM assay and Mr. K.C.K. Deraniyagala, Senior Staff Technical officer, Department of Mechanical Engineering, The Open University of Sri Lanka, for the technical support provided for maintenance of some equipment are also gratefully acknowledged.

REFERENCES

- Agyare C., Boakye Y.D., Bekoe E.O., Hensel A., Dapaah S.O. & Appiah T. (2016). Review: African medicinal plants with wound healing properties. *Journal of Ethnopharmacology* **177**: 85–100.
DOI: <https://doi.org/http://dx.doi.org/10.1016/j.jep.2015.11.008>
- Barnhill R.L. & Ryan T.J. (1983). Biochemical modulation of angiogenesis in the chorioallantoic membrane of the chick embryo. *Journal of Investigative Dermatology* **81**(6): 485–488.
DOI: <https://doi.org/10.1111/1523-1747.ep12522728>
- Bauer S.M., Bauer R.J. & Velazquez O.C. (2005). Angiogenesis, vasculogenesis, and induction of healing in chronic wounds. *Vascular and Endovascular Surgery* **39**(4): 293–306.
- Beldon P. (2010). Basic science of wound healing. *Surgery* **28**(9): 409–412.
DOI: <https://doi.org/10.1016/j.mpsur.2010.05.007>
- Beserra F.P., Xue M., Lemos G., Maia D.A., Rozza A.L. & Jackson C.J. (2018). Lupeol, a pentacyclic triterpene, promotes migration, wound closure, and contractile effect *in vitro*: possible involvement of PI3K/Akt and p38/ERK/MAPK pathways. *Molecules* **23**:1–17.
DOI: <https://doi.org/10.3390/molecules23112819>
- Bopage N.S., Kamal Bandara Gunaherath G.M., Jayawardena K.H., Wijeyaratne S.C., Abeysekera A.M. & Somaratne S. (2018). Dual function of active constituents from bark of *Ficus racemosa* L. in wound healing. *BMC Complementary and Alternative Medicine* **18**(29).
DOI: <https://doi.org/10.1186/s12906-018-2089-9>
- Burns D., Reynolds W.F., Buchanan G., Reese P.B., Enriquez R.G. (2000). Assignment of ¹H and ¹³C spectra and investigation of hindered side-chain rotation in lupeol derivatives. *Magnetic Resonance in Chemistry* **38**(7): 488–493.
DOI: [https://doi.org/10.1002/1097-458x\(200007\)38:7<488::aid-mrc704>3.0.co;2-g](https://doi.org/10.1002/1097-458x(200007)38:7<488::aid-mrc704>3.0.co;2-g)
- Gerritsen M.E. (2008). Angiogenesis. In: *Hand Book of Physiology Microcirculation* (eds. R.F. Tuma, W.N. Durán & K. Ley), pp. 351–383.

- Academic Press, USA.
DOI: <https://doi.org/https://doi.org/10.1016/B978-0-12-374530-9.00008-5>
- Hamill F.A., Apio S., Mubiru N.K., Mosango M., Bukenya-ziraba R., Maganyi O.W. & Soejarto D.D. (2003). Traditional herbal drugs of southern Uganda Part III: Isolation and methods for physical characterization of bioactive alkanols from *Rubus apetalus*. *Journal of Ethnopharmacology* **87**: 15–19.
DOI: [https://doi.org/10.1016/S0378-8741\(03\)00097-7](https://doi.org/10.1016/S0378-8741(03)00097-7)
- Heil N., Bravo K., Montoya A., Robledo S. & Osorio E. (2017). Wound healing activity of *Ullucus tuberosus*, an Andean tuber crop. *Asian Pacific Journal of Tropical Biomedicine* **7**(6): 538–543.
DOI: <https://doi.org/10.1016/j.apjtb.2017.05.007>
- Krishnappa P., Venkatarangaiah K., Venkatesh, Rajanna S.K.S. & Balan R.K. (2016). Wound healing activity of *Delonix elata* stem bark extract and its isolated constituent quercetin-3-rhamnopyranosyl-(1-6) glucopyranoside in rats. *Journal of Pharmaceutical Analysis* **6**(6): 389–395.
DOI: <https://doi.org/10.1016/j.jpha.2016.05.001>
- Kumar B., Vijayakumar M., Govindarajan R. & Pushpangadan P. (2007). Ethnopharmacological approaches to wound healing-exploring medicinal plants of India. *Journal of Ethnopharmacology* **114**:103–113.
DOI: <https://doi.org/10.1016/j.jep.2007.08.010>
- Kumarasinghe A. (1987). *King Buddhadasa's Saratha Sangrahaya: a Medical Pharmacopeia*, 1st edition, pp. 964. Department of National Museum, Colombo, Sri Lanka.
- Kuppast I.J. & Kumar K.V.S. (2012). Wound healing activity of aqueous and alcoholic extracts of fruits of *Zizyphus oenoplia*. *International Journal of Chemical Sciences* **10**(2): 1021–1027.
- Lee J.H., Kim H.L., Lee M.H., You K.E., Kwon B.J., Seo H.J. & Park J.C. (2012). Asiaticoside enhances normal human skin cell migration, attachment and growth in vitro wound healing model. *Phytomedicine* **19**: 1223–1227.
DOI: <https://doi.org/10.1016/j.phymed.2012.08.002>
- Liang C.C., Park A.Y. & Guan J.L. (2007). *In vitro* scratch assay: A convenient and inexpensive method for analysis of cell migration *in vitro*. *Nature Protocols* **2**(2): 329–333.
DOI: <https://doi.org/10.1038/nprot.2007.30>
- Lindley L.E., Stojadinovic O., Pastar I. & Tomic-Canic M. (2016). Biology and biomarkers for wound healing. *Plastic and Reconstructive Surgery* **138**(3S): 18–28.
DOI: <https://doi.org/10.1097/PRS.0000000000002682>
- Lipton A., Klinger I., Paul D. & Holley R.W. (1971). Migration of mouse 3T3 fibroblasts in response to a serum factor. *Proceedings of the National Academy of Sciences of the United States of America* **68**: 2799–2800.
- Mahapatra S.S., Mohanta S. & Nayak A.K. (2011). Preliminary investigation of the angiogenic potential of *Ziziphus oenoplia* root ethanolic extract using the chorioallantoic membrane model. *Science Asia* **37**: 72–74.
DOI: <https://doi.org/10.2306/scienceasia1513-1874.2011.37.072>
- Mahato S.B. & Kundu A.P. (1994). ¹³C NMR Spectra of pentacyclic triterpenoids-a and some salient features compilation and some salient features. *Phytochemistry* **37**(6): 1517–1575.
- Majumder P. (2012). Evaluation of wound healing potential of crude extracts of *zyziphus oenoplia* L. Mill (indian jujuba) in wistar rats. *International Journal of Phytomedicine* **4**(3): 419–428.
- Maurya S.K., Pandey D.P., Singh J.P. & Pandey V.B. (1995). Constituents of *Ziziphus oenoplia*. *Pharmazie* **50**(5): 372.
- Moon E., Lee Y.M., Lee O., Lee M., Lee S., Chung M., Park Y., Sung C., Choi J. & Kim K. (1999). A novel angiogenic factor derived from *Aloe vera* gel: β -sitosterol, a plant sterol. *Angiogenesis* **3**: 117–123.
- Nadkarni K.M. (1976). *Indian Materia Medica*, volume 01, 3rd edition, pp.1317. Popular Parkashan Private Limited, Bombay, India.
- Nahar N., Das R.N., Shoeb M., Mamma M.S., Aziz M.A. & Mosihuzzaman M. (1997). Four triterpenoids from the bark of *Zizyphus rugosa* and *Zizyphus oenoplia*. *Journal of Bangladesh Academy of Sciences* **21**(2): 151–158.
- Park S.Y., Kim J.S., Lee S.Y., Bae K. & Kang S.S. (2008). Chemical constituents of *Lathyrus davidii*. *Natural Product Sciences* **14**(4): 281–288.
- Pommerville J.C. & Alcamo I. E. (2004). *Alcamo's Fundamentals of Microbiology*, 7th edition, pp.903–904. Jones & Barlett, Sudbury, USA.
- Prabhavathi S. & Vijayalakshmi S. (2016). Identification of new aliphatic hydroxy ether from the root bark of *Ziziphus oenoplia*. *Journal of Pharmacognosy and Phytochemistry* **3**(6): 150–152.
- Prabhavathi S. & Vijayalakshmi S. (2015). New hydroxy carboxylic acid from the root bark of *Ziziphus oenoplia*. *Journal of Pharmacognosy and Phytochemistry* **25**(1): 85–86.
- Rashmi K., Mishra S., Dubey V. & Singh R. (2018). Review on *Ziziphus oenoplia* shrub in various aspect related to their pharmacological properties. *European of Biomedical and Pharmaceutical Sciences* **5**(5): 230–232.
- Ribatt D., Vacca A., Ranieri G., Sorino S. & Roncali L. (1996). The chick embryo chorioallantoic membrane as an *in vivo* wound healing model. *Pathology - Research and Practice* **192**: 1068–1076.
DOI: [https://doi.org/10.1016/S0344-0338\(96\)80050-1](https://doi.org/10.1016/S0344-0338(96)80050-1)
- Rodeheaver G.T., Gentry S., Saffer L. & Edlich R.F. (1980). Topical antimicrobial cream sensitivity testing. *Surgery, Gynecology and Obstetrics* **151**(6): 747–752.
- Rousselle P., Braye F. & Dayan G. (2019). Re-epithelialization of adult skin wounds: Cellular mechanisms and therapeutic strategies. *Advanced Drug Delivery Reviews* **146**: 344–365.
DOI: <https://doi.org/10.1016/j.addr.2018.06.019>
- Serra R., Grande R., Buffone G., Molinari V., Perri P., Perri A., Amato B., Colosimo M. & Franciscis S.D. (2014). Extracellular matrix assessment of infected chronic venous leg ulcers: role of metalloproteinases and inflammatory cytokines. *International Wound Journal* **13**(1): 53–58.
DOI: <https://doi.org/10.1111/iwj.12225>
- Shukla A., Garg S., Garg A., Mourya P. & Jain C.P. (2016). Investigations on hydroalcoholic extract of *Zizyphus oenoplis* for analgesic and antinociceptive activity. *Asian Journal of Pharmacy and Pharmacology* **2**(1): 15–18.
- Shyamala R. & Manikandan R. (2019). Determination of bioactive compounds in *Ziziphus oenoplia* leaves extract using gas chromatography and mass spectroscopic technique. *Journal of Pharmacognosy and Phytochemistry* **8**(5): 157–160.

- Singh A.K. & Singh V.P. (2012). Chemical constituents from *Zizyphus oenoplia*. *Journal of the Indian Chemical Society* **89**: 433–434.
- Singh M., Govindarajan R., Nath V., Kumar A., Rawat S. & Mehrotra S. (2006). Antimicrobial, wound healing and antioxidant activity of *Plagiochasma appendiculatum* Lehm. et Lind. *Journal of Ethnopharmacology* **107**(1): 67–72.
DOI: <https://doi.org/https://doi.org/10.1016/j.jep.2006.02.007>
- Suksamram S., Suwannapoch N., Aunchai N., Kuno M., Ratananukul P., Haritakun R. & Ruchirawat S. (2005). Ziziphine N, O, P and Q, new antiplasmodial cyclopeptide alkaloids from *Zizyphus oenoplia* var. *brunoniana*. *Tetrahedron* **61**: 1175–1180.
DOI: <https://doi.org/10.1016/j.tet.2004.11.053>
- Surekha K.L., Waghchoude M. & Ghaskadbi S. (2013). Enhancement of angiogenesis by a 27 kDa lectin from perivitelline fluid of horseshoe crab embryos through upregulation of VEGF and its receptor. *Journal of Natural Products* **76**: 117–120.
DOI: <https://doi.org/10.1021/np3005198>
- Talekar Y.P., Apte K.G., Paygude S.V., Tondare P.R. & Parab P.B. (2017). Studies on wound healing potential of polyherbal formulation using *in vitro* and *in vivo* assays. *Journal of Ayurveda and Integrative Medicine* **8**: 73–81.
DOI: <https://doi.org/10.1016/j.jaim.2016.11.007>
- Thakur R., Jain N., Pathak R. & Sandhu S.S. (2011). Practices in wound healing studies of plants. *Evidence-Based Complementary and Alternative Medicine* **2011**: 1–17.
DOI: <https://doi.org/10.1155/2011/438056>
- Theoret C. (2017). Physiology of wound healing. In: *Equine Wound Management* (eds. C. Theoret & J. Schumacher), pp.1–13. John Wiley & Sons Inc., UK.
DOI: <https://doi.org/10.1002/9781118999219.ch1>
- Tuenter E., Exarchou V., Apers S. & Pieters L. (2017). Cyclopeptide alkaloids. *Phytochemistry Reviews* **16**: 623–637.
DOI: <https://doi.org/10.1007/s11101-016-9484-y>
- Viet T.D., Xuan T.D. & Anh L.H. (2021). α -amyrin and β -amyrin isolated from *Celastrus hindsii* leaves and their antioxidant, anti-xanthine oxidase, and anti-tyrosinase potentials. *Molecules* **26**: 7248.
DOI: <https://doi.org/10.3390/molecules26237248>
- Wadhwa B.M. (1996). Rhamnaceae. In: *A revised Handbook to the Flora of Ceylon*, volume X (eds. M.D Dasanayaka & W.D. Clayton), pp 360–382, Oxford & IBH Publishing Co. Pvt. Ltd., New Delhi and Calcutta, India.
- Weragoda P.B. (1980). The traditional system on medicine in Sri Lanka. *Journal of Ethnopharmacology* **2**: 71–73.
DOI: [https://doi.org/10.1016/0378-8741\(80\)90033-1](https://doi.org/10.1016/0378-8741(80)90033-1)
- Werner S. & Grose R. (2003). Regulation of wound healing by growth factors and cytokines. *Physiological Reviews* **83**: 835–870.
DOI: <https://doi.org/10.1152/physrev.00032.2002>
- Yarrow J.C., Perlman Z.E., Westwood N.J. & Mitchison T.J. (2004). A high-throughput cell migration assay using scratch wound healing, a comparison of image-based readout methods. *BMC Biotechnology* **4**.
DOI: <https://doi.org/10.1186/1472-6750-4-21>
- Yun-Choi H.S., Jin J.L., Hong S.W., Lee Y.Y. & Lee J.H. (2003). Constituents of *Euphorbia milii*. *Natural Product Sciences* **9**(4): 270–272.

**In-vitro wound healing potential of leaf and bark of *Ziziphus oenoplia* (L.) Miller
Supplementary material**

- S1.** Mean percentages of wound closure at 24 h in SWA at a concentration of 20 mg/Land mean vascular indices in CAM assay at a dose of 10 µg of extracts of *Z. oenoplia* with positive and negative controls.

Plant part	Extract	Mean % wound Closure	Mean vascular index
		(±SD)*	(±SD)*
Leaf	Hexanes	78.0 (3.4) ^c	27.0 (2.7) ^e
	Dichloromethane	80.1 (5.7) ^c	27.2 (2.2) ^e
	Ethyl acetate	80.9 (2.5) ^c	37.2 (3.5) ^e
	Methanol	21.6 (4.3) ^e	42.8 (3.7) ^b
Bark	Hexanes	75.5 (4.3) ^c	33.6 (3.6) ^{cd}
	Dichloromethane	23.6 (0.9) ^e	27.2 (3.5) ^e
	Ethyl acetate	12.5 (3.8) ^f	30.4 (3.5) ^{de}
	Methanol	20.9 (6.2) ^e	34.2 (2.8) ^{cd}
	Positive control [†]	90.2 (1.1) ^a	48.6 (2.0) ^a
	Negative control [‡]	19.5 (2.6) ^e	14.6 (2.9) ^f

* Different letters in the same column indicate significant differences at $t=1.98$ and $p \leq 0.05$ level.

[†] Asiaticoside (25 µM) was used in the SWA; β -sitosterol (10 µg) was used in the CAM assay.

[‡]1% DMSO in 20% DMEM was used in the SWA; DMSO was used in the CAM assay.

- S2.** Mean diameters of inhibition zones developed against different extracts of *Z. oenoplia* and the positive control (Amoxicillin, 10 µg) with *B. subtilis*, *S. aureus*, *E. coli*, and *P. aeruginosa* at 500 µg/disc.

Plant part	Extract	Mean diameter of inhibition zone (mm) (±SD)*			
		<i>B. Subtilis</i>	<i>S. aureus</i>	<i>E. coli</i>	<i>P. aeruginosa</i>
Leaf	Hexanes	9.4 (0.5) ^d	NA	NA	NA
	Dichloromethane	10.1 (0.7) ^c	8.5 (0.5) ^d	7.4 (0.5) ^c	8.5 (0.5) ^c
	Ethyl acetate	12.3 (0.4) ^b	9.5 (0.6) ^c	NA	NA
	Methanol	7.1 (0.3) ^f	9.3 (0.4) ^c	NA	NA
Bark	Hexanes	NA	NA	8.7 (0.4) ^b	NA
	Dichloromethane	8.3 (0.4) ^c	10.6 (0.4) ^b	8.9 (0.2) ^b	9.7 (0.4) ^b
	Ethyl acetate	10.2 (0.4) ^c	7.3 (0.4) ^c	7.5 (0.5) ^c	NA
	Methanol	NA	NA	NA	NA
	Amoxicillin (10 µg)	25.0 (0.8) ^a	31.9 (0.8) ^a	20.8 (0.5) ^a	12.3 (0.6) ^a

* Different letters in the same column indicate significant differences at $t=1.98$ and $p \leq 0.05$ level.

NA = Not active; Clear zone not observed.

- S3.** Spectroscopic data of lupeol (1), α -amyirin (2), β -amyirin (3), hexacosanol (4) and octacosanol (5).

Lupeol (1) – ¹H NMR (400 MHz, CDCl₃) δ (ppm): 4.68 (1H, br H-29b), 4.56 (1H, br, H-29a), 3.18 (1H, br dd, J = 5.1, 11.1 Hz, H-3), 2.37 (1H, m, H-19); ¹³C NMR (100 MHz, CDCl₃) δ (ppm): 150.9 (C-20), 109.3 (C-29), 79.0 (C-3), 55.3 (C-5), 50.4 (C-9), 48.3 (C-18), 48.0 (C-19), 43.0 (C-17), 42.8 (C-14), 40.8 (C-8), 40.0 (C-22), 38.8 (s, C-4), 38.6 (C-1), 38.0 (C-13), 37.1 (C-10), 35.6 (C-16), 34.3 (t, C-7), 29.8 (C-21), 28.0 (C-23), 27.5 (C-15), 27.4 (C-2), 25.1 (C-12), 20.9 (C-11), 19.3 (C-30), 18.3 (C-6), 18.0 (C-28), 16.1 (C-25), 15.9 (C-26), 15.4 (C-24), 14.5 (C-27).

GC-MS, Retention time (t_R): 18.211 min.; m/z (rel. int., %): 426 [M⁺] (13.7), 339.3 (1.6), 370.2 (0.9), 344.2 (0.4), 315.3 (4.3), 286.2 (1.3), 257.1 (4.7), 218.2 (100.0), 207.15 (19.6), 203.2 (29.0), 189.2 (36.3), 175.1 (13.0), 161.15 (16.1), 147.0 (16.8), 143.0 (2.0), 119.1 (20.9), 109.1 (22.8), 107.1 (24.7), 95.1 (26.7), 81.1 (22.4), 67.1 (14.7), 57.1 (7.4), 41.1 (10.8).

α -Amyrin (2) – ¹H NMR (400 MHz, CDCl₃) δ (ppm): 5.12 (1H, t, J = 3.4 Hz, H-12), 3.22 (1H, dd, J = 4.8, 10.9 Hz, H-3); ¹³C NMR (100 MHz, CDCl₃) δ (ppm): 139.6 (C-13), 124.4 (C-12), 79.0 (C-3), 59.0 (C-18), 55.2 (C-5), 47.7 (C-9), 42.1

(C-14), 41.5 (C-22), 40.0 (C-8), 39.8 (C-19), 39.6 (C-20), 38.8 (C-1 and C-4), 36.9 (C-10), 33.7 (C-17), 32.9 (C-7), 31.3 (C-21), 28.7 (C-15), 28.1 (C-23 and C-28), 27.3 (C-2), 26.6 (C-15), 23.4 (C-11), 23.3 (C-27), 21.4 (C-30), 18.4 (C-6), 17.5 (C-29), 16.8 (C-26), 15.7 (C-25), 15.6 (C-24).

GC-MS, t_R : 18.211 min.; m/z : 426.4 [M⁺]; 426.4 (12.2), 411.4 (4.7), 393.4 (1.4), 366.3 (0.2), 341.1 (2.0), 315.3 (3.1), 281.1 (6.9), 253.0 (2.9), 218.2 (100.0), 218.2 (100), 203.2 (26.2), 189.2 (30.1), 179.1 (1.9), 161.2 (13.8), 147.1 (16.6), 135.1 (25.3), 121.1 (19.3), 81.1 (18.9), 69.1 (16.3), 55.1 (14.8), 41.1 (9.4).

β -Amyrin (**3**); ¹H-NMR (400 MHz, CDCl₃) δ (ppm): 5.18 (1H, t, J = 3.4 Hz, H-12), 3.22 (1H, dd, J = 4.8, 10.9 Hz, H-3); ¹³C-NMR (100 MHz, CDCl₃) δ (ppm): 145.2 (C-13), 121.7 (C-12), 79.0 (C-3), 55.2 (C-5), 47.6 (C-9), 47.2 (C-18), 46.8 (C-19), 41.7 (C-14), 38.9 (C-4), 38.8 (C-8), 38.7 (C-1), 37.2 (C-22), 37.0 (C-10), 34.7 (C-21), 33.3 (C-29), 32.6 (C-7), 32.5 (C-17), 31.1 (C-20), 28.4 (C-28), 28.1 (C-23), 27.2 (C-2), 27.0 (C-16), 26.2 (C-15), 26.0 (C-27), 23.7 (C-30), 23.5 (C-11), 18.4 (C-6), 16.8 (C-26), 15.6 (C-25), 15.5 (C-24).

GC-MS, t_R : 17.720 min.; m/z (rel. int., %): 426.4 [M]⁺ (4.4), 408.4 (0.2), 393.4 (0.7), 281.1 (4.2), 218.2 (100), 203.2 (49.3), 189.2 (14.9), 161.2 (5.0), 135.1 (10.3), 95.1 (11.8), 69.1 (10.9), 43.1 (6.1)

Hexacosanol (**4**) and Octacosanol (**5**); ¹H NMR (400 MHz, CDCl₃) δ (ppm): 3.60 (t, J =6.4 Hz, CH₂OH), ¹³C NMR (100 MHz, CDCl₃) δ (ppm): 63.1 (C-1), 32.8 (C-2), 31.9 [C-24 (**4**) and C-26 (**5**)], 29.3 – 29.7 [C-4 to C-23 (**4**) and C-4 to C-25 (**5**)], 25.7 (C-3), 22.7 [C-25 (**4**) and C-27 (**5**)], 14.1 [C-26 (**4**) and C-28 (**5**)].

Hexacosanol (**4**); GC-MS, t_R : 13.955 min.; m/z (rel. int., %): 364.4 [M-H₂O]⁺ (2.3), 336.3 (2.5), 181.1 (3.2), 135.1 (0.6), 125.1 (29.3), 111.1(55.1), 97.1 (100), 83.1 (96.9), 57.1 (90.5), 41.1 (36.5)

Octacosanol (**5**); GC-MS, t_R : 15.345 min.; m/z (rel. int., %): 392.4 [M-H₂O]⁺ (2.4), 364.4 (2.6), 336.4 (0.6), 181.1 (3.6), 153.1 (8.2), 125.1 (31.0), 111.1(57.0), 97.1 (100), 83.1 (95.2), 69.1 (74.3), 57.1 (90), 55.1 (68.9), 43.1 (63.4), 41.1 (32.5).

RESEARCH ARTICLE

Coastal Dynamics

Spatial and temporal changes of land use land cover distribution in selected sites of the southern coastal zone of Sri Lanka

WMIC Wijesundara^{1*}, DUV Gunathilaka¹, SK Madarasinghe¹, J Andrieu², G Muthusankar², NR Kankanamge³ and KAS Kodikara¹

¹ Department of Botany, Faculty of Science, University of Ruhuna, Matara, Sri Lanka.

² GEOSpatial Monitoring and Information Technology (GeoSMIT) Department, French Institute of Pondicherry (IFP), Pondicherry, 605001, India.

³ Earth and Ocean Sciences, School of Natural Sciences and Ryan Institute, National University of Ireland Galway H91 TK33, Ireland.

Submitted: 21 November 2021; Revised: 30 July 2022; Accepted: 26 August 2022


Abstract: The southern coastal zone of Sri Lanka has been subjected to a variety of natural and anthropogenic influences over the past three decades. Understanding impacts of such influences on Land Use Land Cover (LULC) is vital for proper management of the coastal zone. This study, therefore, focused on mapping the change/s in the distribution of selected LULC in the selected sites, Bundala, Galle, Kalametiya, and Hambantota of the southern coastal zone, over last 24 years using satellite imagery. LULC maps of nine classes (mangrove, inland vegetation, marsh and grass, sand, bare land, built-up, cultivation, water, and unclassified) were created by employing an on-screen digitization technique achieving an accuracy of >70%. Trend analysis and two-sample proportion tests were used for statistical analyses, whereas geometric calculations were used for descriptive analyses. The results showed the highest overall change in LULC in Kalametiya, followed by Hambantota, Galle, and Bundala. The changes in the LULC classes are mainly attributed to the conversion of water to mangroves, marsh and grass areas in Kalametiya, water to built-up areas in Hambantota, cultivations to built-up areas in Galle, and marsh and grass areas to bare lands in Bundala. The causes of LULC changes were site specific. Trend analyses indicate the least LULC changes in Bundala possibly by 2025. The study highlights the significance of taking into account geographical dislocations when considering and anticipating the potential impacts of development projects over broader extents.

Keywords: Land cover distribution, mapping, satellite imagery, southern coastal zone, spatial and temporal changes.

INTRODUCTION

A coastal zone in any country can be defined as the interface between the land and water (Ahmad, 2019; Adade *et al.*, 2021). Coastal architecture comprises a continuum of coastal and terrestrial lands, aquatic systems including the network of rivers and estuaries, islands, transitional and intertidal areas, salt marshes, wetlands, and beaches (Batista *et al.*, 2017; Bini & Rossi, 2021). From an ecosystem perspective it harbours kelp forests, mangroves, seagrass meadows, rocky shores, sandy shores, and salt marshes along the 620,000 km of coastline on earth (Ewel *et al.*, 1998). Due to high productivity and structural complexity, ecosystems residing in the coastal zone are capable of provisioning manifold goods such as wildlife resources, fisheries, agriculture resources, water supply and energy resources, and ecosystem services such as climate mitigation, erosion control, recreation, tourism, and storm protection, which are of ecological, economic and social significance. Thus, these systems are crucial habitats that are integral for the existence of life (Ewel *et al.*, 1998; McLeod *et al.*, 2011).

Globally, more than one third (>40%) of the population is concentrated in the coastal zone (Gedan *et al.*, 2011). At present, coastal zones are undergoing tremendous anthropogenic pressures attributed to increased population density, excessive reliance on resources, and urbanization driven by development projects (Neumann *et al.*, 2015; Zhao *et al.*, 2021). It was estimated that over half of the world's coastal habitats and natural

* Corresponding author (isuruwmic@gmail.com;  <https://orcid.org/0000-0001-8200-458X>)



This article is published under the Creative Commons CC-BY-ND License (<http://creativecommons.org/licenses/by-nd/4.0/>). This license permits use, distribution and reproduction, commercial and non-commercial, provided that the original work is properly cited and is not changed in anyway.

landscapes have been degraded in the recent past due to human activities, making them the most threatened and vulnerable areas of land-use change (Hyndes *et al.*, 2014; Macreadie *et al.*, 2017). The degradation of coastal habitats has profound impacts on their capacity in provisioning goods and services (Post & Kwon, 2000; Neumann *et al.*, 2015).

Sri Lanka is a tropical island with a total land extent of 65,525 km² located in the Indian Ocean between latitudes 5° 55' and 9° 51' and longitudes 79° 52' and 81° 51' (Rathnayake *et al.*, 2020). The country has a narrow coastal belt along the coastline of 1,730 km of which the land extent can be attributed to 24% of the total land extent of the country (Senevirathna *et al.*, 2018). The coastal zone of the country is occupied by a variety of ecosystems, including mangroves, saltmarshes, seagrass meadows, marshes, grasslands, sand dunes. All of them, play a crucial ecological role. Moreover, being an island nation, the economy and social life of the country is excessively reliant on the coastal zone where over 65% of the population of Sri Lanka is concentrated in the narrow coastal stretch (Senevirathna *et al.*, 2018). Following the introduction of an open economic policy in the late 1970s, multiple socioeconomic and political changes have taken place within the country, which triggered the initiation of multipurpose development projects including irrigation projects, transportation and road development projects, agriculture expansion, the establishment of industrial zones and urban development projects (Mapa *et al.*, 2002). The civil war which prevailed for 30 years since the 1980s afflicted negative impacts on the economy of the country, curtailing development, particularly on the Northern and Eastern coasts (Rathnayake *et al.*, 2020). In 2004, the country experienced a natural catastrophic tsunami event, which hazardously affected the economy of the country as well as social life (De Alwis & Noy, 2019). Moreover, the adverse impacts the tsunami had on the coastal habitats, particularly on the Eastern and Southern coastal zones, and the post-tsunami restoration efforts of coastal ecosystems are of significant concern (Mukherjee *et al.*, 2015; Kodikara *et al.*, 2017). Many development projects have excessively been launched on the southern coastal zone, which primarily included highway development, tourism expansion, and exacerbated urbanization after the end of the civil war in 2009 (Rathnayake *et al.*, 2020).

Considering the major historical events that occurred within the country, it is apparent that the natural land-use patterns have heavily been affected leading to manifold changes (Mapa *et al.*, 2002). This is particularly true to the southern coastal zone where many past and recent development projects have been carried out. Thus, pristine coastal habitats were transformed or converted to a variety of other land uses such as infrastructure developments, tourism expansions, crop cultivations, and aquaculture developments (Gunawardena & Rowan, 2005).

The use of satellite images for mapping the land use and land cover (LULC) of landscapes is a highly recognized tool to determine LULC changes over multiple spatial and temporal scales (Kennedy *et al.*, 2015). Thus, LULC maps can be used to monitor changes in natural habitats, biodiversity, natural productivity, and climate (Kennedy *et al.*, 2015). Among the techniques available, the on-screen digitization is proven to be a better method for LULC mapping over pixel-based and unsupervised classification methods, particularly for areas having high fragmentation in the land-use (Herold *et al.*, 2002; Madarasinghe *et al.*, 2020).

Despite the wide acknowledgement of employing satellite remote sensing techniques for LULC mapping, the lack of accurate LULC maps is a major drawback for Sri Lanka, particularly to the southern coastal zone (Dissanayake, 2020). Therefore, this study focused on selected locations of the southern coastal zone of the country to address the key questions: (a) what is the present status of the LULC distribution in the coastal zone (b) what are the changes that occurred in the LULC during the past 24 years (c) what is the rate of changes in each LULC class when retrospective changes are considered, (d) what would be the area coverage of LULC for the next 5 years (by 2025) if the same rate of changes continue, and (e) which recommendations can be made for the better management of the southern coastal zone.

MATERIALS AND METHODS

Study area

The southern coastal zone of Sri Lanka is bordered by the Indian Ocean from the south and southwest and is located in the Southern province, about 116 km down south from the main city, Colombo. It covers the three

districts Galle, Matara, and Hambantota, which together represents a wide range of climatic zones ranging from wet to dry climate. The wet zone receives a higher annual rainfall about 2500 mm, distributed throughout the year and the dry zone receives an annual rainfall less than 1750 mm mainly during the northeast monsoon period from December to March (Bellio & Kingsford, 2013). The four study locations were: Galle ($6^{\circ}1'31.84''\text{N}/80^{\circ}15'11.47''\text{E}$; 2,267 ha), Kalametiya ($6^{\circ}5'31.52''\text{N}/80^{\circ}56'2.03''\text{E}$; 3,063 ha), Hambantota ($6^{\circ}8'40.97''\text{N}/81^{\circ}7'48.61''\text{E}$; 3,076 ha), and Bundala ($6^{\circ}10'56.56''\text{N}/81^{\circ}12'54.41''\text{E}$; 3,003 ha) located in the Southern coastal zone of Sri Lanka (Figure 1).

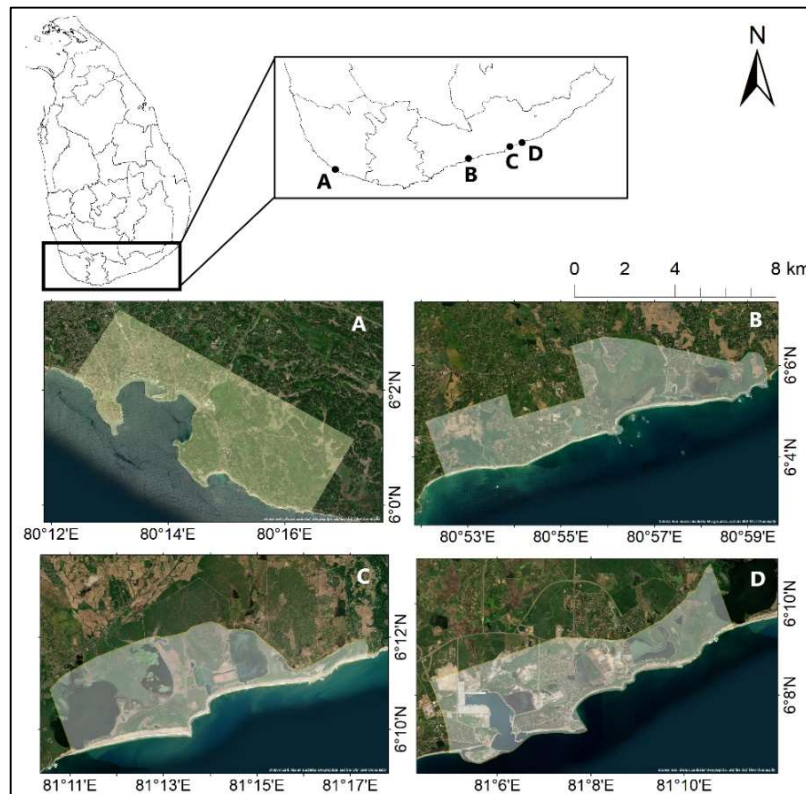


Figure 1: Study locations in the southern coastal zone of Sri Lanka. (A): Galle (B): Kalametiya (C): Hambantota, and (D): Bundala. The area demarcations of the study sites are shaded.

These locations were selected since they represent an array of diverse coastal habitats along the coastal stretch and are subjected to varying levels of protection within their ecological significance and level of conservation required. Thus, it makes a better representation of the southern coastal zone and enables to understand the effectiveness of policy measures towards conservation. Bundala is a protected area (National Park) managed under the provisions of the Fauna and Flora Protection Ordinance (FFPO) of 1993, which is administered by the Department of Wildlife Conservation (DWC) (Perera & De Vos, 2007). Further, giving consideration to its outstanding ecological value as a wetland, it was granted the Ramsar status (Piyankarage *et al.*, 2004; Bellio & Kingsford, 2013). Consequently, coastal habitats in the area play a vital role in sustaining ecological significance. The study site Kalametiya is a partially protected area, where protection is enforced only to the extent of the Kalametiya sanctuary. Thus, human interference could be observed within the area beyond protection. After the civil war ended in mid-2009, the government focused on enhancing the country's infrastructure, especially through highway and reservoir construction (Rathnayake *et al.*, 2020). Hambantota is an area heavily subjected to development projects since 2008 with the initiation of the Hambantota port construction (Kavirathna *et al.*, 2021), followed by construction of the southern expressway and associated developments. Consequently, Galle can be considered the most urbanized compared to the other three sites, probably because those experiences intensified anthropogenic influences primarily being a tourism and heritage hotspot (Dissanayake, 2020).

Further, following the tsunami in 2004, it received greater attention where many infrastructure development projects were initiated focusing on rehabilitation of the areas affected. Thus, rapid expansion in the infrastructure was prominent compared to other sites (Dissanayake, 2020).

Satellite data collection

LULC maps available at the survey department of Sri Lanka were obtained for the two years 1996 and 2007. Further, Google Earth archive images for the year 2017 and QuickBird-2 high-resolution (0.5 m) satellite imagery for the year 2020 were obtained to create LULC maps for the study areas. The satellite image selection was done depending on the image availability. A summary of the satellite imagery used for the study is given in Table 1.

Table 1: Summary of satellite imagery used for the study

Location	Source	Satellite platform	Date of acquisition	Spatial resolution (m)
Bundala	Google Earth Pro	CNES/Airbus	15/10/2017	1.0
	Digital Globe	QuickBird-2	19/08/2020	0.5
Galle	Google Earth Pro	Maxar Technologies	07/02/2017	1.0
	Digital Globe	QuickBird-2	23/04/2020	0.5
Kalametiya	Google Earth Pro	Maxar Technologies	02/01/2017	1.0
	Digital Globe	QuickBird-2	23/04/2020	1.0
Hambantota	Google Earth Pro	CNES/Airbus	01/05/2017	1.0
	Digital Globe	QuickBird-2	19/08/2020	0.5

These images were georeferenced using 20-30 ground control points obtained by GPS (eTrex Gamin). Image processing was carried out using ArcGIS 10.3 software. Study areas were extracted from the satellite images by clipping with the boundary polygons delimitating study sites. Mosaics were created for imagery obtained from the Google Earth platform for each site, maintaining a consistent spatial resolution of 1.0 m. True colour composites were created for the QuickBird imagery prior to use for mapping.

Mapping of study sites

Mapping was carried out using ArcGIS 10.3 software. Nine LULC classes were considered which include categories; mangrove, inland vegetation, marsh and grass, sand, bare land, built-up, cultivation, water, and unclassified. The on-screen digitization technique was employed for the mapping. Digitizing of all satellite imagery was performed manually maintaining a consistent eye altitude ratio of 1:1500 (m). Each LULC type was identified using image attributes such as size, texture and tonality coupled with ground verification and was demarcated using shapefile polygons. The description of criteria used to refer LULC classes are described in Table 2.

Table 2: Description of LULC classes considered during the study

LULC class	Description of reference criteria
Built-up area	Areas of main towns, cities, build-ups, homestead and gardens
Bare land	Areas of bare soil without significant vegetation and build-up and water regions
Cultivation	Areas of main plantation crops (paddy, coconut, tea, rubber and <i>chena</i>)
Inland vegetation	Areas of natural forest, scrub and patches of vegetation larger than 0.01 ha
Mangrove	Areas of mangrove distribution
Marsh and grass	Areas of marsh and grass distribution
Sand	Areas of sand and beaches including scattered vegetation
Unclassified	Areas not belonging to any of the classes concerned
Water	Areas of natural water bodies and artificial waterways and channels

Area estimations were obtained for each polygon representing the respective LULC type, and maps were superimposed to obtain area gains and losses between the two years 1996 and 2020 using overlay analysis.

Map accuracy assessment

Accuracy Assessment for the LULC maps was carried out for the year 2020 using 50 random locations for each study site, created using ArcGIS 10.3 software. Ground verification of each random location was carried out through observations using field validation achieved by onsite visits to the study sites. Overall, accuracy was then calculated for each study site using Equation 1 (Janssen & Vanderwel, 1994).

$$\{\text{Overall accuracy} = \text{No. of confirmed observations} / 50 * 100\} \quad \dots (1)$$

Statistical analyses

All statistical analyses, including descriptive and inferential, were performed using R statistical software with a significance level of 0.05. Mean and standard deviation for the area values was calculated as descriptive statistics. The significance in the area change of each LULC class resulting from the overlay analysis was obtained using the two-sample proportion test, considering the area statistics of 1996 and 2020 for each study site. To assess the rate of change in the LULC over the study period, a trend analysis was carried out for the area statistics of each LULC class for all years. Linear and quadratic functions were utilized for trend analysis. The inference of the rate of change of each LULC class over the period was used to predict the area cover by 2025. Separate two-sample proportion tests were carried out for each study site, considering each LULC class, to assess the significance of area change between 2020 and the area predicted for the year 2025.

RESULTS AND DISCUSSION

The overall accuracy of the maps created for all the study sites exceeded 70%; Galle reported the highest level of accuracy (84%), while Kalametiya, Bundala and Hambantota sites achieved 82.2, 79.5 and 72.3% overall accuracy, respectively. The distribution of LULC classes varied between the study locations. A high degree of dominance in the built-up areas was prominent in Galle, where over 60.9% of the distribution of the total land extent was reported at all temporal scales. In contrast, the Bundala site experienced a dominance in inland vegetation and water with 41.7 and 38.8% of distribution, respectively, compared to other categories. Comparatively intermediate dominancy was observed in the LULC class distribution for the Kalametiya and Hambantota sites.

According to the results of the two-sample proportion test, all sites reported significant changes in the LULC distribution between 1996 and 2020. The details of the overall area changes of the LULC classes of study sites are given in Table 3.

Bundala

All the classes, except the built-up area category, reported significant land cover changes during the study period in the Bundala site. The bare land class showed the highest area change with a gain of 157.4 ha, which is attributed to a 5.1% change during the reporting period. The second most dynamic land cover class was inland vegetation, which changed by a loss of 4.5%. Marsh and grass category declined by 4.0% during the period, which was the third most dynamic class. Water and sand categories indicated significant gains of 2.2% while a loss of 2.2% was reported for the cultivation category.

Galle

The highest land cover change in the Galle site was observed for cultivation, where it experienced a loss of 335.8 ha representing a change of 14.8% during the study period. A comparatively similar change was reported for the built-up area category indicating a gain of 14.4% of its land cover. The increase in the inland vegetation cover was by 2.4%. Abatement of mangrove cover was significant which reported a reduction of 1.2% of its cover during the study period. Despite being significant, comparatively less (<1.1%) area changes were reported for other LULC categories. Marsh, grass, and sand LULC classes changed insignificantly.

Kalameitiya

The highest significant land cover change in Kalameitiya was reported for mangrove, marsh, and grass categories, resulting in a total area gain of 633.7 ha, which attributed to a change of 20.7%. The second highest change was for water, which resulted in a loss of 569.4 ha representing a change of 18.6%. Loss of cultivation (7.5%) was observed as the third-largest change in Kalameitiya. Other land-use classes, except unclassified, reported significant gains for the study period.

Table 3: Area estimations of LULC classes in 1996 and 2020 and the overall area changes from 1996 to 2020. Area gains over the period are indicated with '+' signs while area losses are with '-' signs. Significant area changes ($p < 0.05$) are marked with an asterisk (*). p values obtained through the two-sample proportion test for the area statistics in 1996 and 2020 indicate the level of significance in area change at 95% confidence level

LULC classes	Area (ha)		Area change (1996-2020)		p value
	1996	2020	ha	%	
Bundala					
Built-up areas	75.2	78.1	+2.9	+0.1	0.877
Bare land	0.0	157.4	+157.4*	+5.2	< 2.2e-16
Cultivation	66.9	0.0	-66.9*	-2.2	5.396e-16
Inland vegetation	1386.4	1252.6	-133.8*	-4.5	0.001
Marsh and grass	143.7	22.2	-121.5*	-4.0	< 2.2e-16
Sand	150.4	231.4	+81.0*	+2.7	2.328e-05
Water	1180.9	1261.9	+80.9*	+2.7	0.036
Galle					
Built-up areas	1380.9	1707.2	+326.3*	+14.4	< 2.2e-16
Bare land	0.0	16.9	+16.9*	+0.7	0.000
Cultivation	613.9	278.1	-335.8*	-14.8	< 2.2e-16
Inland vegetation	10.0	64.2	+54.2*	+2.4	4.749e-10
Mangrove	61.4	33.4	-28.0*	-1.2	0.005
Marsh and grass	91.2	112.5	+21.3	+0.9	0.1456
Sand	22.5	12.5	-10.0	-0.4	0.1267
Unclassified	32.5	13.0	-19.5*	-0.9	0.006
Water	54.7	29.1	-25.5*	-1.1	0.007
Kalameitiya					
Built-up areas	937.7	809.4	-128.4*	-4.2	0.000
Bare land	0.0	44.7	+44.7*	+1.5	5.373e-11
Cultivation	590.2	361.6	-228.6*	-7.5	9.987e-16
Inland vegetation	556.5	754.2	+197.7*	+6.5	8.904e-10
Mangrove, marsh and grass	93.6	727.4	+633.7*	20.7	< 2.2e-16
Sand	40.8	88.1	+47.3*	+1.5	3.762e-05
Unclassified	2.9	6.1	+3.2	+0.1	0.463
Water	841.7	272.3	-569.4*	-18.6	< 2.2e-16
Hambantota					
Built-up areas	630.5	1346.0	+715.5*	+12.0	2.2e-16
Bare land	0.0	1.3	+1.3	+0.04	0.792
Cultivation	58.1	31.9	-26.2*	-0.9	0.007
Inland vegetation	1157.9	1055.3	-102.6*	-3.3	6.954×10 ⁻⁰³
Marsh and grass	28.0	86.2	+58.2*	+1.9	6.555e-08
Sand	164.4	85.6	-78.8*	-2.6	5.07e-07
Unclassified	60.7	31.3	-29.4*	-1.0	1.126e-06
Water	976.7	438.4	-538.5*	-17.5	2.2e-16

Hambantota

Loss of 538.3 ha of water areas (17.5%), and a gain of 715.5 ha of built-up areas (12.0%) were the significant changes observed in the Hambantota site. Changes in other LULC classes in the Hambantota site were less than 3.3% where losses were observed for the categories, cultivation, inland vegetation, sand, and unclassified, while gains were observed for marsh and grass. Although a gain was reported for the bare land category, the change was insignificant.

Further, to determine the area changes of the LULC classes, a major objective of the study was to graphically illustrate the locations where the changes (loss and gain) have occurred for each LULC class throughout the study. Such an understanding is vital to determine the relationships that exists between LULC classes within a study site. This was achieved through superimposing LULC maps of 1996 with 2020 using overlay analysis.

Bundala

The resulting LULC maps of the Bundala site together with respective area gain and loss maps are illustrated in Figure 2. The change in the LULC class distribution between years was a continuous evolution during the study period. Of the changes reported between 1996 and 2020, the transformation of marsh and grass patches located on the eastward side of the Embilikala lagoon (water body in the middle) and the southward extent of the Malala lagoon (the lagoon located further westward) to bare land was the major change observed. Over this period, the disappearance of cultivated lands was observed, which existed during 1996 on the east, north, and westward extent of the study site. They were reported to have been replaced by natural inland vegetation by 2020. Expansion of the built-up areas towards inland vegetated areas, particularly on the northward extent of the Bundala salt ponds (the largest built-up area of the site), was observed. Further, when the inland vegetation along the coast declined, the sand cover increased. Gains of water areas in the inland vegetated areas and gains of inland vegetated areas in the water areas were observed elsewhere in the map in a discontinuous manner.

Galle

LULC maps of Galle over the study period and respective area gain and loss maps are illustrated in Figure 3. The highest change in the distribution of LULC classes was reported between 1996 and 2007. Results of the overlay analysis between the years 1996 and 2020 show excessive urbanization of cultivated lands in the western part of the study site, which represents Galle's main city and adjacent towns. Moreover, built-up areas were further expanded in the cultivated areas of the eastern part to a lesser extent compared to that of the west, which primarily represents homesteads and gardens. A reduction in the built-up areas in some parts along the coast was reported, which were replaced by inland vegetation and sand; this could be attributed to destruction that occurred due to the tsunami in the year 2004. The conversion of mangrove areas to marsh and grass was a prominent observation. Further, the reduction in the overall mangrove cover during the study period is of significance. However, mangrove area gains were also reported in some areas of marsh and grass. Marsh and grass areas towards the eastward side of the study site remained unchanged.

Kalameitiya

The LULC maps of the Kalameitiya study site, along with the overlay gain and loss maps, are illustrated in Figure 4. The changes to the LULC classes between the years were observed as continuous changes over the study period; rapid changes were not observed. The most prominent change reported through the overlay analysis between 1996 and 2020, was the conversion of the water extent of the Kalameitiya lagoon to a mixed area composed of mangrove, marsh, and grass. Further, inland vegetation and built-up areas (primarily homesteads and gardens) in the westward part of the site were transformed into a marsh and grass area. Some parts of the built-up areas in the eastward part of the site were converted to inland vegetation. Vegetated areas along the coast were converted to sandy beaches. Further, it was observed that built-up areas (140.3 ha) in close proximity to the main lagoon and marsh and grass habitats, which were inhabited by inland vegetation during 1996 showed significant gains.

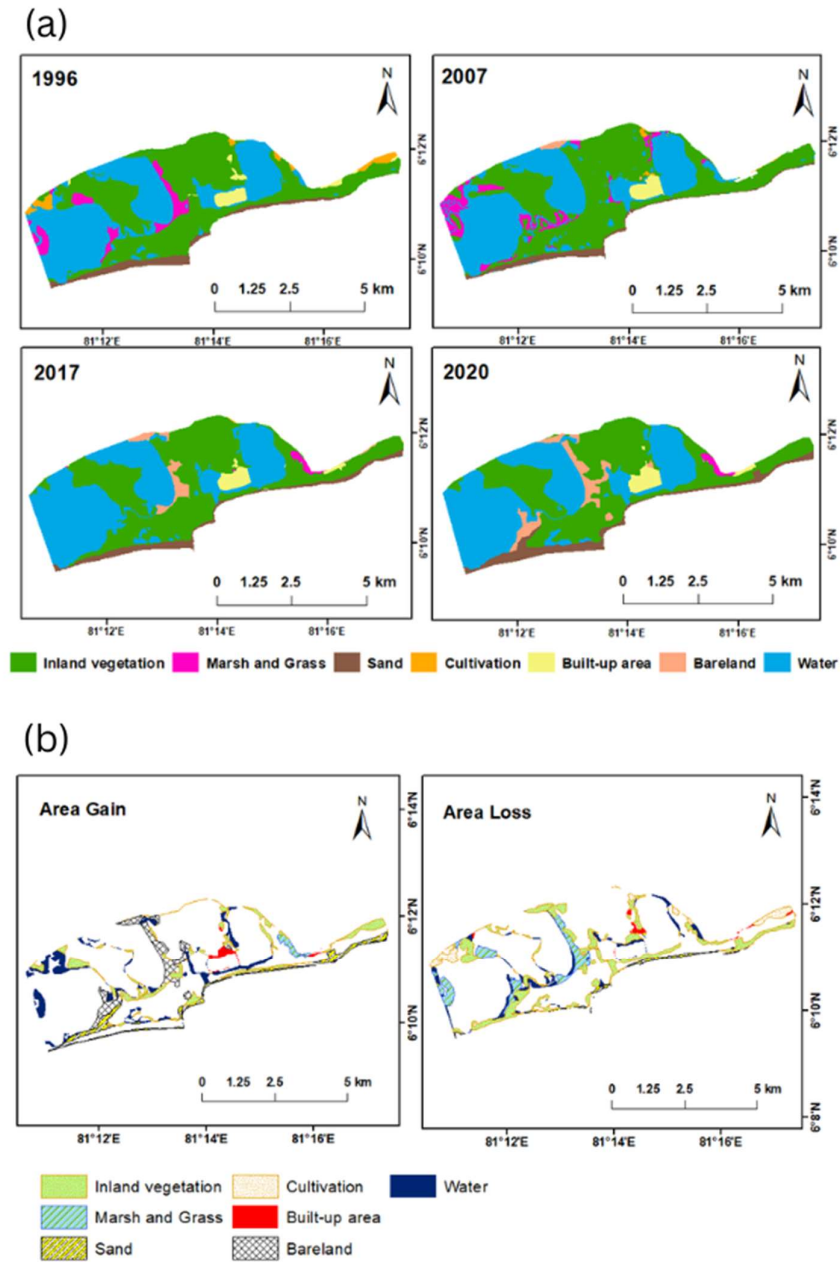


Figure 2: LULC and Overlay maps of Bundala study site. (a) LULC maps for 1996, 2007, 2017 and 2020; (b) Overlay maps representing areas of loss and gain between 1996 and 2020.

Hambantota

The resulting LULC maps of the Hambantota site, together with respective area gain and loss maps, are illustrated in Figure 5. Rapid changes in the LULC classes were observed between 1996 and 2017. A significant increase in built-up areas replacing water areas, particularly infrastructure development, was observed towards the in part of the site. Moreover, further decreases in the water areas were observed, which were replaced by built-up areas in the middle part of the site. Inland vegetation that existed in the eastward part of the site has transformed into built-up areas. Further, it was observed that to a lesser extent, inland vegetation has emerged in the areas of cultivation.

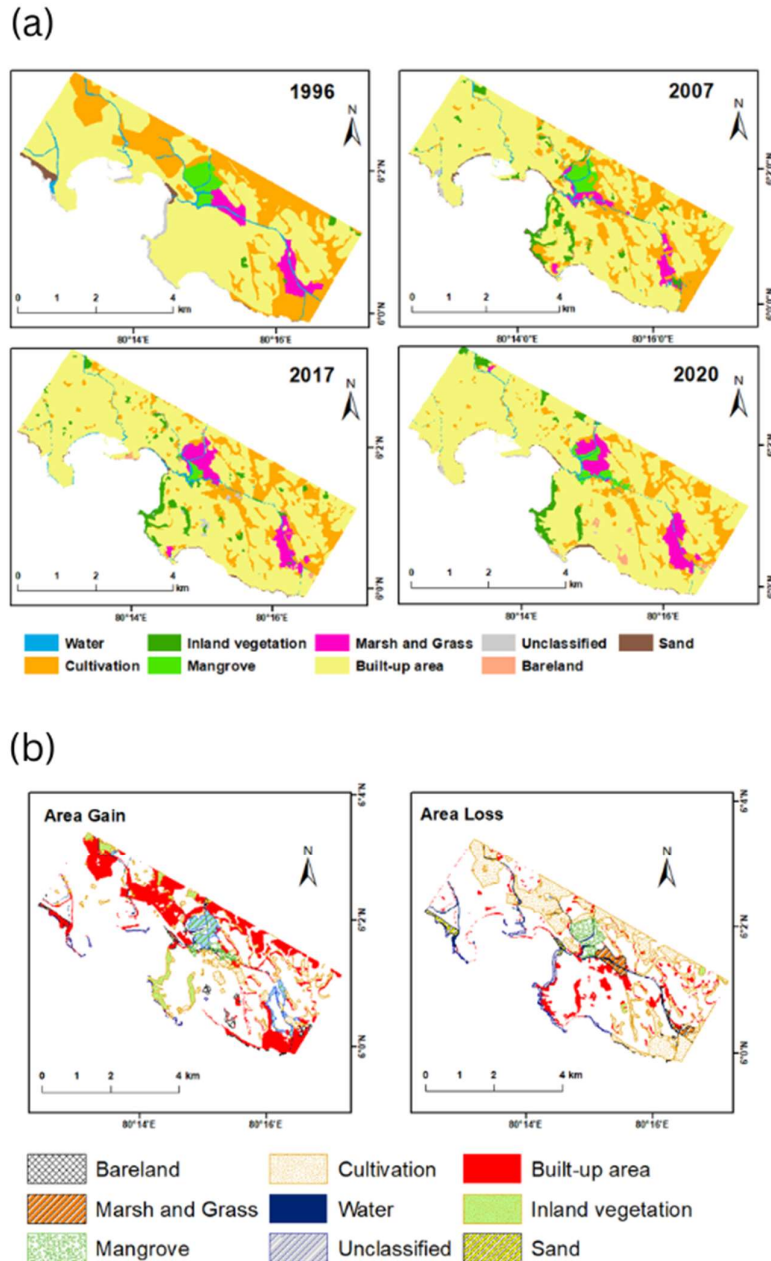


Figure 3: LULC and Overlay maps of Galle study site. (a) LULC maps for 1996, 2007, 2017, and 2020; (b) Overlay maps representing areas of loss and gain between 1996 and 2020.

The high value of the LULC change at Kalametiya is primarily related to the conversion of water areas to mangrove, marsh, and grass, which cumulatively contributed to 39.3% of the overall change. The transformation in the LULC distribution confirms the findings of Madarasinghe *et al.* (2020), who explained rapid siltation as a consequence of excessive freshwater input to the lagoon from the Udawalawa inland irrigation project, which came into operation in 1967. Rapid siltation and reduction in salinity contributed to excessive growth of *Sonneratia caseolaris* and *Typha angustifolia*, reducing the extent of mixed mangroves (Madarasinghe *et al.*, 2020). The expansion of marsh and grass in the westward part of the Kalametiya site replacing inland vegetation could underlie a similar cause of sedimentation, as the area directly connects with a body of water with freshwater inputs. It was apparent from the 2007 LULC map that the built-up areas that existed during 1996

were converted to inland vegetation by 2007. From the field surveys, it was perceived that some of the tsunami-affected homesteads in the area were abandoned. Thus, the reported conversion could be mainly attributed to the 2004 tsunami event. The extent of sand along the shoreline is highly dynamic, dependent on the seasonality where narrow shorelines could be observed during the southwest monsoon spanning from May to September (Warnasuriya *et al.*, 2018). The imagery of 2020 was obtained during the onset of the southwest monsoon. Thus, the gains in sand during the receding inland vegetation, particularly scattered beach vegetation, in 2020 could be explained as a natural phenomenon of beach variability. Despite the area underlying the Kalametiya lagoon being subjected to protection under the provisions of the FFPO, considerable human influences were observed at the immediate boundaries. Expansion of built-up areas in the areas of inland vegetation is evident in this aspect.

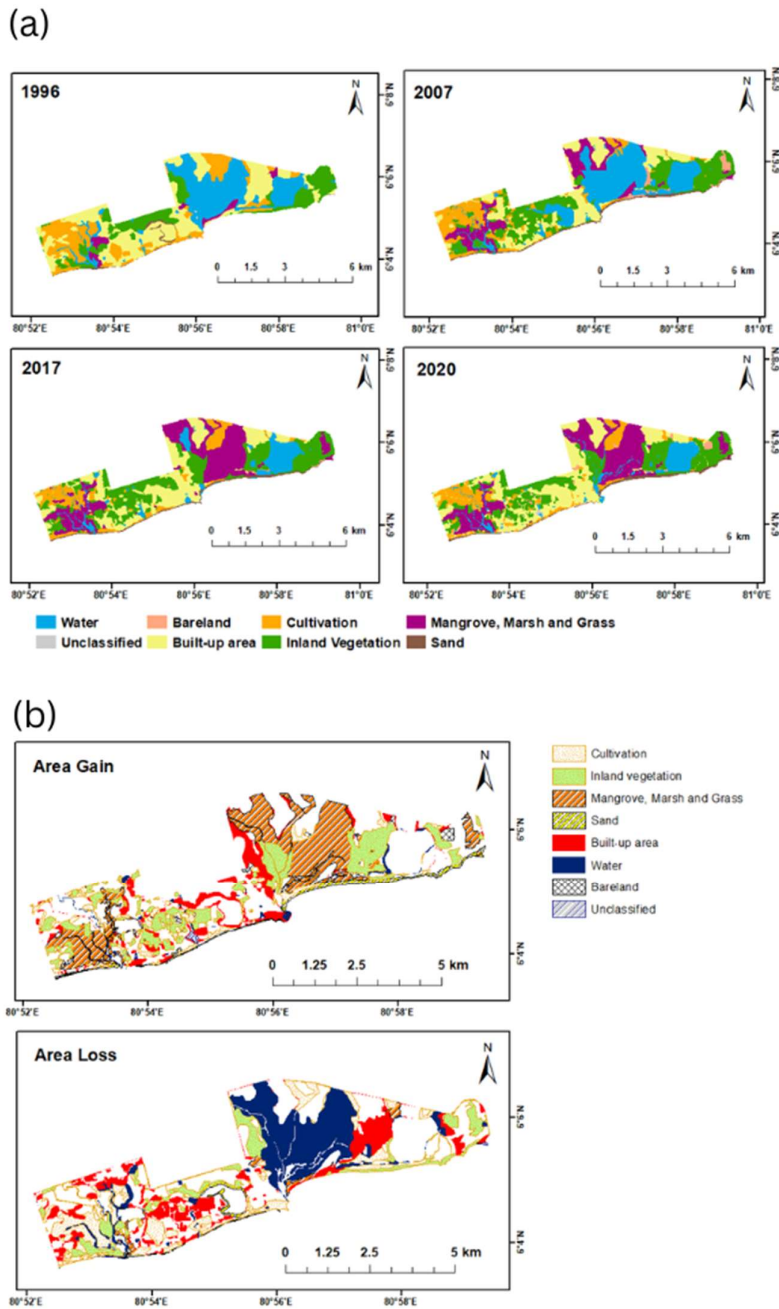


Figure 4: LULC and Overlay maps of Kalametiya study site. (a) LULC maps for 1996, 2007, 2017, and 2020; (b) Overlay maps representing areas of loss and gain between 1996 and 2020.

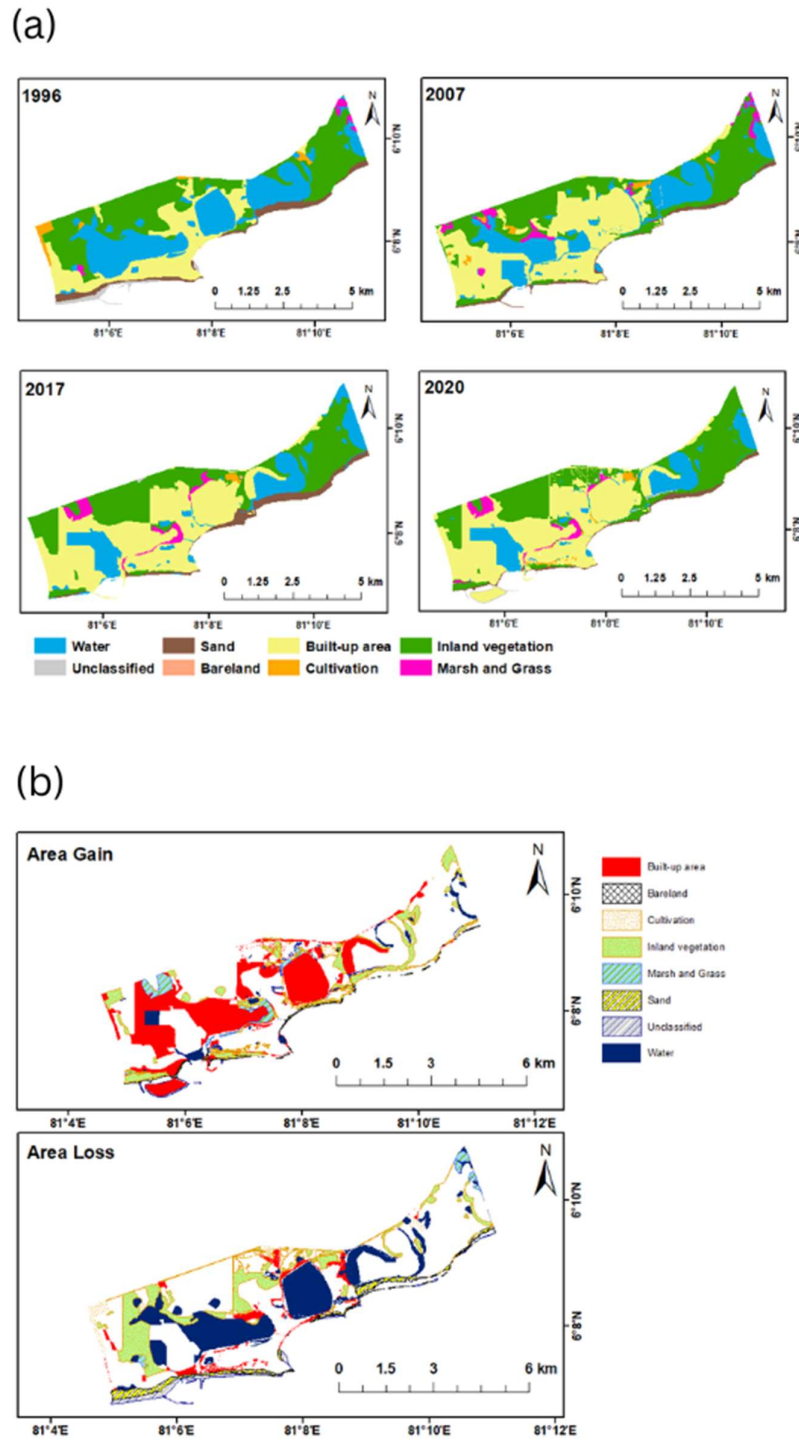


Figure 5: LULC and Overlay maps of Hambantota study site. (a) LULC maps for the 1996, 2007, 2017, and 2020; (b) Overlay maps representing areas of loss and gain between 1996 and 2020.

Most of the changes in Hambantota were attributed to an increase in built-up areas and reduction in water areas. This change in the land cover is recognisable owing to the construction of the Hambantota International Port, which was initiated during this period (Kavirathna *et al.*, 2021). In the course of the port construction, the area was dredged inland to accommodate the port, such that substantial water cover of the natural water body was

denied allowing the receding water. Hambantota has received substantial attention for development since 2009 after the end of the civil war. The government has initiated multiple projects such as the construction of the Hambantota-Wellawaya (CGHW) highway and the Magam Ruhunupura International Convention Centre (MRICC), which brought significant changes in the LULC distribution in the district. However, the study area was confined mostly to the area where the port was constructed. Therefore, changes attributed to other development activities were not considered during the study. Cultivated lands that existed during 1996 were reported to have receded since 2007. Thus, considering the time scale, it's difficult to emphasize that such changes are a result of the seasonality of cultivation.

The third highest overall LULC change was reported for Galle compared to the total land extent. Of this, 79.1% is attributed to the conversion of cultivated lands to built-up areas. This exemplifies the exacerbated urbanization in the area over the period. Importantly, from the study, it was perceived that most of the built-up area occurred (55.6%) during the period between 1996 and 2007. This was likely due to rehabilitation programs initiated during the post-tsunami period to develop the affected and destructed areas. Comparatively, coastal habitats conjointly confronted a less overall change accounting for 15.6% of the overall land cover change. However, the notion that coastal habitats have undergone less overall change should not be considered in light of the fact that they have been less affected, given the extent of coastal habitats compared to built-up area cover (>60.9% of the total area). Mangroves have receded by 45.6% during the period, where the highest depletion (77.6%) was recorded from 2007 to 2017. This could be primarily attributed to land reclamation for the construction of the Southern Express Highway, during the period. Following 2017, an emergence of mangrove cover was observed, which could be due to natural restoration of the area and improved efforts of mangrove conservation. The receded areas of mangroves were replaced by marsh and grass, resulting in an overall gain for marsh and grass during the period. This observation could be closely related to natural succession coming along with the gap-filling scenario as described by Wali, (1999). Thus, it is worth accentuating the significance of natural phenomena on land cover changes in the coastal habitats along with anthropogenic factors. Therefore, more comprehensive research related to natural succession is required. Replacement of inland vegetation and sand in the built-up areas, particularly close to the shoreline, which was observed after 2007 could be due to abandonment of built-up areas following damages caused by the tsunami. Significant losses in the water areas were observed. This is primarily due to seasonality changes, which cause variations in the rainfall and thus the area flooded.

Bundala reported the least overall land cover change compared with other study sites relative to the total land extent. The area consists of three main lagoons, Malala, Embilikala, and Bundala, which can be observed in the LULC maps and are located west to east of the site (Piyankarage *et al.*, 2004). These water bodies primarily govern the ecology and diversity underlying the area (Piyankarage *et al.*, 2004; Chandana *et al.*, 2012). Malala and Embilikala lagoons receive freshwater drainage from the upstream irrigation scheme 'Kirindi Oya Irrigation settlement' (came into operation in 1989) throughout the year, preventing the water bodies from drying out during the dry season (Piyankarage *et al.*, 2004; Bellio & Kingsford, 2013). However, contrastingly Bundala lagoon shows the natural flood and drying cycles following seasonal fluctuations in rainfall (Bellio & Kingsford, 2013). Among the reported changes, the major change, the conversion of marsh and grass areas to bare land, can be attributed to the hydrology of the area. Long-term drying out of certain areas at the edges of lagoons could result in barren land. Changes in the water areas could also be due to seasonal variations in the rainfall. The construction of salt ponds in the westward part of the Bundala lagoon was initiated during the 1980s, (Rathnayake, *personal communication*, 15 July 2021), which has expanded since then. The disappearance of cultivated lands could be attributed to improved enforcement of regulations hindering cultivation practices within the protected area.

Anticipated area changes by 2025

The summary results of the trend analysis predicting the areas for 2025 of each LULC class and the predicted rate of change in the LULC classes are given in Table 4. All the LULC classes of the Bundala and Hambantota sites failed to demonstrate a significant model, which enabled a precise prediction of the area change given that the p-value was less than the 95% confidence level. Moreover, according to the 2-sample proportionate test, the Bundala site did not show any significance in the predicted area change for all the LULC classes from 2020 to 2025. However, in Hambantota, there were significant losses in the LULC classes of water area (120.4 ha),

cultivation (19.6 ha), and unclassified (29.2 ha), and a significant gain in the built-up areas (181.6 ha). In contrast, in Galle, there was a significant loss in the LULC class cultivation (68.2 ha), and significant gains in the LULC classes built-up areas (77.6 ha) and inland vegetation (30.9 ha) (Figure 6). Although the Galle mangroves resulted in a predicted area change (a loss of 21.6 ha), the trend analysis failed to demonstrate any significance. The LULC class marsh and grass in Kalametiya resulted in a significant area gain of 189.0 ha (Figure 6).

Table 4: Results of the trend analysis for LULC classes in the southern coastal belt. LULC classes with significant trends are indicated with an asterisk (*) based on the p values obtained through trend analysis at the 95% confidence level; significant area changes from 2020 to 2025 are indicated with a double asterisk (**) based on the p values obtained through two-sample proportion tests at the 95% confidence interval. The rate of area change for LULC classes was calculated for the 2020 – 2025 period.

LULC classes	Area (ha)				Predicted area in 2025 (ha)	p value trend analysis	Area change (2020-2025) ha	p value 2-sample proportion test	Rate of change 2020 -2025 (ha/y)
	1996	2007	2017	2020					
Bundala									
Built-up areas	75.2	61.4	65.3	78.1	70.1	0.327	-8.0	0.560	-1.6
Bare land	0.0	19.1	79.5	157.4	151.8	0.103	-5.6	0.788	-1.1
Cultivation	66.9	9.9	2.3	0.0	-20.5	0.080	-20.5	NC	-4.1
Inland vegetation	1386.4	1458.8	1371.1	1252.6	1296.8	0.224	44.2	0.259	8.8
Marsh and Grass	143.7	168.9	23.5	22.2	-0.7	0.286	-23.0	NC	-4.6
Sand	150.4	119.0	231.4	231.4	203.8	0.336	203.8	0.186	40.8
Water	1180.9	1166.0	1261.9	1261.9	1302.0	0.520	1302.0	0.308	260.4
Galle									
Built-up areas*	1380.9	1565.4	1676.2	1707.2	1784.8	0.006	77.6**	0.007	15.5
Bare land	0.0	5.9	9.4	16.9	17.3	0.056	0.4	1.000	0.08
Cultivation*	613.9	434.1	239.2	278.1	210.0	0.005	-68.2**	0.001	-13.6
Inland vegetation*	10.0	94.7	79.8	64.2	95.1	0.048	30.9**	0.015	6.2
Mangrove	61.4	42.4	9.6	33.4	11.9	0.513	-21.6**	0.002	-4.3
Marsh and Grass	91.2	57.4	103.5	112.5	108.1	0.237	-4.4	0.814	-0.9
Sand	22.5	24.0	11.4	12.5	9.9	0.342	-2.6	0.735	-0.5
Unclassified	32.5	9.9	13.6	13.0	6.3	0.183	-6.7	0.194	-1.3
Water	54.7	34.1	34.4	29.1	23.8	0.090	-5.3	0.552	-1.0
Kalametiya									
Built-up areas	937.7	573.2	742.9	809.4	700.0	0.686	-109.4**	0.001	-21.9
Bare land	0.0	60.1	12.1	44.7	44.1	0.713	-0.6	1.000	-0.1
Cultivation	590.2	405.5	338.3	361.6	275.8	0.062	-85.8**	0.000	-17.1
Inland vegetation	556.5	710.4	820.9	754.2	853.1	0.080	98.9**	0.004	19.8
Mangrove, marsh and grass*	93.6	368.1	756.0	727.4	916.4	0.015	189.0**	0.000	37.8
Sand	40.8	80.3	78.0	88.1	97.9	0.106	9.7	0.512	1.9
Unclassified	2.9	2.5	0.0	6.1	3.4	0.871	-2.7	0.581	-0.5
Water	841.7	863.6	315.5	272.3	173.1	0.103	-99.2**	0.000	-19.8
Hambantota									
Built-up areas	630.5	1121.7	1279.4	1346.0	1527.6	0.141	+181.6	0.001	-25.5
Bare land	0.0	0.0	1.6	1.3	1.8	0.385	0.5	1.000	0.1
Cultivation	58.1	33.9	12.1	31.9	12.3	0.422	-19.6**	0.005	-3.9
Inland vegetation	1157.9	1030.8	1024.0	1055.3	1000.0	0.063	-55.3	0.142	-11.1
Marsh and Grass	28.0	95.0	93.1	86.2	111.0	0.050	24.9	0.085	5.0
Sand	164.4	90.3	166.7	85.6	103.5	0.879	17.9	0.212	3.6
Unclassified	60.7	3.1	2.8	31.3	2.2	0.208	-29.2**	0.000	-5.8
Water	976.7	701.8	496.9	438.4	318.0	0.170	-120.4**	0.000	37.7

NC: Not calculated

However, all other LULC classes failed to demonstrate such a trend for the Kalametiya site. Further, significant area losses between 2020 and 2025 were reported for the built-up area (109.4 ha), bare land (0.6 ha), cultivation (85.8 ha) and water (99.2 ha), and a gain for inland vegetation (98.9 ha) in Kalametiya.

Bundala, which is a protected area, has changed the least over the 24 years of the study period, and is expected to change at an insignificant rate during the next five years. This is mainly due to the level of protection provided for the area where the anthropogenic influence is minimal. Although Hambantota failed to demonstrate any significance in the prediction model, it is important to recognize that the area change between 2020 and 2025 reported significant losses in the LULC classes of water and cultivation and gains in the built-up areas. The values forecast for area gain for water could be affected by the seasonal variation of the satellite imagery used for digitization. Kalametiya resulted in gains in the marsh and grass cover in the preceding five years at a rate of 37.8 ha/year, which is a 1.2% increase per year. This could be due to continuing siltation of the area, which enables more space for the occurrence of marsh and grass. Galle was recognized as a site largely vulnerable for changes in the LULC distribution predominantly for built-up area, inland vegetation, and cultivation. This suggests, Galle will continue its urbanization converting its agricultural lands during the next 5 years at a rate of 15.5 ha/year, which represent a 0.7% increase per year.

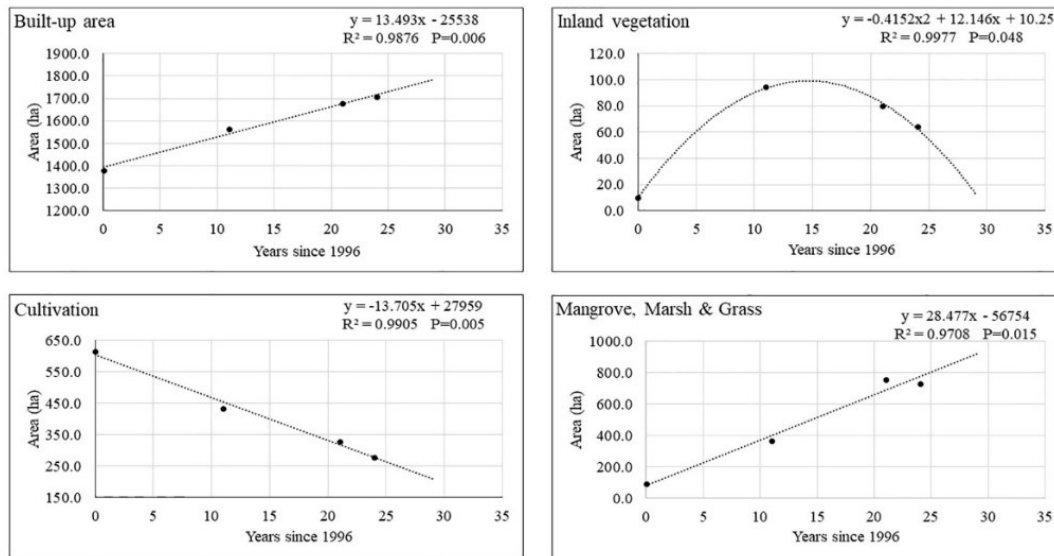


Figure 6: Graphs showing the trends of area changes in LULC classes for Galle (built-up area, inland vegetation, and cultivation) and Kalametiya (mangrove, marsh and grass). The data points of each graph align to 0, 11, 21 and 24 of the x axis, which represents the years 1996, 2007, 2017, and 2020, respectively. The trend line is forecast for the year 2025, which is 29 years after the reference year (1996).

Recommendations

This study indicated that changes in the LULC between the study sites are varied, depending on the level of anthropogenic influences, natural phenomena, and the level of protection measures imposed. Therefore, policy measures should be highly localised, addressing key drivers of LULC changes and providing solutions for areas of concern. Further, the imposition of protection measures to prevent localised human activities alone will not provide adequate resistance to changes in LULC. Rather, attention should be paid to anticipating the possible consequences of development projects despite geographical dissociation. It is apparent that anthropogenic influences are a major driving force triggering changes in habitat distribution. However, natural factors may lead to drastic changes in coastal habitats in the long term. Enhancing knowledge of natural phenomena affecting habitat alteration such as natural succession and gap-filling scenarios, is vital for a better understanding of

changes associated with coastal habitats. Thus, further research on the topic should be encouraged. A monitoring scheme that is capable of reporting short-term changes at very high resolution is recommended. The use of modern technology employing drones is recommended.

Limitations of the study

Although on-screen digitization was performed between years for each site employing high-resolution satellite imagery, they represent different seasons of the monsoons. Thus, understanding the causes of some LULC changes, particularly those governed by rainfall and hydrology, was constrained. Uncertainties such as political instability, debt and financial instability, health and safety, and national security were not included in the prediction model. Thus, predictions could also be affected by these uncertainties.

CONCLUSION

This study empirically investigated the spatial-temporal changes of LULC in Bundala, Galle, Kalametiya, and Hambantota, which are located in the southern coastal zone of Sri Lanka. Changes in the LULC between different locations along the southern coastal zone are varied, depending on the level of anthropogenic influences, natural phenomena, and the level of protection measures imposed. The results of the study revealed the highest changes in the LULC in Kalametiya, followed by Hambantota, Galle, and Bundala. Bundala, being a protected area, would be the least susceptible to future LULC changes. The causes of changes in the LULC are highly localised to individual sites. Consequently, management should follow a similar trajectory. This study highlights the significance of providing considerable attention to anticipating possible consequences of development projects before initiation despite geographical dislocation.

Conflict of interest statement

Authors have no conflict of interest to disclose.

Acknowledgement

The authors acknowledge the FSPI-SEDRIC grant funded by French cooperation under the umbrella of the French Embassy at Colombo for providing financial support.

REFERENCES

- Adade R., Aibinu A.M., Ekumah B. & Asaana J. (2021). Unmanned Aerial Vehicle (UAV) applications in coastal zone management- a review. *Environmental Monitoring and Assessment* **193**(3): 1–12.
DOI: <https://doi.org/10.1007/s10661-021-08949-8>
- Ahmad H. (2019). Bangladesh coastal zone management status and future trends. *Journal of Coastal Zone Management* **22**(1): 1–7.
- Batista C.M., Suárez A. & Saltarén C.M.B. (2017). Novel method to delimitate and demarcate coastal zone boundaries. *Ocean and Coastal Management* **144**: 105–119.
DOI: <https://doi.org/10.1016/j.ocecoaman.2017.04.021>
- Bellio M. & Kingsford R.T. (2013). Alteration of wetland hydrology in coastal lagoons: Implications for shorebird conservation and wetland restoration at a Ramsar site in Sri Lanka. *Biological Conservation* **167**: 57–68.
DOI: <https://doi.org/10.1016/j.biocon.2013.07.013>
- Bini M. & Rossi V. (2021). Climate change and anthropogenic impact on coastal environments. *Water* **13**(9): 1182.
DOI: <https://doi.org/10.3390/w13091182>
- Chandana E.P.S., Amarasinghe N.D.S. & Samayawardhena L.A. (2012). Factors affecting the avi-faunal distribution in the three lagoons (Malala, Embillakala and Bundala Lewaya) of Bundala National Park (A Ramsar Wetland) in Sri Lanka. *Ruhuna Journal of Science* **3**(3).
- De Alwis D. & Noy I. (2019). Sri Lankan households a decade after the Indian Ocean tsunami. *Review of Development Economics* **23**(2): 1000–1026.
DOI: <https://doi.org/10.1111/rode.12586>
- Dissanayake D.M.S.L.B. (2020). Land use change and its impacts on land surface temperature in Galle City, Sri Lanka. *Climate* **8**(5): 65.
DOI: <https://doi.org/10.3390/CLI8050065>

- Ewel K., Twilley R. & Ong J.I.N. (1998). Different kinds of mangrove forests provide different goods and services. *Global Ecology and Biogeography Letters* 7(1): 83–94.
DOI: <https://doi.org/10.2307/2997700>
- Gedan K.B., Kirwan M.L., Wolanski E., Barbier E.B. & Silliman B.R. (2011). The present and future role of coastal wetland vegetation in protecting shorelines: answering recent challenges to the paradigm. *Climatic Change* 106(1): 7–29.
DOI: <https://doi.org/10.1007/s10584-010-0003-7>
- Gunawardena M. & Rowan J.S. (2005). Economic valuation of a mangrove ecosystem threatened by shrimp aquaculture in Sri Lanka. *Environmental Management* 36(4): 535–550.
DOI: <https://doi.org/10.1007/s00267-003-0286-9>
- Herold M., Scepan J. & Clarke K.C. (2002). The use of remote sensing and landscape metrics to describe structures and changes in urban land uses. *Environment and Planning* 34(8): 1443–1458.
DOI: <https://doi.org/10.1068/a3496>
- Hyndes G.A., Nagelkerken I., McLeod R.J., Connolly R.M., Lavery P.S. & Vanderklift M.A. (2014). Mechanisms and ecological role of carbon transfer within coastal seascapes. *Biological Reviews* 89(1): 232–254.
DOI: <https://doi.org/10.1111/brv.12055>
- Janssen L.L. & Vanderwel F.J. (1994). Accuracy assessment of satellite derived land-cover data: a review. *Photogrammetric Engineering and Remote Sensing (United States)* 60(4): 419–426.
- Kennedy R.E., Yang Z., Braaten J., Copass C., Antonova N., Jordan C. & Nelson P. (2015). Attribution of disturbance change agent from Landsat time-series in support of habitat monitoring in the Puget Sound region, USA. *Remote Sensing of Environment* 166: 271–285.
DOI: <https://doi.org/10.1016/j.rse.2015.05.005>
- Kodikara K.A.S., Mukherjee N., Jayatissa L.P., Dahdouh-Guebas F. & Koedam N. (2017). Have mangrove restoration projects worked? An in-depth study in Sri Lanka. *Restoration Ecology* 25(5): 705–716.
DOI: <https://doi.org/10.1111/rec.12492>
- Kavirathna C.A., Hanaoka S., Kawasaki T. & Shimada T. (2021). Port development and competition between the Colombo and Hambantota ports in Sri Lanka. *Case Studies on Transport Policy* 9(1): 200–211.
DOI: <https://doi.org/10.1016/j.cstp.2020.12.003>
- Macreadie P.I., Nielsen D.A., Kelleway J.J., Atwood T.B., Seymour J.R., Petrou K., Connolly R.M., Thomson A.C., Trevathan-Tackett S.M. & Ralph P.J. (2017). Can we manage coastal ecosystems to sequester more blue carbon? *Frontiers in Ecology and the Environment* 15(4): 206–213.
DOI: <https://doi.org/10.1002/fee.1484>
- Madarasinghe S.K., Yapa K.K.A.S. & Jayatissa L.P. (2020). Google Earth imagery coupled with on-screen digitization for urban land use mapping: A case study of Hambantota, Sri Lanka. *Journal of the National Science Foundation of Sri Lanka* 48(4): 357–366.
DOI: <https://doi.org/10.4038/jnsfsr.v48i4.9795>
- Mapa R.B., Kumaragamage D., Gunarathne W.D.L. & Dassanayake A.R. (2002). Land use in Sri Lanka: Past, present and the future. In: *Proceedings of the 17th World Congress of Social Science*, Bangkok, Thailand, pp. 14–21.
- McLeod E., Chmura G.L., Bouillon S., Salm R., Björk M., Duarte C.M., Lovelock C.E., Schlesinger W.H. & Silliman B.R. (2011). A blueprint for blue carbon: toward an improved understanding of the role of vegetated coastal habitats in sequestering CO₂. *Frontiers in Ecology and the Environment* 9(10): 552–560.
DOI: <https://doi.org/10.1890/110004>
- Mukherjee N., Dahdouh-Guebas F., Koedam N. & Shanker K. (2015). An interdisciplinary framework to evaluate bioshield plantations: Insights from peninsular India. *Acta Oecologica* 63: 91–100.
DOI: <https://doi.org/10.1016/j.actao.2014.01.005>
- Neumann B., Vafeidis A.T., Zimmermann J. & Nicholls R.J. (2015). Future coastal population growth and exposure to sea-level rise and coastal flooding—a global assessment. *PLoS one* 10(3): e0118571.
DOI: <https://doi.org/10.1371/journal.pone.0118571>
- Perera N. & de Vos A. (2007). Marine protected areas in Sri Lanka: a review. *Environmental Management* 40(5): 727–738.
DOI: <https://doi.org/10.1007/s00267-005-0154-x>
- Post W.M. & Kwon K.C. (2000). Soil carbon sequestration and land-use change: processes and potential. *Global Change Biology* 6(3): 317–327.
DOI: <https://doi.org/10.1046/j.1365-2486.2000.00308.x>
- Piyankarage S.C., Mallowatantri A.P., Matsuno Y. & Pathiratne K.A.S. (2004). Human impacts and the status of water quality in the Bundala RAMSAR wetland lagoon system in Southern Sri Lanka. *Wetlands Ecology and Management* 12(5): 473–482.
DOI: <https://doi.org/10.1007/s11273-004-6566-1>
- Priyashantha A.K.H. & Taufikurahman T. (2020). Mangroves of Sri Lanka: distribution, status and conservation requirements. *Tropical Plant Research* 7: 654–668.
DOI: <https://doi.org/10.22271/tpr.2020.v7.i3.083>
- Rathnayake C.W., Jones S. & Soto-Berelov M. (2020). Mapping land cover change over a 25-year period (1993–2018) in Sri Lanka using Landsat time-series. *Land* 9(1): 27.

- DOI: <https://doi.org/10.3390/land9010027>
- Rupasinghe M.S. & Perera M.S.J. (2008). Some aspects of coastal zone management in Sri Lanka including impact of tsunami: A review. In: *Proceedings of the International Workshop on Coastal Ecosystems: Hazards, Management and Rehabilitation*, Purwokerto, Indonesia, p. 36.
- Senevirathna E.M.T.K., Edirisooriya K.V.D., Uluwaduge S.P. & Wijerathna K.B.C.A. (2018). Analysis of causes and effects of coastal erosion and environmental degradation in Southern Coastal Belt of Sri Lanka special reference to unawatuna coastal area. *Procedia Engineering* **212**: 1010–1017.
DOI: <https://doi.org/10.1016/j.proeng.2018.01.130>
- Wali M.K. (1999). Ecological succession and the rehabilitation of disturbed terrestrial ecosystems. *Plant and Soil* **213**(1): 195–220.
DOI: <https://doi.org/10.1023/a:1004475206351>
- Warnasuriya T.W.S., Gunaalan K. & Gunasekara S.S. (2018). Google earth: A new resource for shoreline change estimation—Case study from Jaffna Peninsula, Sri Lanka. *Marine Geodesy* **41**(6): 546–580.
DOI: <https://doi.org/10.1080/01490419.2018.1509160>
- Zhao L., Fan X. & He D. (2021). Landscape changes and their socio-economic driving factors in coastal zone. *Polish Journal of Environmental Studies* **30**(5): 4855–4869.
DOI: <https://doi.org/10.15244/pjoes/133240>

RESEARCH ARTICLE

Marine Science

Preliminary study on surface phytoplankton assemblages and physicochemical parameters, off the west and south-west coasts of Sri Lanka

HB Jayasiri*

Faculty of Engineering and Management, Ocean University of Sri Lanka, 51, Pannanada Mawatha, Colombo 15, Sri Lanka.

Submitted: 21 November 2021; Revised: 30 July 2022; Accepted: 26 August 2022


Abstract: This study evaluates the phytoplankton community structure in relation to physicochemical properties in the western and southwestern coastal waters of Sri Lanka. Phytoplankton and water samples were collected from March to April, 2017 at three transect lines towards offshore in Colombo, Beruwala, and Mirissa, each containing 10 sampling sites. The distance between sampling stations on each transect line was approximately 2 km. Phytoplankton samples were collected towing a net (10 μm mesh) by vertical hauls from known depth (2.5 m) and preserved in Lugol's solution. The phytoplankton were identified to the lowest possible taxonomic level and counted under the Sedgwick rafter cell using a light microscope. Water samples were collected at 0.5 m depth using the Ruttner Sampler and analysed for chlorophyll-a, nutrients, and total suspended solids (TSS). This study identified 57 phytoplankton species comprised of diatoms (33 species), dinoflagellates (23 species), and cyanobacteria (1 species). In general, phytoplankton abundance and species diversity decreased towards offshore in the three transects. Total phytoplankton and diatom abundances varied significantly among the three transect lines, and significantly higher abundance was reported at Mirissa and Colombo than at Beruwala (One-way ANOVA; $p < 0.05$). Total phytoplankton abundance significantly correlated with dinoflagellates, toxic species of dinoflagellates, chlorophyll-a, and nitrate-N ($p < 0.01$). Ten toxic species of dinoflagellates were reported in the study. Diatoms dominated (60%) in the study area, followed by cyanobacteria (31%) and dinoflagellates (9%). Diatoms of *Cerataulina* sp. (31%) and *Navicula* sp. (50%) were dominant in Colombo and Mirissa respectively, while cyanobacteria of *Trichodesmium* sp. (85%) dominated in Beruwala, indicating the possibility of blooms of this species at study sites when environmental conditions are favourable.

Keywords: Diatoms, dinoflagellates, physicochemical properties, phytoplankton, Sri Lanka.

INTRODUCTION

Marine phytoplankton represent less than 1% of the Earth's photosynthetic biomass, but are responsible for more than 45% of our planet's annual net primary production and contribute more than 90% of photosynthetic carbon fixation (Field *et al.*, 1998). The productivity of marine phytoplankton is influenced by environmental factors, many of which are affected by human activities, so that they undergo massive changes due to global climate change, ozone depletion, and pollution (Behrenfeld *et al.*, 2006). Phytoplankton sustain the aquatic food web, drive the marine ecosystem, and constrain the global fish catch. In addition, the phytoplankton absorb solar radiation and control the upper ocean heat flux, thereby influencing climate processes and biogeochemical cycles, particularly the carbon cycle (Roxy *et al.*, 2015). Phytoplankton have rapid turn-over times (in the order of days) and are sensitive indicators of environmental stresses (Findlay & Kling, 2001). Due to their high turnover rates and sensitivity to changes in environmental conditions, phytoplankton are useful indicators of changing oceanographic conditions, climate change, and deterioration in water quality (Beaugrand, 2009; Poloczanska *et al.*, 2013).

Marine phytoplankton range in size from $<1 \mu\text{m}$ to about 1 mm and include representatives from at least five eukaryotic phyla together with cyanobacteria. This wide size range and phylogenetic diversity present challenges for quantifying and characterizing phytoplankton communities. Marine phytoplankton, especially diatoms and

* Corresponding author (panagodagehan@yahoo.com;  <https://orcid.org/0000-0003-4983-8560>)



This article is published under the Creative Commons CC-BY-ND License (<http://creativecommons.org/licenses/by-nd/4.0/>). This license permits use, distribution and reproduction, commercial and non-commercial, provided that the original work is properly cited and is not changed in anyway.

dinoflagellates, are considered as major contributors to ecosystem structure and functions (Margalef, 1978; Reynolds, 1997).

Some species of phytoplankton can have harmful effects on organisms at different trophic levels. Blooms of some otherwise harmless species result in massive fish kills by depleting dissolved oxygen content or by clogging the gills of fish. Rapid cell division and population growth in phytoplankton can produce millions of cells per litre of seawater, resulting in visible blooms or 'red tides'. At least 90 of cyst producing species are known to be harmful (Sournia, 1995) and a minimum of 45 species are considered as toxic dinoflagellates (Sournia, 1995; Smayda, 1997; Hallegraeff, 2003). At certain times, the occurrence of a toxin-producing species of phytoplankton may affect wildlife, causing illness or death. Human consumers of certain seafood items (especially bivalve shellfish) are also at risk in the absence of adequate monitoring programmes.

The study of phytoplankton in the east coast of India has indicated the high diversity and low production. A large number of phytoplankton species (193) has been recorded during the monsoon season (Geetha & Kondalarao, 2004). Ecological indices are generally used for describing eutrophication, water quality and community structure. The commonly used indices are Diversity (H'), Evenness (J'), and Dominance (D') (Kumari & Julie, 2003).

The concentrations of N and P usually vary according to regional environmental changes and therefore may affect the physiological and ecological responses of phytoplankton to the anthropogenic stressors, such as ocean acidification and warming of sea surface. Decreased pH and increased temperature are known to interact with UV radiation to influence photosynthesis and/or growth of typical phytoplankton species (Gao *et al.*, 2012). The reversal of monsoon currents affects the hydrodynamic features of the coastal area, which in turn affect phytoplankton productivity. In addition, physico-chemical features have been thought to control the phytoplankton community dynamics by determining species composition, species seasonality, species biomass, and productivity biomass (Harris, 1986). Also, rivers are often subjected to increased nutrient concentrations due to run off of fertilizers from adjacent fields, to a point that they must be considered as pollution. This eutrophication deteriorates the water quality and affects consumers higher up in the food web (Hutchins *et al.*, 2010).

A few studies on marine phytoplankton have been conducted in Sri Lankan waters such as the Gulf of Mannar and the Palk Strait, and bathing sites (Jayasiri, 2007; Jayasiri & Priyadarshanie, 2007; Weerakoon *et al.*, 2017) including a few localised studies off Thalawila in north-west coast, Maruthankerny, off Jaffna, off Colombo, and southern coast (Jayasiri *et al.*, 2014, 2016; Ekanayaka *et al.*, 2016; Wickramasingha & Jayasiri, 2016). Many studies have been conducted in coastal waters in localised areas on a small scale, and there is no information on phytoplankton community structure in offshore waters and spatially in a large area, which includes three districts for comparison. Phytoplankton assemblages are essential for understanding the quality of primary production in the marine environment

Thus, this study provides valuable information on spatial distribution of phytoplankton community structure in waters off the western and south-western coasts of Sri Lanka.

MATERIALS AND METHODS

Three sampling sites (Colombo, Beruwala, and Mirissa), each containing 10 locations in a transect line towards offshore, were selected for collection of samples. The distance between sampling positions is 2 km with total of 30 sampling positions (Figure 1). Field surveys were carried out from March to April 2017 which comes under the first inter-monsoon. To study the nutrient levels, water samples were collected at the depth of 0.5 m from the surface using the Ruttner Sampler and analysed by standard methods for nitrate, nitrite, phosphate, and silicate (Grasshoff *et al.*, 1999). Further, water samples were collected to analyse the chlorophyll-a (Parsons & Strickland, 1963). Phytoplankton sampling was carried out using an open net with a mesh size of 10 μm and diameter of 35 cm of the opening. The plankton hauls were collected by towing the net vertically through the water column from the known depth of 2.5 m to the surface. The phytoplankton samples were preserved in Lugol's solution (0.8 mL to 200 mL sample: Willén, 1976) and they were put into labelled amber coloured glass sampling bottles.

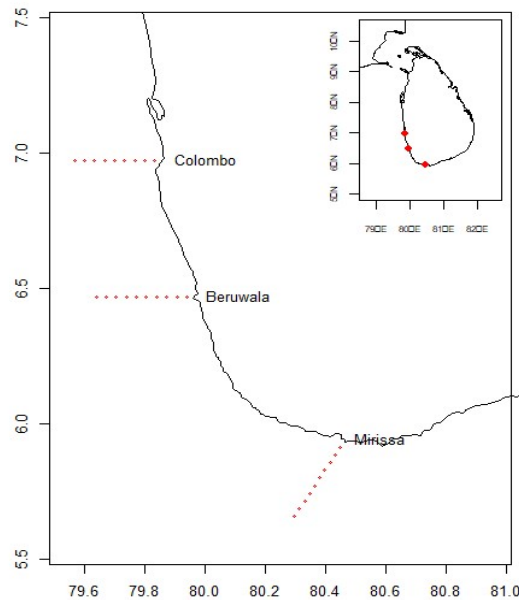


Figure 1: Map of the study area showing sampling transects

Determination of chlorophyll-a content in waters

Chlorophyll-a was determined by filtering 1.00 L of the water sample using GF/F filters (nominal pore size 0.7 μm) under low vacuum. The pigment extraction was done with 10 mL of 90% acetone. The optical density (absorbance) of the extract was determined using a UV Visible spectrophotometer (Optizen 3220uv) (Richards & Thompson, 1952; Parsons & Strickland, 1963). Chlorophyll-a concentrations were calculated using the equations of Parsons *et al.* (1984).

Phytoplankton and chemical analysis

The samples were homogenized and 1 mL of the sample was placed in a Sedgwick rafter cell and the number of phytoplankton was observed and counted under the light microscope (Olympus Bx41). Identification was done using standard keys to the lowest possible taxon (Hasle & Syvesten *et al.*, 1997; Hoppenrath *et al.*, 2009; Jayasiri, 2009; Phyto'pedia, 2012; Guiry & Guiry, 2013). Phytoplankton abundance, species composition, species richness, and biodiversity indices were calculated using standard formulae.

From each sampling point another 4 L of surface water were collected to analyse chemical parameters including dissolved inorganic nutrients (nitrate, nitrite, phosphate, and silicate) and total suspended solids (TSS). Dissolved inorganic nutrient concentrations were determined colorimetrically with an UV-VIS spectrophotometer according to standard methods for seawater analysis (Grasshoff *et al.*, 1999). The gravimetric procedure was used to determine the TSS.

Data analysis

Phytoplankton abundance is calculated as follows;

When a circular net is used, the volume of water filtered can be calculated by the formula given below:

$$V = \pi r^2 d$$

Where

V = Volume of water filtered (m³)

r = The radius of the mouth of the net (m)

d = Length of the water column traversed by the net (m)

v = volume of phytoplankton sample (mL)

N = number of organisms in 1mL of the sample

vN = number of organism in volume v

Phytoplankton abundance = $\frac{vN}{V \times 1000}$ number of organisms in unit volume (No. L⁻¹).

Phytoplankton species composition was calculated as per the following formula.

$$C = \frac{p_i}{p_t} \times 100$$

where C is the composition of individual species at a site, p_i is the abundance of individual species and p_t is the total abundance.

Diversity indices were calculated using following formulae

Shannon-Weaver species diversity Index (Shannon & Weaver, 1949)

$$H = -\sum p_i \ln p_i$$

Where p_i = n_i/N, n_i = number of individuals of one species and N = total number of organisms.

Evenness Index (Pileou, 1966)

$$J' = H'/\ln(S)$$

Where H = Shannon-Weaver Index of general diversity; S = Number of species

Statistical analysis was done by using statistical software SPSS version 23 for Windows. The comparisons of phytoplankton abundance, physicochemical parameters and diversity indices were made using One-way ANOVA. The Pearson's correlation and principal component analysis were performed in order to evaluate the relationships between phytoplankton abundance (diatoms and dinoflagellates) and physicochemical parameters.

RESULTS AND DISCUSSION

The mean (±SE) abundance of phytoplankton in Colombo, Beruwala and Mirissa (n = 30) was 671 ± 97 No. L⁻¹ with a range of 43 – 2030 No. L⁻¹. In general, the phytoplankton abundance decreased towards the offshore. The phytoplankton abundance of this study is consistent with most of the studies conducted in Sri Lankan waters (Table 1). However, higher abundances have been reported in the Palk Strait and Gulf of Mannar than in this study (Table 1). Also, the phytoplankton abundance in the coastal waters of the Arabian Gulf (100 – 1903 No. L⁻¹) is in line with this study (El Gammal *et al.*, 2017). The phytoplankton abundance reported in this study is higher than that of the four commercial harbours of Sri Lanka (Table 1). In contrast to this study, low abundance (15 to 148.5 cells L⁻¹) is reported by Sekadende *et al.*, 2021 in Pemba Channel waters in Tanzania. This study identified a total of 57 phytoplankton species comprised of diatoms (33 taxa), dinoflagellates (23 taxa), and cyanobacteria (1 taxon) (Table 2). Consistent with this study, 61 phytoplankton taxa have been reported in the Palk Strait (Jayasiri, 2007). In contrast to this study, a total of 119 species of phytoplankton were identified belonging to four taxonomic groups, with domination of diatoms (95.93%), in bathing sites of Mt. Lavinia, Unawatuna, and Polhena (Weerakoon *et al.*, 2017). Some 45 species of phytoplankton belonging to 5 groups have been reported in the Arabian Gulf with dominance of diatoms (48% and 23 species; El Gammal *et al.*, 2017). A total of 62 phytoplankton species belonging to the same groups reported in Sri Lanka have been reported in the Uppanar

Estuary, on the southeast coast of India (Saravanakumar *et al.*, 2021). A total of 79 species have been identified in the micro-phytoplankton community of the Pemba Channel, Tanzania with 55 diatom species (62.5% of total), followed by 31 dinoflagellate species (35.2%) and 2 cyanobacteria species (2.27%) (Sekadende *et al.*, 2021).

Table 1: Phytoplankton abundance in studies carried out in Sri Lankan marine environment

Study area	Abundance		Reference
	Range	Mean \pm SE	
Coastal seawater			
Palk Strait	12–1067 $\times 10^2$ No. L ⁻¹	-	Jayasiri, 2007
Gulf of Mannar	34–584 $\times 10^2$ No. L ⁻¹	-	Jayasiri & Priyadarshani, 2007
Thalawila, Kalpitiya	300–26,320 No. L ⁻¹	3273 \pm 771 No. L ⁻¹	Jayasiri <i>et al.</i> , 2014
Bathing sites			
Mulative	279–866 No. L ⁻¹	554 \pm 201 No. L ⁻¹	Jayasiri <i>et al.</i> , 2016
Colombo	66–11,738 No. L ⁻¹	2810 \pm 780 No. L ⁻¹	Wickramasinghe & Jayasiri, 2016
Southern Bay of Bengal	-	419 \pm 72 No. L ⁻¹	Kumara, 2016
Southern Coast of Sri Lanka	164–315,640 cells L ⁻¹	-	Ekanayaka <i>et al.</i> , 2016
Southern Coast	-	1729 \pm 257 cells L ⁻¹	Wijesinghe, 2016
Eastern Coast	-	584 \pm 117 cells L ⁻¹	Wijesinghe, 2016
Commercial harbours			
Colombo	55–255 No. L ⁻¹	142 \pm 12 No. L ⁻¹	PBBS, 2016
Trincomalee	66–174 No. L ⁻¹	102 \pm 31 No. L ⁻¹	PBBS, 2017
Hambantota	25–289 No. L ⁻¹	110 \pm 24 No. L ⁻¹	PBBS, 2018a
Galle	85–188 No. L ⁻¹	128 \pm 33 No. L ⁻¹	PBBS, 2018b
West and southwest coasts	43–2030 No. L ⁻¹	671 \pm 97 No. L ⁻¹	Present study

One-way ANOVA revealed that abundance of total phytoplankton, diatoms and cyanobacteria varied significantly among the sites ($p < 0.05$; Table 3) while there was no significant difference for dinoflagellates among three transects studied ($p > 0.05$; Table 3). The abundances of total phytoplankton in Mirissa (denoted by the letter b) and Colombo (denoted by the letter B) were significantly higher than that of Beruwala (denoted by letters a and A in Figure 2) and it might be due to the freshwater discharges of the Kelani and Nilwala Rivers which bring an ample amount of inorganic nutrients. Increasing nutrients from anthropogenic discharge stimulates the growth of phytoplankton through photosynthesis, as has been reported (Effendi *et al.*, 2016).

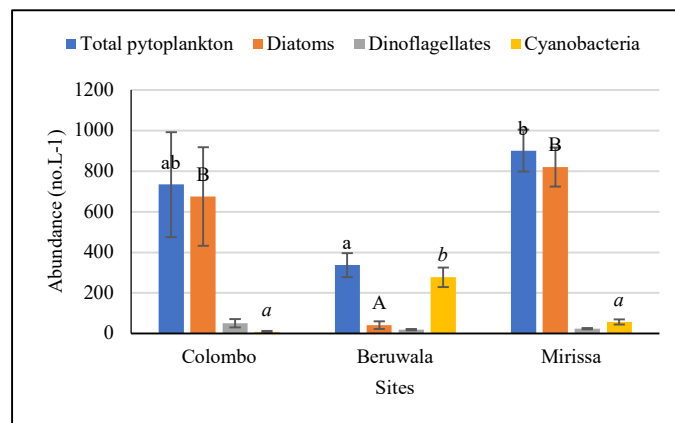


Figure 2: Abundance of total phytoplankton, diatoms, dinoflagellates and cyanobacteria in Colombo, Beruwala and Mirissa. The bars with different letters in lowercase vary significantly among sites for total phytoplankton, uppercase for diatoms and lowercase italic for cyanobacteria ($p < 0.05$).

Table 2: List of phytoplankton species recorded in three transects of Colombo, Beruwala and Mirissa with relative percentage composition of species

Taxonomic group	Species/genus	Relative composition		
		Colombo	Beruwala	Mirissa
Bacillariophyceae (Diatoms)	<i>Asterionellopsis glacialis</i>	0.49	-	5.35
	<i>Bacteriastrum</i> sp.	0.50	-	0.01
	<i>Bellerochea malleus</i>	0.25	0.05	13.76
	<i>Cerataulina</i> sp.	30.78	0.26	0.18
	<i>Chaetoceros</i> sp.1	0.21	0.45	0.07
	<i>Chaetoceros danicus</i>	0.00	0.04	0.29
	<i>Chaetoceros lorenzianus</i>	0.05	0.06	0.01
	<i>Coscinodiscus</i> sp.	0.03	0.56	0.06
	<i>Coscinodiscus granii</i>	0.67	0.26	0.03
	<i>Coscinodiscus stellaris</i>	0.00	-	0.02
	<i>Coscinodiscus concinnus</i>	0.08	-	0.09
	<i>Coscinodiscus radiatus</i>	1.58	0.08	3.16
	<i>Ditylum</i> sp.1	3.13	-	0.57
	<i>Ditylum brightwellii</i>	1.23	-	0.22
	<i>Eucampia zodiacus</i>	0.04	-	0.37
	<i>Guinardia striata</i>	0.94	1.65	7.30
	<i>Hemidiscus</i> sp.	0.49	0.03	0.54
	<i>Lauderia</i> sp.	0.01	0.18	0.01
	<i>lingulodinium polyedrum</i>	0.55	0.07	0.85
	<i>Meuniera membranacea</i>	0.04	-	0.84
	<i>Nitzschia</i> sp.1	0.00	1.51	0.07
	<i>Nitzschia sigma</i>	3.74	-	0.66
	<i>Navicula</i> sp.	0.59	1.20	49.93
	<i>Pseudo Nitzschia</i>	0.01	0.02	0.14
	<i>Odontella</i> sp. 1	10.80	0.03	1.07
	<i>Odontella mobiliensis</i>	2.94	0.10	0.40
	<i>Odontella sinensis</i>	3.14	0.02	0.47
	<i>Pleurosigma</i> sp.1	0.00	0.14	0.13
	<i>Pleurosigma capense</i>	0.03	-	0.02
	<i>Pleurosigma directrum</i>	0.11	0.16	0.01
	<i>Proboscia</i> sp	0.44	0.01	0.16
	<i>Rhizosolenia</i> sp.	3.30	0.89	3.30
	<i>Thalassionema nitzschioides</i>	0.02	-	0.25
Cyanobacteria	<i>Trichodesmium</i> sp	3.79	84.91	0.14
	<i>Trichodesmium</i> (bundle)	0.37	1.02	0.42
Dinophyceae (Dinoflagellates)	<i>Alexandrium</i> sp.1	2.23	1.95	0.15
	<i>Alexandrium catenella</i>	0.04	0.13	0.00
	<i>Alexandrium monilatum</i>	1.42	0.31	0.00
	<i>Ceratium furca</i>	2.43	0.37	0.96
	<i>Ceratium tripos</i>	0.53	0.19	0.15
	<i>Ceratium horridum</i>	0.18	0.19	0.03
	<i>Ceratium lineatum</i>	0.48	0.19	0.67
	<i>Ceratium fusus</i>	0.21	0.08	0.02
	<i>Dinophysis</i> sp.	0.18	0.20	0.04
	<i>Diplopelta bomba</i>	0.15	0.02	0.01
	<i>Gyrodinium</i> sp.1	0.07	0.37	0.03
	<i>Gymnodinium</i> sp.1	0.84	0.02	0.01
	<i>Noctiluca scintillans</i>	0.08	-	0.01
	<i>Protoperidinium</i> sp.1	0.34	0.29	0.01
	<i>Protoperidinium diabolium</i>	0.78	-	0.02
	<i>Protoperidinium depressum</i>	0.04	0.04	0.11
	<i>Protoperidinium cerasus</i>	1.16	0.68	0.01
	<i>Protoperidinium curtipes</i>	0.01	-	0.06
	<i>Protoperidinium meuniere</i>	1.24	0.48	0.18
	<i>Protoperidinium Obtusum</i>	0.80	-	0.19
	<i>Prorocentrum</i> sp.1	0.45	0.06	0.01
	<i>Prorocentrum micans</i>	0.80	0.45	0.08
	<i>Prorocentrum redfeildii</i>	0.45	0.28	0.05

- Not reported

Among abiotic interactions, fresh water inflow influences greatly the abundance of planktonic organisms in the marine ecosystem (Cloern, 1996). However, significantly high cyanobacteria were reported in Beruwala due to the presence of *Trichodesmium* species. The abundance of cyanobacteria in the study area is 114 ± 27 No. L^{-1} . *Trichodesmium* blooms appear and disappear with suddenness (Qasim, 1972). The mean abundance of dinoflagellates was 31.2 ± 7.2 No. L^{-1} in this study.

Table 3: P values of one-way ANOVA for total phytoplankton, diatoms, dinoflagellates and cyanobacteria for effect of site (df=2)

Categories	P value
Total phytoplankton	0.042
Diatoms	0.003
Dinoflagellates	0.146
Cyanobacteria	0.000

Significant ($p < 0.05$)

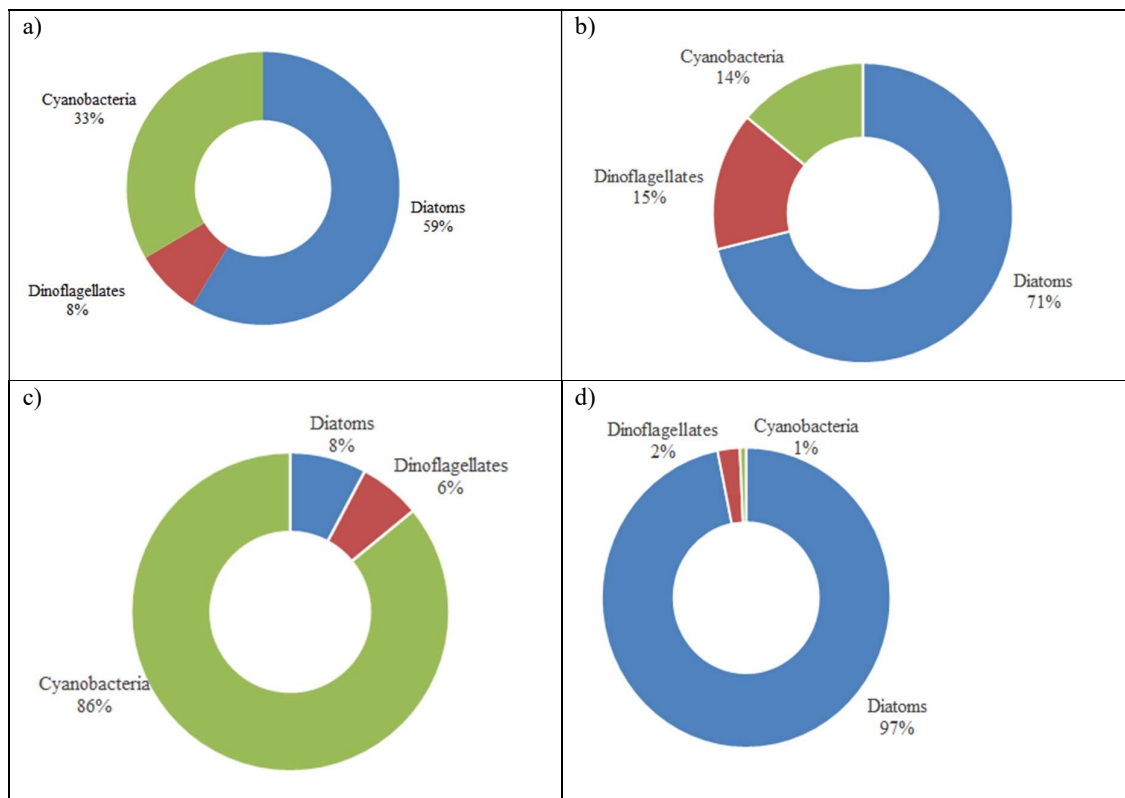


Figure 3: Relative composition of phytoplankton groups in the study area a) Overall; b) Colombo; c) Beruwala; d) Mirissa

Diatoms dominated (60%) in the study area followed by cyanobacteria (31%) and dinoflagellates (9%) (Figure 3a). Diatoms dominated at the three transects of Colombo, Beruwala and Mirissa (78, 60 and 96%) respectively while cyanobacteria were highly abundant in Beruwala (31%) (Figure 3b-3d). The dinoflagellate percentage was higher in Colombo (17%) than in other sites (Figure 3). The dominance of diatoms (83.3%) was also reported by Uttah *et al.*, (2013) and these are regarded as the most abundant phytoplankton in turbulent, nutrient-rich waters (Tréguer *et al.*, 2018). Further, a higher diatom percentage (91%) was reported in Thalawila, off Kalpitiya (Jayasiri *et al.*, 2014) than in this study. Furthermore, the dominance of diatoms has been reported in the Southwestern

Caspian Sea with 58.2% (19 genera, 25 species) followed by dinoflagellates (16.3%) with 7 taxa (Bagheri *et al.*, 2012).

Diatoms were dominant (59%) in the study area followed by cyanobacteria (33%) and dinoflagellates (8%) (Figure 3a). Diatoms dominated in the two transects of Colombo and Mirissa (71 and 97 %) respectively while cyanobacteria dominated in Beruwala (86%) (Figure 3b-d). Dinoflagellate percentage was comparatively high in Colombo (15%) than that of other sites (Figure 3). The dominance of diatoms (83.3%) also reported by Uttah *et al.*, 2013 and is regarded as the most abundant phytoplankton in turbulent, nutrient-rich waters (Tréguer *et al.*, 2018). Further, higher diatom percentage (91%) was reported in Thalawila, off Kalpitiya (Jayasiri *et al.*, 2014) than this study. Furthermore, the dominance diatoms has been reported in the Southern Caspian Sea with 58.2% (19 genera, 25 species) followed by dinoflagellates (16.3%) with 7 taxa (Bagheri *et al.*, 2012).

There was no observation of any preponderance of harmful phytoplankton species in the study area. The blue green algae were minimal in species richness and abundance except in Beruwala. Only *Trichodesmium* was present in the forms of bundles and single cells, and it was not in opportunistic proportions. *Trichodesmium* is known to occur even in the nutrient-poor waters of the warm oceanic gyres (Hegde *et al.*, 2008). The eutrophication-indicating species and abundances were not reported in the area during the study. Human activities and physical processes likely influenced diversity and abundance of phytoplankton (Effendi *et al.*, 2016).

Table 4: Summary of One-way ANOVA for physicochemical parameters among study sites (df=2)

Parameter	Sum of squares	Mean square	F	p-value
Chlorophyll-a	25.482	12.741	10.383	0.000
TSS	10.346	5.173	2.860	0.050
Nitrite	3.866	1.933	68017.014	0.000
Nitrate	0.004	0.002	4.119	0.027
Phosphate	2.058	1.029	65300.219	0.000
Silicate	2.879	1.439	99.652	0.000

Table 5: Physicochemical parameters in Colombo, Beruwala and Mirissa

Site	Chlorophyll-a ($\mu\text{g/L}$)	TSS (mg/L)	Nitrite (mg/L)	Nitrate (mg/L)	Phosphate (mg/L)	Silicate (mg/L)
Colombo	2.38 \pm 1.83 ^b	4.94 \pm 0.90 ^b	0.770 \pm 0.009 ^b	0.034 \pm 0.035 ^{ab}	0.566 \pm 0.005 ^c	0.746 \pm 0.045 ^b
Beruwala	0.68 \pm 0.55 ^a	3.51 \pm 0.74 ^a	0.009 \pm 0.002 ^a	0.016 \pm 0.003 ^a	0.013 \pm 0.004 ^b	0.124 \pm 0.202 ^a
Mirissa	0.25 \pm 0.12 ^a	4.09 \pm 2.01 ^a	0.009 \pm 0.001 ^a	0.044 \pm 0.014 ^b	0.008 \pm 0.002 ^a	0.059 \pm 0.019 ^a
Mean \pm SD	1.10 \pm 1.42	4.18 \pm 1.42	0.263 \pm 0.365	0.031 \pm 0.024	0.196 \pm 0.266	0.310 \pm 0.336
Range	0.10–5.51	2.0–7.3	0.01–0.79	0.00–0.08	0.01–0.75	0.04–0.81

The different superscript letters in columns indicate significant variation among sites for physicochemical parameters ($p < 0.05$).

Physicochemical parameters

All the physicochemical parameters significantly varied among the study sites of Colombo, Beruwala, and Mirissa (One-way ANOVA; $p < 0.05$; Table 4). The chlorophyll-a level was significantly higher in Colombo than in the other two sites. The TSS level was significantly higher in Colombo than in the other sites, while it was intermediate at Mirissa. Nitrate-N was significantly higher in Colombo and Mirissa than in Beruwala. Phosphate-P was significantly higher in Colombo than in the other sites, while it was intermediate in Beruwala. Silicate-Si was significantly higher in Colombo than in the other sites (Table 5). High nutrient concentrations cause a preferential increase in the biomass and primary production (Chisholm, 1992; Agawin *et al.*, 2000). The mean chlorophyll-a concentration in the surface waters off Thalawila was $0.52 \pm 0.10 \text{ mg m}^{-3}$ with a wide variation of $0.07\text{--}2.70 \text{ mg m}^{-3}$ (Jayasiri *et al.*, 2014), while it is higher in Palk Strait, and chlorophyll-a concentration coincides with a high phytoplankton abundance (Jayasiri, 2007).

Table 6: Summary of one-way ANOVA for diversity indices (df=2)

Index	Sum of squares	Mean square	F	P value
Shannon -Weaver diversity index (H')	7.637	3.818	22.142	0.000
Species richness	313.267	156.633	5.760	0.008
Evenness (J') index	0.688	0.344	25.201	0.000

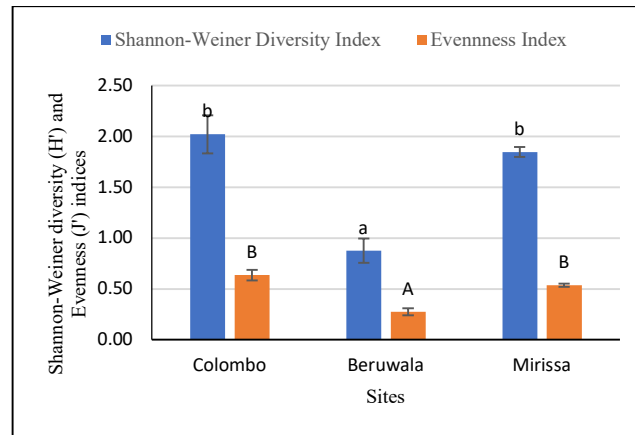


Figure 4: Shannon-Weaver diversity and Pielou's evenness indices at Colombo, Beruwala, and Mirissa. The bars with different letters in lowercase vary significantly among sites for the Shannon-Weaver diversity index and uppercase letters for Pielou's evenness indices ($p < 0.05$).

Diversity indices

Shannon-Weaver and Pielou indices (Magurran, 1996) were used to describe the phytoplankton diversity in the area. According to Bibi and Ali (2013), the values of Shannon-Weaver Index usually fall between 1.5–3.5 and only rarely does it surpass 4.5. In this study, the Shannon-Weaver diversity index and evenness were significantly higher in Colombo ($H' = 2.02 \pm 0.19$) and Mirissa ($H' = 1.85 \pm 0.40$) than in Beruwala ($H' = 0.87 \pm 0.12$). The Shannon-Weaver diversity index and evenness (J) index in the Palk Strait have varied in the range 1.6–2.7 and 0.6–0.9 respectively (Jayasiri, 2007), while in the Gulf of Mannar they are 0.06–2.4 and 0.5–1.0, respectively (Jayasiri & Priyadarshani, 2007).

Ten (10) species of toxic dinoflagellates were reported in the study area. They include: *Alexandrium catenella*, *Alexandrium monilatum*, *Gymnodinium sanguineum*, *Protoperidinium depressum*, *Protoperidinium curtipes*, *Prorocentrum micans*, *Prorocentrum redfeildii*, *Dinophysis caudate*, *Noctiluca scintillans*, and *Gymnodinium* sp.

Total phytoplankton abundance significantly correlated with diatoms, dinoflagellates, chlorophyll-a and nitrate-N at $p = 0.01$. Diatoms significantly correlated with dinoflagellates, chlorophyll-a and nitrate-N at $p = 0.01$. Dinoflagellates significantly correlated with chlorophyll-a at $p = 0.01$, and nitrate-N and phosphate-P at $p = 0.05$ (Table 7). Jayasiri *et al.* (2014) also reported that chlorophyll-a significantly correlated with the phytoplankton density ($r = 0.66$). Most diatom and dinoflagellate species have been correlated inversely to nutrients in saline pools in the Red Sea (Touliabah *et al.*, 2016). Furthermore, Jayasiri (2007) reported a high coefficient of determination ($r^2 = 0.71$) for the relationship between phytoplankton abundance and chlorophyll-a concentration in the surface waters of the Palk Strait.

Table 7: Pearson's bivariate correlations of phytoplankton and physicochemical parameters

Parameter	Diatoms	Dinoflagellates	Cyanobacteria	Chl-a	TSS	NO ₂ -N	NO ₃ -N	PO ₄ ³⁻ -P	SiO ₄ ⁴⁻ -Si
Total phytoplankton	0.97 ^a	0.78 ^a	-0.21	0.60 ^a	0.23	0.11	0.78 ^a	0.10	0.08
Diatoms		0.74 ^a	-0.45	0.58 ^a	0.28	0.21	0.81 ^a	0.21	0.15
Dinoflagellates			-0.20	0.79 ^a	0.19	0.37 ^b	0.45 ^b	0.37 ^b	0.34
Cyanobacteria				-0.19	-0.30	-0.52	-0.32	-0.51	-0.39
Chlorophyll-a					0.34	0.65 ^a	0.43 ^b	0.66 ^a	0.62 ^a
TSS						0.38 ^b	0.37 ^b	0.38 ^b	0.33
Nitrite							0.09	1.00 ^a	0.94 ^a
Nitrate								0.08	0.04
Phosphate									0.93 ^a

^a Correlation is significant at the 0.01 level (2-tailed).

^b Correlation is significant at the 0.05 level (2-tailed).

The phytoplankton and physicochemical parameters were distributed in different PCA factors. According to the results of the PCA, the original variables could be reduced to three components with eigenvalues greater than 1 (Figure 5), which accounted for 86.5% of the total variance. Chlorophyll-a, NO₂⁻, PO₄³⁻, diatoms and dinoflagellates loaded positively in the component 1 which accounts for 50% of the total variance (Table 8).

Table 8: Significant factor loadings (bold) from phytoplankton and physicochemical properties and percentage of variance explained for the individual component extracted

Parameter	Component		
	1	2	3
Chlorophyll-a	0.86	-0.01	0.38
TSS	0.51	-0.09	-0.50
NO ₂ ⁻	0.76	-0.63	0.03
NO ₃ ⁻	0.60	0.61	-0.30
PO ₄ ³⁻	0.76	-0.63	0.03
SiO ₄ ⁴⁻	0.70	-0.64	0.12
Total phytoplankton	0.70	0.69	0.10
Diatoms	0.76	0.60	-0.09
Dinoflagellates	0.77	0.33	0.41
Cyanobacteria	-0.55	0.17	0.61
Variance (%)	49.84	25.58	10.62
Total variance (%)	86.05		

The component plot in rotated space for the present study revealed that total phytoplankton and taxonomic groups are affected positively by nitrate (Figure 6). Nitrogen is generally considered as the nutrient with the greatest potential to limit phytoplankton productivity in estuaries and coastal marine waters (Ryther & Dunstan, 1971). Nitrate is the most oxidized form of nitrogen and the end product of the aerobic decomposition of organic nitrogenous matter (Renuka & Rudresh, 2014). The Canonical Correspondence Analysis for the Red Sea has revealed that cyanophyta had a strong positive relationship with water temperature, orthophosphate, ammonia, and reactive silicate while a negative relation has been found between cyanophyta and salinity (Touliabah *et al.*, 2016). However, despite the high community diversity, silicate has been found to have a potential role in shaping the community structure (Baraka *et al.*, 2021).

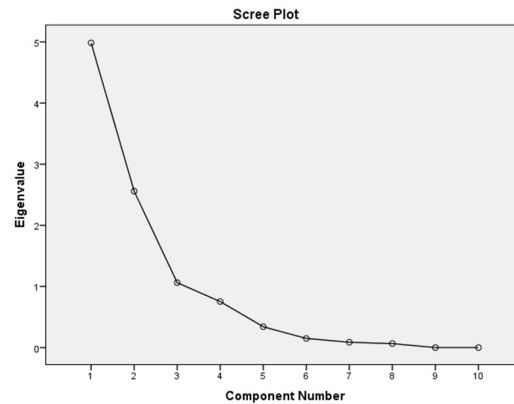


Figure 5: Scree plot for phytoplankton species and physico-chemical parameters

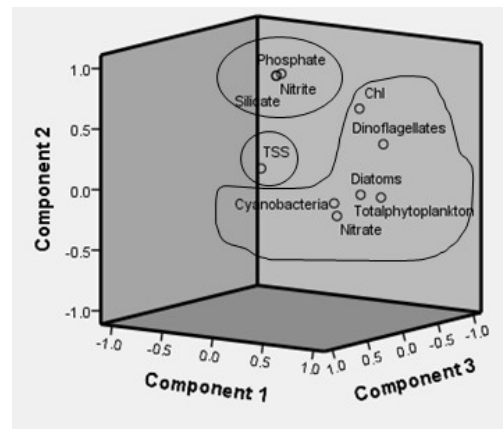


Figure 6: Component plot in rotated space for phytoplankton groups and physicochemical parameters

CONCLUSION

This study documented valuable information on the phytoplankton assemblages in the west and south-west of Sri Lanka in relation to physicochemical parameters. Phytoplankton density is comparatively low in Beruwala compared to Colombo and Mirissa, due to the freshwater discharge of the Kelani and Nilwala Rivers, respectively. High species diversity of phytoplankton was found in Colombo and Mirissa. The study revealed that the contribution of diatoms was higher than those of other taxonomic groups to the total phytoplankton population during the sampling period. Nitrate was found have a potential role in shaping the community structure. There is a possibility of blooming of cyanobacteria in Beruwala when environmental conditions are favourable. However, the low abundance of toxic species of dinoflagellates reported in this study indicates that they would not be a threat to our marine environment. Whilst this study does not record the full community diversity due to the mesh size of the plankton net used and an inability to examine the pico- and nanoplankton, it does demonstrate the low abundance with high diversity pattern of phytoplankton, typical of tropical waters. Diversity and abundance of phytoplankton communities essentially reflects the resource supply into the ecosystem and this information can be used as baseline information for any ocean based disaster or hazard. Thus, regular monitoring of phytoplankton community structure including physicochemical parameters around the seas of Sri Lanka is recommended.

Acknowledgement

The author acknowledges the National Aquatic Resources Research and Development Agency for funding this study and Dr Jagath Rajapaksha for making the location map.

REFERENCES

- Agwin N.S., Duarte C.M. & Agustí S. (2000). Nutrient and temperature control of the contribution of picoplankton to phytoplankton biomass and production. *Limnology and Oceanography* **45**(3): 591–600.
DOI: <https://doi.org/10.4319/lo.2000.45.3.0591>
- Bagheri S., Mansor M., Turkoglu M., Makaremi M., Maznah W.W.O. & Negarestan H. (2012). Phytoplankton species composition and abundance in the Southwestern Caspian Sea. *Ekoloji* **21**(83): 32–43.
DOI: <https://doi.org/10.5053/ekoloji.2012.834>
- Baraka C.S., Michael A., Painter S.C., Shayo S., Noyon M. & Margareth S.K. (2021). Spatial variation in the phytoplankton community of the Pemba Channel, Tanzania, during the south-east monsoon. *Ocean and Coastal Management* **212**: 105799.
DOI: <https://doi.org/10.1016/j.ocecoaman.2021.105799>
- Beaugrand G. (2009). Decadal changes in climate and ecosystems in the North Atlantic Ocean and adjacent seas. *Deep-Sea Research Part II: Topical Studies in Oceanography* **56**: 656–673.
DOI: <https://doi.org/10.1016/j.dsr2.2008.12.022>
- Behrenfeld M.J., O'Malley R.T., Siegel D.A., McClain C.R., Sarmiento J.L., Feldman G.C., Milligan A.J., Falkowski P.G., Letelier R.M. & Boss E.S. (2006). Climate-driven trends in contemporary ocean productivity. *Nature* **444**(7120): 752–755.
DOI: <https://doi.org/10.1038/nature05317>
- Bibi F & Ali Z. (2013). Measurement of diversity indices of avian communities at Taunsa Barrage Wildlife Sanctuary, Pakistan. *Journal of Animal and Plant Sciences* **23**: 469–474.
- Chisholm S.W. (1992). Phytoplankton size. In *Primary productivity and biogeochemical cycles in the sea*, pp. 213–237. Springer, Boston, USA.
DOI: https://doi.org/10.1007/978-1-4899-0762-2_12
- Cloern J.E. (1996). Phytoplankton bloom dynamics in coastal ecosystems: a review with some general lessons from sustained investigation of San Francisco Bay, California. *Reviews of Geophysics* **34**(2): 127–168.
DOI: <https://doi.org/10.1029/96RG00986>
- Effendi H., Kawaroe M., Lestari D.F. & Permadi M.T. (2016). Distribution of phytoplankton diversity and abundance in Mahakam Delta, East Kalimantan. *Procedia Environmental Sciences* **33**: 496–504.
DOI: <https://doi.org/10.1016/j.proenv.2016.03.102>
- Ekanayaka K.B.S.S.J., Jayasiri H.B. & Ranasinghe P.N. (2016). Phytoplankton abundance in relation to nutrient dynamics during southwest monsoon, southern coast of Sri Lanka. *NARA Scientific Sessions*, 9 March. NARA, Colombo 15, Sri Lanka.
- El Gammal M.A.M., Nageeb M. & Al-Sabeb S. (2017). Phytoplankton abundance in relation to the quality of the coastal water – Arabian Gulf, Saudi Arabia. *Egyptian Journal of Aquatic Research* **43**: 275–282.
DOI: <https://doi.org/10.1016/j.ejar.2017.10.004>
- Field C.B., Behrenfeld M.J., Randerson J.T. & Falkowski P.G. (1998). Primary production of the biosphere: integrating terrestrial and oceanic components. *Science* **281**: 237–240.
DOI: <https://doi.org/10.1126/science.281.5374.237>
- Findlay D.L. & Kling H.J. (1988). Protocols for Measuring Biodiversity: Phytoplankton in Freshwater. Available at www.eman-rese.ca/350/eman/ecotools/protocols/freshwater/phytoplankton/intro.html
- Gao J., Gu F., Abdella N.H., Ruan H. & He G. I. (2012). Investigation on culturable microflora in Tibetan kefir grains from different areas of China. *Journal of Food Science* **77**(8): 425–33.
DOI: <https://doi.org/10.1111/j.1750-3841.2012.02805.x>
- Geetha V. & Kondalarao B. (2004). Distribution of phytoplankton in the coastal waters of east coast of India. *Indian Journal of Marine Sciences* **33**(3): 262–268.
- Grasshoff K., Kremling K. & Ehrhardt M. (1999). *Methods of Seawater Analysis*. 3rd edition. pp. 632. Weinheim: Wiley-VCH, Weinheim, Germany.
DOI: <https://doi.org/10.1002/9783527613984>
- Guiry M.D. & Guiry G.M. (2013). *AlgaeBase*. World-Wide Electronic Publication. National University of Ireland, Galway. Available at <http://www.algaebase.org>, Accessed 20 September 2021.
- Hallegraeff G.M. (2003). Harmful Algal Blooms: A Global Overview. In: *Manual on Harmful Marine Microalgae. Monographs on Oceanographic Methodology* (eds. M. Hallegraeff, D.M. Anderson & A.D. Cembella) 2nd Edition, pp. 25–49. IOC-UNESCO, Paris, France.
- Harris G.P. (1986). *Phytoplankton Ecology: Structure, Function and Fluctuation*. Chapman & Hall, London, UK.

- Hasle G.R. & Syvertsen E.E. (1997) Marine diatoms. In: *Identifying Marine Diatoms and Dinoflagellates* (ed. C.R. Tomas), pp. 5–385. Academic Press, San Diego, California, USA.
DOI: <https://doi.org/10.1016/B978-012693018-4/50004-5>
- Hegde S., Anil A., Patil J., Mitbavkar S., Krishnamurthy V. & Gopalakrishna V. (2008). Influence of environmental settings on the prevalence of *Trichodesmium* spp. In the Bay of Bengal. *Marine Ecology Progress Series* **356**: 93–101.
DOI: <https://doi.org/10.3354/meps07259>
- Hoppenrath M., Elbrächter M. & Drebes G. (2009). Marine Phytoplankton: Selected microphytoplankton species from the North Sea around Helgoland and Sylt, pp. 49. Kleine Senckenberg - Reihe, Frankfurt, Germany.
- Hutchins M., Johnson A., Deflandre-Vlandas A., Comber S., Posen P. & Boorman D. (2010). Which offers more scope to suppress river phytoplankton blooms: Reducing nutrient pollution or riparian shading? *Science of the Total Environment* **408**(21): 5065–5077.
DOI: <https://doi.org/10.1016/j.scitotenv.2010.07.033>
- Jayasiri H.B. (2007). Diversity and abundance of marine plankton and benthos of selected locations of Gulf of Mannar and Palk Bay, Sri Lanka. *Journal of National Aquatic Resources Research and Development Agency* **38**: 45–59.
- Jayasiri H.B. (2009). A guide to the Marine Plankton, Gulf of Mannar and Palk Strait, Sri Lanka. Oceanography Division, NARA, Colombo 15, Sri Lanka.
- Jayasiri H.B. & Dahanayaka D.D.G.L. (2012). Saltwater Intrusion and Its Impact on Koggala Lagoon and associated waters, Southern Coast of Sri Lanka. *Asian Journal of Water, Environment and Pollution* **9**(2): 73–84.
- Jayasiri H.B., Arulananthan K. & Jinadasa S.U.P. (2014). Characterization of bio-physical features in Thalawila fishing ground, North-western coast of Sri Lanka. *Journal of the National Foundation of Sri Lanka* **42**(3): 229–238.
DOI: <https://doi.org/10.4038/jnsfsr.v42i3.7399>
- Jayasiri H.B. & Priyadarshani W.N.C. (2007). Composition, abundance and spatial variation of phytoplankton and zooplankton –off Jaffna (Palk Strait). *Journal of National Aquatic Resources Research and Development Agency* **38**: 60–76.
- Jayasiri H.B., Dahanayaka D.D.G.L. & Arulananthan K. (2016). Diversity and abundance of marine plankton and benthos of Mruthankerny, off Jaffna, Sri Lanka. *21st International Forestry and Environmental Symposium*, 23-24 September, Heritance, Kandalama, Dambulla, Sri Lanka.
DOI: <https://doi.org/10.31357/fesympo.v21i0.3049>
- Kumara Y.P. (2016). Diversity and abundance of marine plankton in relation to nutrients in southern Bay of Bengal. *MSc. Thesis*, Postgraduate Institute of Science, University of Peradeniya, Sri Lanka.
- Kumari K. & Julie J. (2003). Biomass and quantitative indices of phytoplankton in Mandovi-Zuari estuary. *Indian Journal of Fisheries* **50**(3): 401–404.
- Margalef R. (1978). Life forms of phytoplankton as survival alternatives in an unstable environment. *Oceanology Acta* **1**:493–509.
- Magurran A.E. (1996) Ecological diversity and its measurements, pp.192. Chapman & Hall, London, UK.
- Mooser K.A., Macdonald G.M. & Smol J.P. (1996). Applications of freshwater diatoms to geographical research. *Progress in Physical Geography* **20**: 21–52.
DOI: <https://doi.org/10.1177/030913339602000102>
- Parsons T.R. & Strickland J.D.H. (1963). Discussion of Spectrophotometric determination of marine-plant pigments, with revised equations for ascertaining chlorophyll a and carotenoids. *Journal of Marine Research* **21**: 55–63.
- Parsons T.R., Maita Y. & Lalli C.M. (1984). A manual of chemical and biological methods for seawater analysis, pp. 163. Pergamon Press, Toronto, Canada.
DOI: <https://doi.org/10.1016/B978-0-08-030287-4.50048-7>
- Phyto'pedia (2012). *The Phytoplankton Encyclopaedia Project 2012*. Available at <https://www.eoas.ubc.ca/research/phytoplankton/>, Accessed on 18.12.2020.
- Pielou E.C. (1966). The measurement of diversity in different types of biological collections. *Journal of Theoretical Biology* **13**: 131–144.
DOI: [https://doi.org/10.1016/0022-5193\(66\)90013-0](https://doi.org/10.1016/0022-5193(66)90013-0)
- Poloczanska et al. (20 authors) (2013). Global imprint of climate change on marine life. *Nature Climate Change* **3**: 919–925.
DOI: <https://doi.org/10.1038/nclimate1958>
- PPBS (2016). *Port Biological Baseline Survey Report: Volume 1- Port of Colombo*. Marine Environment Protection Authority (MEPA), Ministry of Mahaweli Development and Environment, Colombo, Sri Lanka.
- PPBS (2017). *Port Biological Baseline Survey Report: Volume 2- Port of Trincomalee*. Marine Environment Protection Authority (MEPA), Ministry of Mahaweli Development and Environment, Colombo, Sri Lanka.
- PPBS (2018a). *Port Biological Baseline Survey Report: Volume 2- Port of Hambantota*. Marine Environment Protection Authority (MEPA), Ministry of Mahaweli Development and Environment, Colombo, Sri Lanka.
- PPBS (2018b). *Port Biological Baseline Survey Report: Volume 3- Port of Galle*. Marine Environment Protection Authority (MEPA), Ministry of Mahaweli Development and Environment, Colombo, Sri Lanka.
- Qasim S.Z. (1972). Some observations on *Trichodesmium* blooms. *Proceedings of the Symposium on Taxonomy Biology of Blue-Green Algae*, 8-13 January 1970. Madras, India, pp. 433–438.
- Reynolds C.S. (1997). Vegetation processes in the pelagic: A model for ecosystem theory. *Excellence in Ecology* **9**: 70–71.
DOI: <https://doi.org/10.2216/i0031-8884-37-1-70.1>

- Richards F.A. & Thompson T.G. (1952). The estimation of characterization of plankton populations by pigment analyses, A spectrophotometric method for the estimation of plankton pigments. *Journal of Marine Research* **11**: 156–72.
- Roxy M.K., Modi A., Murutugudde R., Valsala V., Panickal S., Prasanna Kumar S., Ravichandran M., Vichi M. & Levy M. (2015). A reduction in marine primary productivity driven by rapid warming over the tropical Indian Ocean. *Geophysical Research Letters* **43**(2): 826–833.
DOI: <https://doi.org/10.1002/2015GL066979>
- Ryther J.H. & Dunstan W.M. (1971). Nitrogen, phosphorus, and eutrophication in the coastal marine environment. *Science* **171**(3975): 1008–1013.
DOI: [10.1126/science.171.3975.1008](https://doi.org/10.1126/science.171.3975.1008)
- Saravanakumar M., Murugesan P., Damotharan P. & Punniyamoorthy R. (2021). Multivariate approach to determine the ecological preferences of phytoplankton in Uppanar estuary, southeast coast of India. *International Journal for Modern Trends in Science and Technology* **7**(10): 23–33.
DOI: <https://doi.org/10.46501/IJMTST0710004>
- Sekadende B.C., Michael A., Painter S. C., Shayo S., Noyon M. & Kyewalyanga M.S. (2021). Spatial variation in the phytoplankton community of the Pemba Channel, Tanzania, during the south-east monsoon. *Ocean and Coastal Management* **212**: 105799.
DOI: <https://doi.org/10.1016/j.ocecoaman.2021.105799>
- Shannon C.E. & Weaver W. (1949). *The Mathematical Theory of Communication*. University of Illinois Press, USA.
DOI: https://doi.org/10.4319/lo.1997.42.5_part_2.1132
- Smayda T. J. (1997). What is a bloom? A commentary. *Limnology and Oceanography* **42**(5): 1132–1136.
- Sournia A. (1995). Red Tide and toxic marine phytoplankton of the world ocean: An inquiry into biodiversity In: *Harmful Marine Algal Blooms* (eds. P. Lassus, G. Arzul, E. Erard-Le-Denn, P. Gentien & C. Marcaillou-Le-Baut), pp. 103–112. Technique et Documentation, Lavoisier, Intercapt Ltd., France.
- Touliabah H.E., Elbassat R.A., Turki A.J., Affan M.A., Hariri M.S., Hassanine R.M.E., Abdulwassi N.I.H. & Almutairi A.W. (2016). Plankton and some environmental variables as a water quality indicator for saline pools at the Western Red Sea (Saudi Arabia). *Journal of Coastal Zone Management* **19**(1): 1000417.
DOI: <https://doi.org/10.4172/2473-3350.1000417>
- Touliabah H.E., Abu El-Kheir W.S., Kuchari M.G. & Abdulwass N.I.H. (2010). Phytoplankton composition at Jeddah coast-Red Sea, Saudi Arabia in relation to some ecological factors. *Journal of King Saud University - Science* **22**(1): 115–131.
DOI: <https://doi.org/10.4197/Sci.22-1.9>
- Tréguer *et al.* (16 authors) (2018). Influence of diatom diversity on the ocean biological carbon pump. *Nature Geoscience* **11**:27–37.
DOI: <https://doi.org/10.1038/s41561-017-0028-x>
- Uttah E.C., Ukpong G.I., Akwari A. & Osim S. (2013). Phytoplankton checklist of a near-shore estuarine transect in the equatorial Atlantic. *Transnational Journal of Science and Technology* **3**(9): 58–66.
- Weerakoon A.P., Jayasiri H.B., Jayamanne S.C. & Guruge K.P.G.K.P. (2017). Phytoplankton abundance and diversity in three sea bathing sites in Western and Southern Coasts of Sri Lanka. *5th International Symposium on Advances in Civil and Environmental Engineering Practises for Sustainable Development (ACEPS-2017)*, 16 March. Faculty of Engineering, University of Ruhuna, Galle, Sri Lanka.
- Wickramasingha L.A.A.N. & Jayasiri H.B. (2016). Investigation of phytoplankton diversity and abundance in relation to chemical parameters, off Colombo. *NARA Scientific Sessions*, 9 March, NARA, Colombo 15, Sri Lanka.
- Wijesinghe W.E.K. (2016). Diversity and abundance of phytoplankton and zooplankton in off southern and north-eastern coast of Sri Lanka. *B.Sc. Thesis*, University of Ruhuna, Matara, Sri Lanka.
- Willén E. (1976). A simplified method for phytoplankton counting. *British Phycological Journal* **11**: 265–278.
DOI: <https://doi.org/10.1080/00071617600650551>

RESEARCH ARTICLE

Mathematical Modelling

Comparative analysis of three memory selection methods for time integration of Fractional Reaction-Diffusion Equations

LW Somathilake

Department of Mathematics, Faculty of Science, University of Ruhuna, Matara, Sri Lanka.

Submitted: 08 November 2021; Revised: 30 September 2022; Accepted: 28 October 2022

Abstract: By discretising in space, non-linear time fractional reaction-diffusion equations (TFRDEs) can be converted into a system of time-fractional differential equations (TFDEs). The full memory method (FMM) and short memory method (SMM) are well-established memory selection methods used in the time integration of TFDEs. The main drawbacks of FMM and SMM are higher computational cost and uncontrollable error respectively. The only way to increase the accuracy of SMM is by increasing short memory length which causes an increase in computational cost. Especially when we apply these two methods to integrate TFRDEs, we have to solve a large system of TFDEs. Therefore, the drawbacks of these two methods affect seriously, when these are applied to solve TFRDEs. This paper aims to investigate the accuracy and efficiency of the memory selection method, Exponentially Decreasing Random Memory Method (EDRMM), and compare it with FMM and SMM when these methods apply to integrate TFRDEs. Based on these three memory selection methods, three semi-implicit numerical schemes namely semi-implicit scheme with full memory method (SI-FMM), semi-implicit scheme with short memory method (SI-SMM), and semi-implicit scheme with exponentially decreasing random memory method (SI-EDRMM) are proposed and the accuracy and CPU time (computational time (CT)) of these three numerical schemes are compared. To do this comparison, these three numerical schemes are applied to four TFRDEs whose exact solutions are known. Numerical experiments confirm that the accuracy and efficiency of the SI-EDRMM are better than that of SI-SMM and the efficiency of SI-EDRMM is higher than that of SI-FMM. Therefore, EDRMM is better than SMM and FMM for the integration of TFRDEs.

Keywords: Fractional differential equations, Full memory method, Short memory method, Time fractional reaction-diffusion equations.

INTRODUCTION

Fractional order models can be more appropriate than standard order (with integer-order derivatives and integrals) models as fractional derivatives and integrals bring forwards the temporal and spatial memory heredity of materials and processes. This is the main advantage of fractional-order models when compared to those with integer-order models. In a usual reaction-diffusion equation, both time derivative and spacial derivative (diffusion term) are integer order. This paper considers reaction-diffusion equations with fractional order time derivatives and integral order diffusion terms. This type of models are called time fractional reaction-diffusion equations (TFRDEs). There

* Corresponding author (lwsoma@gmail.com; <https://orcid.org/0000-0002-7276-1357>)



This article is published under the Creative Commons CC-BY-ND License (<http://creativecommons.org/licenses/by-nd/4.0/>). This license permits use, distribution and reproduction, commercial and non-commercial, provided that the original work is properly cited and is not changed in anyway.

is no unique definition for the fractional derivative. Caputo fractional derivative and Riemann-Liouville derivative are the more well-known fractional derivatives. In this paper, Caputo fractional derivative is applied to solve TFRDEs. Throughout this paper $\lceil x \rceil$ denotes the smallest integer greater than the real number x .

Definition 1 (Caputo derivative Podlubny & Igor (1999)). *The Caputo fractional derivative of order γ of $u(t)$ is defined as*

$${}^C D_t^\gamma u(t) = \begin{cases} \frac{1}{\Gamma(n-\gamma)} \int_a^t (t-\tau)^{n-\gamma-1} \frac{d^n u(\tau)}{d\tau^n} d\tau, & n-1 < \gamma < n, \\ \frac{d^n u(t)}{dt^n}, & \gamma = n, \end{cases} \quad (1)$$

where, $\Gamma(z)$ ($z \in \mathbb{C}$) denotes the Euler Gamma function defined by $\Gamma(z) = \int_0^\infty x^{z-1} e^{-x} dx$, γ is the order of the derivative, $n = \lceil \gamma \rceil \in \mathbb{N}$, $a \in \mathbb{R}$ is the initial time.

In this paper time fractional reaction diffusion equations (TFRDEs) of the following form are considered with suitable initial and boundary conditions.

$$\frac{\partial^\gamma u(x,t)}{\partial t^\gamma} = d\Delta u(x,t) + F(u(x,t), x, t), \quad x \in \bar{\Omega} \subset \mathbb{R}^l, \quad 0 < \gamma \leq 1, \quad 0 \leq t \leq T. \quad (2)$$

Here, $\gamma, d, T \in \mathbb{R}$, $l \in \mathbb{N}$, and the fractional differential operator is in the sense of Caputo derivative. Since $0 < \gamma < 1$, in order to solve this type of TFRDEs uniquely, one initial condition and boundary conditions are required. In physical applications, meanings of the fractional-order derivatives are unknown, but physical meanings of the integer-order derivatives are known. Therefore, in physical applications, implementing the Riemann-Liouville derivative is inappropriate as fractional order derivatives of initial conditions are necessary to implement this derivative. However, it is possible to implement fractional-order Caputo derivative in physical applications as just integer-order derivatives of initial conditions are sufficient in this derivative, and the physical meanings of these derivatives are known. Therefore, in this paper, fractional-order Caputo derivative is applied in constructing numerical schemes.

Basic theoretical aspects of fractional order differential equations have been reported by Podlubny & Igor (1999), Lakshmikantham & Vatsala (2008), Zhou *et al.* (2012), El-Sayed & El-Maghrabi (2008), and Caballero *et al.* (2011). Different types of instabilities in time fractional reaction-diffusion systems are reported by Gafiychuk & Datsko (2010). Approximate analytical solutions of some fractional reaction-diffusion equations are presented by Khan *et al.* (2012). A method to find numerical solutions of space fractional reaction-diffusion equations, based on operator splitting method, is proposed by Baeumer *et al.* (2008).

Adams type predictor-corrector method for numerical solutions of fractional differential equations is discussed by Diethelm *et al.* (2002). The author Deng (2007), has used a predictor-corrector approach where the short memory principle is applied to solve fractional differential equations. A numerical scheme for fractional differential equations based on Grünwald-Letnikov fractional-order derivative has been discussed by Scherer, Kalla, Tang & Huang (Scherer *et al.*). In that paper stability, convergence, and error propagation of the numerical scheme are discussed. The short memory principle has been applied for solving fractional order Abel differential equation by Xu & He (2011). Stability properties and order of convergence of some numerical schemes for TFDEs have been explained by Deng & Li (2012). The fast predictor-corrector method has been applied for fractional differential equations by Deng *et al.* (2016).

An implicit difference approximation for TFRDEs has been explained by Zhuang & Liu (2006). The author Rida *et al.* (2010) has used the generalized differential transform method to solve TFRDEs. Finite difference approaches have been applied to simulate TFRDEs by Murio (2008), and Zheng *et al.* (2017). In these works, full memory has been considered and it causes high computational cost. Reducing computational cost by controlling numerical errors is the main challenge in the integration of TFRDEs. This paper aims to investigate the effectiveness of the exponentially decreasing random memory method (Somathilake (2020)) in solving TFRDEs.

MATERIAL AND METHODS

In order to integrate TFRDEs of the form (2), at first it is transformed into a system of TFDEs by discretising in space.

Space discretisation

By discretising in space, the time fractional reaction-diffusion equation (2) can be approximated to a system of ODEs of the form

$$\frac{d^\gamma \mathbf{u}}{dt^\gamma} = -\frac{1}{h^2} A \mathbf{u} + \mathbf{F}(\mathbf{u}, \mathbf{x}, t), \quad t \in [0, T], \quad \mathbf{u}(0) = \mathbf{u}^0, \tag{3}$$

on finite time interval $[0, T]$. The vectors \mathbf{x} , \mathbf{u} and \mathbf{F} represent the spatial discretisations of x , u and F respectively, and A is the discrete Laplacian operator coupled with relevant boundary conditions. For example, the discrete Laplacian operator, A , on $[0, L_1]$, obtained with a finite difference approximation on a uniform mesh of $n_1 + 1$ nodes with step size $h = L_1/n_1$ is given by

$$A = \begin{pmatrix} 1 & -1 & & & \\ -1 & 2 & -1 & & \\ & \ddots & \ddots & \ddots & \\ & & -1 & 2 & -1 \\ & & & -1 & 1 \end{pmatrix}_{(n_1+1) \times (n_1+1)}, \quad \text{and } A = \begin{pmatrix} 2 & -1 & & & \\ -1 & 2 & -1 & & \\ & \ddots & \ddots & \ddots & \\ & & -1 & 2 & -1 \\ & & & -1 & 2 \end{pmatrix}_{(n_1-1) \times (n_1-1)}$$

subject to homogeneous Neumann boundary conditions and Dirichlet boundary conditions respectively. The discrete Laplacian in higher dimensions can be obtained by taking Kronecker (tensor) products of respective one-dimension discrete Laplacian embedding boundary conditions.

Constructed systems of ODEs are solved using numerical schemes explained in the next section and these numerical schemes are compared.

Numerical implementation of Caputo derivative with full memory

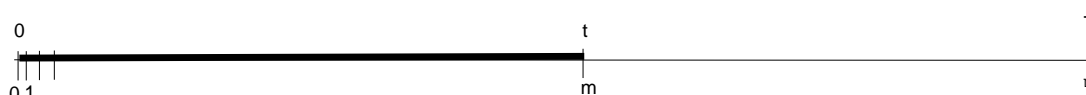


Figure 1: Sketch for the selection of full memory length

Discretising the time fractional Caputo derivative of order γ ($0 < \gamma < 1$) using finite difference formula Karatay *et al.* (2011), we get

$${}_{FM}D_{0,t}^\gamma \mathbf{u}(t_m) = \frac{1}{(\Delta t)^\gamma} \sum_{k=0}^m g_k^\gamma (\mathbf{U}^{m-k} - \mathbf{U}^0), \tag{4}$$

where \mathbf{U}^k denotes the numerical approximation to the exact value $\mathbf{u}(t)$ at $t = t_m = m\Delta t$. Here, $g_k^\gamma = (-1)^k \binom{\gamma}{k}$

where $\binom{\gamma}{k} = \frac{\Gamma(\gamma+1)}{k! \Gamma(\gamma-k+1)}$ represents the fractional binomial coefficients. Also, g_k^γ satisfies the recursive relation $g_0^\gamma = 1, g_k^\gamma = \left(1 - \frac{\gamma+1}{k}\right) g_{k-1}^\gamma$ for $k > 1$.

Numerical implementation of Caputo derivative with fixed (short) memory length

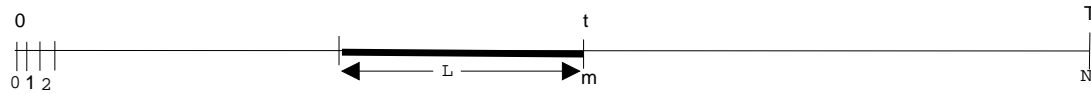


Figure 2: Sketch for the selection of short memory length

Definition 2. Let $0 < \gamma < 1$, $L \geq 0$, and $u(t)$ an integrable function in the interval $[t - L, t]$. Then the fractional derivative with fixed (short) memory length L of $u(t)$, ${}_{SM}D_{0,t}^\gamma \mathbf{u}(t)$, can be defined (base on Abdelouahab & Hamri (2016)) as

$${}_{SM}D_{0,t}^\gamma \mathbf{u}(t_m) = \begin{cases} \frac{1}{(\Delta t)^\gamma} \sum_{k=0}^{\lceil L/\Delta t \rceil} g_k^\gamma (\mathbf{U}^{m-k} - \mathbf{U}^0), & \text{if } t_m > L, \\ \frac{1}{(\Delta t)^\gamma} \sum_{k=0}^m g_k^\gamma (\mathbf{U}^{m-k} - \mathbf{U}^0), & \text{if } t_m \leq L. \end{cases} \quad (5)$$

Numerical implementation of Caputo derivative with exponentially decreasing random memory

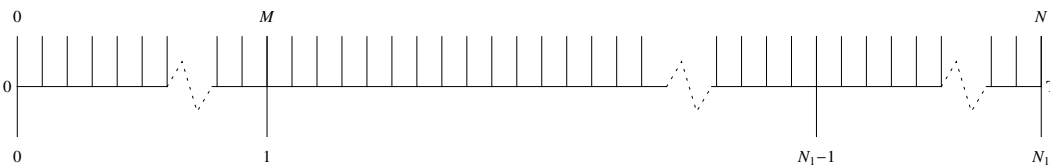


Figure 3: Sketch for the discretisation of the time interval $[0, T]$.

A discrete fractional order derivative on uniform meshes choosing memory points randomly and exponentially decreasing along the tail of the memory is introduced by Somathilake (2020). We called this method the exponentially decreasing random Memory method (EDRMM). In the derivation of this method the full-time interval $[0, T]$ is discretised into N number of partitions with equal step size Δt . M and N_1 are integers such that $N_1 = N/M$ (see Figure 3). That is the interval $[0, T]$ is divided into N_1 number of partitions P_1, P_2, \dots, P_{N_1} with equal length $M\Delta t$. The fractional order derivative with exponentially decreasing random memory is defined as follows (please see Somathilake (2020)).

$${}_{RM}D_{0,t}^\gamma u(t_m) = \begin{cases} \frac{1}{(\Delta t)^\gamma} \sum_{k=0}^m g_k^\gamma (U^{(m-k)} - U^0), & m < 2M, \\ \frac{1}{(\Delta t)^\gamma} \left(\sum_{k=0}^{n_2} g_k^\gamma (U^{(m-k)} - U^0) + \sum_{j=1}^{n_1-1} w_j \sum_{i=1}^{R_j} g_{l_{i,j}}^\gamma (U^{(m-l_{i,j})} - U^0) \right), & m \geq 2M. \end{cases} \quad (6)$$

Here, $t = m\Delta t$, $n_1 = \lceil \frac{m}{M} \rceil - 1$, $n_2 = m - M(n_1 - 1)$ if $n_1 \geq 2$, $R_j = \lceil M e^{(-\alpha j/N_1)} \rceil$; $w_j = M/R_j$ for $j = 1, 2, \dots, n_1 - 1$, $l_{i,j} = n_2 + (j - 1)M + a_i^j$. Also, α is a real number that determines the decreasing speed of the number of memory points from the partition P_i to P_{i+1} for $i = 1, 2, \dots, n_1 - 1$ and $\{a_1^i, a_2^i, \dots, a_{R_i}^i\}$ is a set of R_i number of random integers chosen in the i^{th} partition P_i ($i = 1, 2, \dots, N_1$).

Numerical methods

This section introduces three semi-implicit numerical schemes based on the fractional order derivatives described in the previous section.

A semi-implicit scheme with full memory method (SI-FMM)

Replacing the fractional derivative of order γ of (3), by the finite difference formula (4) we get

$$\frac{1}{(\Delta t)^\gamma} \sum_{k=0}^m g_k^\gamma (\mathbf{U}^{(m-k)} - \mathbf{U}^0) = -\frac{1}{h^2} A \mathbf{U}^m + \mathbf{F}^{m-1}, \quad m = 1, 2, \dots, N, \quad (7)$$

where $\mathbf{U}^m = \mathbf{U}(\mathbf{x}, t^m)$, $\mathbf{F}^m = \mathbf{F}(\mathbf{U}^m, \mathbf{x}, t^m)$, $t^m = m\Delta t$. Rearranging the system (7) we get a semi-implicit scheme:

$$\left(I + \frac{(\Delta t)^\gamma}{h^2} A \right) \mathbf{U}^m = \mathbf{U}^0 - \sum_{k=1}^m g_k^\gamma (\mathbf{U}^{(m-k)} - \mathbf{U}^0) + (\Delta t)^\gamma \mathbf{F}^{m-1}, \quad m = 1, 2, \dots, N. \quad (8)$$

In the summation at the right hand at the m^{th} time step, m number of vector summations has to be done.

A semi-implicit scheme with short memory method (SI-SMM)

By replacing the fractional derivative of order γ of (3), by the finite difference formulas (5) and rearranging terms we obtained the following semi-implicit numerical scheme.

$$\left(I + \frac{(\Delta t)^\gamma}{h^2} A \right) \mathbf{U}^m = \begin{cases} \mathbf{U}^0 - \sum_{k=1}^m g_k^\gamma (\mathbf{U}^{(m-k)} - \mathbf{U}^0) + (\Delta t)^\gamma \mathbf{F}^{m-1}, & \text{if } m \leq N_L, \\ \mathbf{U}^0 - \sum_{k=1}^{N_L} g_k^\gamma (\mathbf{U}^{(m-k)} - \mathbf{U}^0) + (\Delta t)^\gamma \mathbf{F}^{m-1}, & \text{if } m > N_L, \end{cases} \quad (9)$$

for $m = 1, 2, \dots, N$. Here, $N_L = \lceil L/\Delta t \rceil$.

A semi-implicit scheme with exponentially decreasing random memory method (SI-EDRMM)

By replacing the fractional derivative of order γ of (3), by the finite difference formulas (6) and rearranging the terms we obtain following numerical scheme.

$$\left(I + \frac{(\Delta t)^\gamma}{h^2} A \right) \mathbf{U}^m = \begin{cases} \mathbf{U}^0 - \sum_{k=1}^m g_k^\gamma (\mathbf{U}^{(m-k)} - \mathbf{U}^0) + (\Delta t)^\gamma \mathbf{F}^{m-1}; & \text{if } m < 2M, \\ \mathbf{U}^0 - B + (\Delta t)^\gamma \mathbf{F}^{m-1}; & \text{if } m \geq 2M, \end{cases} \quad (10)$$

where $B = \sum_{k=1}^{n_2} g_k^\gamma (\mathbf{U}^{(m-k)} - \mathbf{U}^0) + \sum_{j=1}^{n_1-1} w_j \sum_{i=1}^{R_j} g_{i,j}^\gamma (\mathbf{U}^{(m-l_{i,j})} - \mathbf{U}^0)$.

RESULTS AND DISCUSSION

Numerical experiments

Three TFRDEs in one dimension and one TFRDE in two dimensions of the form (2) are considered for the numerical experiments. These TFRDEs were converted into a system of TFDEs of the form (3) by discretising in space and solved using numerical schemes as explained in the above section. Algorithms for these numerical schemes were implemented and solved using Matlab on a 2.3GHz, Intel Core i5 laptop computer that had 8GB of RAM and Microsoft Windows 10. In this section, we demonstrate the accuracies and computational cost of the numerical schemes discussed in section based on the numerical solutions of these three TFRDEs.

TFRDE 1 (in one dimension): The first TFRDE is

$$\left. \begin{aligned} \frac{\partial^\gamma u(x,t)}{\partial t^\gamma} &= \frac{\partial^2 u(x,t)}{\partial x^2} + F(x,t), \quad (0 < x < 1, 0 < t < T, T > 0), \\ u(x,0) &= 0, \quad 0 \leq x \leq 1, \\ u(0,t) &= t^2, \quad u(1,t) = t^2 e, \quad 0 \leq t \leq T, \end{aligned} \right\}. \quad (11)$$

Here $F(x,t) = t^2 \left(\frac{2e^x t^{-\gamma}}{\Gamma(3-\gamma)} - 1 \right)$. The exact solution of this fractional reaction-diffusion equation is $u(x,t) = t^2 e^x$.

TFRDE 2 (in one dimension): The second TFRDE is

$$\left. \begin{aligned} \frac{\partial^\gamma u(x,t)}{\partial t^\gamma} &= \frac{\partial^2 u(x,t)}{\partial x^2} + G(x,t), \quad (0 < x < 1, 0 < t < T, T > 0), \\ u(x,0) &= 10x^2(1-x), \quad 0 \leq x \leq 1, \\ u(0,t) &= u(1,t) = 0.0, \quad 0 \leq t \leq T, \end{aligned} \right\}. \quad (12)$$

Here $G(x,t) = 10x^2(1-x) \left(\frac{t^{2-\gamma}}{\Gamma(3-\gamma)} + \frac{t^{1-\gamma}}{\Gamma(2-\gamma)} \right) - 20(t+1)^2(1-3x)$.

The exact solution of this time fractional reaction-diffusion equation is $u(x,t) = 10x^2(1-x)(1+t)^2$.

TFRDE 3 (in one dimension): Considered third TFRDE is

$$\left. \begin{aligned} \frac{\partial^\gamma u(x,t)}{\partial t^\gamma} &= \frac{\partial^2 u(x,t)}{\partial x^2} + F(u) + G(x,t), \quad (0 < x < 1, 0 < t < T, T > 0), \\ u(x,0) &= 0.0, \quad 0 \leq x \leq 1, \\ u(0,t) &= 0.0, \quad u(1,t) = t, \quad 0 \leq t \leq T, \end{aligned} \right\}. \quad (13)$$

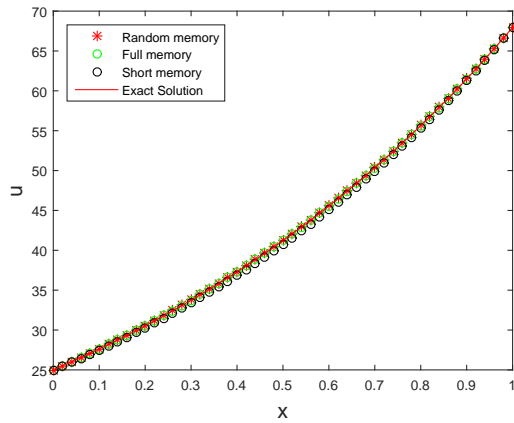
Here $F(u) = u(1-u)$, $G(x,t) = \frac{x^2 t^{1-\gamma}}{\Gamma(2-\gamma)} - x^2 t(1-x^2 t) - 2t$.

The exact solution of this time fractional reaction-diffusion equation is $u(x,t) = x^2 t$.

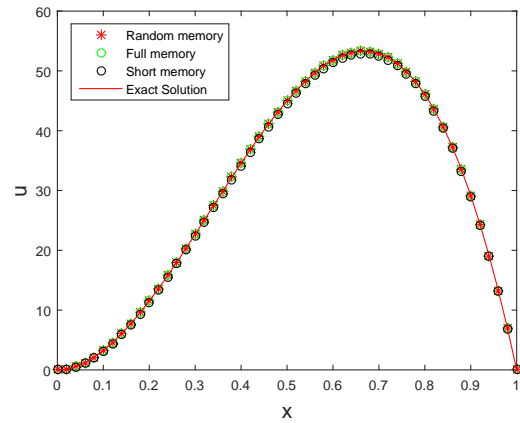
TFRDE 4 (in two dimensions): The time-fractional diffusion equation (11) in two dimension is:

$$\left. \begin{aligned} \frac{\partial^\gamma u(x,y,t)}{\partial t^\gamma} &= \frac{\partial^2 u(x,y,t)}{\partial x^2} + \frac{\partial^2 u(x,y,t)}{\partial y^2} + t^2 \left(\frac{2t^{-\gamma} e^{x+y}}{\Gamma(3-\gamma)} - 1 \right), \\ u(x,y,0) &= 0, \quad u(x,0,t) = e^x t^2, \quad u(0,x,t) = e^y t^2, \\ u(x,1,t) &= e^{1+x} t^2, \quad u(1,y,t) = e^{1+y} t^2, \end{aligned} \right\}. \quad (14)$$

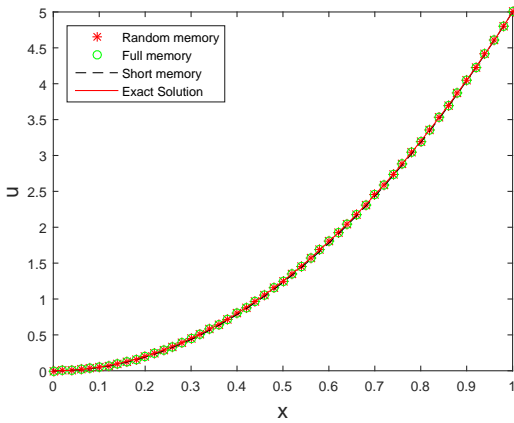
Here, $0 < x, y < 1, 0 < t < T, T > 0$. The exact solution of this time fractional reaction-diffusion equation is $u(x,y,t) = t^2 e^{x+y}$.



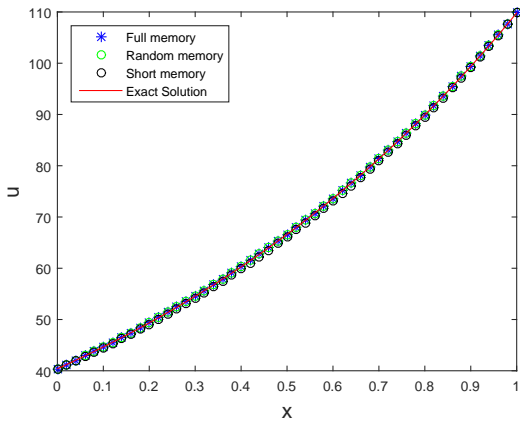
(a) Solutions of (11).



(b) Solutions of (12).

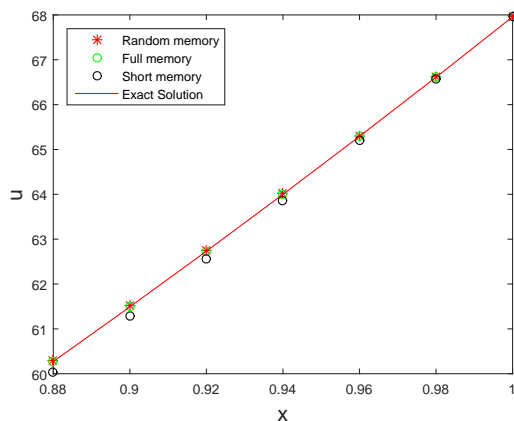


(c) Solutions of (13).

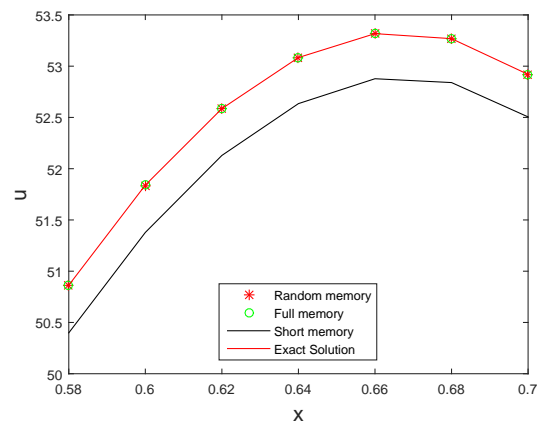


(d) Solutions of (14).

Figure 4: Exact solutions and numerical solutions of the time fractional reaction-diffusion equations (11)-(14) at $t = 5$ for the range $0 \leq x \leq 1$. Solution of (14) is evaluated at $y = 0.5$.



(a) Solutions of (11) at $t = 5$ for $0.88 \leq x \leq 1.0$.



(b) Solutions of (12) at $t = 5$ for $0.58 \leq x \leq 0.7$.

Figure 5: Exact solutions and numerical solutions of the time fractional reaction-diffusion equations (11) and (12) for short ranges of space variable x .

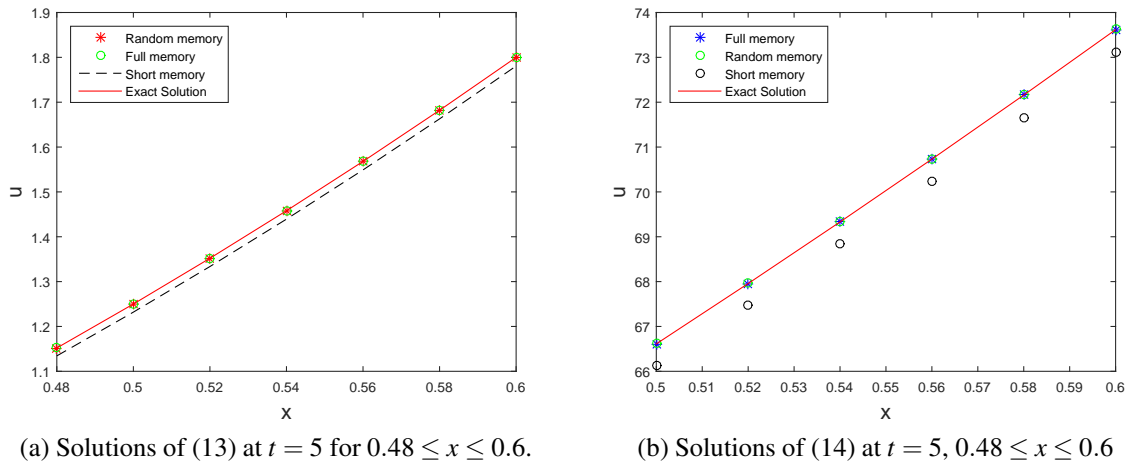


Figure 6: Exact solution and numerical solutions of the time fractional reaction-diffusion equation (13) and (14) for short ranges of space variable x .

Figures 4, 5, and 6 show the solutions of the TFRDEs (11)-(14) on space interval $0 \leq x \leq 1$ and short space intervals respectively. For these numerical simulations, $\Delta t = 0.0005$, $\Delta x = 0.02$, $L = 1$ and $\gamma = 0.9$, percentage memory length (PML) = 20 in SI-SMM and $\alpha = 3$, $M = 100$ in SI-EDRMM). Solutions of (14) are relevant to $y = 0.5$. Slight differences between exact solutions and solutions obtained by three numerical schemes are invisible in the plots of full range $0 \leq x \leq 1$ (Figure 4). But these slight differences are visible in the plots of short ranges of space variable x (Figures 5 and 6).

Comparison of numerical schemes

In this section comparison of CPU time (computation time (CT)) and numerical errors of the numerical schemes SI-FMM, SI-SMM, and SI-EDRMM are presented. Numerical errors are compared using Mean Square Error (MSE) between numerical solutions and exact solutions of the considered models. To do this comparison, we define the term “percentage decrease of computational time (PD-CT)” of the numerical scheme SI-SMM as follows

$$PD-CT \text{ of SI-SMM} = \frac{CT \text{ of SI-FMM} - CT \text{ of SI-SMM}}{CT \text{ of SI-FMM}} 100\%.$$

PD-CT of SI-EDRMM can be defined in a similar manner. Table 1 shows the CT spent to integrate equations (11), (12),(13) and (14) up to $t = 5$ by the numerical schemes SI-FMM, SI-SMM (for $PML = 20$), SI-EDRMM (for $\alpha = 3$, $M = 100$) and corresponding PD-CT. According to these data, the CT of SI-EDRMM is less than that of SI-SMM and SI-FMM. Also, PD-CT of SI-SMM and SI-EDRMM are approximately 65 and 70 respectively for the TFRDEs (11)-(13) and those values for (14) are approximately 50 and 60 respectively. Therefore, the computational cost of the proposed method has been dropped to more than 60 percent and it is a good performance and successfully faces the challenge of the computational cost of TFRDEs. Table 2 shows the MSE between exact solutions and numerical solutions at $t = 5$ of the above four TFRDEs obtained by the numerical schemes SI-FMM, SI-SMM, and SI-EDRMM. The MSE of SI-EDRMM is less than that of SI-SMM. Therefore, the proposed numerical scheme, SI-EDRMM, is more accurate and efficient than SI-SMM.

Table 1: CT (in seconds) spent to integrate (11), (12), (13) and (14) up to $t = 5$ by SI-FMM, SI-SMM and SI-EDRMM when $\Delta t = 0.0005$, $\Delta x = 0.02$, $L = 1$, $\gamma = 0.9$, ($PML = 20$ in SI-SMM and $\alpha = 3$, $M = 100$ in SI-EDRMM) and corresponding PD-CT values.

TFRDE	CT			Percentage decrease of CT	
	SI-FMM	SI-SMM	SI-EDRMM	SI-SMM	SI-EDRMM
(11)	137.7898	47.1847	37.5596	65.75603	72.74138
(12)	132.4256	46.9760	37.5890	64.5265	71.6150
(13)	128.3693	44.8422	37.7369	65.06782	70.60286
(14)	217.2794	102.5300	84.0766	52.81191	61.30485

Table 2: Mean square error between exact solutions and numerical solutions of the TFRDEs (11), (12), (13) and (14) at $t = 5$ obtained by the numerical schemes SI-FMM, SI-SMM, and SI-EDRMM when $\Delta t = 0.0005$, $\Delta x = 0.02$, $L = 1$, $\gamma = 0.9$, ($PML = 20$ in SI-SMM and $\alpha = 3$ and $M = 100$ in SI-EDRMM).

TFRDE	MSE		
	SI-FMM	SI-SMM	SI-EDRMM
(11)	4.2569×10^{-08}	0.0123	4.2869×10^{-06}
(12)	2.6898×10^{-09}	0.0118	3.5075×10^{-06}
(13)	1.7036×10^{-09}	2.6144×10^{-05}	7.6338×10^{-09}
(14)	6.4782×10^{-08}	0.0077	1.7931×10^{-05}

Table 3: Variation of CT (in seconds) against α of the scheme SI-EDRMM when it applies to simulate models (11), (12), (13) and (14) up to time $t = 5$. ($\Delta t = 0.0005$, $\Delta x = 0.02$ and $M = 100$, $\gamma = 0.9$).

α	CT			
	TFRDE 1	TFRDE 2	TFRDE 3	TFRDE 4
1	127.3680	128.0008	129.5068	191.9183
2	68.8961	68.2440	67.9349	123.7108
3	37.5596	37.5890	37.7369	84.0766
4	24.1688	24.2491	24.4602	66.5762
5	17.1975	17.3299	17.5972	56.7681
6	13.0471	12.5416	13.2837	50.7292

Tables 3 and 4 show the variation of CT and MSE between exact solutions and numerical solutions of the TFRDEs (11), (12), (13) and (14) at $t = 5$ obtained by SI-EDRMM method at different levels of α respectively. We can observe that CT of each model decreases as α increases and MSE is least at $\alpha = 3$ for all four TFRDEs. Therefore, the case $\alpha = 3$ of the SI-EDRMM is more efficient and accurate for these models and the case $\alpha = 3$ can be used for long time integration of these models.

Table 4: Variation of MSE between exact solutions and numerical solutions at time $t = 5$ against α of the SI-EDRMM when it applies to simulate models (11), (12), (13) and (14) ($\Delta t = 0.0005$, $\Delta x = 0.02$, $\gamma = 0.9$ and $M = 100$).

α	MSE of TFRDE			
	(11)	(12)	(13)	(14)
1	4.4946×10^{-05}	7.2598×10^{-05}	1.3503×10^{-07}	8.6866×10^{-05}
2	9.4744×10^{-05}	7.6337×10^{-05}	3.7272×10^{-08}	2.0793×10^{-05}
3	4.2869×10^{-06}	3.5075×10^{-06}	7.6338×10^{-09}	1.7931×10^{-05}
4	6.0004×10^{-04}	9.2545×10^{-04}	2.2156×10^{-06}	2.8102×10^{-04}
5	0.0056	0.0061	9.8472×10^{-05}	0.0036
6	0.0290	0.0257	8.7491×10^{-05}	0.0184

Numerical experiments for simulations on large time intervals

CT and MSE corresponding to integration of TFRDEs (11), (12) and (13) for large time (T=200) by the numerical schemes SI-FMM, SI-SMM, and SI-EDRMM are shown in Tables 5 and 6 respectively. These data confirm that if the proposed method SI-EDRMM is used then computational cost reduces approximately 70 percent for the large-time integrations also.

Table 5: CT (in seconds) spent to integrate (11), (12), (13) and (14) up to $T = 200$ by SI-FMM, SI-SMM and SI-EDRMM when, $\Delta x = 0.02$, $\Delta t = 0.0005$, $L = 1$ and $\gamma = 0.8$, ($PML = 20$ in SI-SMM and $\alpha = 3$, $M = 100$ in SI-EDRMM).

TFRDE	CT			Percentage decrease of CT	
	SI-FMM	SI-SMM	SI-EDRMM	SI-SMM	SI-EDRMM
(11)	551.3747	193.8450	149.1851	64.84333	72.94306
(12)	549.6185	186.1952	146.7626	66.12283	73.29737
(13)	12784.0	4704.7	3794.0	63.19853	70.32228

To compare the accuracy of SI-SMM and SI-EDRMM against SI-FMM, we compare mean square error relative to the exact solution of each numerical scheme. Mean square error relative to the exact solution of SI-FMM ($RMSE_E(SI-FMM)$) as follows.

$$RMSE_E(SI-FMM) = \frac{MSE(S_{SI-FMM} - S_E)}{\|S_E\|},$$

where S_{SI-FMM} and S_E are the solution at $T = 200$ obtained by SI-FMM and exact solution respectively. $RMSE_E(SI-EDRMM)$ and $RMSE_E(SI-SMM)$ can be defined in a similar manner. Table 6 shows the mean square errors of the numerical schemes. It can be observed that the relative mean square error of EDRMM is less than that of SMM.

Table 6: Relative mean square error between exact solutions and numerical solutions of the models (11), (12), (13) and (14) at $T = 200$ obtained by the numerical schemes SI-FMM, SI-SMM ($PML = 20$) and SI-EDRMM ($\alpha = 3$ and $M = 100$). $\Delta x = 0.02$, $L = 1$ and $\gamma = 0.8$, $\Delta t = 0.0005$ for TFRDEs (11), (12) and $\Delta t = 0.002$ for (13).

TFRDE	$RMSE_E$		
	SI-FMM	SI-SMM	SI-EDRMM
(11)	8.3800×10^{-08}	6.8971×10^{-04}	5.7845×10^{-06}
(12)	7.8361×10^{-12}	4.8271×10^{-04}	6.4764×10^{-07}
(13)	8.2416×10^{-10}	2.6203×10^{-09}	2.0417×10^{-09}

Simulation of a time-fractional reaction-diffusion system

In this section, a time fractional reaction-diffusion system that forms spatial-temporal patterns is simulated using the proposed three numerical schemes, and their performance is discussed. The analytical solution of this system is unknown. Consider the following time fractional reaction-diffusion system that appears in Somathilake & Burrage (2021).

$$\begin{aligned} \frac{\partial^\gamma u}{\partial t^\gamma} &= \Delta u + 1 - u - \beta^2 uv^2, \quad (x, y) \in \Omega \subset \mathbb{R}^2, \quad 0 \leq t \leq T, \\ \frac{\partial^\gamma v}{\partial t^\gamma} &= d\Delta v - \lambda v + \beta^2 uv^2, \quad (x, y) \in \Omega \subset \mathbb{R}^2, \quad 0 \leq t \leq T, \end{aligned} \tag{15}$$

subject to homogeneous Neumann boundary conditions:

$$\left. \begin{aligned} \nabla u \cdot \mathbf{n} &= 0, \quad x \in \partial\Omega \\ \nabla v \cdot \mathbf{n} &= 0, \quad x \in \partial\Omega \end{aligned} \right\}. \tag{16}$$

The pattern formation parameter region of the model is explained in the same paper. This model is simulated on the domain $\Omega = (1, 2) \times (1, 2)$ up to time $T = 20$ using initial conditions as a small perturbation of the equilibrium state of the model relevant to the parameter values $\beta = 7.75, \lambda = 3.5, \gamma = 0.9, d = 0.005$, which lie in the pattern formation parameter region. Isosurfaces of the numerical solutions obtained by three numerical schemes are shown in Figure 7. In these simulations, grid sizes are chosen as $\Delta x = \Delta y = 0.05, \Delta t = 0.001$. Also, $\alpha = 3, M = 200$ for SI-EDDRM and PML=10 for SI-SMM.

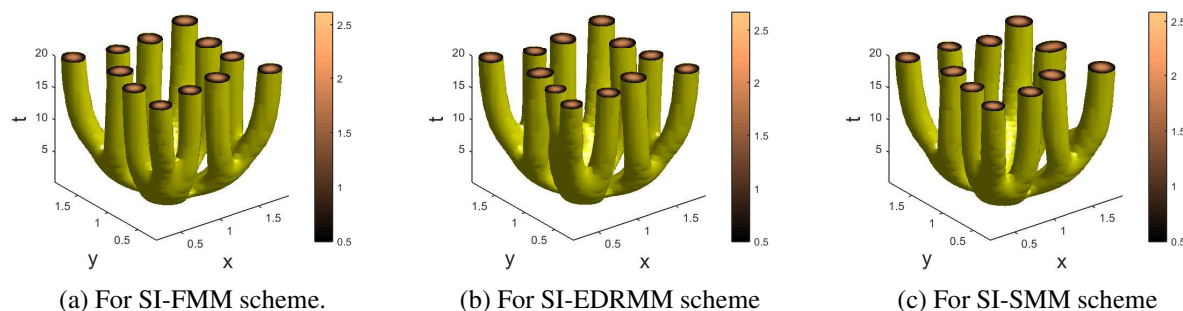


Figure 7: Isosurfaces of numerical solutions $v(x, y, t)$ for numerical schemes SI-FMM ($PML = 20$), SI-EDRMM ($\alpha = 3$ and $M = 100$) and SI-SMM for the parameter values $\lambda = 3.5, \beta = 7.75, d = 0.005$ and $\gamma = 0.9$.

Numerical solutions obtained by three numerical schemes are almost the same. To compare the numerical schemes SI-SMM and EI-EDRMM we define the mean square error of the solution of the last time step relative to the solution obtained by SI-FMM. Define the relative mean square error of SI-SMM ($RMSE_{FMM}(SI-SMM)$) as follows.

$$RMSE_{FMM}(SI-SMM) = \frac{MSE(S_{SI-FMM} - S_{SI-SMM})}{\|S_{SI-FMM}\|},$$

where S_{SI-FMM} and S_{SI-SMM} denote the solutions obtained by SI-FMM and SI-SMM respectively. ($RMSE_{FMM}(SI-EDRMM)$ can be defined in a similar manner.

Table 7: RMSE and CT of the numerical schemes in simulating the system (15).

Numerical scheme	RMSE _{FMM}	CT	Percentage decrease of CT
SI-FMM	-	1612.1	-
SI-SMM	15.08497×10^{-5}	951.3	41
SI-EDRMM	2.83664×10^{-5}	757.4	53

Also, according to the data in Table 7, the computational cost of SI-EDRMM is less than that of SI-FMM and SI-SMM, and the relative mean square error of EDRMM is less than that of SI-SMM. Therefore, SI-EDRMM is more efficient than SI-FMM and SI-SMM and is more accurate than SI-SMM in simulating the above system of TFRDEs for the chosen set of parameters.

CONCLUSION

In simulating TFRDEs, large systems of TFDEs have to be solved. As such, numerical integration of time-fractional reaction-diffusion equations is computationally expensive as computational cost mainly depends on the number of vector summations over the considered memory points in the past at each time step. Reducing computation cost is the main challenge in the numerical integration of TFRDEs. Applying well-established memory selection methods FMM and SMM for integration of TFRDEs is very difficult due to the high computational cost and uncontrollable error respectively. This paper compares the memory selection method, EDRMM proposed by Somathilake (2020), FMM, and SMM in time integration of TFRDEs. For this, the author suggests three

semi-implicit numerical schemes SI-EDRMM, SI-FMM, and SI-SMM based on three memory selection methods EDRMM, FMM, and SMM respectively. These three numerical schemes are compared by simulating four TFRDEs whose exact solutions are known and one system of TFRDEs whose exact solution is unknown.

The accuracy and efficiency of SI-EDRMM can be controlled by varying the parameter values α and M of this method. It is observed that the most accurate solutions of the considered models are given at $\alpha = 3$ of SI-EDRMM. The computational cost of SI-EDRMM (for $\alpha = 3$) is less than that of SI-FMM and SI-SMM (for PML=20). Therefore, SI-EDRMM is more efficient than SI-FMM and SI-SMM.

The MSE between exact solutions and numerical solutions obtained by SI-EDRMM ($\alpha = 3$) is less than that of SI-SMM. That is SI-EDRMM ($\alpha = 3$) is more accurate than the SI-SMM (PML=20). Therefore, SI-EDRMM is better for the numerical integration of chosen TFRDEs, because of its adequate accuracy and low computational cost. Similar results were observed when simulating the chosen system of TFRDEs.

REFERENCES

- Abdelouahab M.-S. & Hamri N.-E. (2016). The Grünwald–Letnikov fractional-order derivative with fixed memory length. *Mediterranean Journal of Mathematics* **13**(2): 557–572. DOI: <https://doi.org/10.1007/s00009-015-0525-3>.
- Baeumer B., Kovács M. & Meerschaert M. M. (2008). Numerical solutions for fractional reaction–diffusion equations. *Computers & Mathematics with Applications* **55**(10): 2212–2226. DOI: <https://doi.org/10.1016/j.camwa.2007.11.012>.
- Caballero J., Harjani, J. & Sadarangani K. (2011). Existence and uniqueness of positive solution for a boundary value problem of fractional order. In *Abstract and Applied Analysis*, volume **2011** Hindawi. Article ID 165641, 12 pages.
DOI: <http://10.1155/2011/165641>.
- Deng J., Zhao L. & Wu Y. (2016). Fast predictor-corrector approach for the tempered fractional differential equations. *Numerical Algorithms*, 1–38.
DOI: <https://doi.org/10.1007/s11075-016-0169-9>.
- Deng W. (2007). Short memory principle and a predictor–corrector approach for fractional differential equations. *Journal of Computational and Applied Mathematics* **206**(1): 174–188
.DOI: <https://doi.org/10.1016/j.cam.2006.06.008>.
- Deng W. & Li C. (2012). *Numerical schemes for fractional ordinary differential equations*. INTECH Open Access Publisher.
- Diethelm K., Ford N. J. & Freed A. D. (2002). A predictor-corrector approach for the numerical solution of fractional differential equations. *Nonlinear Dynamics*, **29**(1): 3–22.
- El-Sayed A. & El-Maghrabi E. (2008). Stability of a monotonic solution of a non-autonomous multidimensional delay differential equation of arbitrary (fractional) order. *Electronic Journal of Qualitative Theory of Differential Equations*, **2008**(16): 1–9.
- Gafiychuk V. & Datsko B. (2010). Mathematical modeling of different types of instabilities in time fractional reaction-diffusion systems. *Computers & Mathematics with Applications* **59**(3): 1101–1107. DOI: <https://doi.org/10.1016/j.camwa.2009.05.013>.
- Karatay, İ., Bayramoğlu Ş. R., & Şahin A. (2011). Implicit difference approximation for the time fractional heat equation with the nonlocal condition. *Applied Numerical Mathematics*, **61**(12): 1281–1288. DOI: <https://doi.org/10.1016/j.apnum.2011.08.007>.

- Khan N. A., Khan N.-U., Ara A. & Jamil M. (2012). Approximate analytical solutions of fractional reaction-diffusion equations. *Journal of King Saud University-Science* **24**(2): 111–118.
DOI: <http://10.1016/j.jksus.2010.07.021>.
- Lakshmikantham, V. & Vatsala, A. (2008). Basic theory of fractional differential equations. *Nonlinear Analysis: Theory, Methods & Applications*, **69**(8), 2677–2682.
DOI: <https://doi.org/10.1016/j.na.2007.08.042>.
- Murio D. A. (2008). Implicit finite difference approximation for time fractional diffusion equations. *Computers & Mathematics with Applications* **56**(4), 1138–1145.
DOI: <http://10.1016/j.camwa.2008.02.015>.
- Podlubny & Igor (1999). *Fractional Differential Equations, an introduction to fractional derivatives, fractional differential equations, to methods of their solution and some of their applications*. Mathematics in science and engineering, 198. San Diego : Academic Press.
- Rida S., El-Sayed, A., & Arafa, A. (2010). On the solutions of time-fractional reaction–diffusion equations. *Communications in Nonlinear Science and Numerical Simulation* **15**(12), 3847–3854.
DOI: <https://doi.org/10.1016/j.cnsns.2010.02.007>.
- Scherer R., Kalla, S. L., Tang, Y., & Huang, J. The grünwald–letnikov method for fractional differential equations. *Computers & Mathematics with Applications* **62**, number=3, pages=902–917, year=2011, publisher=Elsevier, note=
DOI: <https://doi.org/10.1016/j.camwa.2011.03.054>.
- Somathilake, L. W. (2020). An efficient numerical method for fractional ordinary differential equations based on exponentially decreasing random memory on uniform meshes. *Journal of the National Science Foundation of Sri Lanka* **48**(2), 163–174.
DOI: <http://dx.doi.org/10.4038/jnsfsr.v48i2.9026>.
- Somathilake, L. W. & Burrage, K. (2021). Pattern formation in a time fractional reaction-diffusion system. *Journal of Fractional Calculus and Applications*, **12**(1), 9–24. <http://math-frac.org/JFCA/>.
- Xu Y. & He, Z. (2011). The short memory principle for solving abel differential equation of fractional order. *Computers & Mathematics with Applications*, **62**(12), 4796–4805.
DOI: <https://doi.org/10.1016/j.camwa.2011.10.071>.
- Zheng M., Lju, F., Liu, Q., Burrage, K., & Simpson, M. J. (2017). Numerical solution of the time fractional reaction–diffusion equation with a moving boundary. *Journal of Computational Physics*, **338**, 493–510.
DOI: <http://dx.doi.org/10.1016/j.jcp.2017.03.006>.
- Zhou W.-X., Peng, J.-G., & Chu, Y.-D. (2012). Multiple positive solutions for nonlinear semipositone fractional differential equations. *Discrete Dynamics in Nature and Society*, **2012**. Article ID 850871, 10 pages.
DOI: <http://doi.org/10.1155/2012/850871>.
- Zhuang P. & Lju, F. (2006). Implicit difference approximation for the time fractional diffusion equation. *Journal of Applied Mathematics and Computing*, **22**(3), 87–99.
DOI: <https://doi.org/10.1007/BF02832039>.